# ATOMIC SCALE CHARACTERISATION OF OXIDE DISPERSION STRENGTHENED STEELS FOR FUSION APPLICATIONS

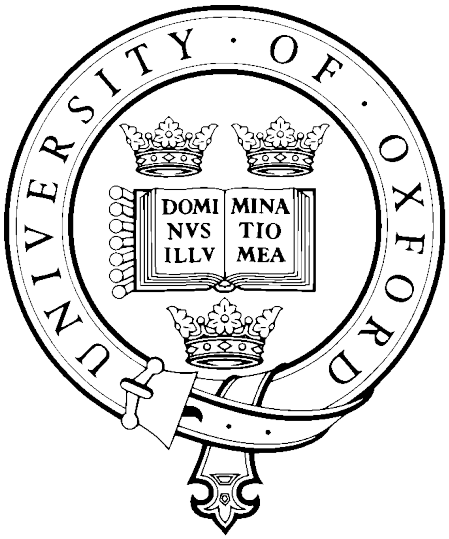


**Ceri Williams**

Linacre College

*A thesis submitted for the degree of Doctor of Philosophy*

Michaelmas Term 2011

This is what I have observed to be good: that it is appropriate for a person to eat, to drink and to find satisfaction in the toilsome labour under the sun during the few days of life God has given them…

*Ecclesiastes 5:18*

# Abstract

Reduced-activation ferritic steels are considered as the primary candidate materials for structural applications within nuclear fusion power plants. It is known that by mechanically alloying ferritic steel powder with Y (usually in the form of $Y_2O_3$) then consolidating the material by hot isostatic pressing, a nanoscale dispersion of oxygen rich nanoclusters as small as ~2nm is introduced into the microstructure. This vastly improves high temperature strength and creep resistance, and the nanoclusters also act as trapping sites for helium and point defects produced under irradiation.

In this thesis, the evolution of the oxide nanoclusters in a Fe-14Cr-2W-0.3Ti & $0.3Y_2O_3$ ODS alloy was investigated primarily using atom probe tomography. The microstructure was characterised at various points during processing to give an insight into the factors influencing the formation of the nanoclusters. It was found that the nanoclusters nucleated during the mechanical alloying stage, then followed near classical nucleation and growth mechanisms keeping the same composition of ~8%Y, ~12%Ti,~25%O and ~45%Cr throughout. The formation and evolution of 5-15nm grain boundary oxides was also observed, and these were shown to form first as $Cr_2O_3$ particles that subsequently transform into a Y-Ti-O based oxide on further processing.

The influence of mechanical alloying with 0.5wt.%$Fe_2Y$ rather than 0.3wt.%$Y_2O_3$ was also investigated, and this showed that there was no difference in the final microstructure produced provided the level of Ti in the starting powder was tightly controlled. Without sufficient Ti, the nanoclusters were Y-O based and ~6nm diameter. Both the Y-O and Y-Ti-O nanoclusters were moderately stable on annealing at 1200°C for up to 100 hours, with only minimal coarsening observed. Ti was found not to influence the coarsening rate of the nanoclusters significantly.

The stability of the oxide nanoclusters under irradiation was investigated by using $Fe^{2+}$ ion irradiation to simulate displacement cascade damage in the ODS-Eurofer material (the official European candidate material for testing in the ITER fusion test reactor). Doses up to ~6 dpa at 400°C were used, and there was no significant change to the nanocluster distribution. However segregation of Mn to dislocations was observed after irradiation.

These results indicate that ODS steels are good candidate structural materials, as the microstructure is stable at high temperature and under irradiation. The starting powders, and processing parameters need to be tightly controlled in order to produce the optimal material for use in service.

# Preface

This doctoral thesis is an account of the work carried out by the author in the Department of Materials, University of Oxford between October 2008 and November 2011 under the supervision of Dr. Emmanuelle Marquis, Professor George Smith and Professor Steve Roberts. All of the work is original, and where the work of others is included it is clearly referenced and acknowledged in the text. Figures reproduced from journal articles are done so with the permission of Elsevier. No part of this thesis has been submitted or accepted for any other degree at this university or elsewhere.

Parts of this work have been published in the following peer reviewed journals:

C.A. Williams, J.M. Hyde, G.D.W. Smith, E.A. Marquis,**The effect of Ti on the coarsening behavior of oxygen-rich nanoparticles in oxide-dispersion-strengthened steels after annealing at 1200 °C** *Scripta Materialia* (2012).

P. Unifantowicz, T. Płociński, C.A. Williams, R. Schäublin, N. Baluc. **Structure of complex oxide nanoparticles in a Fe-14Cr-2W-0.3Ti-0.3$Y_2$O3 ODS RAF steel** *Journal of Nuclear Materials*, Submitted article (2011).

C.A. Williams, J.M. Hyde, G.D.W. Smith, E.A. Marquis, **Effects of Heavy-ion Irradiation on Solute Segregation to Dislocations in Oxide-dispersion-strengthened Eurofer 97 steel**, *Journal of Nuclear Materials,* 412 (2011) 100-5.

C.A.Williams, P. Unifantowicz, Z. Oksiuta, N. Baluc, G.D.W. Smith, E.A. Marquis, **Atom probe tomography analysis of Ti-Y-O clustering during processing of nanoscale oxide particles in 14%Cr ODS ferritic steels**, *Materials Research Society Symposium Proceedings*, 1298 (2011) 15-20.

C. A. Williams, E.A. Marquis, A. Cerezo, G.D.W. Smith , **Nanoscale Characterisation of ODS Eurofer 97 Steel: An Atom-probe Tomography Study**, *Journal of Nuclear Materials,* 400 (2010) 37 – 45.

E.A. Marquis, J.M. Hyde, D.W. Saxey, S. Lozano-Perez, V. de Castro, D. Hudson, C. Williams, S. Humphry-Baker, and G.D.W. Smith, **Nuclear Reactor Materials at the Atomic Scale**, *Materials Today*, 11 (2009) 30 - 37.

# Acknowledgments

I would like to express my gratitude to the many people who have supported me throughout my time in Oxford. This work would not have been completed without them. First and foremost, I would like to thank my primary supervisors Dr. Emmanuelle Marquis and Prof. George D. W. Smith for shaping my scientific project and providing motivation, continuous ideas and guidance throughout. Dr. Marquis was instrumental in my training in almost all aspects of my research, and I am incredibly grateful for all the time and energy she put in. I am also indebted to Prof. Alfred Cerezo for his enthusiasm and support at the outset of the project, and to Prof. Steve Roberts for taking over some of the more tedious supervisory tasks towards the end.

I thank the Department of Materials at Oxford for awarding me an EPSRC DTA Studentship that has funded this research. Much of this work would not be possible without the collaboration with Prof. Nadine Baluc and Dr. Paulina Unifantowicz from EPFL, and I thank them for a generous supply of materials and for many useful discussions. I acknowledge the Royal Society for financial support of this collaboration through the International Joint Project Grant. I also thank Dr. Rainer Lindau of KIT for supplying the ODS-Eurofer material.

Many researchers have contributed to the work in this thesis. I am particularly grateful to Dr. Daniel Haley for patience in teaching me the basics of computer programming and for creating the posgen and splicepos software, which I have used extensively in this work. Dr. Jon Hyde also provided support and assistance with many aspects of this thesis, and I thank him for his time and efforts in reading through my work, and for creating tools for data analysis in the PosAT software. I also acknowledge Dr. Baptiste Gault for guidance with MATLAB, and for the provision of many useful scripts. I thank Dr. Gareth Hughes and Dr. Daniel Hudson for assistance with FIB, and Dr. Chris Salter for EPMA analysis. I would also like to thank the technical staff at the Department of Materials, particularly Mr. Bob Lloyd, Mr Laurie Walton, and Mr. Ron Doole.

The FIM group has provided a great working atmosphere, and I thank you all (past and present) for helpful discussions and making work enjoyable over last few years. I also thank the Cardo girls, all at OUWPC, and those from JPG at St. Aldates for fun and friendship during my time at Oxford. Finally, I acknowledge a deep faith in Jesus Christ, and thank my parents and my sister Ruth for all their love and encouragement to the end.

# Table of Contents


**1 INTRODUCTION ..... 1**

**2 LITERATURE REVIEW ..... 4**

**2.1 Introduction to nuclear fusion ..... 4**

**2.2 The development of reduced activation ferritic/martensitic steels ..... 8**
2.2.1 Base alloy development ..... 8
2.2.2 Base alloy compositions ..... 9
2.2.3 Behaviour under irradiation ..... 11
2.2.4 Mechanical properties at high temperature ..... 12

**2.3 The improvement of RAFM steels for fusion applications by ODS ..... 14**
2.3.1 Processing routes ..... 15
2.3.2 Microstructure ..... 17
2.3.3 Nanoscale oxide particles ..... 18
2.3.3.1 Oxide particle formation ..... 18
2.3.3.2 Oxide particle composition ..... 20
2.3.3.3 Oxide particle coherency ..... 23
2.3.4 Mechanical properties ..... 24

**2.4 Approaches to developing the optimal ODS microstructure ..... 27**
2.4.1 Optimisation of microstructure by varying processing conditions ..... 27
2.4.1.1 Milling ..... 27
2.4.1.2 Consolidation ..... 28
2.4.1.3 Post consolidation thermal/mechanical treatments ..... 28
2.4.2 Optimisation of microstructure by varying powder composition ..... 29
2.4.2.1 Variation in oxide composition ..... 29
2.4.2.2 Variation in $Y_2O_3$ concentration ..... 30
2.4.2.3 Effect of minor alloying elements (Ti, Al, etc) ..... 30

**2.5 Stability of the ODS microstructure at high temperature ..... 32**

**2.6 Behaviour of the ODS microstructure under irradiation ..... 33**
2.6.1 Effectiveness of particles in trapping helium ..... 36

**2.7 Summary ..... 38**

**3 MATERIALS AND EXPERIMENTAL METHODS ..... 39**

**3.1 Materials ..... 39**
3.1.1 ODS steels ..... 39
3.1.2 Bulk oxides ..... 40

**3.2 Transmission electron microscopy ..... 41**

**3.3 Atom probe tomography ..... 41**
3.3.1 Overview ..... 41
3.3.2 Specimen preparation ..... 45
3.3.2.1 Electropolishing ..... 45
3.3.2.2 Focussed ion beam milling (FIB) ..... 47
3.3.3 Selecting appropriate analysis conditions ..... 49
3.3.4 Mass spectrum analysis ..... 52
3.3.4.1 Mass peak ranging ..... 54
3.3.4.2 Peak deconvolution ..... 54
3.3.5 3-D Reconstruction ..... 55
3.3.5.1 Determination of the field factor ..... 56
3.3.5.2 Determination of the ICF ..... 58
3.3.6 Data visualisation ..... 61
3.3.7 Common APT artefacts ..... 62

**3.4 Ion implantation ..... 62**

**4 APT DATA ANALYSIS TECHNIQUES ..... 65**

**4.1 Introduction ..... 65**

**4.2 Data processing ..... 65**

**4.3 Composition measurements ..... 66**

**4.4 Assessment of data quality ..... 67**
4.4.1 Background correction ..... 69
4.4.2 Peak tail correction ..... 69

**4.5 Analysis of oxide particles and clusters ..... 71**
4.5.1 Proxigram ..... 71
4.5.2 Maximum separation cluster selection method ..... 72
4.5.2.1 Matrix correction ..... 74
4.5.3 Method of selecting appropriate cluster selection parameters ..... 75
4.5.3.1 Solute selection ..... 76
4.5.3.2 Dmax and Nmin selection ..... 77
4.5.3.3 L selection ..... 79
4.5.4 Influence of cluster selection parameters on the characterisation of the clusters ..... 79
4.5.4.1 Effect of cluster selection parameters on cluster composition ..... 79
4.5.4.2 Effect on number density of clusters and the cluster size distribution ..... 81
4.5.4.3 Effect on nanocluster size and volume fraction ..... 83
4.5.5 Statistics of the nanocluster distribution ..... 84
4.5.5.1 Number density ..... 84
4.5.5.2 Nanocluster size ..... 85
4.5.5.3 Nanocluster volume fraction ..... 86

**4.6 1-D composition profile for the analysis of grain boundaries ..... 86**

**4.7 Cylindrical radial composition profile for the analysis of dislocations ..... 86**

**5 APT ANALYSIS OF OXIDE COMPOSITION ..... 87**

**5.1 Introduction ..... 87**
5.1.1 Background to the analysis of oxides using APT ..... 88

**5.2 Reference study on bulk $Y_2O_3$ ..... 89**
5.2.1 Experimental conditions ..... 89
5.2.2 Mass spectrum analysis ..... 89
5.2.3 Possible causes of compositional inaccuracy ..... 90
5.2.3.1 Evaporation between pulses ..... 90
5.2.3.2 Loss of ions during multiple ion evaporation events ..... 91
5.2.3.3 Summary ..... 99

**5.3 Y-O nanoclusters in the EPFL-PA-$Fe_2Y$ alloy ..... 99**
5.3.1 Influence of laser power on the characterisation of the clusters ..... 100
5.3.2 Multi-hit analysis ..... 104
5.3.2.1 Correlated ion evaporation in Y-O clusters ..... 105
5.3.2.2 Implications for the accuracy of the measured composition of the oxide clusters ..... 107

**5.4 Titanium-containing oxides ..... 109**
5.4.1 Bulk oxide analysis ..... 109
5.4.1.1 Mass Spectrum analysis ..... 109
5.4.1.2 Multi-hit analysis ..... 110
5.4.1.3 Correlated ion evaporation ..... 111
5.4.1.4 Self-ion pairs ..... 113
5.4.1.5 Incorrect ion identification within multi-hits ..... 114
5.4.1.6 Discussion ..... 117

**5.5 Y-Ti-O nanoclusters in the EPFL-PA-$Y_2O_3$ alloy ..... 117**
5.5.1 Mass spectrum analysis ..... 118
5.5.2 Evaporation behaviour of the nanoclusters under varying field conditions ..... 118
5.5.3 Correlated ion evaporation ..... 119
5.5.4 Implications for the accuracy of the measured composition of the nanoclusters ..... 120

**6 STABILITY OF OXIDE NANOCLUSTERS AT HIGH TEMPERATURES ..... 123**

**6.1 Introduction ..... 123**

**6.2 Characterisation of EPFL pre-alloyed ODS alloys ..... 124**
6.2.1 EPFL-PA-$F_{E2}Y$ material ..... 124
6.2.1.1 Core-shell structure ..... 126
6.2.2 EPFL-PA-$Y_2O_3$ material ..... 126
6.2.2.1 Core-shell structure of the nanoclusters ..... 127

**6.3 Annealing at high temperature – 1200°C ..... 129**
6.3.1 EPFL-PA-$FE_2Y$ material ..... 129

6.3.1.1 Effect on nanocluster distribution ..... 129
6.3.1.2 Effect on nanocluster composition ..... 130
Effect of annealing on the Cr shell ..... 131
6.3.2 EPFL-PA-$Y_2O_3$ material ..... 132
6.3.2.1 Effect on nanocluster distribution ..... 132
6.3.2.2 Effect on nanocluster composition ..... 133
6.3.3 Influence of Ti on particle stability ..... 134
6.3.3.1 Effect of the Cr shell on nanocluster coarsening ..... 135

**6.4 Annealing at operating temperatures - 700°C ..... 136**

**7 DEVELOPMENT OF ODS MICROSTRUCTURE DURING PROCESSING ..... 138**

**7.1 Introduction ..... 138**

**7.2 Evolution of microstructure after mechanical alloying with $Y_2O_3$ ..... 139**
7.2.1 Overall microstructure ..... 139
7.2.2 Oxide nanocluster development ..... 143
7.2.3 Grain boundary analysis (including grain boundary oxides) ..... 147

**7.3 Evolution of microstructure after mechanically alloying with $Fe_2Y$ ..... 150**
7.3.1 Comparison of powder after MA with $Fe_2Y$ and $Y_2O_3$ ..... 150
7.3.1.1 Grain boundary analysis ..... 151
7.3.2 Consolidated material made from elemental powders MA with $Fe_2Y$ ..... 152
7.3.2.1 Comparison of EPFL-PA-$FE_2Y$ (MA with pre-alloyed powder) and EPFL- E-$FE_2Y$ (MA with elemental powder) using EPMA ..... 153
7.3.3 Significance of MA with $Fe_2Y$ ..... 154

**8 UNDERSTANDING ASPECTS OF THE ODS MICROSTRUCTURE ..... 157**

**8.1 Key results from APT analysis of EPFL alloys ..... 157**
8.1.1 APT analysis of oxide composition ..... 157
8.1.2 Stability of nanoclusters after high temperature annealing ..... 157
8.1.3 Evolution of nanoclusters and grain boundary particles ..... 157

**8.2 HREM observations ..... 158**
8.2.1 EPFL-PA-$FE_2Y$ material ..... 158
8.2.2 EPFL-E-$Y_2O_3$ material ..... 158

**8.3 Thermodynamically stable oxide phases ..... 159**
8.3.1 Possible stable oxide phases for nanoclusters ..... 160
8.3.2 Crystal structures of stable oxide phases ..... 162
8.3.3 Interface coherency and the influence of ‘lattice matching’ ..... 163

**8.4 Composition of the oxide nanoclusters ..... 164**
8.4.1 Cr content of the nanoclusters ..... 164
8.4.1.1 Evidence in favour of a Cr shell around the nanoclusters ..... 165
8.4.1.2 Evidence in favour of Cr at the nanocluster core ..... 166

8.4.1.3 Discussion ..... 166
8.4.2 Composition of the Y-O clusters (in the EPFL-PA-$FE_2Y$ alloy) ..... 168
8.4.3 Composition of the Y-Ti-O clusters (EPFL-PA-$Y_2O_3$ and EPFL-E-$Y_2O_3$ alloys) ..... 170

**8.5 Formation and evolution of the oxide nanoclusters ..... 171**
8.5.1 Nanocluster nucleation ..... 171
1.1.1.1 The influence of Y, Ti and O on the formation of the nanoclusters ..... 172
8.5.1.1 The influence of volumetric expansion and interfacial energy on the formation of the nanoclusters ..... 174
8.5.1.2 Summary of the effect of Ti on the nanocluster formation ..... 175
8.5.2 Nanocluster growth ..... 176
8.5.3 Nanocluster coarsening ..... 176

**8.6 Grain boundary oxide particle formation ..... 178**

**9 EFFECTS OF IRRADIATION OF ODS MICROSTRUCTURE ..... 182**

**9.1 Introduction ..... 182**

**9.2 Ion implantation of ODS-Eurofer 97 ..... 185**
9.2.1 Nanocluster analysis after irradiation ..... 185
9.2.2 Dislocation analysis ..... 188
9.2.2.1 As-received material ..... 188
9.2.2.2 Irradiated Material ..... 190
9.2.2.3 Annealed Material ..... 194

**9.3 Discussion ..... 196**
9.3.1 Validity of the experimental set-up ..... 196
9.3.2 Stability of nanoclusters under irradiation ..... 198
9.3.3 Effect of irradiation on dislocations ..... 200

**9.4 Conclusions ..... 202**

**10 SUMMARY AND CONCLUSIONS ..... 204**

**10.2 Implications of these findings ..... 206**

**10.3 Future research ..... 207**

**11 REFERENCES ..... 208**

**12 APPENDIX A ..... I**

**13 APPENDIX B ..... II**

# 1 Introduction

Due to an increase in global demand for clean, low-carbon energy sources, there is renewed interest in obtaining commercial power from nuclear fusion. One of the limiting factors in the development of fusion power plant has been engineering suitable structural materials to withstand the high neutron flux and operating temperatures >500°C. In this context, a considerable amount of work has been dedicated to the development of a range of reduced activation ferritic/martensitic steels with oxide-dispersion-strengthening (ODS). These alloys exhibit significant improvement in high temperature strength and stability under irradiation over their non-ODS counterparts. Despite all this effort, optimization of the alloy microstructure for any particular application has yet to be achieved. This will only be possible by establishing a greater understanding of the processing, microstructure and mechanical properties.

ODS steels are usually produced by ball milling of alloy powder with $Y_2O_3$ powder followed by hot isostatic pressing (HIP). It has been suggested that the $Y_2O_3$ powder completely dissolves during the ball milling process [1] and re-precipitates during consolidation. The number density and size of the oxides depends on the alloy chemistry – Ti for instance was shown to significantly refine the precipitate structure [2]. The nucleation mechanisms are unclear and so is the exact nature of the nucleating phase. Understanding the oxide nanocluster formation mechanism is important for two reasons. Firstly, understanding the role of alloy composition and the processing conditions in the particle formation means that processing parameters can then be tailored to obtain a particular microstructure. The second point is that it will allow the effects of irradiation on the microstructure to be better understood. It is clear from the literature that there is very little mechanistic understanding of the role of particles in maintaining the stability of the microstructure; but in order

to comprehend the effects of irradiation and thermal annealing, the detailed structure of the particles and how they evolve must be characterised.

This work focuses on the high resolution characterization of the oxide nanoclusters forming in several ODS alloys of different chemistry, primarily using atom probe tomography (APT). The effect of irradiation on the ODS microstructure is also investigated by using self-ion implantation to simulate the displacement cascades expected in a fusion reactor. The literature review in **Chapter 2** summarises the development of ODS alloys and the current understanding of the microstructure. The chapter goes on to describe the status of current research into the stability of the microstructure at high temperature and under irradiation.

APT has the potential to give very accurate chemical analysis on the atomic scale; but careful interpretation of the results, and comparisons with other techniques are also required. A considerable portion of this study was devoted to determining appropriate analysis conditions for APT analysis, and ascertaining the most suitable methods to analyse the data. **Chapter 3** gives an overview of the APT technique and analysis conditions, together with all other experimental techniques used in the study. **Chapter 4** is devoted to the methods used to analyse the APT data, and **Chapter 5** is concerned with the quantification of the oxide composition from APT data.

The characterisation of 14Cr-2W-0.3Ti ODS alloys developed by Baluc et. al at EPFL is presented in **Chapter 6**. The core-shell structure of the nanoclusters is presented, and the coarsening behaviour of the nanoclusters is investigated. The kinetics and formation mechanisms of the oxide phases are investigated by analyzing powder flakes subjected to different annealing treatments in **Chapter 7**. The nanoclusters in the power are then compared to those in the consolidated material. The results presented in Chapter 6 and 7 are discussed in detail in **Chapter 8**. The controlling factors in the formation and evolution of the nanoclusters are considered, with particular emphasis on the effect of Ti on the stability of the nanoclusters.

Finally the stability of the nanoclusters under irradiation is considered. The ODS-Eurofer alloy is a material scheduled to be tested in the ITER test fusion reactor. **Chapter 9** addresses how displacement cascades created by self ion implantation are likely to impact the nanoclusters in the ODS-Eurofer. Solute segregation to dislocations enhanced by the ion implantation is also presented. The major findings of all work presented are then summarised in **Chapter 10.**

**Appendix A** shows a table of possible mass-to-charge-state ratios used to identify peaks in the mass spectrum generated by APT.

**Appendix B** presents scripts written in MATLAB to perform some of the APT data analysis described in Chapters 4 and 5. Some codes written by colleagues from the Oxford FIM group have been utilised in these scripts, and are referenced where appropriate, but the code itself is not included.

# 2 Literature Review

For decades, there has been substantial interest in generating power by nuclear fusion. The appeal of fusion energy is that vast amounts of energy can theoretically be obtained from minimal quantities of fuel, with no atmospheric pollution. Llewellyn Smith writes that the lithium from one laptop computer battery, combined with half a bath of water could generate as much electricity as 40 tons of coal [3]. Harnessing the energy that powers the sun has proven to be one of the world's greatest scientific and engineering challenges, and unfortunately, is far more difficult than originally anticipated. While nuclear fusion has been demonstrated on an experimental level, a number of issues need to be resolved before the experiment can be scaled up to a commercial power plant.

This review of current scientific literature introduces the concept of nuclear fusion, together with some of the major problems associated with building a commercial reactor. The difficulties in designing structural materials capable of operating at high temperature and withstanding high neutron doses are presented, and current research on potential solutions to these problems is reviewed.

## 2.1 Introduction to nuclear fusion

The mass of a helium atom is less than the combined mass of four hydrogen atoms. The difference between the two is the origin of the energy that we hope to capture in a fusion reactor. The atoms first need to be travelling fast enough to overcome their Coulomb repulsion, and it is found that the fastest reaction rates occur between two rare forms of hydrogen – deuterium and tritium [3]. The plasma temperatures required for the reaction shown below are still in excess of 200 million degrees Celsius [3].

$$^{2}H + {}^{3}H \quad \rightarrow \quad {}^{4}He + 14MeV \text{ neutron} + 3.5MeV\ \alpha\text{-particle}$$

The energy released is far greater than any current fission reaction, and generates no radioactive waste directly. The challenges are therefore building a reactor to confine the fusion reaction, supplying the initial energy, and extracting heat to generate electricity. The 14MeV neutrons are also a significant concern, as they are can penetrate deep into the structure of the reactor causing transmutation and other radiation-induced defects.

Fusion has been achieved experimentally using the method of magnetic confinement in the Joint European Torus [4]. An experimental test reactor (ITER – illustrated in Figure 2.1) is currently under construction. The design involves constraining a plasma in a toroidal magnetic field – a 'Tokamak' [5]. Initially heat must be applied externally, providing a small proportion of the plasma with sufficient energy for fusion to occur. Once fusion occurs above a certain rate, the energetic α-particles are absorbed by the plasma, thus sustaining the high temperatures required to maintain the fusion reaction.

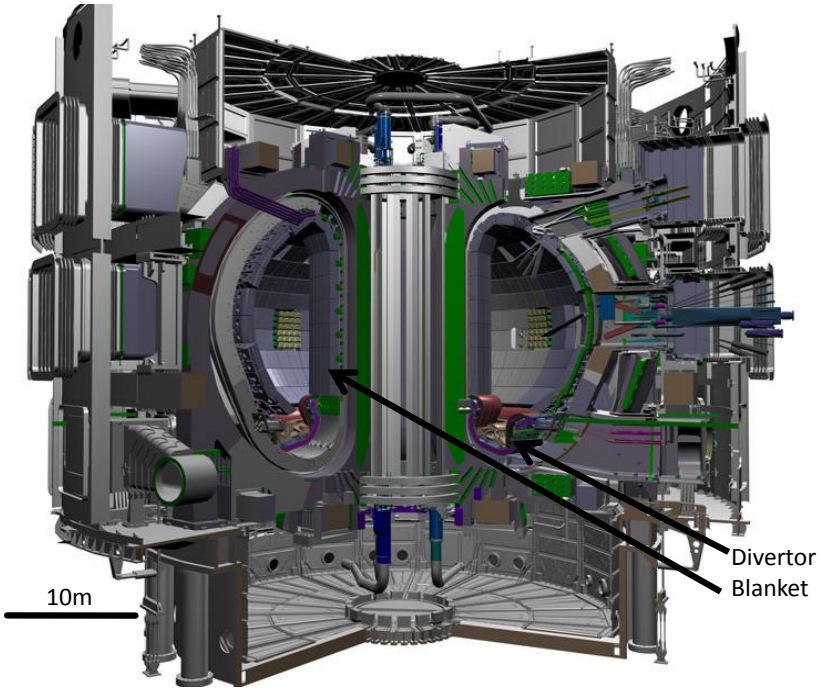


**Figure 2.1 – Artist impression of the ITER test reactor [6]**

### 2.1.1 Requirements of structural materials for commercial scale fusion power

The schematic of the ITER tokamak in Figure 2.1 shows a large and complex structure. The variation in radiation damage rates as a function of distance from the plasma-facing surface can be inferred from Figure 2.2. It is clear that due to the high temperature and high neutron flux, the components nearest the plasma face the greatest materials challenges. The diverter (seen in Figure 2.3) is one component operating in region A of Figure 2.2. Its main function is to purify the plasma by removing impurity ions, and to extract the fusion energy (heat exchange) - thus experiencing temperatures up to ~3000°C [7]. Possible candidates for this very high temperature application include tungsten alloys and carbon based materials, but these materials are outside the scope of this thesis.

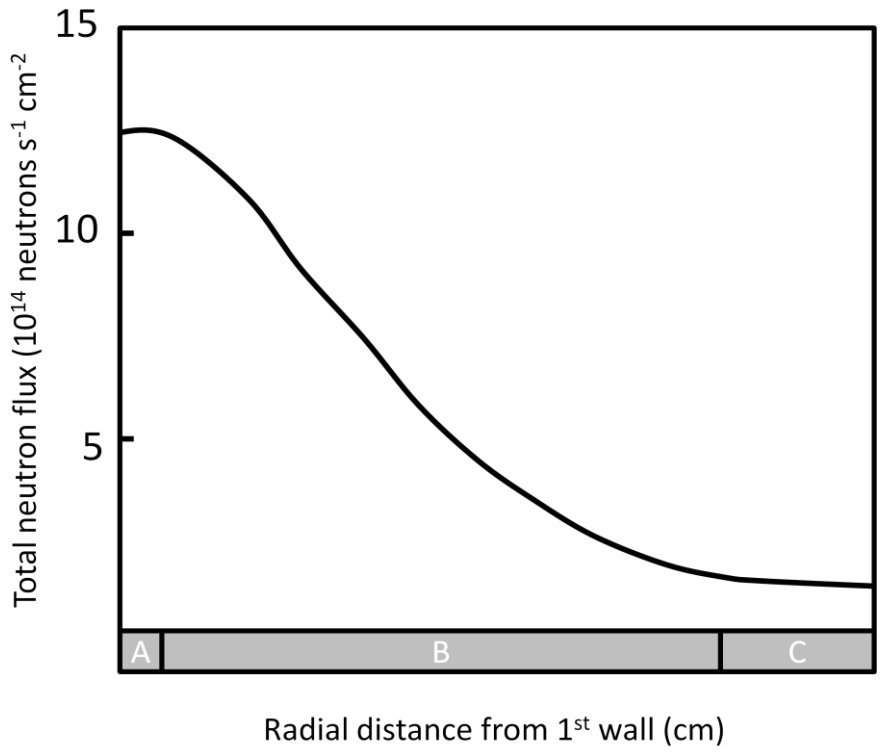


**Figure 2.2 - Variation in neutron flux with distance from the first wall expected in a commercial fusion reactor(based on data from[8]).**

Of particular interest for this review are materials operating in regions B and C of Figure 2.2. The tritium breeding blanket is a key component, as it is also used to extract heat, as well as to manufacture tritium 'in-situ' by reacting with lithium. Figure 2.3 shows a conceptual design of the

blanket for ITER [9]. In its lifetime (~2-5 years), the blanket is likely to experience total damage levels ranging from 3-10dpa (displacements per atom) for ITER, the first DEMO reactor may reach 30-80dpa, and the commercial reactor >100dpa [10].

Reprinted with permission from Elsevier. © 2003 Elsevier Ltd.

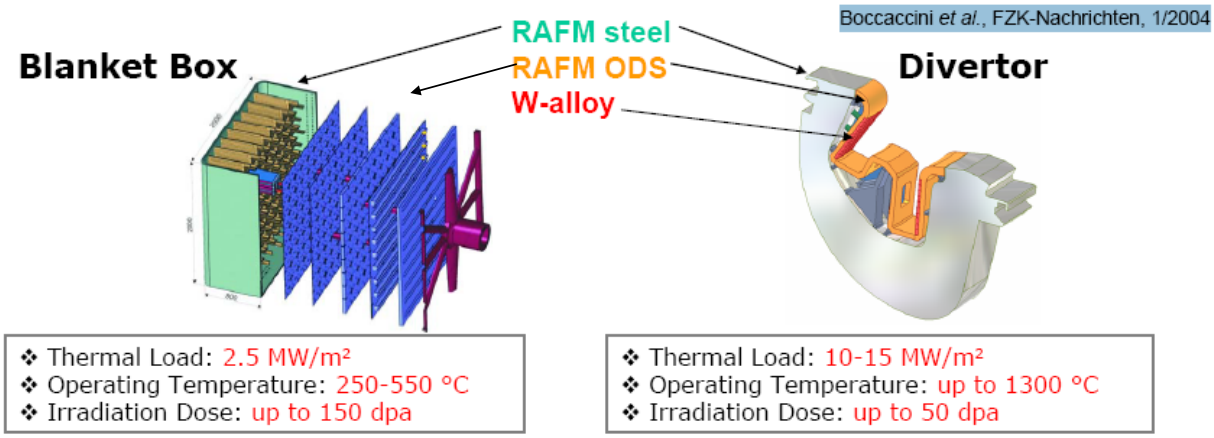


**Figure 2.3 – Conceptual design of blanket and diverter components for the ITER test reactor [9]**

To increase the thermodynamic efficiency of the reactor, there is a drive to increase the operating temperatures of the blanket to >600°C but materials capable of operating at such temperatures are still in developmental stages. Engineering design is crucial when discussing these components, as by the very nature of the heat exchange process, high thermal loads will be applied to the material, and low temperature embrittlement under irradiation means that a lower temperature bound must also be considered [11-12].

Structural materials for the blanket will require:

- High temperature strength
- Large density of sinks for helium and point defects
- Low swelling under irradiation
- Reduced activation composition
- Good compatibility with various coolants
- Low thermal expansion
- High thermal conductivity
- Suitable fracture toughness

Silicon carbide, vanadium alloys and low activation steels are all possible candidate materials, but reduced activation oxide dispersion strengthened steels are by far the most promising and cost effective solution for large-scale applications. There are many issues with this family of materials that remain unresolved, and the subsequent sections of this literature review will address some the issues that are of particular relevance to the research in this thesis.

## 2.2 The development of reduced activation ferritic/martensitic steels

### 2.2.1 Base alloy development

The development of the base alloys began more generally as research into reduced activation steels in the early 1980's. The 'activation' of a steel is limited by the residual radioactivity of the base steel after neutron irradiation, therefore alloying with elements such as Al, Ni, Cu, Nb, Mo or Sn which can generate long-lived radioactive nuclides needs to be avoided [13]. In 1990 the American Society for Testing Metals published a special technical publication to consolidate the progress made on developing reduced activation alloys [14]. Significant research was carried out on the austenitic alloys in the USA, Russia and Japan, with emphasis on replacing Ni by Mn as the primary austenite stabiliser [15-19]. Klueh and Maziaz reported microstructures and mechanical properties comparable to 316 stainless steels using low activation alloying elements [15]. The effect of swelling under irradiation at high neutron doses in austenitic steels was considered so detrimental to the mechanical properties of components that for fusion applications, that low activation austenitic steel research was abandoned by the mid 1990's.

Swelling is a volumetric expansion caused by a combination of cavity formation [20] and irradiation creep [21] . Martensitic and ferritic alloys are less susceptible to swelling, and Odette in 1988 reviewed possible reasons for this [22]. The author concluded that it is likely to be as a consequence of the difference in the available free space within the lattice between the fcc and bcc structures together with high self-diffusion rates (the bcc lattice is filled with only ~68% atoms compared to

~74% in the case of fcc). Ferritic/martensitic steels were favoured over austenitic steels, not only because of their increased resistance to swelling, but also because their thermal expansion coefficient is lower and they have improved thermal conductivity and liquid-metal compatibility [23].

### 2.2.2 Base alloy compositions

The level of chromium in RAFM steels has been varied extensively as reviewed by Klueh et al. [24], and some well characterised alloys are listed in Table 2.1. The choice of Cr content is effectively a trade-off between using a stainless composition for increased corrosion resistance and high temperature properties, and using a lower Cr level for improved microstructural control. Increasing the Cr content gives improved creep resistance at high temperatures. However for the purposes of developing an RAFM steel, 7-9%Cr was originally considered the best range for research, as higher Cr steels are more susceptible to α′ formation under irradiation [24]. Also, above 9%Cr some δ-ferrite is likely to remain in the microstructure, even if extra γ stabilisers such as manganese are added [24].

Low %Cr steels (<3%Cr) with a bainitic microstructure have also been investigated [25], and were found to be either comparable or superior in strength to both ~9%Cr RAFM steels and traditional 2.25%Cr steels [26]. However creep and corrosion resistance at high temperature were deemed to be limiting factors in their use in blanket/first-wall structures of a fusion reactor. Concentrations of up to 12-14%Cr are seen in ODS materials such as 12-YWT or 14-YWT and commercial ODS alloys MA957 and PM2000 [27] as this offers improved corrosion resistance. For fission reactor purposes, 18-20%Cr is preferred for the same reason [28].

Figure 2.4 shows how swelling varies with Cr content for a total radiation dose of 30 dpa in the Fe-Cr alloy system. There is a minimum in total swelling at ~5%Cr with the swelling increasing with increased Cr from that point. A similar trend is reported by Gelles at 200 dpa [29] but, Little et al.

suggest that while the effect is significant in binary alloys, in a fully ferritic microstructure (such as an Fe-14Cr-4Al alloy) swelling is below the detection limit of 0.1% at all irradiation temperatures[30], and so it will not be a significant concern in RAFM steels.

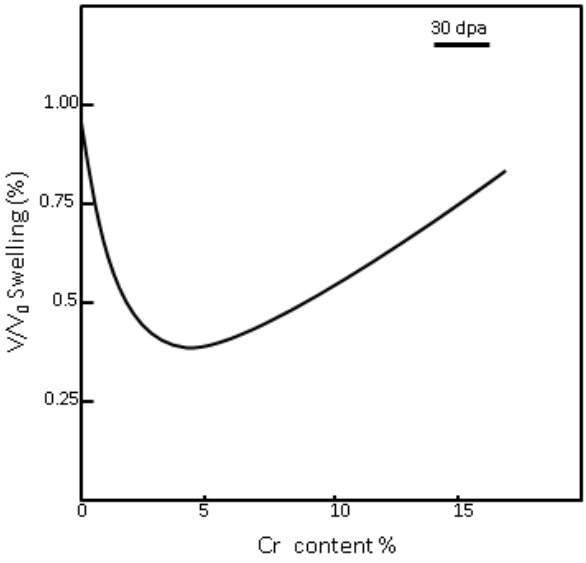


**Figure 2.4 - Magnitude of peak swelling as a function on %Cr in binary Fe-Cr alloys in the temperature range of 380-460°C (based on data from[30])**

Other common alloying elements in RAFM steels are W, V, Mn and Ta. Mn is a strong γ stabiliser, and is included in RAFM steels to a maximum of 0.5wt.%, but Mn promotes χ-phase precipitates on irradiation; therefore the proportion of Mn is limited [31].

Non-reduced activation high temperature steels (such as the Sandvik HT9 alloy) exhibit excellent mechanical properties largely due to the use of Mo and Nb. In low activation steels, W is used in place of Mo as a solid solution strengthener. W is a ferrite stabiliser its concentration needs to be controlled as excess W can lead to δ-ferrite formation and a deterioration in fracture toughness [32]. Alloy compositions developed in recent years such as Eurofer, have a lower W content compared with its Japanese and US equivalents, as a lower W content is expected to lead to a higher tritium breeding ratio[33]. Ta and V are expected to behave in a similar way to Nb (as a carbide/nitride former) and Ta has been shown by Klueh and Maziasz to produce grain refinement as seen in Nb containing steels[34]. An interesting addition of 0.2% Y is included by Huang et al.[35] in the

CLAM alloy. The effect of this was investigated by Li et al.[36] and it is claimed that it refines the lath martensite structure leading to increased irradiation resistance.

| Alloy | % C | % Si | % Mn | % Cr | % V | % W | % Ta | % N | Other |
|---|---|---|---|---|---|---|---|---|---|
| **F82H** | 0.09 | 0.1 | 0.2 | 7.5 | 0.2 | 2 | 0.02 | 0.01 | - |
| **JLF-1** | 0.02 | 0.05 | 0.5 | 8.7 | 0.2 | 2 | 0.03 | 0.03 | - |
| **ORNL 9Cr2WVTa** | 0.1 | - | - | 8.8 | 0.2 | 2 | 0.07 | 0 | - |
| **CLAM** | 0.1 | 0.01 | 0.45 | 9 | 0.2 | 1.5 | 0.15 | 0.02 | 0.2 %Y |
| **Eurofer 97** | 0.1 | - | 0.5 | 8.9 | 0.2 | 1.1 | 0.15 | - | - |

**Table 2.1 – Some RAFM alloy compositions[24, 35]**

### 2.2.3 Behaviour under irradiation

The alloys shown in Table 2.1 have all been extensively tested under various irradiation conditions to ~20dpa [31, 37-39], and there are significant changes to the mechanical properties. To give a general summary, firstly swelling is not notable, remaining below ~1% in all cases. It is also found that below 400°C, irradiation leads to significant hardening with a large reduction in uniform elongation, a loss of fracture toughness and an increase in the ductile to brittle transition temperature (DBTT), as seen in Figure 2.5(a). Hardening effects are reported to saturate around 1.5dpa at 80°C; however this effect is strongly dependent on the irradiation temperature and at 300°C saturation occurs at ~10dpa[40-41] – any hardening is minimal above 400°C.

Saturation in the increase of the DBTT due to irradiation has also been reported [42], and Figure 2.5(b) shows work on the Eurofer alloy by Gaganidze et al. [43] which indicates that the hardening saturates at a lower level of irradiation dose compared to the embrittlement after neutron irradiation.

Reprinted with permission from Elsevier. © 2009 Elsevier B.V.

Reprinted with permission from Elsevier. © 2007 Elsevier B.V.

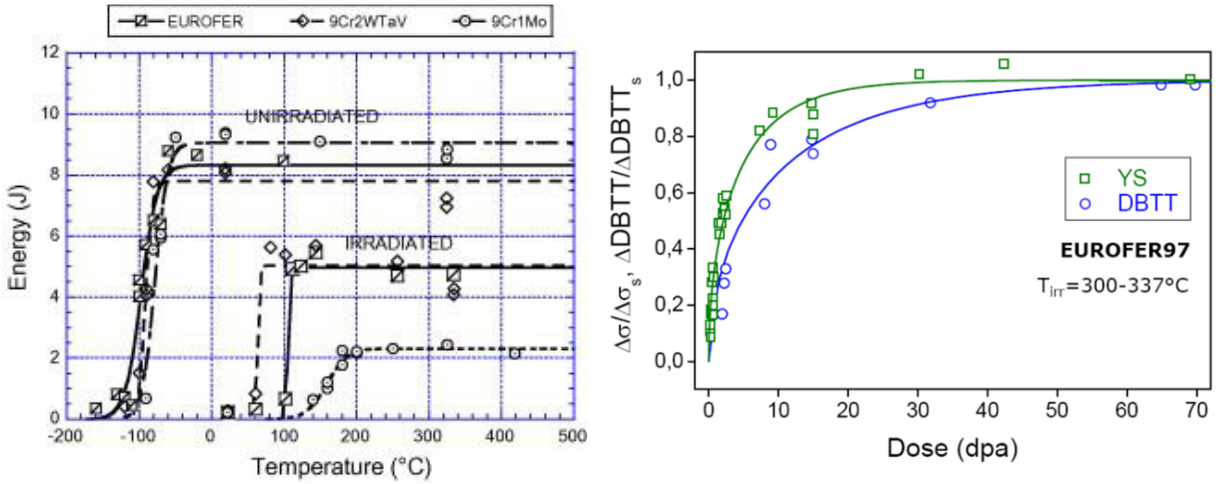


**Figure 2.5 – (a) Comparison of impact properties of EUROFER, 9Cr2WTaV and 9Cr1Mo steels in the unirradiated condition and after irradiation in BOR60 reactor at 325 °C for 32–42 dpa[44] (b)Comparison of hardening and embrittlement at varying dpa for the Eurofer alloy after neutron irradiation in the ARBOR reactor[43]**

### 2.2.4 Mechanical properties at high temperature

At room temperature, RAFM steels are characterised as having yield stresses in the region of 450-650MPa and the UTS is generally ~150MPa above $\sigma_y$. The mechanical properties near the upper operating temperature limit of these alloys are more relevant for fusion applications. It is widely known that the strength of RAFM steels falls away above 500°C [24]. The Eurofer alloy is one of the most creep resistant steels, but even for this alloy at 550°C the creep lifetime is only 3000 seconds for an applied stress of 300MPa [45]. Figure 2.6 compares the creep rupture curves of reduced activation alloys with commercial ferritic/martensitic steels at 650°C. At this test temperature, neither the Eurofer nor F82H alloys are able to compete with the commercial alloys containing Mo. It is believed that higher levels of boron and nitrogen in the commercial steels account for the difference [46]. It is clear that long-term high temperature properties of RAFM steels are not as good as the steels they are designed to replace; therefore ways to improve the creep life have been investigated.

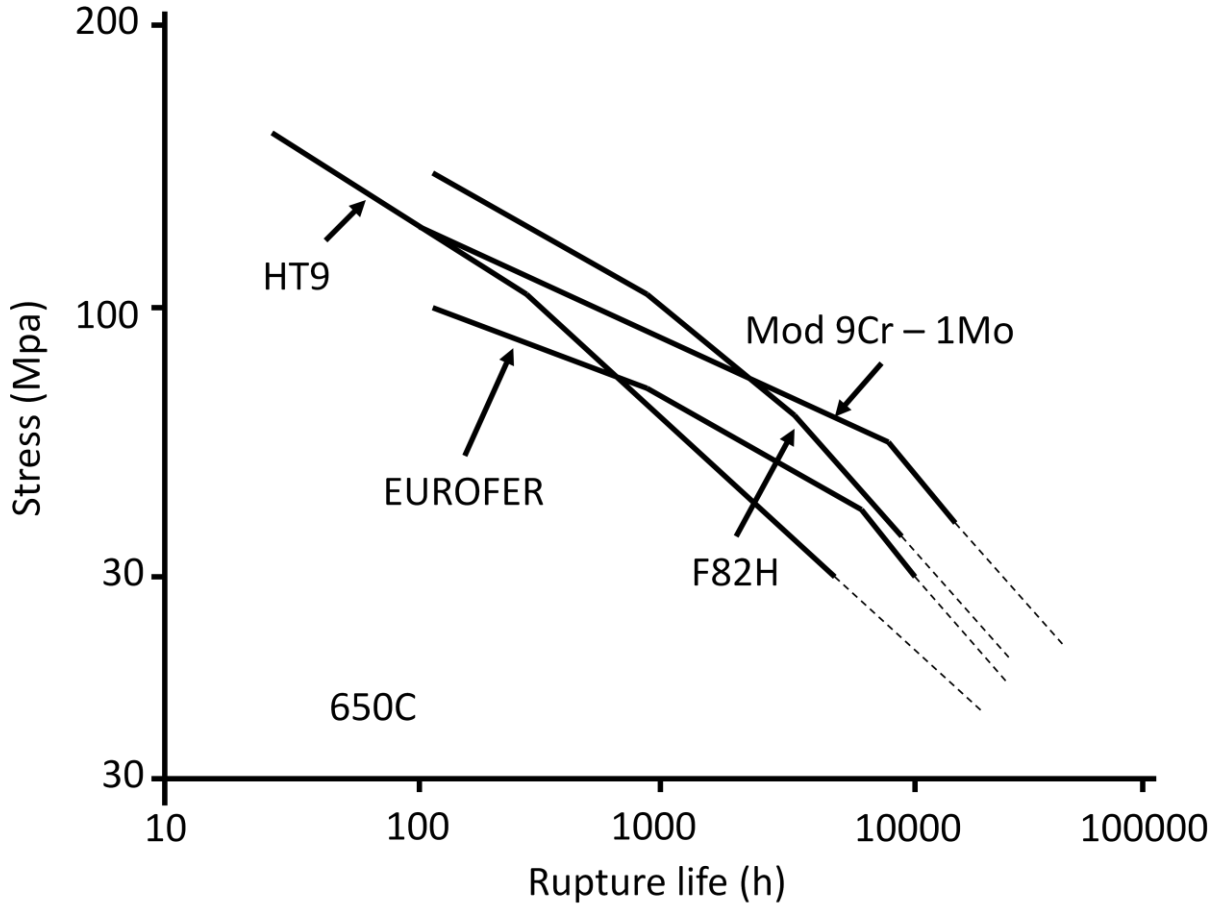


**Figure 2.6 - A comparison of the creep-rupture curves at 650 °C for the reduced activation steels F82H and EUROFER 97 with the commercial steels Sandvik HT9, modified 9Cr–1Mo, and NF616 (redrawn from[46])**

Strengthening mechanisms such as work hardening and solid solution strengthening are not effective above 0.3-0.4$T_m$ (melting temperature), as dislocations are able to move by non-conservative processes with the help of thermal activation. Barriers to dislocation motion such as second phase particles are required; hence the drive to create ODS alloys. Klueh et al. in 2007 developed a thermo-mechanical treatment for tempered martensitic 9-12%Cr nitrogen containing steels that maintained strength up to 700°C [47]. A high number density of nitride and $M_{23}C_6$ particles combined with a high dislocation density was given as the reason for the high temperature strength. Figure 2.7 shows the variation in yield strength with temperature, and the alloy HCM12A-TMT (Fe–12Cr–2W–0.4Mo–1Cu–0.3Ni–0.25V–0.05Nb–0.06N–0.1C) compares favourably with ODS alloy PM2000 (discussed in more detail in Section 2.3) at high temperature.

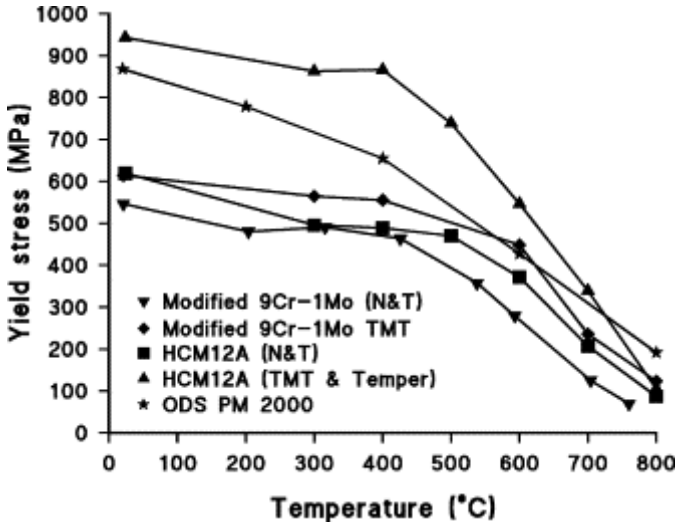


**Figure 2.7 - Variation in yield strength with temperature for a new thermo-mechanically treated reduced activation alloy HCM12A [47]** Reprinted with permission from Elsevier. © 2007 Elsevier B.V.

## 2.3 The improvement of RAFM steels for fusion applications by ODS

As described above, the upper operational temperature limit of the 'plain' RAFM steels is around 500˚C. An insoluble second phase dispersion such as an oxide is more resistant to coarsening and in many cases will remain up to the melting point of the matrix ($T_m$), thus allowing mechanical properties to be maintained at higher temperatures. The idea of introducing oxide to steels is not recent, and for years, the $MnO\text{-}SiO_2\text{-}Al_2O_3$ system has been exploited for the formation of oxide inclusions [48], though in this case the inclusions are much larger than are currently seen in mechanically alloyed (MA) ODS steels. For the purposes of this review, ODS is defined as the inclusion of a nanoscale dispersion of oxide in a metallic matrix. While the majority of published literature relates to steels, there is also a long history of ODS in copper [49], nickel [50] and aluminium [51] alloys and these alloys share many of the same processing routes and characteristics as the ODS-RAFM steels described below. ODS has not been widely used commercially, as conventional melt processing techniques cannot be applied, therefore alternative processing is required, which makes ODS alloys very expensive in comparison to the base alloy.

In RAFM steels, the inclusion of ODS particles has two main functions: firstly to improve mechanical properties at higher temperatures, and secondly to act as trapping sites for He and point

defects to reduce radiation induced hardening and embrittlement– the two main requirements of a structural material for fusion applications. Table 2.2 shows the nominal composition of various ODS alloys that are discussed in this review. Recent progress made in developing ODS alloys with adequate mechanical properties for structural applications will be discussed, and this review will assess how well the alloys fulfil the two criteria mentioned above.

| Alloy | Cr | Ti | W | Y2O3 | Other | Origin |
|---|---|---|---|---|---|---|
| **PM2000** | 20 | 0.5 | - | 0.5 | 5.5Al | Commercial |
| **MA957** | 14 | 1 | - | 0.3 | 0.3Mo | Commercial |
| **M93** | 9 | 0.2 | 2 | 0.35 | - | Japan |
| **Eurofer** | 9 | - | 1 | 0.3 | 0.5Mn 0.2V 0.1Ta | Europe |
| **12-YWT** | 12 | 0.4 | 3 | 0.25 | - | Japan |
| **12-Y** | 12 | - | - | 0.25 | - | Japan |
| **14-YWT** | 14 | 0.4 | 3 | 0.25 | - | US |
| **K1** | 19 | 0.3 | 0.3 | 0.35 | - | Japan |
| **K4** | 19 | 0.3 | 1.8 | 0.35 | 5Al | Japan |

**Table 2.2 - ODS alloy nominal composition in %wt [27, 52]**

### 2.3.1 Processing routes

Due to the density differences between the metal and the oxide to be dispersed, melt processing techniques cannot be used. The only method used extensively is known as mechanical alloying (MA). In 1976 Benjamin developed a process of ball milling fine powders to introduce the oxide into the alloy [53]. The powder is consolidated by hot extrusion [54-56] (HE) or hot isostatic pressing [57-59] (HIP) to give a structure of small grains (typically <5μm), dispersed with nanoscale oxide particles. Initially, there were problems with porosity and microstructural inhomogeneity, but the processing technique has been refined (discussed further in Section 5.2.1) and is now very successful in generating a material with high density and favourable mechanical properties [27]. The major disadvantage of this technique is that it is unsuitable for very large components. It is also energy intensive and time consuming, thus making it very expensive.

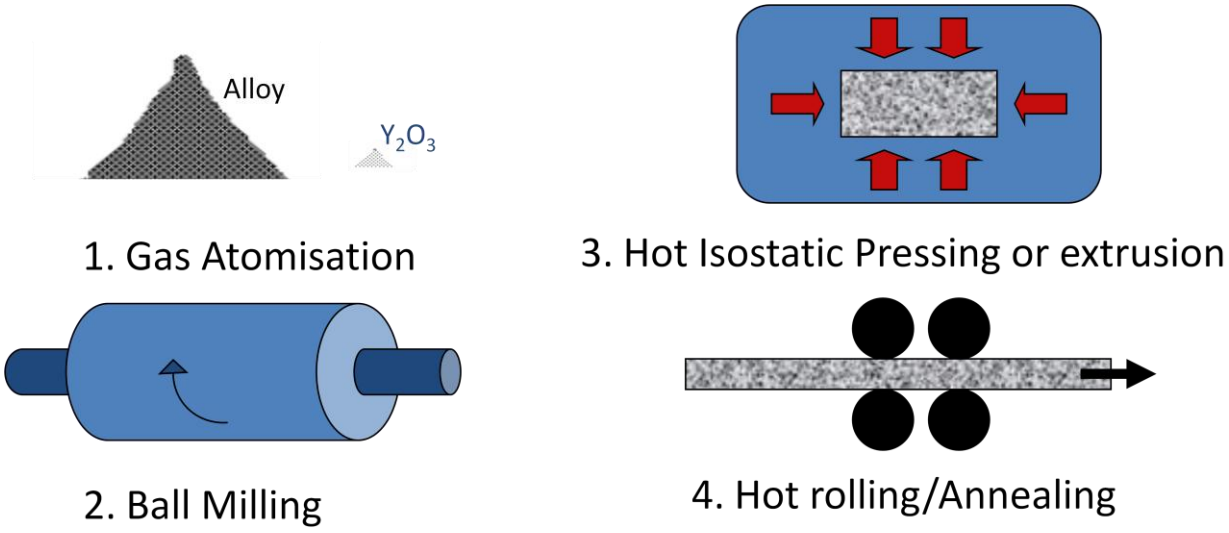


**Figure 2.8 – Schematic representation of the mechanical alloying process[60]**

In recent years attempts have been made to find alternative processing routes. The idea of generating a dispersion of oxides by internal oxidation has been successful in a number of different alloy systems [61-62]. Schneibel and Shim attempted to use $Fe_{17}Y_2$ and $Fe_{11}TiY$ intermetallic precursors in an Fe matrix and internal oxidation to generate microstructures similar to those attained via mechanical alloying [63]. While they were successful in dispersing a variety of Y-Ti-Fe oxides within the Fe matrix, the smallest oxide particles were ~20nm, which is significantly larger than the 2nm particles attainable by mechanical alloying. An article outlining the development of pores that can occur in MA materials (due to trapping of inert gas from the powder atomisation process) suggests that a significant advantage of internal oxidation processing is the elimination of this porosity [64]. While this point is valid, the article overlooks the fact that, as yet, no mechanical testing has been carried out on the internally oxidised alloy therefore its use as a structural material cannot be assessed. As it is reported that the volume fraction of oxide is ~25% [63] compared to 0.2-0.5% in MA materials [27], it is likely that the material will be more brittle.

A more promising technique is described by Verhiest et al. [65]. This involves generating nanopowders by solution combustion synthesis [66] then adding the powder to molten metal without any contact with the crucible before a rapid quench. The technique is in early stages of development

therefore a pure iron matrix was used rather than more complex steels, however the results are promising. The authors claim larger components would be easier to fabricate using this method than by MA, and that there would be a substantial financial saving but it would need to be proven that more complex base alloys could be used. It has also been suggested that the main improvement in resistance to radiation damage is a result of the fine grain structure in MA materials, rather than the introduction of oxide particles [67], therefore a method of controlling the grain size needs to be found. Again, until mechanical testing results are published it is difficult to compare these materials directly with MA.

### 2.3.2 Microstructure

Generating the optimum microstructure during processing is key to attaining the best materials properties for a given alloy system. For ODS-RAFM steels, it is agreed that the optimum microstructure should consist of small, homogenous, equiaxed small grains (to give uniform high temperature strength without loss of ductility via the Hall-Petch effect) with an even distribution of nanoscale oxide particles (to improve creep resistance and act as trapping sites for radiation induced defects) [60]. The MA process is complex, and as will be discussed, many of the processing parameters, such as milling and consolidation techniques, can be varied to affect the particle distribution and/or grain structure. Differences in grain structure are evident in Figure 2.9. Extruded material such as the 18Cr1W example shown here has a columnar grain structure, whereas the HIP-ped material has equiaxed grains.

Reprinted with permission from Elsevier. © 2007 Elsevier B.V.

Reprinted with permission from Elsevier. © 2009 Elsevier B.V.

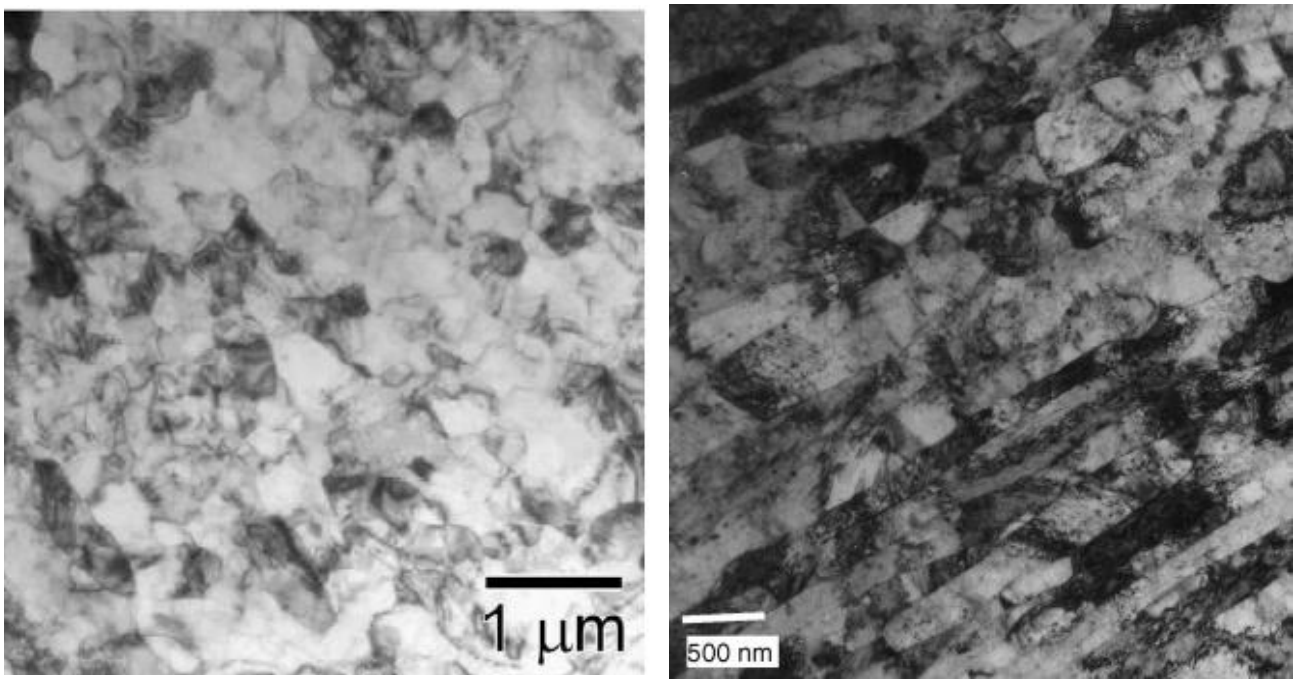


**Figure 2.9 - TEM images of variations in grain structure of the 14-YWT (consolidated by HIP) [68] and Fe–18Cr1W(extruded )[28] alloys. The left hand size image shows a uniform grain size whereas columnar grains are seen in the extruded material.**

One area requiring significant further research is in understanding the fundamental aspects of the formation, composition and stability of the oxide particles. Here, the main issues concerned with the further development of ODS alloys are identified.

### 2.3.3 Nanoscale oxide particles

#### *2.3.3.1 Oxide particle formation*

Lindau et al. originally suggested that ODS particles in the ODS-Eurofer alloy were remnants of the original $Y_2O_3$ powder made spherical by surface diffusion [57]. However, the authors, along with others, have since concluded that complete dissolution of the $Y_2O_3$ powder occurs during MA. The particle sizes of 2-5nm are much smaller than that of the original powder, and spectroscopy studies show no evidence of oxide particles after milling [69-70]. Small angle neutron scattering (SANS) data by Alinger et. al. on 14-YWT (Fe-14Cr-2W-0.3Ti) suggested complete dissolution of Y and O during the mechanical alloying (MA) process and precipitation of the oxide nanoclusters during HIP [10]. However, Brocq et. al. observed clustering of Ti-Y-O in powder after the MA stage in an alloy

with similar base composition [71]. Brocq et. al. also showed that the clusters continued to nucleate and grow during relatively low temperature annealing (<800°C) for short times (5 minutes), and suggested that these clusters formed the basis for the particle distribution seen in consolidated materials. It was originally thought that Ti assisted in the dissolution process [69], but it has been shown that Ti does not significantly affect this stage [72].

A novel experimental method of analysing the particle formation was presented by Sakuma et al [54, 73]. The approach of using dual-beam simultaneous implantation of Y+ and O+ ions to introduce the elements into solid solution in a ferritic steel matrix was expected to give new insights into how the particles form and develop. It was reported that particles ~5nm formed during implantation and the particle density and average size then increased on annealing in-situ at temperatures as low as 573K. The authors reported intensive growth of oxide particles above 8-900K which is consistent with temperatures reported by Okuda and Fujiwara [69]. It is unfortunate the in-situ TEM of the particles was not of sufficient resolution to give more compositional or structural data. This research did however give a new insight into the temperature dependence of the oxide particle precipitation, which has since been investigated further by Sakasegawa et al. using hot extrusion [74]. Extrusion temperature was seen to correlate positively with particle size, indicating that the oxide dispersion can be greatly affected by changes in extrusion temperature.

A first principles study by Fu et al. used density functional theory to calculate binding energies between solute atoms and vacancies in a ferritic alloy [75]. It was found that the binding energy between a vacancy and oxygen is ~1.5eV, but that that this could be increased to ~5eV by combining with Ti and Y atoms. This makes Ti-Y-O nanoclusters with a high number of vacancies more energetically favourable than stoichiometric oxides like $TiO_2$ (4.3eV). The authors therefore suggested a vacancy mechanism as the underlying process by which the O migrates and that the nanoclusters form. Strong interaction of Y with vacancies was also confirmed by Ou et. al. [76]. Positron annihilation spectroscopy experiments have shown that nanocluster-containing alloys

contain a proportion of 4-6 vacancy clusters, which were not observed when no nanoclusters were present [77], indicating that the mechanism predicted by Fu et al. [75] is likely.

Alinger et al. attempted larger-scale modelling using a simple lattice Monte Carlo model to gain a better understanding of the non-equilibrium nanoclusters [78]. Using ab-inito calculations of the mixing enthalpies for bond energies in the context of a regular solution model, they found a reasonably good agreement with atom probe data presented by Miller et al. [79] (with the radii of the particles in this simulation ranging from 0.7-1.1nm if a lattice parameter >1.2nm was assumed) [78]. The compositions of the particles in this model have a very large margin of error, therefore no definite conclusions can be drawn and it should also be noted that the partitioning of Ti and Y in the model is not observed experimentally. There are discrepancies between the atom probe data presented by Miller and the positron annihilation experiments, and at present it is not clear as to whether the findings of Alinger et. al. are compatible.

Hin and Wirth investigated precipitation in Fe–Y–O and Fe–Ti–O alloys also using kinetic Monte Carlo methods, and found that prior to the more stable Y or Ti oxides forming, small $Fe_2O_3$ precipitates formed [80]. Clearly, further research is required in this area to ascertain the exact mechanism of formation, and to understand the influence of other elements such as Cr.

The literature currently uses a wide variety of terms to describe the oxides – nanoclusters, nanofeatures, particles, precipitates etc. Until the oxides are adequately characterised a suitable convention is unlikely to be found.

#### *2.3.3.2 Oxide particle composition*

Due to the very high resolution techniques required to characterise the particles fully, there is a lot of controversy surrounding the precise composition of the smallest particles. Even using one analysis technique, on the same material, the results can vary substantially due to microscopy aberrations. Much of the work carried out to date attempts to match the experimental findings to a

stoichiometric oxide composition. The articles reviewed above suggest a strong possibility that the particles are in fact metastable clusters, and may not have an equilibrium composition. It is important that an accurate method of evaluating the composition of the nanoclusters at various stages in the formation process is found, as this would give some understanding of what mechanisms are operating, and what is driving the particle formation.

In the ODS-Eurofer alloy, it was initially assumed that the composition of the particles was $Y_2O_3$ [57], and indeed there is evidence to suggest that larger 20nm+ particles are cubic $Y_2O_3$, either inferred from the lattice spacing of HRTEM images [81] or by chemical analysis of particles removed from the matrix by chemical etching [82]. Klimenkov et al. analysed particles ~5nm in diameter in the ODS-Eurofer alloy using a 1nm probe and electron energy loss spectroscopy (EELS) [83]. Two regions were identified – a V-Cr rich shell around a Y rich core, and this is also confirmed by APT [84]. Klimenkov et. al. were unsuccessful in assigning a particular oxide composition to each region, but APT results (that also form part of this thesis) suggest a combined metal to oxygen ratio of ~1:1 for the core and the shell [84].

EDX analysis of particles by Kishimoto et. al. suggests that the particles have a Y:Ti ratio of 2:1, which corresponds to the $Y_2TiO_5$ oxide in a Fe–16Cr–0.1Ti ODS steel [85], but EELS measurements suggest a $Y_2Ti_2O_7$ type structure [86]. A Ti containing batch of ODS-Eurofer alloy was analysed by EELS after mechanically alloying with added 0.25wt%Ti [86]. In this case, the authors report a stoichiometry of $Y_{2.2}Ti_{2.3}O_7$ after a background correction accurate to 20%. Sakasegawa et al. also report particles of $Y_2Ti_2O_7$ type in a Ti-containing 9%Cr ODS alloy, very similar in base composition to the Eurofer. The oxide particles were chemically extracted from the matrix, and while $Y_2O_3$ was thought to dissolve in the etching process, both $TiO_2$ and $Y_2Ti_2O_7$ were identified by x-ray diffraction. Recent work by Ribis and de Carlan show that after annealing at 1300°C the crystal structure of the nanoclusters can be clearly identified as a mixture of pyrochlore $Y_2Ti_2O_7$ and cubic $Y_2O_3$ [87]. This is a stark contrast to atom probe results on similar particles

where an M:O ratio of ~1:1 is presented [88]. In this case the compositions of the base alloys differ substantially between the two materials; therefore it is possible that the materials exhibit different oxide phases.

APT allows compositional measurements to be made on the nanoscale, and is therefore an ideal technique for oxide particle analysis. The first APT analyses of ODS steels were carried out by Miller et al. at ORNL on the 12-Y1 and 12-YWT [2, 89], 14-YW and 14-YWT [90] and MA957 [90-91] alloys. Some ambiguity exists over the compositions of the nanoscale Ti-rich yttria-based oxide particles in these analyses. Larson et al. [89] reported an Fe concentration of ~78% in the clusters in 12-YWT, whereas Miller et al. subsequently reported levels of ~40% [2], 20% [88] and only 4% [90]. It is unclear whether the causes of variations are from materials processing, alloy compositions or inherent material inhomogeneity. The most likely explanation is probably related to the way the APT data is interpreted, and the methods by which clusters are defined and local concentrations measured.

Core-shell structures have also been confirmed by APT in another 12Cr-ODS model alloy and the MA957 material [92]. Oka et al. report a twofold increase in the Ti/(Ti+Y) ratio 10nm from the core, which the authors suggest indicates a Y-rich core surrounded by a Ti-rich shell [93]. Interestingly, the authors make no attempt to extract compositional values from the particles in the APT data, and instead rely on the particles orientation relationship with the matrix to suggest that the particles have a complex cubic $Y_2Ti_2O_7$ composition. It is clear that if the issues could be resolved surrounding the exact chemical composition extracted from the APT data, the technique could be very powerful.

Alinger et al. also express concern over the validity of APT measurements, and have conducted small angle neutron scattering (SANS) experiments in order to compare with the APT results [94]. In a strong magnetic field it is possible to determine nuclear or magnetic SANS from the oxide particles due to their density and magnetization contrast with the matrix so the average

radius and number density of the particles can be evaluated. The ratio of magnetic to nuclear scattering (*M/N*) is dependent on the composition of the particles, so having made various assumptions about the character of the particles, it was concluded that M/N of ~0.9 for the J12-YWT alloy was consistent with the particles being $Y_2Ti_2O_7$ [95]. The U14-YWT alloy that was analysed in the most recent study [94] is reported to have M/N of ~2 which does not correspond directly to any known oxide phase, or to the oxide stoichiometries measured by APT. It is suggested that the smallest particles contain some Fe. The authors then explain that if the Fe content of the particles is increased, that affects the atomic density, thus increasing the M/N values which would explain the higher measured values in the 14-YWT alloy. By carrying out seemingly arbitrary adjustments of the Fe content of the particles, reasonable agreement between SANS and APT was obtained; but there appears to be little basis for making the adjustments.

#### *2.3.3.3 Oxide particle coherency*

The particle-matrix interface is likely to strongly affect the migration of point defects and helium, and thus the resistance of the material to radiation damage. Ramar et al. used HREM to determine the nature of the interface in the ODS-Eurofer material [96]. The particles in this study appear different to those reported previously [81, 97-98], with faceting clearly evident in the images presented. Also, the average particle size is larger at 10-30nm. The report shows the particles are bcc-$Y_2O_3$ with lattice parameter of 1.06nm, and are at best semi-coherent with the matrix. A differing orientation relationship is reported by Klimiankou et al. [81] but the particles analysed here are smaller and more spherical therefore it is possible that these particles are a different phase. ODS-Eurofer with added Ti was also analysed by Ramar et al., but it would appear that the coherency with the matrix could not be determined.

Ribis and de Carlan show that after annealing the pyrochlore $Y_2Ti_2O_7$ nanoclusters have a cubic shape, and are fully coherent with a ‘cube on cube’ orientation [87]. Prior to annealing, the authors were unable to distinguish the exact nature of the nanocluster phase. In general, it would appear that

Ti-containing particles are too small for current microscopes to analyse effectively, and it has been suggested that, in light of the APT results that indicate a non-equilibrium oxide phase, it is possible that these smallest particles are indeed a coherent GP type zone or sub-oxide [60].

### 2.3.4 Mechanical properties

As expected, when the tensile properties of materials that contain a large volume fraction of particles that impede dislocation motion (ODS alloys) are compared to the base alloy, the yield stress ($\sigma_y$) is higher, and impact strength is significantly reduced - by up to 40% in some cases [27]. Lindau et al. comprehensively reviewed the changes in mechanical properties when comparing ODS-Eurofer to the base alloy Eurofer [99]. Some data is reproduced in Figure 2.10, as it illustrates trends seen in all ODS alloys.

Figure 2.10(a) shows a tensile strength ~400MPa higher in the ODS Eurofer alloy at room temperature, compared with the base alloy, and it remains above the base alloy up to 700°C. This is associated with the reduction in ductility seen in Figure 2.10 (b). As expected, creep properties also show a vast improvement with ODS (Figure 2.10 (d)).

Reprinted with permission from Elsevier. © 2005 Elsevier B.V.

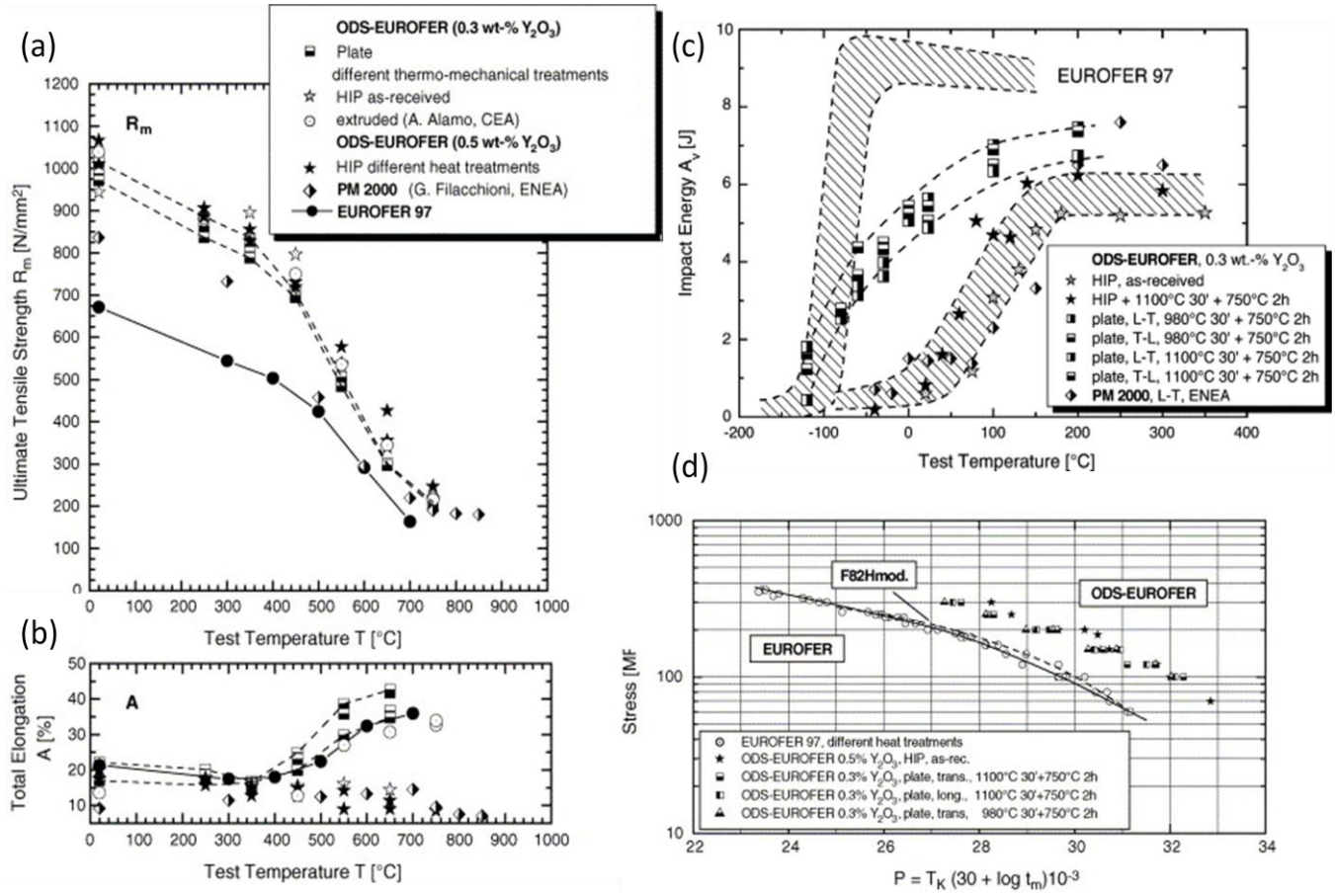


**Figure 2.10 - (a) Variation in UTS with increasing test temperature for Eurofer and ODS-Eurofer of various heat treatments (b) Variation in total elongation with increasing test temperature (c) Impact data from ODS-Eurofer (d) Larson-Miller plot showing creep strength [99].**

The tensile properties of ODS alloys vary considerably depending on the composition of the alloy and the processing conditions, and it can be difficult to establish whether it is composition or processing which causes the difference in measured properties. To illustrate this last point, several alloys are compared in Figure 2.11. These alloys are all formed by hot extrusion, but there is still a large spread in $\sigma_y$ for a given temperature.

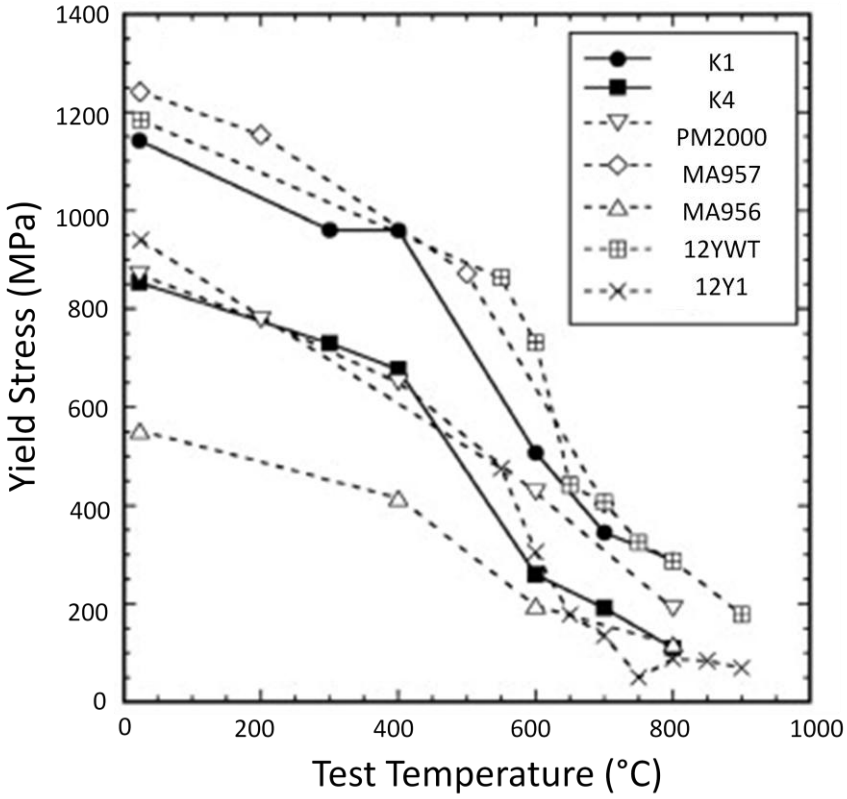


**Figure 2.11- Temperature dependence of 0.2% proof stress evaluated from tensile tests for the K1 and K4 steels with other ODS F/M steels.[52]** Reprinted with permission from Elsevier. © 2007 Elsevier B.V.

To some extent, this spread could be attributed to differences in oxide particle size – K4 and 12-Y1 for example, contain no Ti and as a result exhibit a coarser distribution of 5-10nm oxide particles. In the MA957 (which contains Ti) the nanoclusters are ~2nm in diameter. Reasons for the differences between MA 957 and K1, for example, are less clear. In a review by Odette et. al., the hardest ODS alloys were noted to all contain Ti, but a wide range of yield stresses was observed throughout the literature for each alloy, depending on the exact processing and thermo-mechanical treatments.

The mechanical properties are clearly influenced by the particle dispersion, but other aspects of the processing have a significant effect. At present it is unclear from the literature how critical the particle dispersion is for the mechanical properties of the various alloys. Factors such as the cohesive strength of the grain boundaries could also play a vital role. The boundaries between individual powder grains are believed to be weaker than internal grain boundaries within the powder [99]. This may be the controlling factor for the mechanical properties of these materials.

## 2.4 Approaches to developing the optimal ODS microstructure

Optimising the microstructure has been sought primarily by either varying the processing conditions or adjusting the composition of the initial powders. Progress on investigating the influence of each stage in the MA process on the final microstructure is now summarised.

### 2.4.1 Optimisation of microstructure by varying processing conditions

#### *2.4.1.1 Milling*

In the early developmental stages of the ODS-Eurofer alloy, microstructural inhomogeneity was a serious problem, and regions of >100μm completely free of oxide particles were observed [100]. This was attributed to poor mixing of the $Y_2O_3$ powder, and contamination of the powder during milling. This has been improved, but some inhomogeneity still remains. On investigating the effect of altering the milling parameters, Ramar et al. found that continuous milling in argon atmosphere was superior to degassing regularly [1]. The powder particle size was reported to decrease up to 24hrs milling, however after 12hrs milling the powder morphology changed from flakes to more spherical particles. De Castro et al. suggested ~12hrs milling time was optimal, as by this stage all $Y_2O_3$ powder is thought to be broken down and incorporated into the alloy [101]. This agrees with the conclusions of Ramar et al. who suggested that there is little to be gained by milling past the strain saturation point of the alloy. Recently, milling in a H or He atmosphere has also been investigated, but no definite conclusions can be drawn on what effect this has on the properties and microstructure [70].

Jun-Ho et. al. have successfully demonstrated that a nano-dispersion of oxides can be achieved by using metallic salts to synthesise the oxides in nanoparticle form, and this reduces the milling time to 10hrs to achieve comparable mechanical properties [102].

#### *2.4.1.2 Consolidation*

There is considerable debate over consolidation techniques. Hot extrusion (HE) is favoured for tube manufacture and much of the U.S. and Japanese research focuses on this method [55-56, 68, 103]. Its advantages over HIP are primarily that porosity caused by poor consolidation is virtually eliminated, and the process is much cheaper. Unfortunately a reduction in strength due to grain boundary fracture caused by grain anisotropy is reported [104-105], and the creep strength is also less than expected, apparently due to grain boundary diffusion along elongated grain boundaries [106-107]. Thermo-mechanical heat treatments are required to modify the grain-structure to give suitable mechanical properties.

HIP has been used successfully in the ODS-Eurofer alloy [57] and others [108], and is preferred when isotropic mechanical properties are required. Olier et al. compare HE and HIP in the same alloy, and conclude that superior tensile properties are obtained from the extruded material in the longitudinal direction, with similar impact test results for the HIP and transverse HE samples [70]. This indicates that despite anisotropy in the material formed by HE, the process is likely to be favoured.

#### *2.4.1.3 Post consolidation thermal/mechanical treatments*

Post consolidation treatments are necessary, particularly in the case of HE materials, to refine the grain structure. Achieving equiaxed grains has proven to be difficult, and one reason may stem from unusual recrystallisation behaviour observed in ODS alloys.

A study on the MA957 alloy reported that even at temperatures of 1400°C the grain structure was not recrystallised [109]. It was concluded that excess oxygen was the key factor in dictating the recrystallisation behaviour but deformation texture was also shown to increase the recrystallisation temperature. One explanation of the high recrystallisation temperature given by Bahdeshia et al. supports these conclusions [110]. Here it is assumed that bowing of grain boundaries is the primary

method of grain nucleation, and that as the grain size is very small the grains cannot be considered independent. The many grain boundary junctions act as pinning points to the bowing. Increasing the oxygen content (via introducing more oxide during MA) will also introduce extra pinning points for grain boundaries.

Suitable thermo-mechanical treatments have been developed for extruded materials, and these typically involve a series of either hot or cold work followed by a softening heat treatment [111]. Lindau et al. [99] made the most significant break-through by developing a hot-cross rolling technique after HIP with intermediate annealing stages. Large grains were eliminated from the microstructure, creating a maximum of 290K drop in DBTT and significant improvement in total elongation at high temperatures.

In alloys such as the EPFL-14Cr [59] and ODS-19Cr–2W–4Al [112] where the powder was consolidated by HIP, elongated grains still exist that are detrimental to the mechanical properties. Post consolidation heat treatments have also been unsuccessful in removing elongated grains from the final microstructure in the HIPed material. Given that equiaxed grains have been successfully generated in the Eurofer material [99], this raises the question as to whether the reason for this is related to the higher Cr content in the other HIPed alloys.

### 2.4.2 Optimisation of microstructure by varying powder composition

#### *2.4.2.1 Variation in oxide composition*

$Y_2O_3$ is known to be one of the most stable oxides [113], and is therefore most commonly used to produce oxide dispersion strengthening, but a variety of different oxide powders have been tested. A comparison between 0.3% $Y_2O_3$ and $TiO_2$ ODS was published for a 13%Cr alloy, and yttria was seen to give a finer particle dispersion and improved mechanical properties [114]. $MgAl_2O_4$ was also considered, but as it does not dissolve completely during the mechanical alloying process, a coarser dispersion of particles was observed that caused a degradation in creep properties [115].

There have also been several reports of using alternative methods to introduce Y and O into the matrix during mechanical alloying. Brocq et. al. used a combination of $YFe_3$ and $Fe_2O_3$ and reported a similar particle dispersion to using $Y_2O_3$. Oksiuta used $Fe_2Y$ additions, and assumed sufficient oxygen would be incorporated from the surface of the pre-alloyed powder [116]. In this case, the particles were reported to be larger (~5nm diameter) than with $Y_2O_3$, and the number density lower.

#### *2.4.2.2 Variation in $Y_2O_3$ concentration*

Compositions ranging from 0.2- 0.5wt% $Y_2O_3$ have been tried in various alloys, with inconclusive results. In ODS-Eurofer the 0.5% $Y_2O_3$ variant exhibits greater creep strength, but impact properties and high temperature strength were more favourable when 0.3% $Y_2O_3$ was included [67]. Olier et al. however reported a slight improvement in tensile properties when the $Y_2O_3$ content was increased from 0.3% to 0.5% [70]. It would therefore appear that slight variations in oxide concentration have little effect on the mechanical properties.

#### *2.4.2.3 Effect of minor alloying elements (Ti, Al, etc)*

The oxide dispersion can be affected significantly by the presence of low concentrations (<1wt%) of elements with a high affinity for oxygen. Figure 2.12 shows clearly that additions of Ti have the greatest effect, creating a dispersion of particles 2-4nm in diameter compared with an average of ~12nm with $Y_2O_3$ alone. Zr also refines the nanocluster distribution, but is not appropriate for fusion applications due to the longevity of its radioactive nuclides [117]. It has been repeatedly shown that Ti containing ODS alloys have an increased yield and creep strength compared to those without Ti [67, 118-120]. Consequently Ti is included in many ODS alloys and is added to all known experimental alloys currently in development.

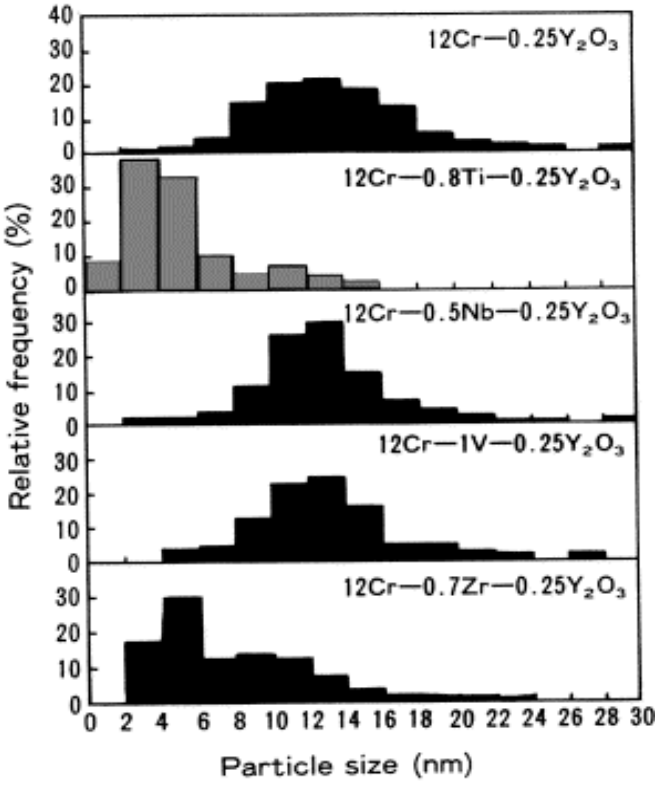


Reprinted with permission from Elsevier. © 2002 Elsevier B.V.

**Figure 2.12 - effect of alloying additions on the oxide particle size distribution of a 12%Cr ODS steel (1989) [121]**

Research into why Ti has such an effect has progressed in recent years. Okuda and Fujiwara carried out an x-ray diffraction study on MA powder [69]. The study convincingly showed no peaks relating to Y-Ti-O complexes in powder after MA, and an increase in Y-Ti-O complex intensity after annealing at temperatures from 1173K to 1573K. An atom probe study of two alloys processed in an identical manner, 12-Y1 and 12-YWT (developed by Kobe steel) also concluded that the Ti played a significant role in the oxide particle formation [2]. The two alloys are very similar in composition with the only major difference being the inclusion of 0.25wt%Ti in the 12-YWT alloy. The dispersion of oxides was much finer in the 12-YWT alloy and the particles were found to contain approximately equal parts Y and Ti, whereas the particles in the 12-Y1 were primarily Y based.

Considerable debate remains over the exact composition of the oxides, and this is discussed in §2.3.3.2 in relation to the various analysis techniques used. What is known is that the Ti containing oxides are more resistant to coarsening [72] [87], and that the concentration of Ti and O in the

matrix need careful control, as if the correct balance is not obtained, the formation of coarser oxides (10nm+) is promoted [106, 119, 122].

Aluminium in another element that is present in oxide particles if included in the base alloy [52, 123]. On occasions stringers of 20nm+ oxide particles have been observed [52], particularly in commercial alloys MA 957 and PM 2000. Al is not included in the base alloys designed for fusion, due to residual radioactivity but, traces of the element may be incorporated during the milling process.

Klimenkov et al. recently reported regions of ordered oxides [124] that closely resemble the stringers reported in the PM2000 alloy and others. While Klimenkov et al. attribute the lines of V-Mn-Cr oxides to internal oxidation of the powder during fabrication, it is more likely to be caused by Al contamination. Alloys which regularly exhibit oxide stringers all contain Al, and whilst the ODS Eurofer should not contain Al, the inclusions in the ordered region are reported to contain 2.5wt% Al [124]. Contamination could explain why a number of batches of ODS Eurofer show this effect, which is potentially very detrimental to the material properties.

## 2.5 Stability of the ODS microstructure at high temperature

One of the main advantages of ODS steels is that the particles remain dispersed in the matrix to very high temperatures, and in the MA957 alloy, the grain structures and dislocation networks are found to be stable up to 2000hrs at 1000°C [125]. In some alloys however, thermal aging is reported to have some effect on mechanical properties [52, 126]. After thermal aging at 475°C, significant embrittlement was seen in 14-20%Cr ODS steels but TEM observations showed no change in the oxide particle size or distribution [126]. The main cause of the embrittlement was attributed to the formation of a Cr-rich α′ phase observed by TEM, and a hardening relationship as a function of increasing Cr content was obtained. Changes to the oxide particle distribution have been observed by APT after aging at temperatures above 1300°C [90] and even then, only a limited amount of

coarsening was observed after aging for 24hrs. SANS studies have shown slight coarsening after 2000hrs at 950/1000°C and more pronounced coarsening after 8000hrs [125]. These results are very promising but it would appear that as yet that no attempt has been made to establish whether any change in particle composition occurs during the coarsening process. This would help establish whether the particles evolve from a metastable state to a more stable phase. It would also be helpful to know if changes to the particle-matrix interface occur during coarsening.

## 2.6 Behaviour of the ODS microstructure under irradiation

At present, a fast neutron source that would simulate fusion reactor conditions is not available, therefore alternative radiation sources must be used. The principal options are to use a low energy neutron source such as the BOR-60 reactor [127], electron radiation in a high energy TEM [93, 128-129], proton radiation or implantation by either light ions ($He^{+}$) [130-132] or heavy ions ( $Fe^{2+}$, $Ni^{2+}$ etc) [133-134]. Heavy ion implantation creates displacement cascades of similar magnitude to high energy neutrons, whereas electron irradiation or light ion implantation creates a larger number of Frenkel pairs. None of these methods are able to replicate the transmutation effects that occur with fast neutrons, however they can provide a useful insight into the effects that are likely to occur. It is unfortunate that in most studies it is not specified as to whether the irradiation source is rastered or continuous. This makes comparisons between studies difficult. Rastering allows some annealing between doses of relatively high displacement damage, which may affect the outcome of the experiment.

As a general rule, the effect of irradiation on the mechanical properties of ODS materials is less severe than that observed in the base alloys reviewed in §2.2.1. Effects such as an increase in yield strength, loss of ductility and saturation of hardening were observed, and have been comprehensively reviewed by Odette et al. [60] ODS materials are very resistant to swelling, but very low levels of heterogeneous swelling have been reported under both neutron and electron

irradiations[129, 135]. In all cases the presence of oxide particles as trapping sites was cited as the reason for the difference between base alloys and the ODS materials.

The effect of irradiation on ODS-nanostructure is less clear, but work is in progress to clarify this. Monnet et al. have examined the effects of different irradiation conditions on oxide particle dissolution, claiming that under 1.2MeV electron irradiation to 100dpa the oxide particles dissolve [136]. They also report changes in composition at all measured dpa values. The paper includes details on ion irradiation with 1MeV He ions, citing no change in oxide particle size, but the total damage in this case was only 0.05dpa. It was suggested that a minimum displacement energy is required, and that energy must be sufficient to displace both a metal and oxygen atom from the lattice simultaneously for dissolution to occur. As particle analysis was carried out using TEM, it should be noted that only the larger oxide particles were investigated.

Much of the work carried out in Japan also uses either electron or neutron irradiation. Work published so far has been at much lower doses than the electron irradiation carried out by Monnet et. al. (typically 5-20dpa) and for example, both Saito [129] and Kinoshita [128] report no change in particle size or distribution. Compositions of the particles were not analysed so it is unknown whether any change had taken place. Under neutron irradiation at 2.5, 7, 14 and 15dpa no change in particle size was reported by Akasaka [137] but at 21dpa Yamashita [138] indicates that the average particle size is slightly increased with small particles disappearing. Yamashita et al. have also recently investigated neutron irradiation in MA 957 [139] up to 100dpa, and at this higher dose rate they reported negligible change in the oxide particle size. Monnet et al. however, report a significant decrease in number density of particles after irradiation to a similar dpa, and also observed haloes of small particles forming around larger (~200nm) oxides [136].

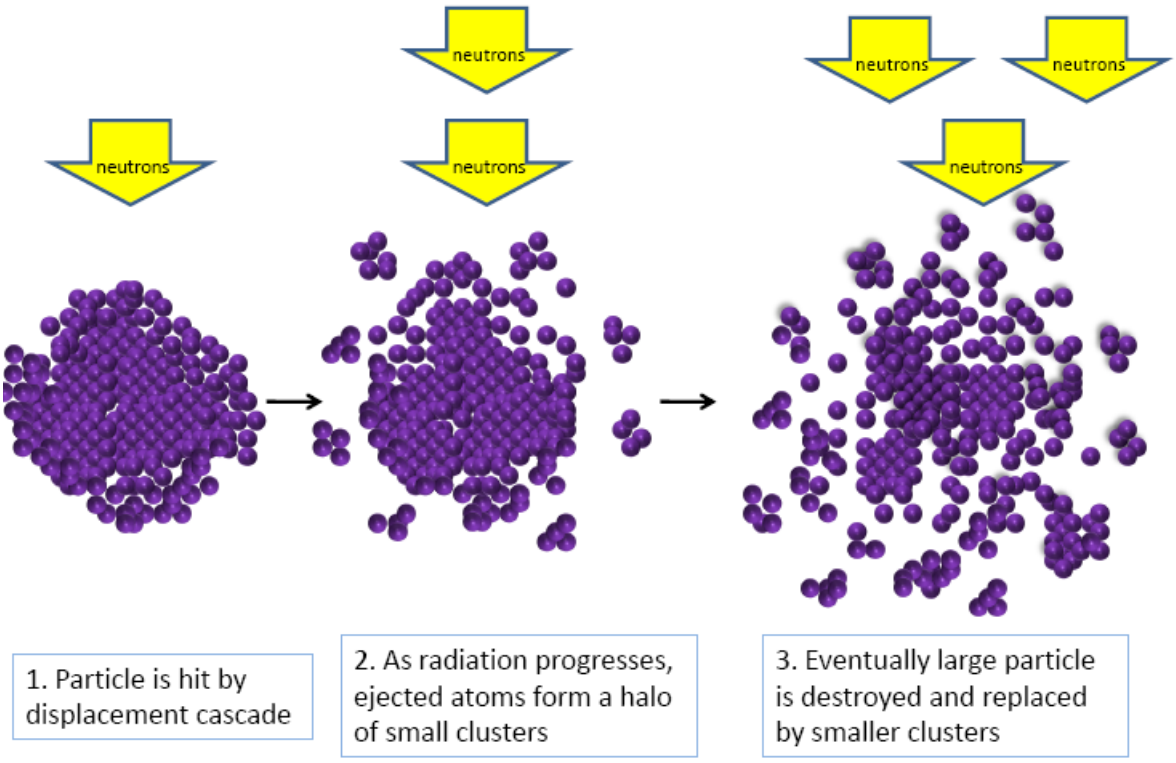


**Figure 2.13 – Possible dissolution and re-precipitation sequence of ODS particles after intense irradiation (based on[140])**

The formation of the haloes is predicted by simulations carried out by Frost and Russell [141]. Russell notes that if a displacement cascade passes partly through a precipitate, solute atoms may be ejected from the particle [140]. These ejected atoms may then back-diffuse to the original particle or remain in the matrix. From the matrix, the solute is free to diffuse to another particle or nucleate a new particle, leading to the sequence shown in Figure 2.13. When the displacement cascade is larger than the oxide, the particles may be completely destroyed (if the cascade has sufficient energy to displace the Y-O solutes). The mechanisms are likely to be different in this case.

Possible mechanisms of dissolution were reviewed by Allen et al. [133] who used heavy ion irradiation to doses of 150dpa on a 9%Cr RAFM-ODS steel over a range of temperatures 500-700˚C. At all temperatures, densification of the small oxide particles was seen [133]. This reduction in size was reported to be temperature dependent, indicating that thermal effects are an important factor, and that radiation damage is not entirely driven by ballistic processes. Allen et al. present an alternative theory to Russell. The displacement energy for Y and O in a Y-O particle was calculated

to be 57eV. As Fe has a displacement energy of 40eV, this would drive a net flux of vacancies to the oxide particle creating an increased vacancy concentration. Interestingly, at low dpa no size reduction was observed. Pareige et al. [134] used atom probe to investigate the stability of clusters in 12-YWT. Heavy ions ($Fe^{2+}$) were used to create large displacement cascades resulting in a damage total of ~0.7dpa. Similar to helium bombardment results, no ballistic dissolution or particle coarsening was observed, even with the improved resolution associated with the atom probe technique. This indicates that the process is dependent on total dpa. It is possible that both ballistic dissolution and particle coarsening occur, but which mechanism dominates is likely to be defined by the particular irradiation conditions.

It is possible that the grain structure will have some effect on the materials response to irradiation. Vogeli et al. investigated nanocrystalline Ni alloys by molecular dynamic simulations, and concluded that grain growth was likely if the grains were smaller than the displacement cascade size [142]. Grain growth has also been seen experimentally in austenitic steels irradiated to 5dpa using $Fe^{2+}$ ion implantation [143]. Wurster and Pippan showed from thermodynamic data first presented by Shen [144] that an optimum grain diameter will exist, that minimises the sum of grain boundary free energy and point defect free energy, so that the annihilation of irradiation induced point defects occurs both at grain boundaries and due to vacancy-interstitial interactions [145]. It was concluded that this grain diameter is influenced by the material and irradiation conditions and is not necessarily the smallest grain size. More research is required to establish what influence the grain structure has on the stability of the ODS microstructure under irradiation. Grain growth under irradiation is likely to alter the mechanical properties of the alloys, and therefore it is vital that these effects are understood.

### 2.6.1 Effectiveness of particles in trapping helium

In order to simulate conditions in a fusion reactor, extra helium must be introduced as fusion neutrons produce approximately 300 appm per irradiation year in ITER in a typical RAFM

steel[146]. One of the most cost effective methods of doing this is by dual-beam ion implantation of heavy ions (such as $Fe^{2+}$) and He [147-148]. The microstructures are then analysed by TEM. This is challenging as it is difficult to distinguish between the oxide particles and the He bubbles, and the smallest bubbles may not be resolved. Yutani et. al. observed He bubbles with mean diameter of ~4nm after 150dpa in the K3-ODS alloy whereas bubbles in the JLF-1 alloy (a non ODS alloy of similar composition and processing) were more than twice as large on average [148]. The bubbles were primarily located on the interfaces between the oxide particles and the matrix, indicating that the particles are successful in trapping the helium in a high density of small bubbles.

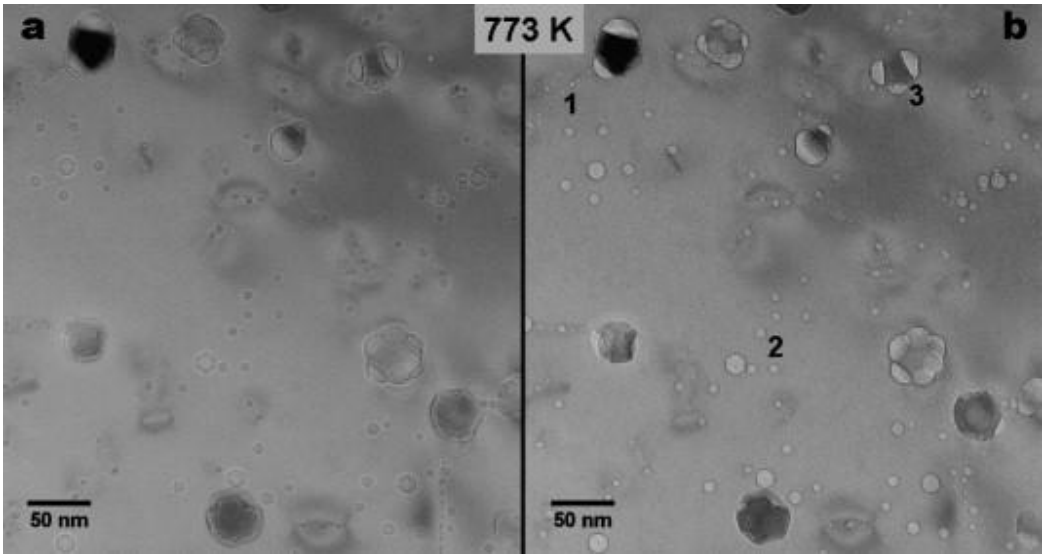


**Figure 2.14 - Helium bubbles trapped at ODS particles in ODS PM2000 alloy. Bright field TEM image where (a) is over-focussed and (b) under-focussed [130].** Reprinted with permission from Elsevier. © 2008 Elsevier B.V.

Another novel method of generating helium during irradiation is to coat the material to be implanted with NiAl so that during irradiation in a high flux isotope reactor, ~40appm/dpa of He is created (due to the transmutation of the Ni) within the region to be analysed by TEM[149]. This technique has been used on both the ODS-Eurofer [150] and MA957-[151], and when the results of these two experiments were compared, it was seen that where there is a lower density of slightly larger oxide particles (in the ODS-Eurofer) the bubbles were also larger (~4nm) and of lower density. Larger voids were also seen in this case, whereas in the MA957 these were not seen. It can be concluded

that as the oxide particles are smaller in the MA 957 alloy (~2nm diameter compared with ~5nm diameter in the ODS-Eurofer), the increase in number density of particles makes the appearance of voids less likely. These results support the theory that increasing the number of small particles improves the control of helium bubble formation during irradiation.

## 2.7 Summary

ODS alloys are excellent candidates for structural applications in advanced nuclear reactors, in particular fusion, as they can operate at high temperature, and are very successful in trapping helium. With regard to processing ODS alloys, it is clear that:

- MA processing is time consuming, expensive and often results in an inhomogeneous microstructure;
- Even after thermo-mechanical treatments the grain size is non-isotropic in many cases;
- The oxide particles are very stable at high temperature;
- There is considerable confusion over the composition of the oxide particles.

This review has covered significant advances in alternatives to MA, and thermo-mechanical treatments that improve homogeneity and grain structure. A summary of pre-irradiation properties has been presented, together with an assessment of how the processing has affected the microstructure and therefore the mechanical properties. Research on the effect of irradiation on the material is in progress, and preliminary results have been described, however further study is required in this area. Many other key areas of research have also been highlighted, including the need to establish how the oxide particles form and develop, and the effect of MA processing parameters on the particles. The remainder of this thesis will now focus on these issues.

# 3 Materials and Experimental Methods

## 3.1 Materials

### 3.1.1 ODS steels

Several ODS alloys have been studied during the course of this research. The nominal composition of the alloys is given in Table 3.1. The alloys were processed by mechanical alloying using the procedure outlined in Section 2.3.1. The specific processing conditions for the main alloys used in this study are given below.

- **ODS-Eurofer 97**

Supplied by Lindau et al. of Forschungszentrum Karlsruhe (Germany,) this alloy composition was gas-atomised and mechanically alloyed with 0.3wt% $Y_2O_3$ powder in an attritor mill before being canned, degassed then subjected to Hot Isostatic Pressing (HIP). After consolidation, the material was hot-rolled in a series of deformation steps with intermediate annealing to produce a final plate of 6mm thickness. Unfortunately, the exact conditions of temperature, time and pressure have been withheld by the manufacturers (Plansee Ltd).

- **EPFL-14Cr-ODS**

Several batches of the alloys supplied by Baluc et. al. of EPFL (Switzerland) were analysed. In each case the nominal composition of the alloy was as shown in Table 3.1.

i. Pre-alloyed, gas-atomised powder was used to create some batches. These were mixed with either 0.3wt.% $Y_2O_3$ (designated EPFL-PA-$Y_2O_3$) or 0.5wt.% $Fe_2Y$ (designated EPFL-PA-$FE_2Y$) and ball milled for 20-40hrs in a planetary ball mill in $H_2$ atmosphere. These powders were

degassed at a lower temperature of 600°C for 4 hours, and consolidated by HIP at 1150°C, 200MPa for 4 hours.

ii. The remainder of the material was processed by mixing elemental powders with either 0.3wt.% $Y_2O_3$ (designated EPFL-E-$Y_2O_3$) or 0.5wt.% $Fe_2Y$ (designated EPFL-E-$FE_2Y$) and ball milling for 50hrs in a planetary ball mill in $H_2$ atmosphere. The powders were degassed at 800°C for 2 hours, and consolidated by HIP at 1150°C, 200MPa for 4 hours. Attritor ball milling was also used in one instance, keeping all other parameters the same.

| | ODS-Eurofer | | EPFL-14Cr ODS | |
|---|---|---|---|---|
| **Element** | Wt.% | At% | Wt.% | At% |
| **Fe** | 88.57 | 87.85 | 83.20 | 83.92 |
| **Cr** | 8.90 | 9.48 | 14.00 | 14.99 |
| **W** | 1.10 | 0.33 | 2.00 | 0.61 |
| **Ti** | - | - | 0.30 | 0.35 |
| **Y** | 0.24 | 0.15 | 0.22 | 0.14 |
| **O** | 0.06 | 0.21 | - | - |
| **Mn** | 0.45 | 0.45 | - | - |
| **Si** | 0.10 | 0.20 | - | - |
| **C** | 0.14 | 0.65 | - | - |
| **N** | 0.11 | 0.44 | - | - |

**Table 3.1 – Nominal composition of main alloys studied in wt. %**

### 3.1.2 Bulk oxides

APT analysis of several bulk oxides were also carried out for reference. As discussed in §2.3.3.2, the most likely stable oxide phases for the nanoclusters are either $Y_2O_3$, $Y_2Ti_2O_7$ or $Y_2TiO_5$.

$Y_2Ti_2O_7$ and $Y_2TiO_5$ specimens were provided by Dr. Lingfeng He (Extreme Energy-Density Research Institute, Nagaoka University of Technology, Japan) and $Y_2O_3$ was provided by Dr. Yann de Carlan (CEA, France). Each oxide is different in terms of metal to oxygen ratio (M:O) and crystal structure, and therefore may behave differently under field evaporation. Table 3.2 summarises the structure and properties of the bulk oxides used in the reference study.

| Oxide | Composition (at. %) | | | Crystal structure |
|---|---|---|---|---|
| | Y | Ti | O | |
| $Y_2O_3$ | 40 | - | 60 | Cubic |
| $Y_2TiO_5$ | 25 | 12.5 | 62.5 | Orthorhombic |
| $Y_2Ti_2O_7$ | 18.2 | 18.2 | 63.6 | Pyrochlore |

**Table 3.2 – Structure and composition of bulk oxides used in reference study**

## 3.2 Transmission electron microscopy

TEM was carried out using an FEI CM20 microscope operated at 200kV. The majority of the images were taken using bright field imaging. For bulk materials, 3mm disks were polished to 0.3mm thickness, then electropolished using a solution of 2% perchloric acid in methanol. Sections of powder were also analysed but in this case the specimens were prepared using focussed ion beam milling (FIB). A powder particle was 'welded' with W to a copper TEM half-grid using FIB, and thinned to <100nm. The initial stages of FIB were undertaken with a 40kV beam of $Ga^+$ ions, and a low energy 2kV final polishing stage was used to avoid excessive Ga implantation into the specimen.

## 3.3 Atom probe tomography

### 3.3.1 Overview

Atom probe tomography is a high resolution analytical technique that is built on the concept of a conductive needle-shaped specimen, subjected to a high voltage. A comprehensive account of the development of the instrument can be found in [152], and will not be discussed in detail here. The basic operating principle involves cooling a specimen of tip radius 50-100nm to <50K in high vacuum. A dc voltage in the range of 3-10kV is applied to the specimen creating very high field strength at the tip. An additional high voltage or laser pulse is then applied, which allows controlled field evaporation of atoms from the surface. The time of flight of each ion between the specimen and the position-sensitive detector is accurately measured so the mass of the ion can be calculated

(shown schematically in Figure 3.1). The original location of the atom on the surface of the specimen can be inferred from the location it hits the detector.

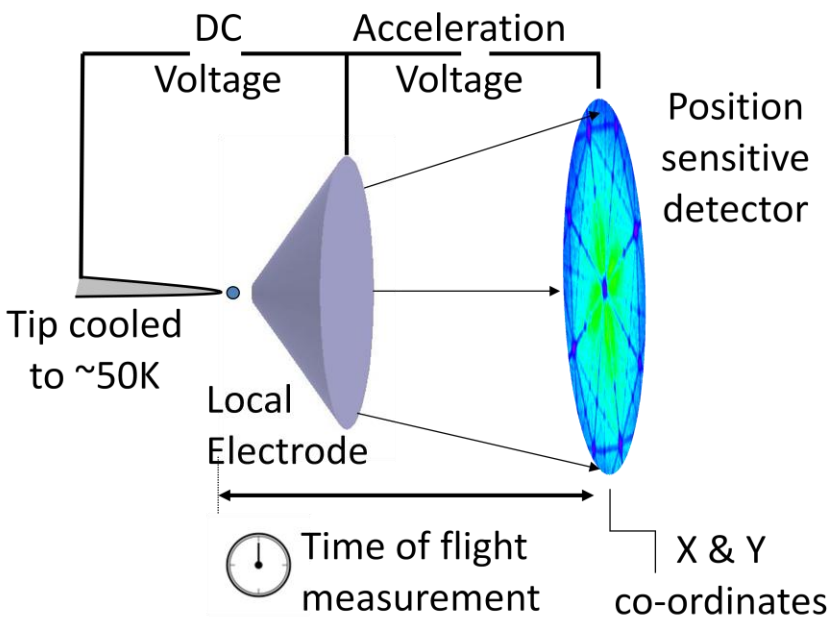


**Figure 3.1 - Schematic representation of the local electrode atom probe (LEAP)**

The use of laser pulsing to induce field evaporation was developed by Kellogg and Tsong [153]. If voltage pulsing is used, the field at the tip of the specimen can be increased to above the threshold required for ion evaporation. By applying a thermal pulse using a laser, instead of increasing the field, the temperature is increased to a point above the threshold required for ion evaporation, as shown in Figure 3.2. Laser pulsing allows specimens with lower conductivity to be analysed, and reduces the probability of premature specimen fracture as less stress is applied to the specimen, compared with specimens analysed in voltage pulsing mode. Increasing the temperature at the tip of the specimen however has several disadvantages. The laser illuminates the specimen from one side. In poorly conducting specimens, ions may evaporate preferentially from that side of the specimen, leading to a non-uniform specimen end-form, and non-uniform field evaporation behaviour. Poor heat dissipation can also lead to a loss of mass resolution. Laser pulsing raises the probability of

surface migration of atoms, and the probability of multiple ions evaporating together is also increased.

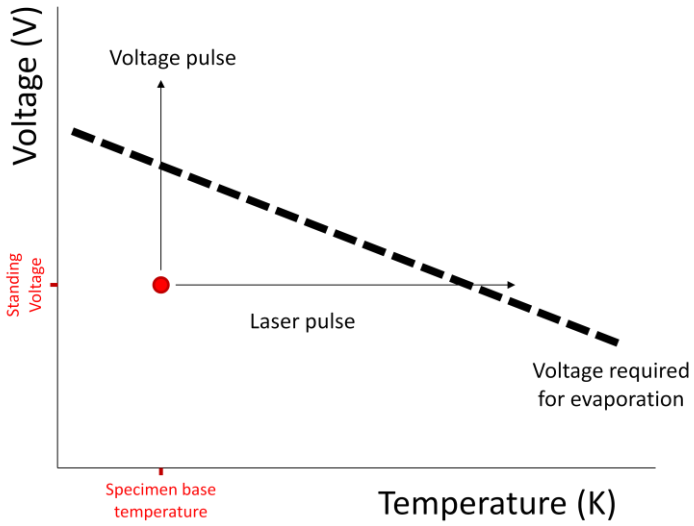


**Figure 3.2 - Schematic showing how changes in either voltage or temperature induce field evaporation**

The instrument used in this study is the Cameca LEAP 3000. In the LEAP, a local electrode is introduced close to the tip to enhance the field, as shown. This improves the mass resolution by reducing the path over which the ions are accelerated, and reduces the voltage required to produce a field sufficient for ionisation by ~50%. This improves data acquisition rates, as higher pulse repetition rates can be achieved at lower voltages. Typically for this instrument, pulse repetition rates of 200kHz are used. The instrument is also fitted with a reflectron lens which compensates for spread in ion energies which occur during voltage pulsing. Due to the arrangement of detectors, only ~37% of ions are detected but all elements are detected with equal probability.

As each atomic layer is evaporated, the positions are recorded so that a 3-D reconstruction can be generated. The detector is designed to register the impact of more than one ion simultaneously. When multiple ions leave the surface of the specimen on the same pulse, the point at which each ion is detected is deciphered by using an arrangement of three delay line detectors orientated at 0°, 45° and 90° respectively, as shown below. When an ion hits the detector at point (x,y) the signal is

amplified by a micro-channel plate, and propagates in both directions along the delay line. Once an ion impacts the detector, there is a reset time of ~3ns before another hit can be detected in that region. The time taken for the signal to reach the end of the delay line allows the spatial location on the ion hit to be identified. For the 0° and 90° delay lines, the x-y coordinates correspond to C( $t_{x2}$-$t_{x1}$ , $t_{y2}$-$t_{y1}$) where C is a constant.

If two ions hit the detector at the same time, there are two possible configurations for the impact coordinates. The 'correct' coordinates ($x_1$, $y_1$), ($x_2$, $y_2$), or the alternative: ($x_2$, $y_1$), ($x_1$, $y_2$). The 45° delay line removes this ambiguity by providing two extra time signals, provided the hits are separated by a minimum distance. This minimum distance is controlled by the waveform of the signal as it propagates down the delay-line: there must be sufficient space/time to allow the signal from the previous hit to travel down the delay-line undisturbed. Effectively this means that any ions of the same mass to charge state ratio that hit the detector very close together are not registered.

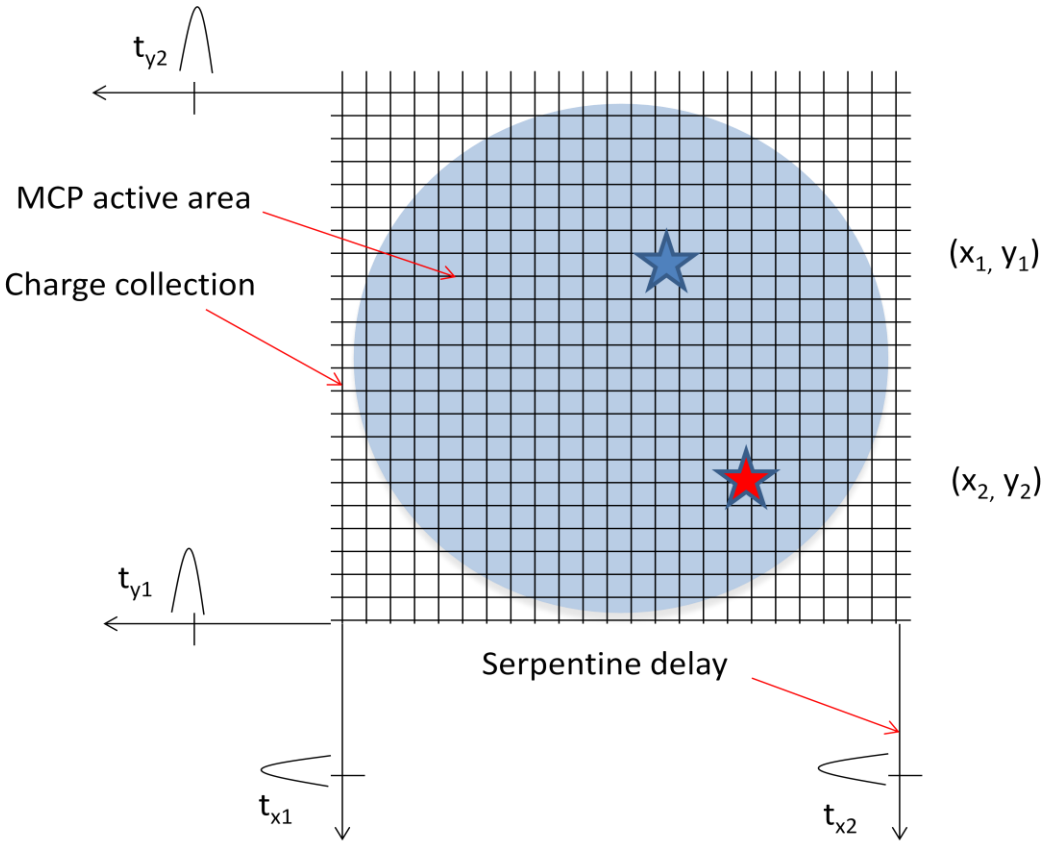


**Figure 3.3 - Schematic of the delay line detector set-up (showing 0° and 90° lines only). Image adapted from [154]**

### 3.3.2 Specimen preparation

The precise specimen geometry can have a significant effect on the quality of the data acquisition and 3-D reconstruction. It is desirable to have a cylindrically symmetric specimen, with a smoothly tapering cone angle towards the apex.

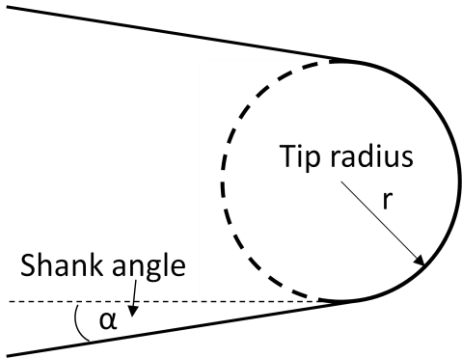


**Figure 3.4 - Schematic of ideal specimen geometry.**

#### *3.3.2.1 Electropolishing*

Specimens were prepared by cutting 0.5 x 0.5 x 15 mm 'matchsticks' using a low-speed saw fitted with a boron-nitride cutting blade. These bars were electropolished in two stages to produce fine needles with typical tip radius of 50-100nm. Figure 3.5 shows the first stage schematically. The matchstick is moved through a layer of electrolyte (25% perchloric acid in 75% acetic acid) until a neck is formed, eventually creating two specimens. The tip radius is often greater than 150nm at this stage therefore the tips are refined using the micropolishing technique illustrated in Figure 3.6. The counter electrode loop allows the specimen to be moved through a very thin layer of electrolyte (2% perchloric acid, 98% 2-butoxyethanol) to produce a tip end radius of 50-100nm. Prepared specimens were stored in a vacuum desiccator to avoid excessive oxidation of the surface.

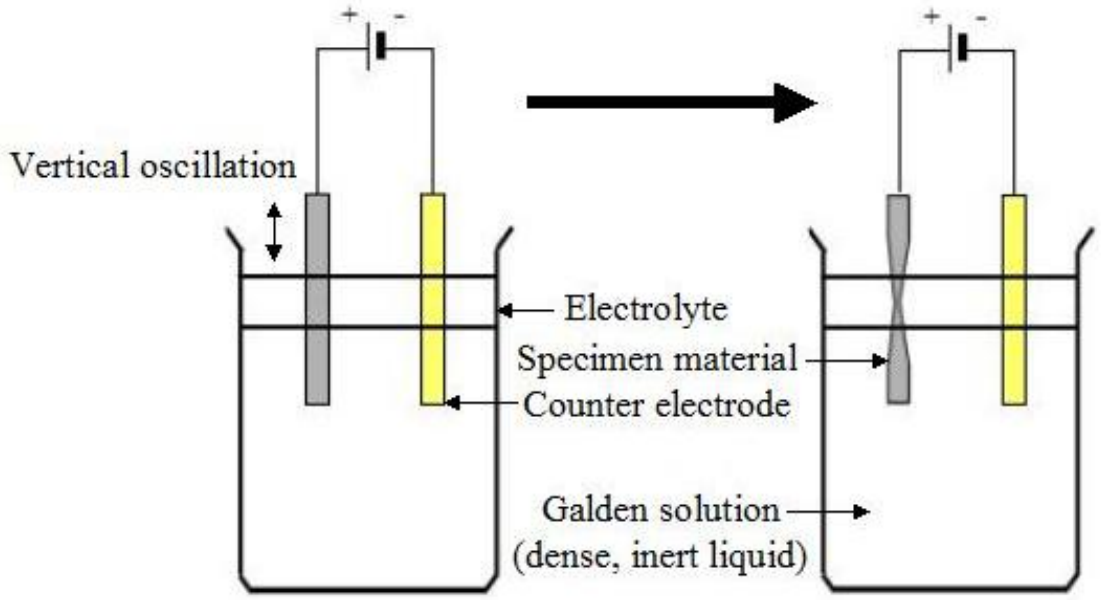


**Figure 3.5 – Schematic showing the primary electropolishing stage (from [155])**

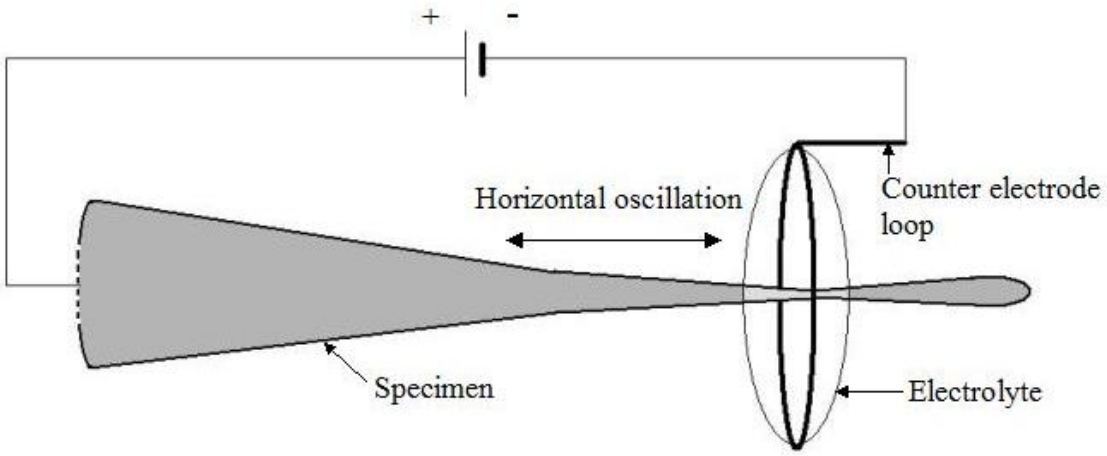


**Figure 3.6 – Schematic showing the micropolishing stage (from [155])**

#### *3.3.2.2 Focussed ion beam milling (FIB)*

It is not possible to create APT specimens from powdered alloys using conventional electropolishing techniques. The Zeiss NVision 40 dual-beam FIB-SEM instrument was used to cut a section of powder 2x20x4μm from a relatively flat region of a powder flake, by sputtering the surface with 40kV Ga ions. The section of powder was then welded to the in-situ Kleindiek micromanipulator, and cut free from the bulk, as shown in Figure 3.7a. An array of silicon posts with end diameter of ~2μm (known as a microtip coupon) was then used as a base to form APT specimens. The section of powder was brought into contact with the top of the silicon post, and 'welded' on from one side with deposited W (Figure 3.7b). The beam was cut free by FIB, and the process repeated to create four specimens. The weld was then strengthened by rotating the post 180° and depositing W on the other side, and a sharp needle formed by annular milling (Figure 3.7 c and d). The energy of the Ga ions was reduced to 2kV to remove the top 100nm of the tip, so that the Ga implanted layer is only several nm.

The end-tip radius and shank angle must be carefully controlled during the annular milling as the thermal conductivity of specimens is reduced when samples are welded to a silicon post. When using laser pulsing, the shank angle is a significant concern, as the heat introduced into the specimen by the laser pulse must be dissipated through the specimen before the arrival of the next pulse. If the shank angle is too small, heat is not dissipated quickly enough from the tip, and the mass resolution is degraded [156]. In this case the base of the specimen is kept as wide as possible, and a tip radius of 100nm is used to improve mass resolution (Figure 3.7d). If the shank angle is too large, the specimen geometry deviates too far from the model of a hemispherical geometry assumed during the reconstruction stage, and the data is not properly reconstructed. The specimen geometry also directly influences the standing voltage required for field evaporation, and the field of view obtained in the x-y plane.

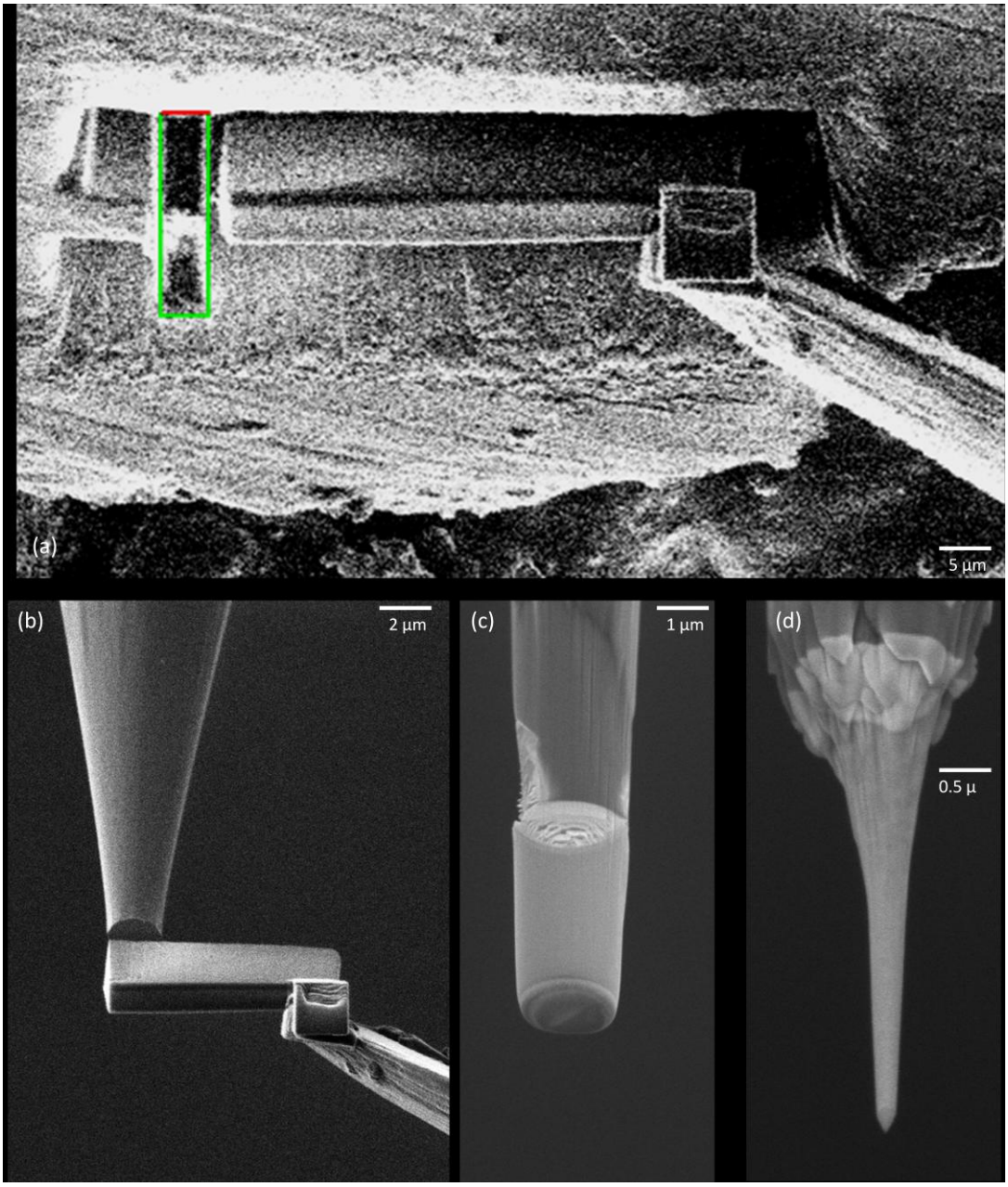


**Figure 3.7 - FIB specimen preparation**

### 3.3.3 Selecting appropriate analysis conditions

The overview of APT operating principles (§3.3.1) indicates that there are several factors that could influence the quality of the data collected. These include

i. Specimen geometry
ii. Orientation and precise distance of specimen from local electrode
iii. Specimen base temperature
iv. If voltage pulsing is to be used, the pulse fraction
v. If laser pulsing is to be used, the laser energy, wavelength, pulse duration and spot size
vi. Evaporation rate

During the specimen preparation stage, care is taken to ensure that specimens are made with appropriate geometry as described above, and when setting up the instrument, the specimen must be perpendicular to the plane of the electrode and the distance from the electrode needs to be 20-30μm. When selecting analysis conditions relating to specimen temperature and pulsing mode, the quality of the data produced is the most important consideration (as shown later in §4.4), however the probability of premature specimen fracture must also be considered, along with ensuring consistency between experiments.

Laser pulsing was used in the majority of experiments, primarily to ensure consistency. In irradiated materials, the increase in hardness caused by irradiation is known to make specimens more prone to fracture [155]. The additional voltage pulse in voltage pulsing mode adds even more stress to the specimen, there was concern that sufficient results would not be obtained if used. As part of this work involved comparing irradiated materials with unirradiated, the characterisation of the unirradiated material was also carried out using laser pulsing. Numerous voltage pulsing experiments were also carried out for reference but unless stated, it should be assumed that all results are obtained using laser pulsing at a specimen temperature of 30K and a laser energy of 0.2-0.4nJ.

A specimen base temperature of 30K was chosen as cooling the specimen reduces the extent of surface migration, thereby improving resolution in the x-y plane. The spread in kinetic energy of field evaporated ions is also reduced. The Cameca LEAP instrument was not capable of operating consistently at temperatures below 30K at the outset of this project, and as no substantial improvements in mass resolution were noted at lower temperatures (and there was a significant increase in specimen fracture rates) the specimen temperature was maintained at 30K throughout this work.

The laser wavelength, pulse duration and spot size are fixed by the instrument. The laser energy was varied slightly from one experiment to another in conjunction with the adjustment in the applied voltage in order to maintain approximately constant field conditions at the specimen apex. In voltage pulsing experiments, this was done automatically by specifying a fractional increase in voltage for the additional voltage pulse to induce field evaporation. In laser pulsed experiments, if the tip radius changes substantially during an experiment, the field can also vary significantly if the laser energy is kept constant. In order to maintain a constant evaporation field in laser pulsing experiments, the charge state ratios of the field evaporated ions as described below. Specimen shank angles of ~5° were also used where possible so that the increase in tip radius during evaporation was kept to a minimum. If the laser energy is too low, the likelihood of evaporation of ions between laser pulses increases. If the laser energy is too high, not only is surface migration increased, but there is also a significant increase in the number of multiple ion peaks detected in the mass spectrum, which increases the error in the mass ranging. This will be expanded in §5.2.3.2 and §5.4.1.2.

Kingham proposes that the existence of higher charge states is caused by post-ionisation of the singly charged species [157]. At high fields, the proportion of $Fe^{2+}$ ions approaches one, therefore the ratio of 1+/2+ peaks can be used as an estimate of field strength. Figure 3.8a shows the theoretical predictions of Kingham, along with the charge state ratios calculated at different values

of laser energy in the EPFL-PA-$FE_2Y$ alloy. Each data point in Figure 3.8b corresponds to the ratio determined from the same specimen with a sample of ~10M ions. By selecting a laser energy that minimised the proportion of $Fe^+$ ions, whilst still detecting a finite number of counts, variation in the field strength from one specimen to another was minimised. In the example given in Figure 3.8, a laser energy of 0.4nJ was chosen. The laser energy chosen can affect the composition measurements, and this is addressed in more detail in §5.3 and §5.5.

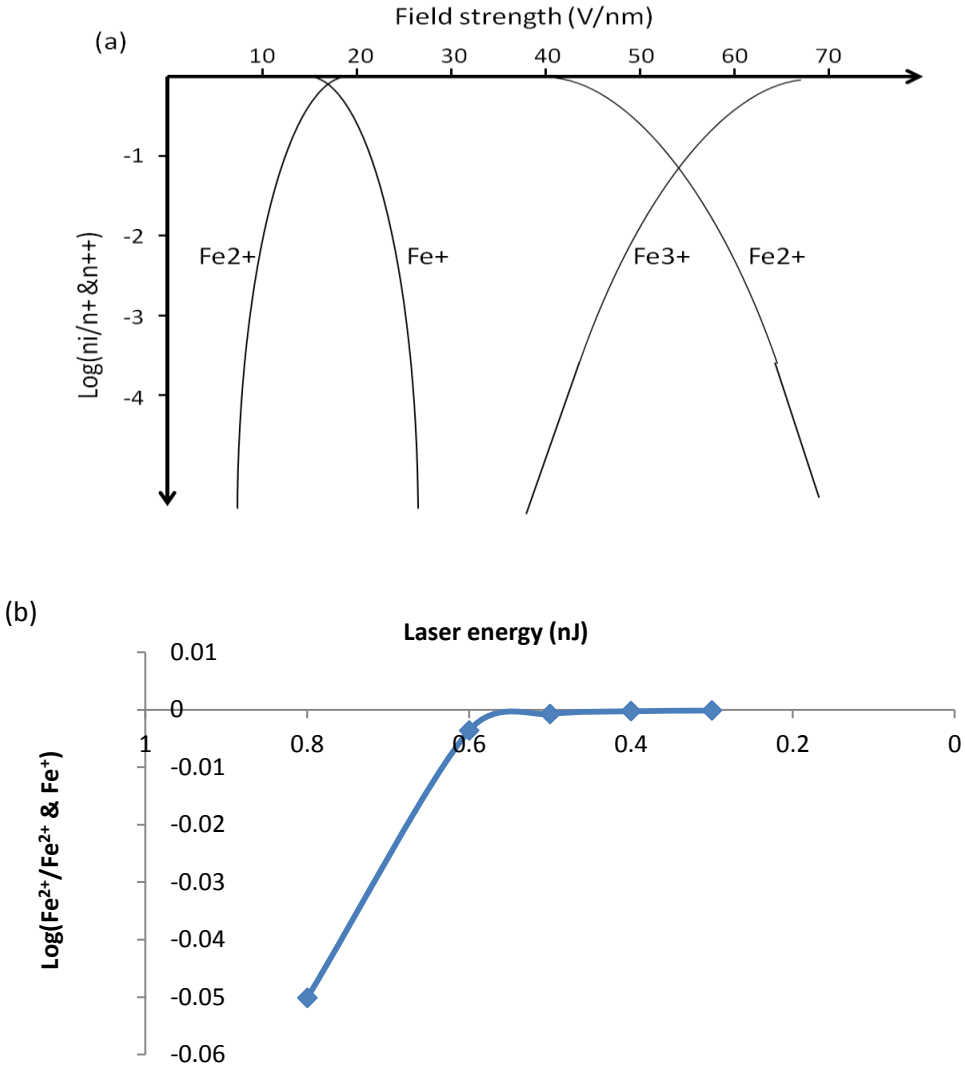


**Figure 3.8 - (a) Variation in charge state ratio (reformatted from Kingham et. al. [157]) (b) Variation in $Fe^{2+}/Fe^{+}$ charge state ratio with decreasing laser power. Specimen base temperature 30K.**

### 3.3.4 Mass spectrum analysis

The mass spectrum obtained from APT analysis of ODS steels is complex due to the number of alloying elements and possible combinations of multiple-ion complexes. A labelled mass spectrum for the EPFL-PA-$Y_2O_3$ alloy is shown as an example in Figure 3.9. In some instances there is degree of ambiguity in the identity of certain peaks. Where this is the case, the following factors are taken into account to ensure that the mass peaks are identified in a consistent manner.

i. Many elements have multiple isotopes (e.g. Ti) and the distinct distribution of peaks can be used to identify them. If a significant change in the isotopic abundances is noted, it is assumed that another element is contributing to that peak.

ii. The position of the ion types is also an important consideration. Oxygen containing complexes are most likely to be seen in the vicinity of oxide particles, whereas carbon containing compounds are more likely to be observed where there is carbon segregation at a grain boundary, or larger carbide.

iii. Where there is a choice between two or more multiple-ion complexes, the simplest complex is assumed to be most likely. The abundance of the elements forming the complex is also an important consideration. For example, Fe containing complexes are chosen above any combinations of C, O and N.

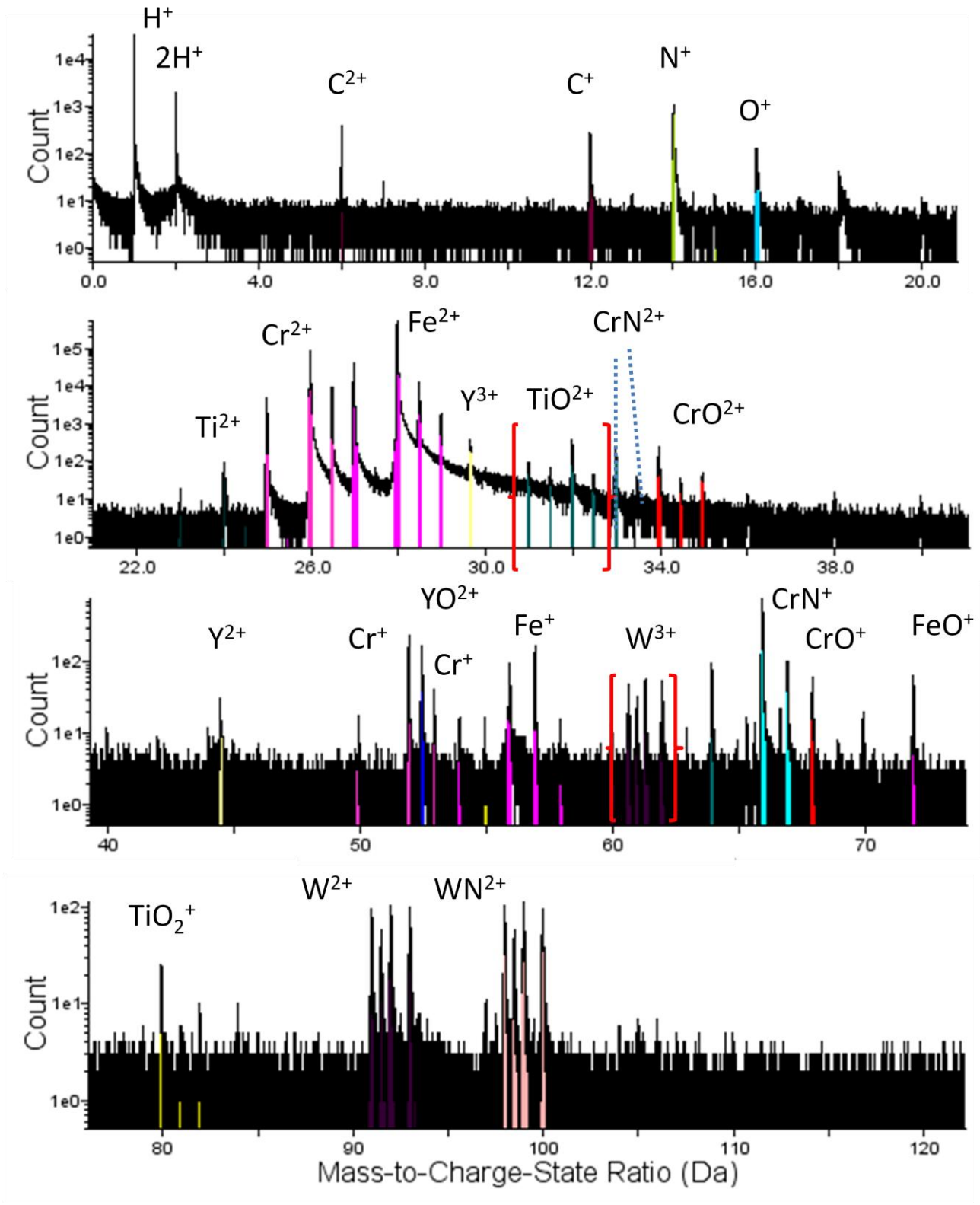


**Figure 3.9- Labelled mass spectrum for EPFL-PA-Y2O3 alloy obtained using lased pulsed atom probe. This mass spectrum was obtained at 30K using 0.3nJ laser energy, and contains approximately 10M ions.**

### *3.3.4.1 Mass peak ranging*

Figure **3.9** shows that there is a range of mass to charge state ratios that corresponds to each mass peak. How the width of that peak is defined directly affects the number of counts of each element that is recorded, particularly for very dilute solute elements. Hudson et. al. used simulated data to test various methods of assigning ranges to mass spectra. They concluded that least variance was recorded if the peak was defined as the full width at 9/10 of the maximum height [158]. FW9/10M was therefore used when ranging all peaks in the mass spectrum. In using this criterion, only ~80% of the detected ions are ranged, and this lowers the effective detector efficiency to approximately 30%. While this is a sizable reduction, the accuracy of the mass to charge state ratio on the remaining ions is improved. As the average specimen analysis volume contains >30,000,000 ions, this is not expected to affect the counting statistics significantly.

### *3.3.4.2 Peak deconvolution*

In some cases the mass peaks of two elements overlap. Where this effect significantly affects the composition measurements, the peaks are decomposed based on the expected number of counts signified by the isotopic abundances of the elements in question. A particularly important example is the overlap of the $O_2^+$ peak and the $TiO^{2+}$ peak at 32 amu in the $Y_2TiO_5$ oxide. The relative isotopic abundances of the minor $TiO^{2+}$ peaks are indicated in Figure 3.10. The total number of counts (highlighted red in Figure 3.10) were summed and this value used to estimate the number of counts associated with the major $TiO^{2+}$ peak. Given that the relative abundance of the major $TiO^{2+}$ peak is 73.7%, approximately 35% of the peak at 32 amu is identified as $TiO^{2+}$. The remainder is assigned to be $O_2^+$ as indicated in blue in Figure 3.10.

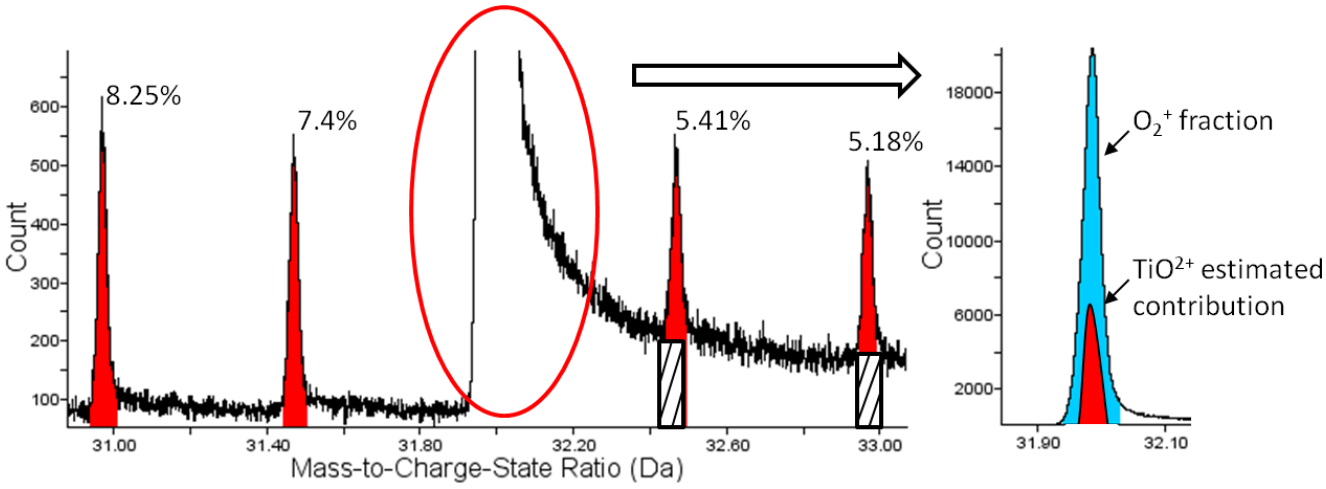


**Figure 3.10 – Schematic representation of the $TiO^{2+}$ contribution to the mass peak (in red) at 32 amu based on the heights of the minor $TiO^{2+}$ peaks.**

### 3.3.5 3-D Reconstruction

The Cameca IVAS software was used to reconstruct the detector hit coordinates into a 3-D atom map, based on a point projection model with the protocol designed by Bas et. al. [159]. The reconstruction of the atomic positions is achieved by first assigning the x and y coordinates of the centre of the detector to be (0,0). The x and y coordinates of the atoms in the reconstruction are calculated by back-projection from the position of impact on the detector ($X_d$ ,$Y_d$) using the following relation:

$$x = \frac{X_d}{\eta} \qquad y = \frac{Y_d}{\eta} \qquad \textbf{Equation 1 \& 2}$$

where η is the magnification. The specimen is assumed to have a hemispherical cap on a shank of small angle. The trajectory of the evaporating ion would be straight and perpendicular to the surface of the specimen if the specimen was fully spherical, but the magnification is reduced by a factor ξ (the image compression factor or ICF) because the field is non-radial due to the specimen shank, and the ion trajectories are bent towards the detector. The magnification is therefore expressed as η= d/ξr where r is the radius of the specimen tip, and d is the flight path to the detector. As the tip radius r is constantly changing during analysis, it is necessary to estimate this value for each atom from the relationship between r, the specimen voltage V, and the evaporation field F:

$$r_t = \frac{V}{kF}$$ **Equation 3 [152]**

The z coordinate is then determined based on the evaporation sequence of ions from the specimen, assuming that the atomic volume is evenly distributed across the surface plane of atoms ($dv/dz=S_a$), where $S_a$ is the specimen apex. The reverse projection argument can be used once again provided a small angle approximation is used, so that the area at the specimen apex can be written as $S_a = \frac{S_D}{\eta^2}$

where $S_D$ is the detector area.

The relationships described allow us to describe the depth increment as:

$$\boldsymbol{dz = \frac{\Omega d^2 k_f^2 F^2}{\xi \eta^2 S_D V^2}}$$ **Equation 4**

Where $k_f$ is the field factor and Ω is the detection efficiency. To use these relationships to generate a 3-D reconstruction of the data therefore involves a knowledge of all the values and parameters mentioned above. However as outlined by Gault et. al. there is currently no direct method to accurately determine three of the key input parameters – $k_f$, the ICF (ξ) and Ω [160]. The Bas et. al. protocol was designed for early atom probe instruments with a limited field of view operating in voltage pulsing mode. Some of the assumptions made about these parameters are not most appropriate for the case of a wide angled local electrode atom probe operating in laser pulsing mode, but as yet there is no other method to reconstruct the data. The Bas model is therefore used throughout this work.

The detection efficiency is a property intrinsic to the specific instrument used, and for the Cameca LEAP 3000 this is taken to be ~37% [161].

#### *3.3.5.1 Determination of the field factor*

For the case of a perfect sphere $r \propto \frac{V}{F}$, and the relationship $r = \frac{V}{k_f F}$ is assumed true for the case of an atom probe specimen due to the field-shielding effect of the specimen shank. Previous APT

studies have used predictions of the low temperature evaporation fields calculated from the image hump model by Tsong [162]. When using laser pulsed APT there is significant uncertainty in the actual value assigned to the field induced at the surface of the specimen. This uncertainty is further increased by the high density of oxide particles present in the material. In this study we must therefore assume that the field F is unknown, and thus, using this relation to estimate the tip radius for the 3-D reconstruction is not valid.

By independently measuring the tip radius by TEM across a range of specimens analysed by APT at different voltages, a value for the combined constant $k_fF$ has been established for the EPFL ODS alloys. The gradient of the line shown in Figure 3.11 gives the value of $k_fF$ as ~55V/nm. This value was used in the reconstruction process to estimate r for individual specimens. The manufacturers of the LEAP (Cameca ltd) assign a default value of 3.3 for $k_f$. If this value is assumed, the effective evaporation field for these ODS materials becomes 17 V/nm, which significantly less than the 33V/nm default value recommended by IVAS.

Figure 3.11 shows TEM and APT measurements from both the EPFL-PA-$FE_2Y$ and EPFL-PA-$Y_2O_3$ materials. These two materials exhibit very different oxide particle dispersions (EPFL-PA-$FE_2Y$ material has Y-O clusters ~5nm in diameter, EPFL-PA-$Y_2O_3$ material has Ti-Y-O clusters ~2nm in diameter) and yet there is no significant difference in the $k_fF$ value obtained. This indicates that the particle dispersion does not significantly affect the overall evaporation behaviour of the material.

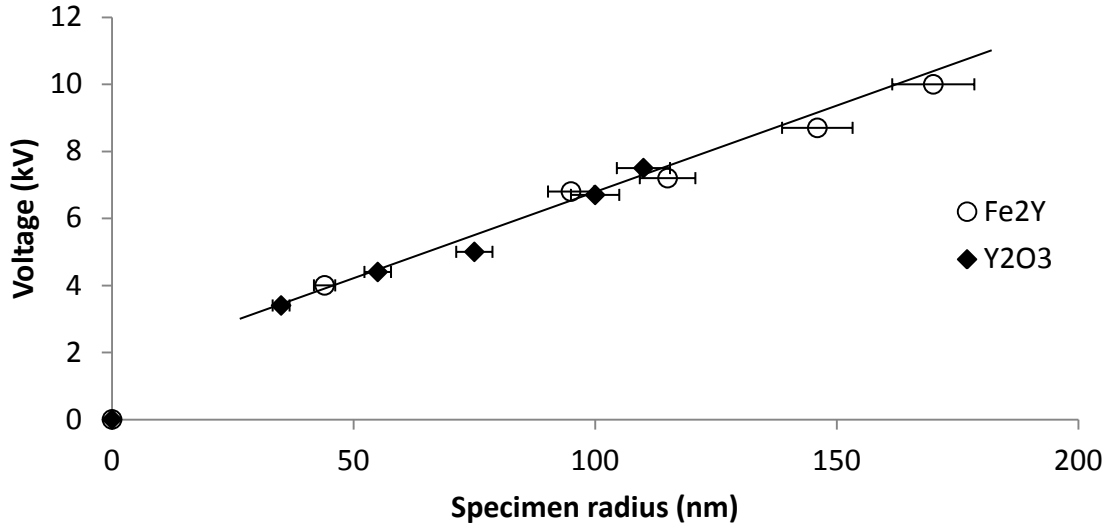


**Figure 3.11 - Plot of specimen tip radius measured from TEM images against APT standing voltage at the beginning of the APT analysis**

### *3.3.5.2 Determination of the ICF*

The field desorption image seen on the detector contains some detail on the crystallography of the specimen. Local field variations occur where major crystallographic poles protrude from the specimen surface, forming a region with a lower density of atoms. The pattern of zone lines around each pole corresponds approximately to a stereographic projection, therefore these poles are easily identifiable. In the vicinity of a pole, some alloy systems allow for planes of atoms to be resolved directly, but this is not possible in the ODS steels due to the extensive number of alloying elements. Instead, a spatial distribution map (SDM) must be generated in order to resolve any crystallography. The SDM is effectively a 3-D histogram plotting the distance of each ion from every other ion [163]. High density regions that correspond to the atomic planes can be seen if the density is plotted along the z-axis as shown in Figure 3.12b. The ICF value for each specimen was obtained by systematically increasing the ICF until the planar spacing measured along the direction of analysis was consistent with the expected value for that pole. An example of two-fold symmetry corresponding to a 110 type pole and SDM is shown in Figure 3.12.

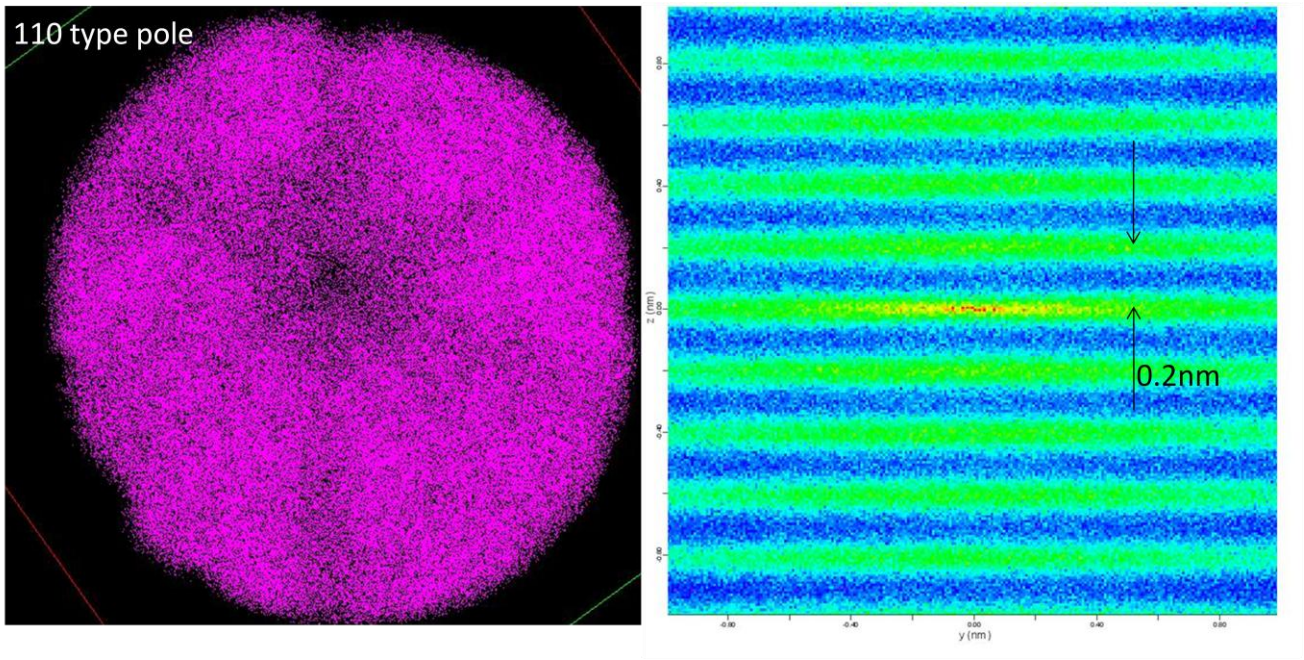


**Figure 3.12 - (i)110 type pole identified from desorption map (ii) spatial distribution map of atoms in the y-z plane. ICF value is adjusted until the interplanar spacing measures 0.2nm.**

This method was verified by scaling the reconstruction using clearly identifiable features as shown in the example in Figure 3.13. The ICF was increased systematically until the distance of the grain boundary from the specimen apex in the 3-D reconstruction was observed to correspond to the distance measured using the TEM. In this case the ICF value was 1.2 but the ICF value varied considerably from one specimen to another, with values ranging from 0.7-1.4 depending on the specimen.

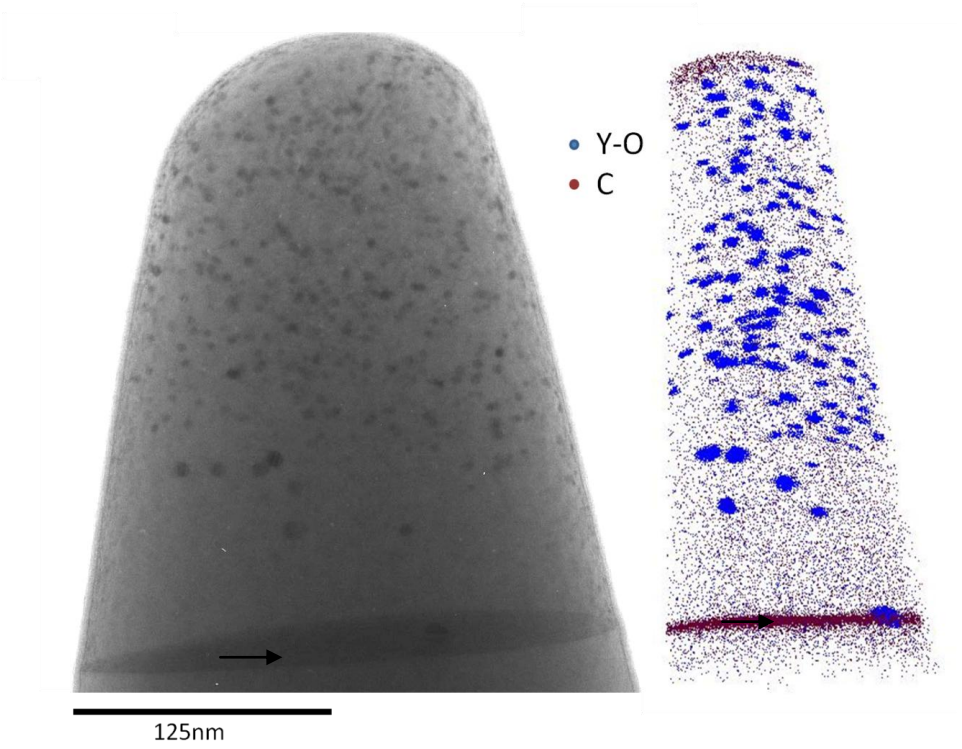


**Figure 3.13 - Scaling of APT reconstruction using a grain boundary**

As the total number of detected ions remains unchanged regardless of the reconstruction parameters used, the 3-D reconstruction itself has no effect on the composition measurements if the composition is calculated from the whole reconstruction. It is possible that the composition of features such as oxide particles is influenced by this. It was found that provided the value of $k_f$ was within 30% of the 'correct' value, no significant change in composition was noted therefore any error in the composition measurements due to this effect is considered negligible.

### 3.3.6 Data visualisation

APT data is commonly displayed on an atom map to highlight particular features as shown in Figure 3.14. A different coloured point is chosen to represent each ion type in the material. As this data is three-dimensional, it is not always possible to avoid overlap of features when representing the data in 2-D.

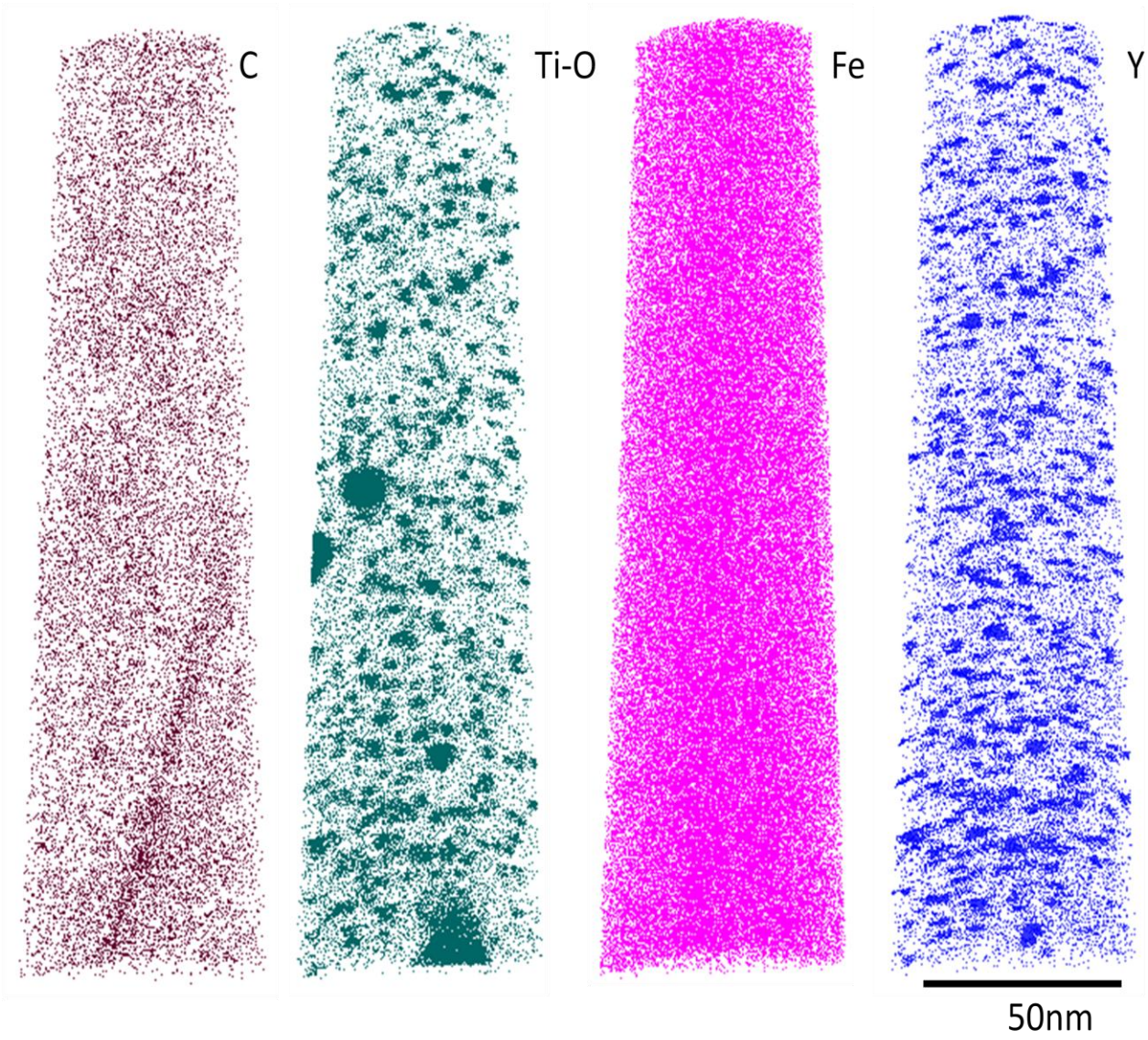


**Figure 3.14 - Atom maps showing the distribution of elements in EPFL-Fe2Y ODS alloy**

### 3.3.7 Common APT artefacts

Features such as grain boundaries and second phase particles can create a degree of uncertainty in the detected position of the ions, as they often cause the surface of the specimen to deviate significantly from the hemispherical tip shape assumed in the reconstruction model. Figure 3.15 shows how these features may affect the tip shape during analysis. The consequences of these artefacts are discussed in relation to the composition of the oxide particles in §4.5.2.1.

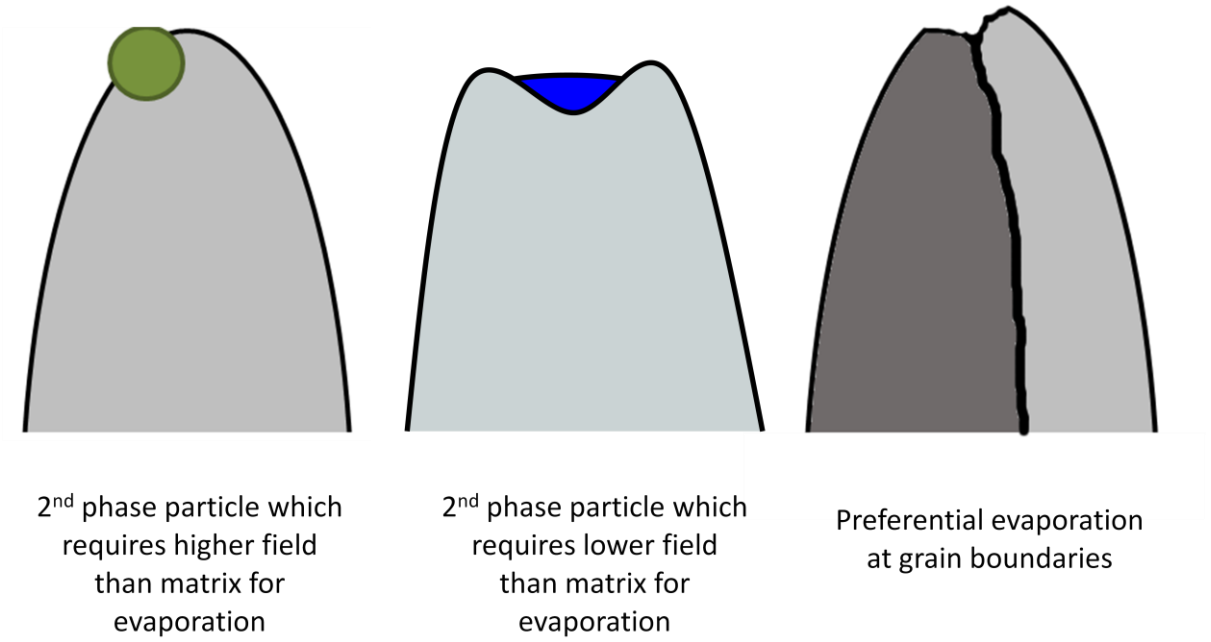


**Figure 3.15 – Exaggerated schematic representation of possible deviations from the hemispherical tip shape assumed in the 3-D reconstruction model**

## 3.4 Ion implantation

Ion implantation was performed at the University of Surrey ion beam facility, using a $Fe^{2+}$ ion beam rastered over a ~80cm$^2$ plate as shown in Figure 3.16. The base-plate was electrically heated and stabilised at 400°C, with the temperature controlled by a thermocouple attached to the back of the base-plate.

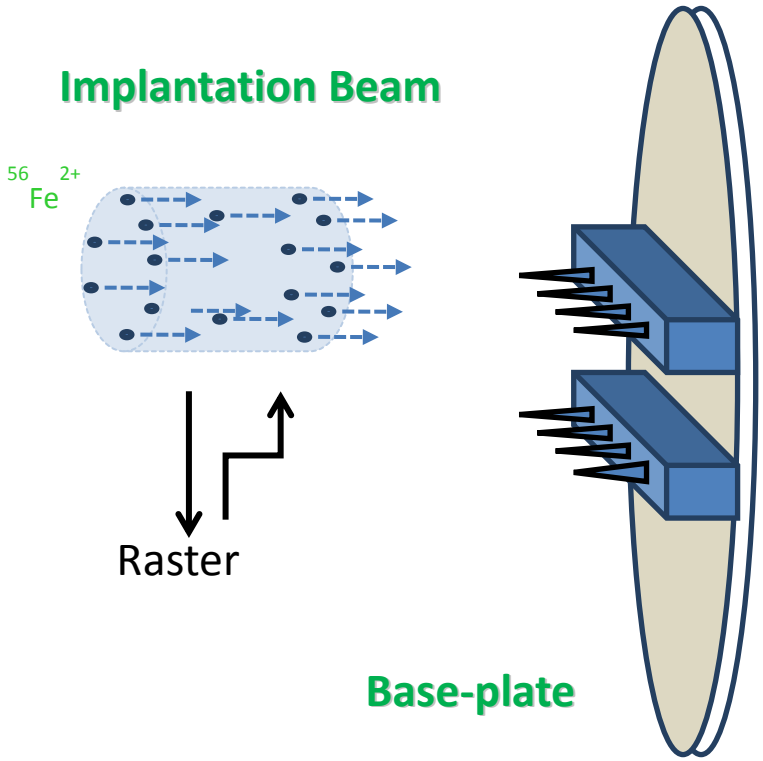


**Figure 3.16 - Ion-implantation set-up**

APT specimens were implanted with the specimen axis parallel to the ion beam. Two energies were used to produced a uniform damage profile (required for TEM analysis in a separate project), and the implantation details are outlined in Table 3.3. For the implantation conditions used in this study, the average number of displacements per atom (dpa) below a flat infinite surface are estimated using SRIM (Stopping Ranges of Ions in Matter) [164] assuming a bcc-Fe matrix and 40eV displacement energy for Fe [165]. The damage profile for both doses is shown in Figure 3.17. The dpa was then calculated using Equation 1, where Φ is the average number of displacements per ion and $N_{at}$ is the number of atoms per unit volume.

$$dpa = \frac{Dose \times \Phi}{N_{at}} \qquad \textbf{Equation 5}$$

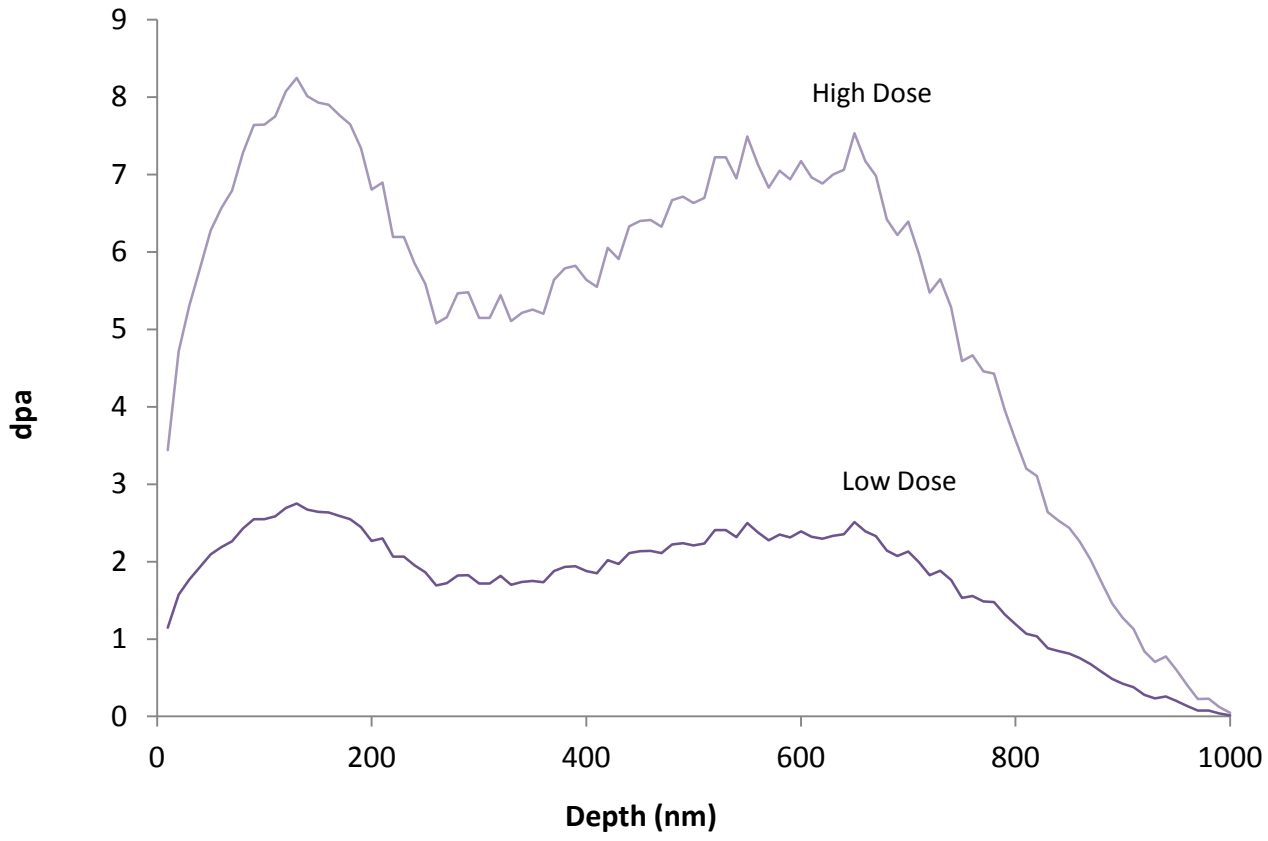


**Figure 3.17 - Damage profile from SRIM calculations**

| Condition | Ion energy(MeV) | Total ion dose per $cm^2$ | Time for implantation (s) | Average number of total dpa* | Temperature (˚C) |
|---|---|---|---|---|---|
| **Low dose** | 2.0 | $2 \times 10^{14}$ | 2400 | 2 | 400 |
| | 0.5 | $1 \times 10^{14}$ | 4000 | | |
| **High dose** | 2.0 | $1 \times 10^{15}$ | 7200 | 6 | 400 |
| | 0.5 | $5 \times 10^{14}$ | 4000 | | |

**Table 3.3 – Ion implantation conditions**

# 4 APT data analysis techniques

## 4.1 Introduction

Like all high resolution analytical techniques, the raw data obtained from APT requires careful interpretation. This chapter outlines methods of data analysis for the raw APT data. These methods are scrutinised to identify to what extent the various parameters influence the measured size and composition of the oxide features. The aim is to promote confidence in the measured changes in the oxide features reported in later chapters.

## 4.2 Data processing

The Cameca IVAS data analysis software provides tools to carry out the majority of the data analysis techniques outlined in this chapter, including proxigrams, basic cluster selection and 1-D (and 2-D) concentration profiles. Additional information for each 3-D reconstruction can be accessed by generating a .epos file during the reconstruction process. The information contained in the .epos file (outlined in Table 4.1) can be used for more advanced data manipulation such as the peak tail correction, and the analysis of multiple-ion evaporation events. MATLAB, a high-level programming environment, was used to process the data. Where applicable, the codes written can be found in Appendix B. The basic code to open the .epos file was kindly provided by Dr. Baptiste Gault.

| Data | Units | Data type | Description |
|---|---|---|---|
| **X** | nm | floating point number | X coordinate in the 3-D reconstruction |
| **Y** | nm | floating point number | Y coordinate in the 3-D reconstruction |
| **Z** | nm | floating point number | Z coordinate in the 3-D reconstruction |
| **M** | amu | floating point number | Atomic mass |
| **TOF** | ns | floating point number | Time of flight |
| **VDC** | V | floating point number | DC voltage applied to specimen at time of evaporation |
| **VP** | V | floating point number | Voltage applied during pulse (Voltage mode only, 0 otherwise) |
| **XDET** | mm | floating point number | X detector co-ordinate |
| **YDET** | mm | floating point number | Y detector co-ordinate |
| **ΔP** | n/a | integer | Number of pulses between this hit and the previous hit |
| **Npulse** | n/a | integer | Number of hits per pulse |

**Table 4.1 - Data contained in .epos file**

## 4.3 Composition measurements

Once the mass peaks have been correctly identified, the composition of any defined analysis volume is calculated from

$$C_a = \frac{N_a}{N_{tot}} \qquad \textbf{Equation 6}$$

where $C_a$ is the atomic fraction of element $a$, $N_a$ is the total number of $a$ ions in the analysis volume and $N_{tot}$ is the total number of ions in the volume of analysis. It is usual to calculate the error in this value to one standard deviation using the following relationship, assuming a binomial distribution exists in a random solid solution:

$$\Delta C_a = \sqrt{\frac{C_a(1-C_a)}{N_{tot}}} \qquad \textbf{Equation 7}$$

This error calculation does not account for variations that are introduced by the experimental factors such as variations in local electrode quality or analysis chamber vacuum level. These are accounted

for by analysing multiple specimens and calculating the standard error from all results. If there are insufficient results to make this possible, Equation 7 will be used, and will be indicated in the text.

## 4.4 Assessment of data quality

Not all data obtained from the atom probe is of the same 'quality' despite best efforts to keep all the experimental conditions the same. This is usually caused by variations in the effective thermal conductivity of the specimen, for example poor thermal connections between the specimen and the cooling stage, or poor welding during FIB preparation. The quality of the data directly impacts the measured composition of the material.

Figure 4.1 shows an example of very different mass spectra obtained from similar specimens of the same material. In this example, the specimens were prepared by electropolishing, and the APT analysis was carried out under the same conditions of 0.3nJ laser power at 30K base temperature. The DC voltage for analysis in the case of the 'good' data was 6kV and for the 'bad' data was 5kV. There are two measurable parameters to assess data quality – the mass resolution, and the noise floor.

- Mass resolution ($R=m/\Delta m$) is measured by FWHM (in amu) of the mass peak divided by the maximum m/e value of the peak.

- Background noise is quantified by means of the noise metric. This is defined by "the number of background counts per one million signal counts per nsec of TOF". The background counts are defined by the background estimate generated by the IVAS reconstruction software.

These values are summarised in Table 4.2 for the example shown in Figure 4.1.

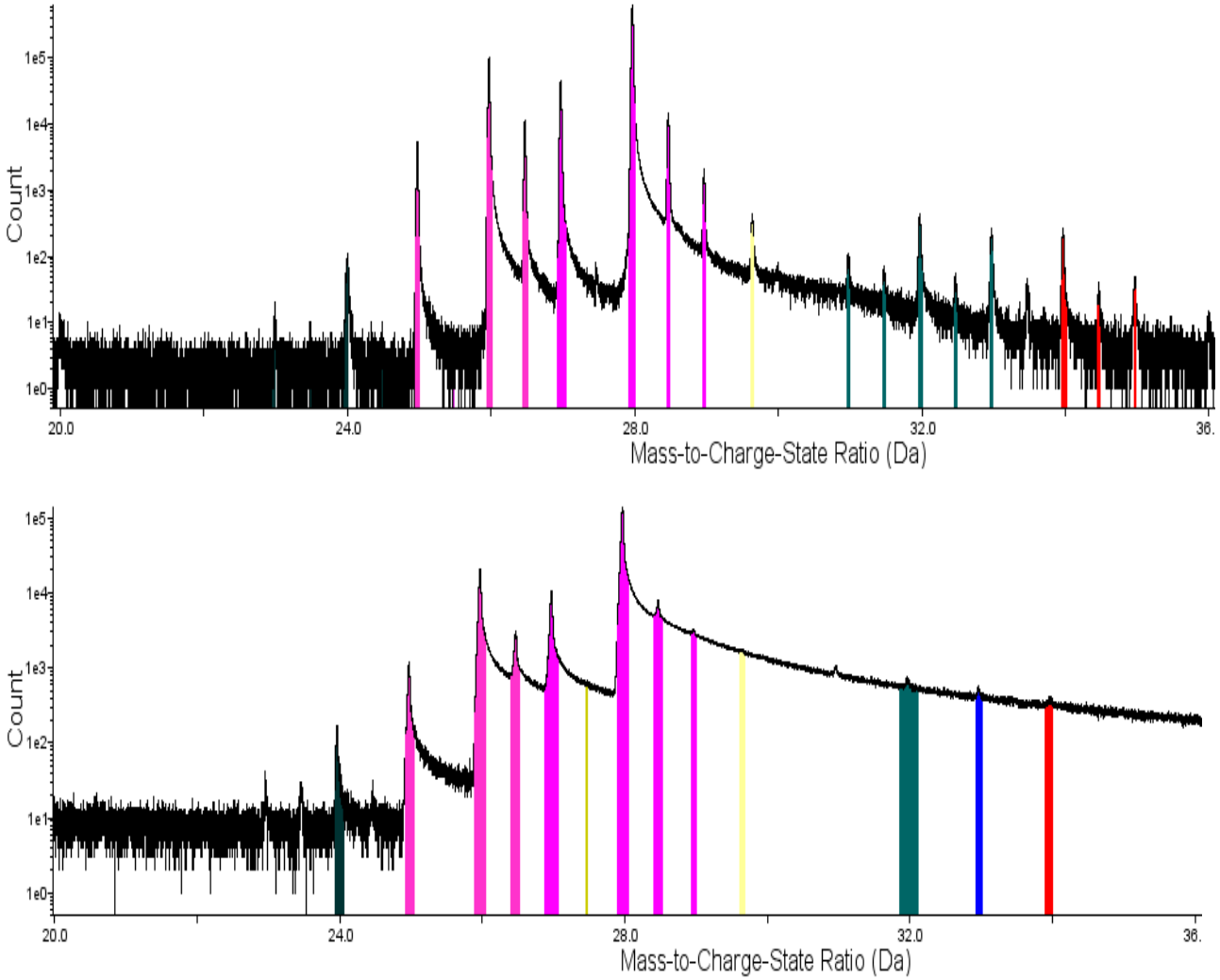


**Figure 4.1 - Mass spectra from EPFL-PA-$Y_2O_3$ alloy. (i) an example of 'good quality' data (ii) an example of 'bad quality' data. The nominal analysis conditions are the same in each case.**

| | Good | Bad |
|---|---|---|
| **Mass Resolution (amu)** | $7.86 \times 10^{-4}$ | $1.36 \times 10^{-3}$ |
| **Noise Metric** | 3.8 | 17.0 |

**Table 4.2 - Data quality parameters for good and bad quality data from the EPFL-PA-$Y_2O_3$ alloy**

Ideally, only 'good quality' data would be used, but when specimens are either irradiated, or prepared by FIB, the specimen preparation is very time consuming. It is sometimes impossible to repeat an experiment indefinitely in order to achieve the very highest level of data quality. Techniques such as the peak tail correction described below minimises the effect of 'bad quality' data on the measured bulk compositions.

### 4.4.1 Background correction

Some mass spectra have a high background noise level, which is often due to poor specimen geometry or emission from a local electrode that is in need of cleaning. In order to eliminate variance in the composition measurements caused by the background, a curve of the form $A/\sqrt{m}$ is fitted to the background using IVAS, and removed before the number of counts in each range is calculated.

The effect of the standard square root background correction on both 'good' and 'bad' quality data is shown in Table 4.3. There is a considerable increase in measured composition of clustered elements such as Y, Ti and O in the 'bad' data. It is clear from Table 4.3 and Figure 4.1 that the standard square root background correction is not sufficient for the analysis of ODS steels because the mass peaks of interest are within the tail of the main Fe peak at 28amu. This can be accounted for by applying a correction to the tail of the peak.

### 4.4.2 Peak tail correction

Poor mass resolution is usually associated with poor thermal conductivity through the specimen. The longer the heat is retained at the specimen apex, the higher the probability of delayed evaporation, which results in long peak tails. Long peak tails are therefore synonymous with mass spectra generated during laser pulsed APT.

The peak tails are assumed to decay exponentially. For the Fe peak, a section of the tail is isolated, and a best-fit curve is produced using a least squares approach. The curve is extrapolated to the background level, and the counts beneath the curve are removed and added to the main peak. The composition is then re-calculated from the corrected mass spectrum. The script corresponding to this process is found in Appendix B.3. Once this correction is applied, the measured compositions for both good and bad quality data fall to within one standard deviation of the mean measured

composition for this material, for clustered elements such as Y, Ti and O. There is however still ~1% discrepancy between the levels of Cr measured from 'good' and 'bad' datasets.

Compared with the composition measured by electron microprobe analysis (carried out by Chris Salter of Oxford Materials Characterisation Service) the overall values of Y and Ti measured by APT are much lower. It is assumed that this is due to the presence of larger oxide particles not seen in the APT volume of analysis. The levels of Cr in the 'good quality' data correspond well to the values obtained by EPMA.

Due to the complex nature of the peak tail correction, an arbitrary cut-off point of 5amu was decided upon. If the noise metric was below this value, the tail correction was deemed to be unnecessary, as the difference was marginal.

| Element | Good (APT) | | | Bad (APT) | | | EPMA |
|---|---|---|---|---|---|---|---|
| | Raw data | Sqrt only | Fe-tail corrected | Raw data | Sqrt only | Fe-tail corrected | |
| **C** | 0.05 | 0.05 | 0.05 | 0.08 | 0.05 | 0.06 | - |
| **Si** | 0.01 | 0.01 | 0.01 | 0.02 | 0.02 | 0.02 | - |
| **N** | 0.34 | 0.34 | 0.34 | 0.34 | 0.33 | 0.28 | - |
| **P** | 0.00 | 0.00 | 0.00 | 0.01 | 0.00 | 0.00 | - |
| **O** | 0.33 | 0.31 | 0.30 | 2.92 | 2.75 | 0.34 | - |
| **Ti** | 0.17 | 0.16 | 0.14 | 1.71 | 1.64 | 0.17 | 0.36 ± 0.02 |
| **Cr** | 13.60 | 13.59 | 13.60 | 12.66 | 12.64 | 12.47 | 13.72 ± 0.19 |
| **V** | 0.00 | 0.00 | 0.00 | 0.02 | 0.01 | 0.01 | - |
| **Fe** | 85.18 | 85.23 | 85.26 | 80.93 | 81.34 | 86.33 | 84.33 ± 0.18 (by diff) |
| **Y** | 0.10 | 0.10 | 0.09 | 0.74 | 0.72 | 0.08 | 0.21 ± 0.01 |
| **Mn** | 0.00 | 0.00 | 0.00 | 0.02 | 0.02 | 0.00 | - |
| **W** | 0.23 | 0.22 | 0.22 | 0.55 | 0.47 | 0.23 | 1.38 ± 0.06 |

**Table 4.3 - Effect of background and peak tail correction on the measured bulk composition of EPFL-PA-$Y_2O_3$**

## 4.5 Analysis of oxide particles and clusters

This work involves the analysis of clustering across multiple length scales, therefore different data analysis methods have been employed to assess the size, composition and number density of the clusters, depending on their size. These methods are briefly reviewed here, highlighting the need for careful choice of analysis parameters if quantitative information is to be extracted.

For large particles, where the core of the oxide feature is >5nm in diameter, the particles are most often analysed using the proxigram method described below. These larger oxide particles are then removed from the data reconstruction to investigate clustering on a finer scale using the maximum separation algorithm (Section 4.5.2). Throughout this thesis, features analysed using the cluster selection algorithm will be referred to as clusters, and larger features referred to as particles.

### 4.5.1 Proxigram

A proxigram is a composition profile generated by plotting concentration against the proximity to a reference surface. In the case of oxide particles, this is particularly useful as an isoconcentration surface can be used to define the particle-matrix interface, and the compositions on either side of that interfaces can then be evaluated.

The 3-D reconstruction is split into an array of voxels $1nm^3$, and the concentration of elements in each voxel is calculated. An iso-concentration surface is then generated by connecting voxels of a specified composition. A typical value for the oxide particle interface in the EPFL-ODS alloys is 0.3%Ti. The surface can take any shape, and once defined, the composition of each voxel for a given distance from the interface can be measured to generate the proxigram [166].

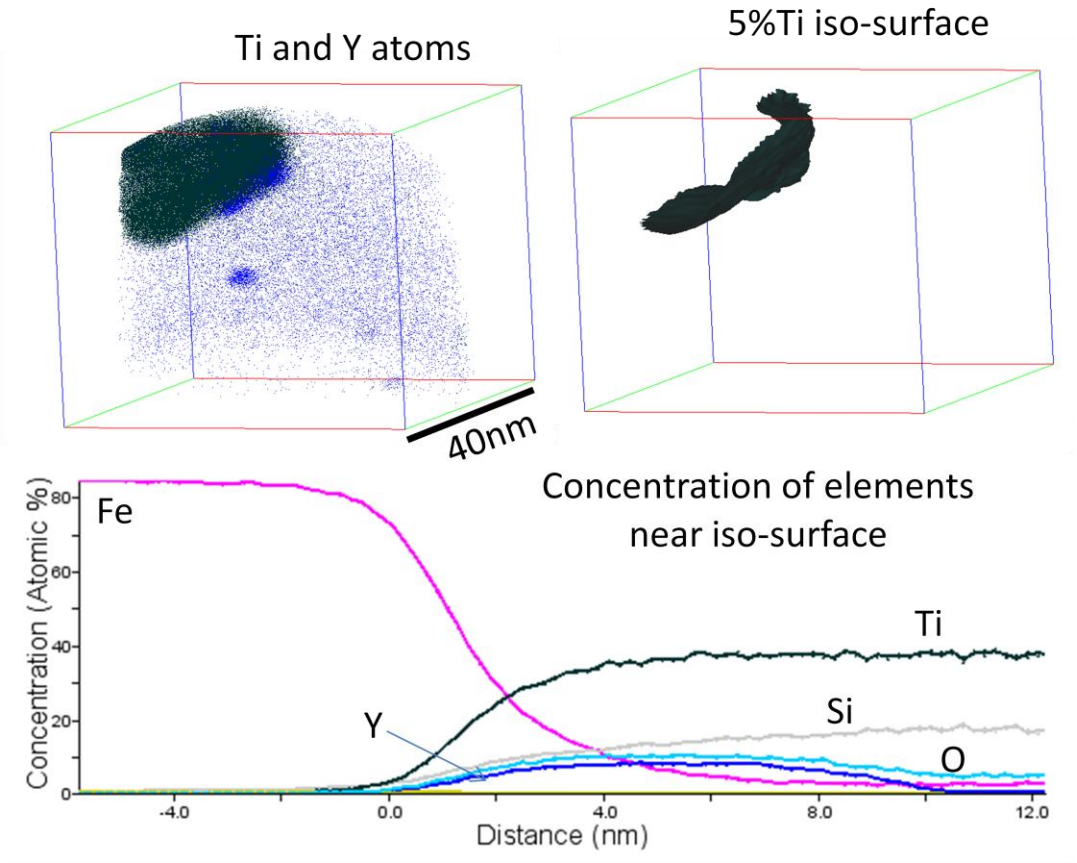


**Figure 4.2 - example of 0.3% Ti iso-concentration surface and associated proxigram for an oxide particle in EPFL-PA-$Fe_2Y$**

### 4.5.2 Maximum separation cluster selection method

Hyde and English developed the maximum separation method to define a cluster based on a concept of nearest neighbour analysis [167]. The process is shown schematically in Figure 4.3. A distance Dmax is chosen (Figure 4.3a), and all solute atoms with neighbours of the same element within this distance are defined as a cluster. Because agglomerations of 2 or more solute atoms are found using this method, and some random fluctuations between solute atoms are expected, a cut-off limit for the minimum size of a cluster Nmin is defined so that random clusters are not included in the analysis. When selecting values for these parameters, it is important not only to limit the number of random clusters that are included, but also to recognise that real clusters could be inadvertently excluded, or that a single cluster could be counted as multiple clusters if the parameters are not defined correctly.

Vaumousse et. al. developed a method for including non-solute atoms, by defining all particles within a chosen distance **L** of a solute atom form part of the cluster (illustrated in Figure 4.3d) [168]. This method will include a shell of matrix atoms that lie less than a distance L from the cluster interface and Vaumousse et. al. suggest using an 'erosion' process to remove these in order of their proximity to a solute atom. Due to an alternative method used to remove excess matrix atoms described below in §4.5.2.1, this step is not used in this present work.

Both the IVAS reconstruction software and 'posgen' software (developed by Dr. Daniel Haley) enable the implementation of these algorithms. The majority of cluster analysis in this thesis has been carried out using 'posgen' as it is easily incorporated into scripts written in MATLAB.

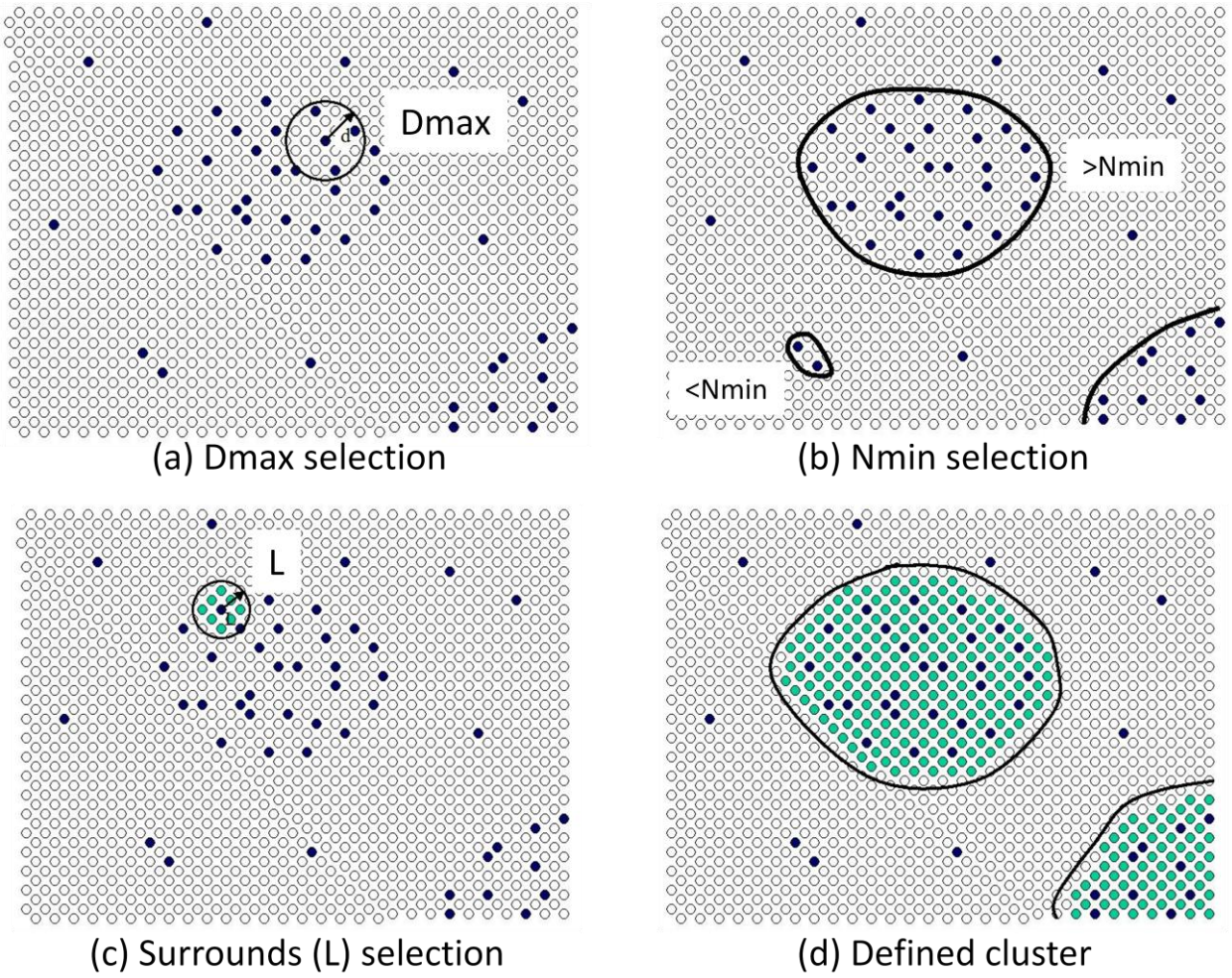


**Figure 4.3 – Schematic representation of the maximum separation cluster selection process**

#### *4.5.2.1 Matrix correction*

Field ion microscopy has shown that the oxide particles evaporate preferentially to the matrix [2]. The atom density maps in Figure 4.4 show that in the regions that correspond to the particles (seen by the density of Y atoms), the density of hits on the detector can be up to three times greater than in regions away from the particles. This leads to the conclusion that the majority of the atoms detected in the cluster regions are due to the trajectory aberrations shown schematically in Figure 4.5. A change in specimen shape caused by the preferential evaporation of a particle can cause ions from the matrix to be projected non-uniformly, so that they are detected in a region that would be expected to only contain ions from the particle. The width of the overlap region is in the order of a few nanometres, but this is highly dependent on the actual tip shape, and the field induced at the specimen apex.

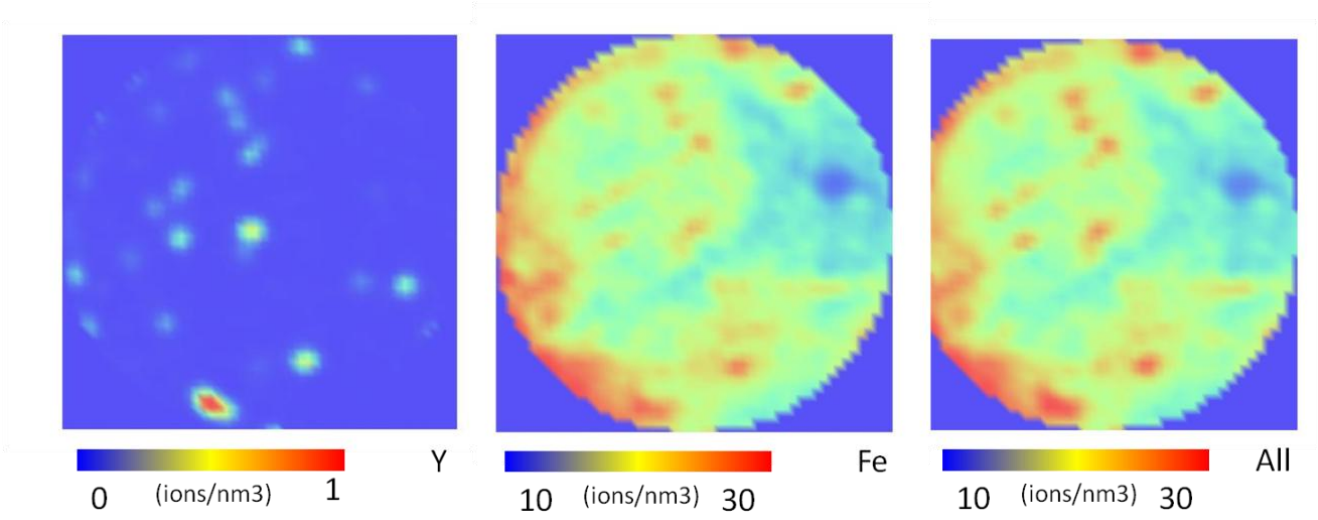


**Figure 4.4 - 2-D atom density map of detector hits for Y, Fe and all ions combined. There are high density regions corresponding to the nanoclusters.**

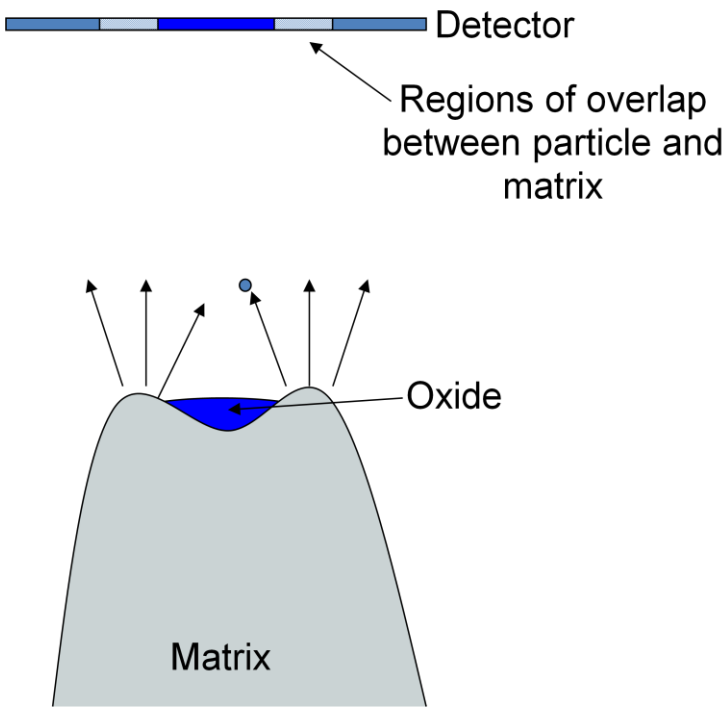


**Figure 4.5 - Schematic illustration of trajectory aberrations caused by the preferential evaporation of an oxide particle**

The contribution of the matrix is assessed by examining the level of Fe in the clusters. The exact quantity of Fe in the clusters is not addressed in this work. Instead, the Fe level in the clusters is artificially set to zero, and the number of Fe atoms is used to estimate the expected quantity of other matrix elements (Cr, W etc.) introduced by trajectory aberrations. This matrix contribution is also removed and the resulting cluster compositions are quoted as 'matrix corrected'.

### 4.5.3 Method of selecting appropriate cluster selection parameters

In the majority of previous studies on clustering that use the maximum separation method to define clusters, values for Dmax, Nmin and L were selected and kept constant although the microstructure under investigation was changing. Examples include different heat treatments in Cu precipitation in steels [169] or Mn-Si precipitation in Al alloys [170]. Stephenson et. al. have proposed a rigorous method for selecting the cluster selection parameters based on nearest neighbour distances of solute atoms [171-172] that could be applied to separate datasets. Due to the mechanical alloying process

in ODS steels the supersaturation of solutes is much higher than in classical systems, particularly in the analysis of the very initial stages of clustering (seen in §7.2.2). There is substantial variation in the nearest neighbour distances of solutes depending on the extent to which the material had been heat treated after ball milling, therefore using the method outlined by Stephenson et. al. and applying the same parameters to all conditions is not appropriate. A consistent method to select the Dmax and Nmin is therefore required so that these parameters can be defined for every individual 3-D reconstruction to ensure that the clusters in each case are accurately defined.

#### *4.5.3.1 Solute selection*

Not only do the values of Dmax Nmin and L directly affect how the clusters are defined, but when there is more than one clustered element, it is important to ensure that as many of these elements are included as solute atoms. In the case of ODS steels there can be up to 8 different clustered ion types. Ideally all clustered ions would be used, but if there is a high proportion of solute in the matrix, there is a higher probability of matrix atoms being included in a cluster. For this reason, the extent of clustering of each ion type was tested.

The analysis volume was divided into blocks containing 1000 ions, and a histogram of the number of blocks containing a given level of solute was produced. The distribution was compared to a series of binomial frequency distributions with the same mean as the individual elements. $\chi^2$ significance testing was then performed, comparing the experimentally determined data with theoretical distributions. By converting the $\chi^2$ values to a Pearson coefficient ($\mu$), the $\chi^2$ values were then normalised to account for the variations in total number of solute atoms in the alloy composition. A $\mu$ value > 0.05 normally indicates that the distribution deviates substantially from a random solid solution.

Table 4.4 gives an example of the differences in the extent of clustering of various solutes for the EPFL-Y2O3 ODS material in the consolidated material, and also in the powder before compaction.

This example highlights how different the clustering can be. The μ- coefficient for all solutes is much higher in the consolidated material, and there are large differences in the clustering of Y in particular. It was found that by only using the 'most clustered' ion types (Ti-O and Cr-O in this particular case) excessive inclusion of matrix atoms was avoided.

| Ion Type | μ (Consolidated Material) | μ (MA Powder) |
|---|---|---|
| **Ti-O** | 0.67 | 0.37 |
| **Cr-O** | 0.59 | 0.31 |
| **Y-O** | 0.50 | 0.08 |
| **Fe-O** | 0.17 | 0.17 |
| **Y** | 0.46 | 0.12 |

**Table 4.4 - Pearson coefficient values for various ion types in EPFL-E-$Y_2O_3$ consolidated material and powder after MA. Larger values indicate 'more clustered'.**

#### *4.5.3.2 Dmax and Nmin selection*

As the composition of the nanoclusters does not change significantly with Dmax or Nmin (provided Dmax>1nm as shown in Figure 4.8b), Dmax and Nmin are chosen based on the measured number of clusters in the analysis volume. Figure 4.6 shows that for the EPFL-PA-$Y_2O_3$ material after consolidation, similar to Figure 4.10, there is a plateau in the number of clusters after Dmax = 1.3nm. In this case, a Dmax value of 1.3 is an appropriate value to choose, as clusters are not artificially split, and any increase in Dmax beyond this will only result in the inclusion of more matrix atoms.

In the powder after MA, there is no clear value of Dmax evident from looking at the number of clusters alone. The initial peak that was observed in the consolidated material is not present, and the most likely reason for this is that the clusters are much smaller, and are therefore much less likely to be split. The level of solutes is also much higher in the matrix, so the detection of random clusters occurs at much smaller values of Dmax and contributes significantly to the number of clusters. It is only as the clusters begin to merge at values of Dmax>1.3 that there is any decline in the number of clusters detected. Clearly in this case, the detection of random clusters needs more careful consideration.

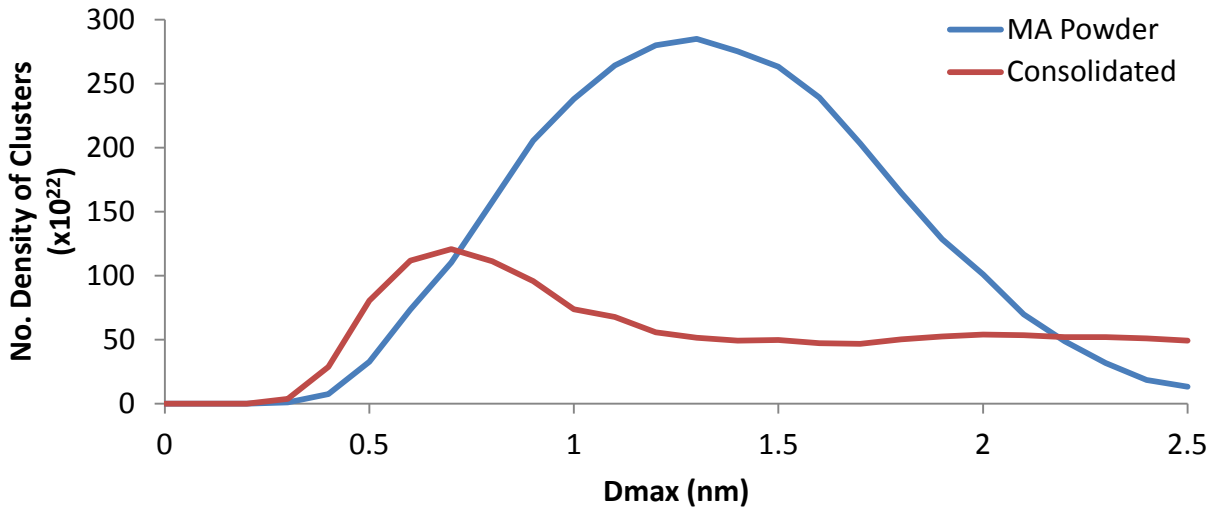


**Figure 4.6 - Variation in number of clusters with increasing Dmax. Consolidated material (red) Mechanically alloyed powder (blue)**

The data was randomised by re-arranging the masses for each of the x-y-z co-ordinates in the data, to give an indication of the number of random clusters likely to be detected for a given set of cluster selection parameters. In Figure 4.7, the number of expected random clusters is removed from the number of clusters detected in the real data, and then normalised by the total number of clusters in the dataset. Where this value is close to 1, random clusters are not considered to influence the number of clusters significantly. A value of Dmax is therefore chosen whereby the number of clusters is maximised within the plateau region of the graph. Figure 4.7 also gives us a criterion by which to select a value of Nmin. The point at which a stable plateau region forms indicates a value of Nmin where the number of random clusters does not contribute significantly to the results. Any value above this risks the unnecessary exclusion of small real clusters. For the example given in Figure 4.7, Nmin=5 is most appropriate. Dmax values range from 0.7-1.3 depending on the individual datasets, but it was found that a stable plateau region was formed with Nmin=5 in all materials and conditions.

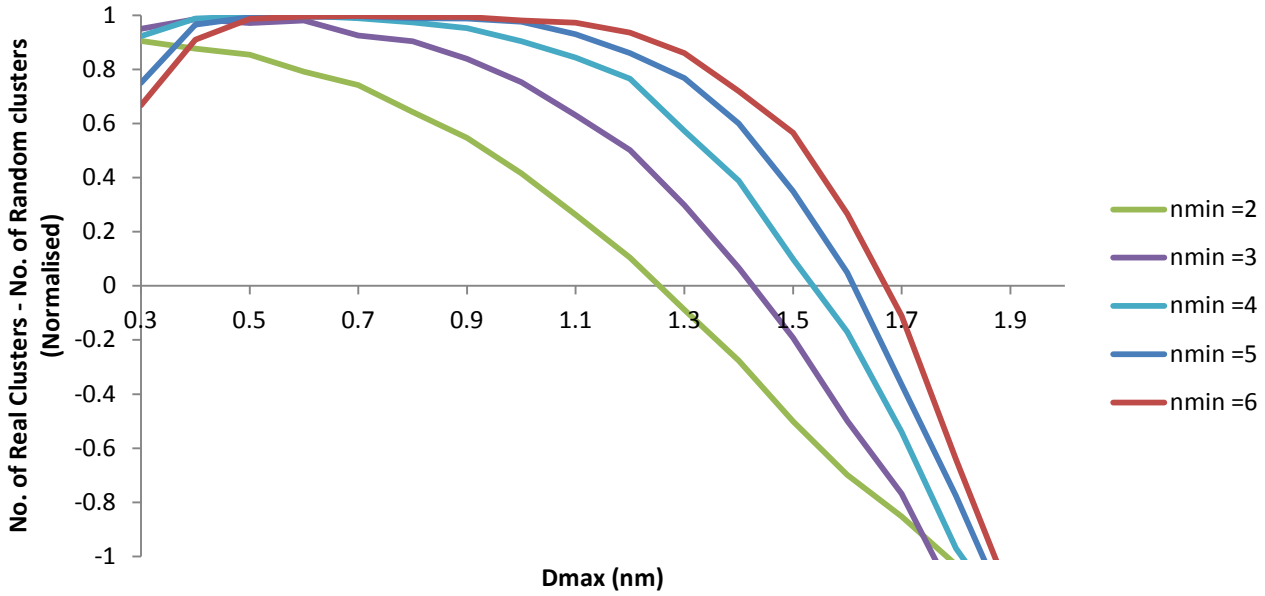


**Figure 4.7 - Variation in the normalised number of clusters when the random clusters are removed, across a range of cluster selection parameters. Plateau region indicates the values of Dmax for which the number of clusters is not affected significantly.**

#### *4.5.3.3 L selection*

As the matrix correction step described below accounts for the inclusion of excess matrix atoms, the surrounds distance L was selected to be as large as possible. If L>Dmax, and two clusters exist very close together, there is the possibility of an atom being counted as part of two clusters simultaneously. To avoid this, L=Dmax was chosen for all clusters.

### 4.5.4 Influence of cluster selection parameters on the characterisation of the clusters

The cluster selection process affects all aspects of the cluster distribution, including the cluster size, number density and composition. A given set of cluster selection parameters may be more appropriate for one aspect than the other.

#### *4.5.4.1 Effect of cluster selection parameters on cluster composition*

The Dmax parameter has the greatest influence on the cluster selection, as this controls how many solute atoms are part of the cluster. The influence of changing Dmax on both the raw and corrected cluster compositions is shown below (L=Dmax). The compositions are the average compositions of

all clusters in a particular specimen of EPFL-PA-$Y_2O_3$ containing approximately 800 clusters. Figure 4.8 shows that once the matrix correction is applied, provided that Dmax is large enough to include all the solute atoms associated with each cluster within the clusters, the measured composition of the clusters is the same across a relatively wide range of parameters. The method of matrix correction not only accounts for the effect of trajectory aberrations, but also reduces the error associated with the measured composition of the clusters due to the cluster selection technique.

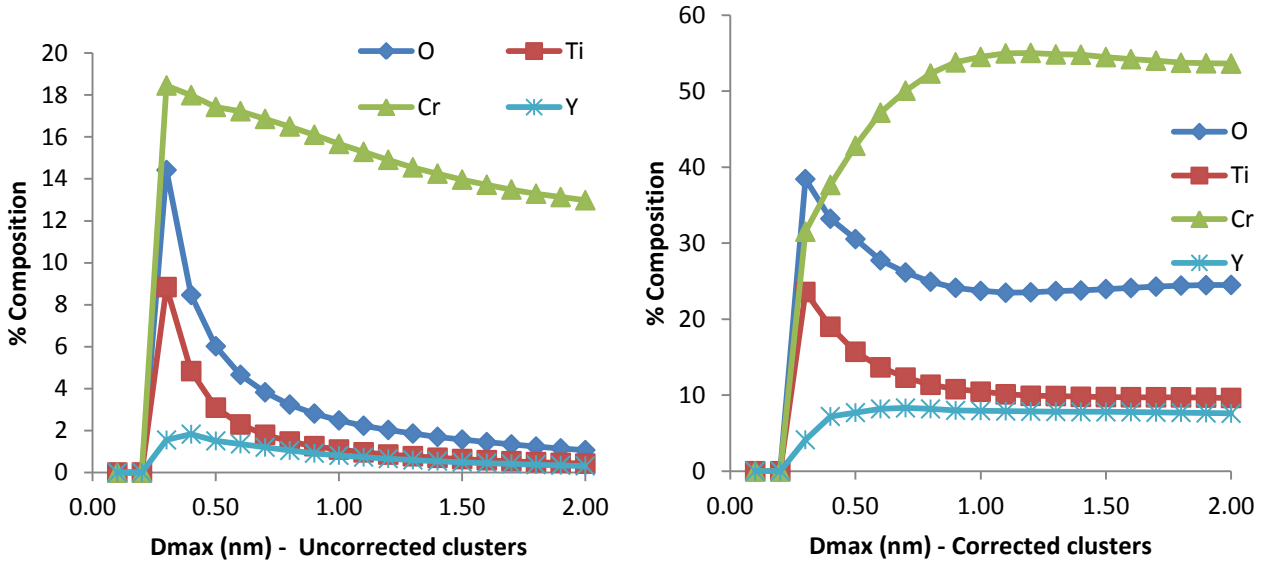


**Figure 4.8 - Change in measured average composition of clusters with increasing Dmax for EPFL-PA-$Y_2O_3$ alloy (i) uncorrected cluster compositions (ii) matrix corrected cluster compositions. The error in these measurements is hidden by the data points.**

The surrounds distance L affects the proportion of 'non-core solute atoms'. The variation in the uncorrected composition of the clusters with increasing surrounds distance is shown Figure 4.9 (generated using code found in Appendix B.2). Above 0.6nm there is no significant change in the

composition of clustered elements.

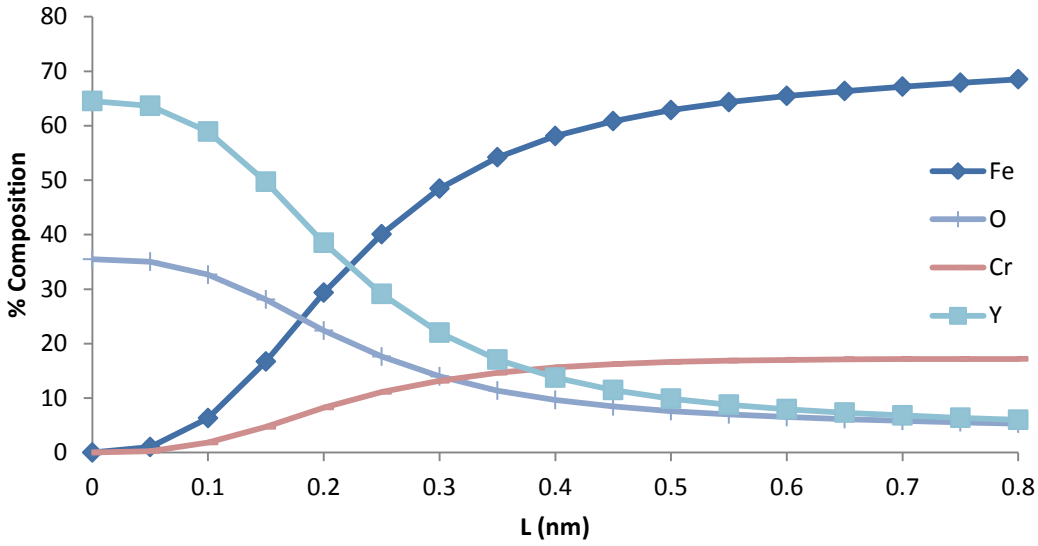


**Figure 4.9 - Variation in surrounds distance (L) when Dmax=0.8 nm**

It was found that if Nmin was varied, there was no significant change in the average corrected composition of the clusters. This is another benefit of the matrix correction step. If random clusters are inadvertently included by selecting a value of Nmin that is too small, the composition of these clusters will be very close to the matrix composition. Once the proportion of matrix is removed, their contribution to the average composition is also removed.

### *4.5.4.2 Effect on number density of clusters and the cluster size distribution*

The number density of clusters is affected by both Dmax and Nmin. Figure 4.10 shows that number of clusters detected varies dramatically depending on the value of Dmax and Nmin chosen. The code written to generate this data is found in Appendix B.1. There is a peak in the number of clusters initially, which indicates that when the Dmax value is not large enough, clusters are artificially split. A plateau region forms after Dmax = 1, when the number of clusters is well defined. At very large Dmax (>3.5), the number of clusters increases again, as random clusters in the matrix are added. Above Nmin=5, the effect on the overall number density is negligible in the plateau region. The Nmin parameter is included in the cluster selection process in order to avoid

the inclusion of random matrix fluctuations, but Figure 4.11 indicates that some random clusters are still present in the data.

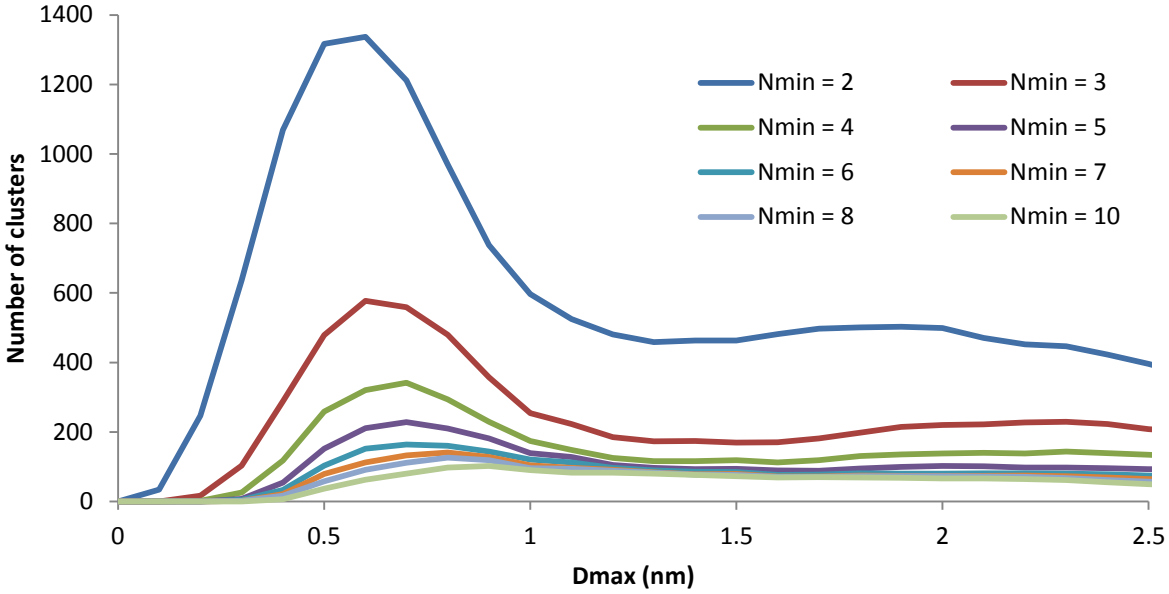


**Figure 4.10 - Variation in number of clusters with increasing Dmax for different values of Nmin in EPFL-PA-$Y_2O_3$**

The most accurate estimate of the number density and cluster size distribution is obtained by removing the proportion of random clusters. The proportion of random clusters is estimated by randomising the mass to charge state ratios of the data, and then running the cluster selection algorithm. By removing this number of random clusters, we gain a clearer understanding of the number of small clusters that would be otherwise discounted by using a larger value of Nmin.

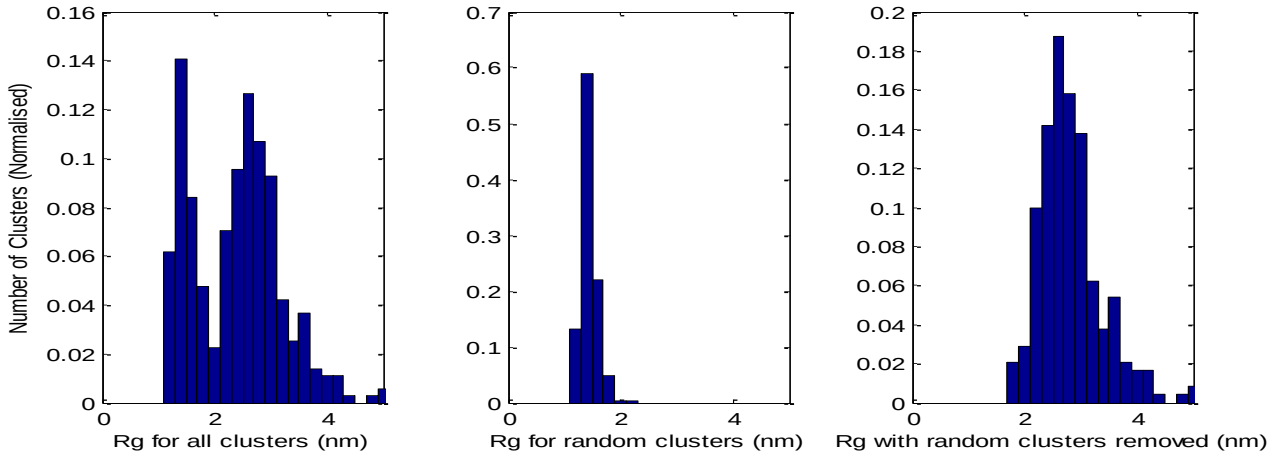

Figure 4.11 – Particle size distribution of clusters in EPFL-PA-$Y_2O_3$ material, together with the size distribution of clusters found in the randomised dataset. In this example Dmax is chosen to be less than the optimal value (Dmax=1nm), to amplify the contribution of the random clusters to the particle size distribution.

### *4.5.4.3 Effect on nanocluster size and volume fraction*

The value of Dmax affects the cluster $R_g$ quite significantly as shown in Figure 4.12. This effect can be minimised if the Rg is calculated for the core solute atoms only, rather than including all ranged atoms, as fewer matrix atoms are taken into account. The average $R_g$ of the clusters in this instance is seen to plateau around 1.5nm for the appropriate range of Dmax.

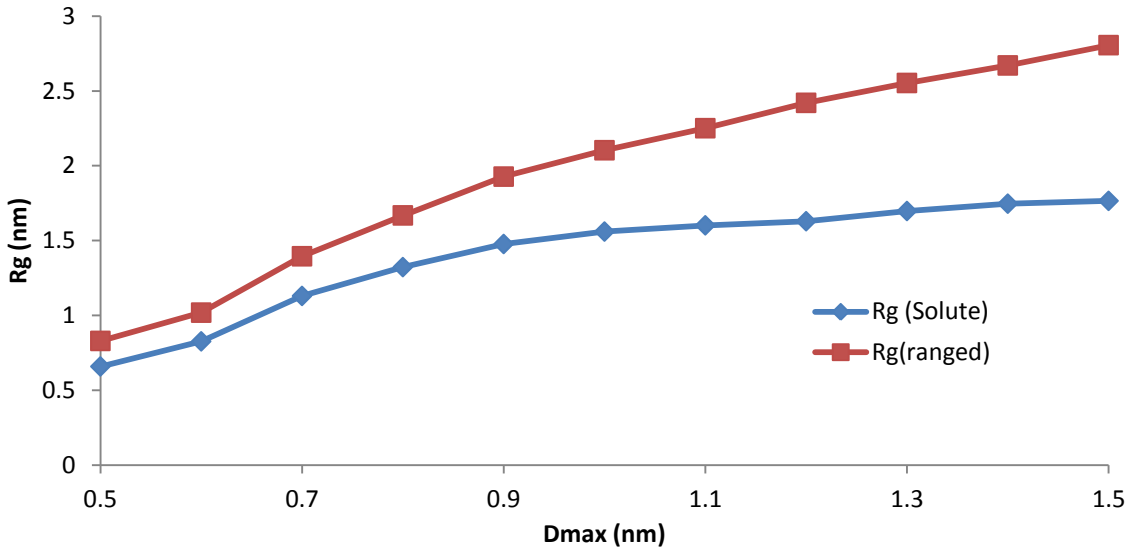


**Figure 4.12 - Variation in median Rg with Dmax, for core solute atoms only, and for all ranged atoms in the cluster. Rg plateaus when only solute atoms are used.**

Figure 4.13 shows clusters isolated using the maximum separation method alongside clusters imaged in the TEM. By eye, the sizes of the clusters compare favourably. The average particle size was calculated from this TEM image using the particle size analyzer macro for the open source ImageJ software. The average cluster diameter from the TEM is 3.3±0.5nm, which is within error of the APT measurement of 3.9±0.1nm. The slight discrepancy may be due to the influence of the focus conditions on the apparent diameter of the clusters in the TEM.

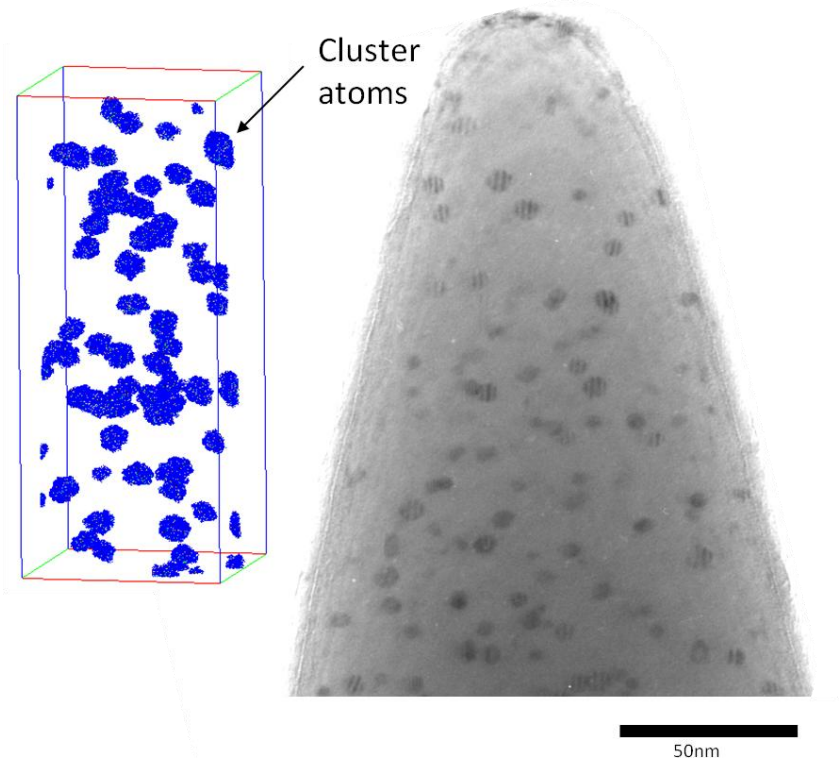


**Figure 4.13 – Comparison of clusters isolated using the maximum separation algorithm, and those observed by TEM.**

### 4.5.5 Statistics of the nanocluster distribution

#### *4.5.5.1 Number density*

Once the nanoclusters have been identified, it is useful to be able to describe the nanocluster population. The number density of nanoclusters is calculated as:

$$\textbf{No. Density} = \frac{N_{NC}\xi}{N_{tot}\Omega} \qquad \textbf{Equation 8}$$

Where $N_{NC}$ is the number of nanoclusters, $\xi$ is the detection efficiency, $N_{tot}$ is the total number of atoms and $\Omega$ is the atomic volume. The confidence of these results is taken as the standard error of the mean established from multiple analyses of the same condition.

In cases where the number density varies substantially with cluster selection parameters, the number density is defined as the number density of the real data with the number of expected random clusters (estimated from the same data with the position coordinates randomised) removed.

### *4.5.5.2 Nanocluster size*

There are many ways by which to define the size of a nanocluster, and both the mean cluster size and size distribution are often of interest. For spherical features, a common measurement of size is the radius of gyration ($R_g$).

Miller defines $R_g$ as "the radius of a hypothetical body having all its mass concentrated at a single distance from its centre of mass ( $\bar{x}$ , $\bar{y}$ , $\bar{z}$ ) whilst having the same mass $m_0$ and moment of inertia $I_0$ of the object" [152]. In 3-D this is given by

$$l_g = \sqrt{\frac{\sum_{i=1}^{n} (x_i - \bar{x})^2 + (y_i - \bar{y})^2 + (z_i - \bar{z})^2}{n}} \qquad \textbf{Equation 9}$$

where $x_i$, $y_i$, $z_i$ are the known atom positions within a given cluster containing $n$ atoms and the co-ordinates of the centre of mass are determined by

$$\bar{x} = \frac{\sum_{i=1}^{n} x_i m_i}{\sum_{i=1}^{n} m_i} \quad ; \quad \bar{y} = \frac{\sum_{i=1}^{n} y_i m_i}{\sum_{i=1}^{n} m_i} \quad ; \quad \bar{z} = \frac{\sum_{i=1}^{n} z_i m_i}{\sum_{i=1}^{n} m_i} \qquad \textbf{Equation 10, 11 \&12}$$

Due to trajectory aberrations, the number of ions identified as part of a cluster is much higher than is actually the case, therefore the $R_g$ value can be artificially inflated. This is offset by the fact that the radius of gyration always underestimates the size of the feature [152]. As a measure to compare cluster sizes within APT data $R_g$ is very useful, but is not necessarily appropriate to compare with other methods of size measurement. A conversion from $R_g$ to the 'Guinier radius' is often used, as the Guinier radius is believed to accurately represent the size of the feature [152]. No concrete description of the Guinier radius could be found in relation to APT data in the available literature. Kolli et. al. argue that the conversion factor of $\sqrt{5}/3$ suggested by Miller [152] has no physical basis in APT data and should not be used [173]. This combined with the added complications of the trajectory aberrations means that the Guinier radius is not used in this study.

#### *4.5.5.3 Nanocluster volume fraction*

The volume fraction of precipitates can influence the hardness of the material, and is therefore an important consideration. The discrepancy between the $R_g$ measurements and TEM analysis shown above means that using $R_g$ as a means to calculate volume fraction will underestimate the cluster volume fraction. Furthermore, the total number of atoms defined as a cluster will grossly overestimate the volume fraction due to the trajectory aberrations. In this study therefore the volume represented by a particular cluster is defined as the volume occupied by the number of cluster atoms once the matrix correction is applied.

## 4.6 1-D composition profile for the analysis of grain boundaries

Composition profiles are used to examine the variation in composition across an interface, or planar feature. A cylindrical volume is defined within the 3-D reconstruction perpendicular to the feature of interest, and the composition is measured at 1nm slices along the long axis of the cylinder.

## 4.7 Cylindrical radial composition profile for the analysis of dislocations

In APT data, dislocations are not usually visible unless they exhibit solute segregation, in which case they are indirectly imaged through enhanced solute concentrations along linear features [79]. In this work, the maximum separation method [174] was used to identify small regions enriched in solute atoms. As will be shown in more detail in §9.2.2, many of these regions are closely separated and observed to line up with each other, indicating the presence of dislocation lines. The crystallographic core of the dislocations cannot be observed in the APT data. The core of each dislocation was therefore defined as the region exhibiting the highest levels of solute segregation. Using the PosAT software written by Dr. Jon Hyde, the dislocation was represented by an interpolated smooth line joining the centres of mass of approximately aligned, and adjacent, solute-enriched regions. This line was used as the core of a cylinder, and the composition was calculated at 1nm intervals radially from the core to give an indication of the changing solute concentration.

# 5 APT analysis of oxide composition

This chapter assesses the suitability of APT as a characterisation technique for the oxide nanoclusters in ODS steels. It includes

A reference study on the evaporation behaviour of bulk oxides $Y_2O_3$, $Y_2TiO_5$ and $Y_2Ti_2O_7$.

A comparison of the evaporation behaviour of Y-O nanoclusters and Y-Ti-O nanoclusters

Discussion of possible causes of compositional inaccuracies in the composition measurements of bulk oxides

Discussion of possible compositions of the oxide nanoclusters in ODS steels

## 5.1 Introduction

As outlined in the literature survey in Chapter 2.3.3.2, there is considerable ambiguity over the exact composition of the oxide particles. The interpretation of APT data has been addressed in the previous chapter, but the accuracy of the raw data has not yet been considered. The application of APT to bulk oxides is relatively new, and is only usually possible with laser pulsing due to poor electrical and thermal conductivity of the specimens. Despite major advances in the field of pulsed-laser atom probe tomography (PLAPT), there have been very few studies published on bulk insulating ceramics. It is necessary first to assess the possible limitations of the technique in the measurement of oxide composition. The application to oxide particles embedded in a metal matrix (as is the case in ODS steels) will then be discussed.

The simplest case of a Y-based oxide will be considered in detail, before investigating the more complex Y-Ti containing oxides.

### 5.1.1 Background to the analysis of oxides using APT

The PLAPT technique is proven to work for bulk alumina samples [175], and has also been applied to a zirconia spinel [176], MgO [177] $CeO_2$ [178] and Fe-O based wustite [179]. The oxide compositions reported are within 5% of the expected stoichiometry in all cases. In the case of alumina, the measured composition was reported to be deficient in oxygen [175] whereas a slight surplus of oxygen was reported in the $CeO_2$ when a high laser energy was used [178]. As with the APT analysis of any material, the choice of analysis parameters is very important, however the optimum parameters are likely to be different to those often used for conducting specimens, as discussed below.

It is widely accepted that for conducting specimens both decreasing the specimen base temperature, and increasing the applied field at the apex of the specimen (by lowering laser energy) improves both the mass resolution and signal-to-noise ratio of the APT analysis (as discussed in §4.4). Decreasing the wavelength also improves both these characteristics [180]. However, the relationship between attaining 'good' APT data and laser wavelength may not be as straight forward for all materials. It was found that the mass resolution in the Fe-based oxide wurstite was improved significantly when using infra-red wavelengths rather than either visible or ultra-violet. The measured oxygen concentration was also seen to depend on the laser energy used, and the oxygen detected increased with increasing laser energy up to a point, before decreasing again [179].

The mechanisms of field evaporation in oxides (and other semi-insulating materials) are somewhat different from conductors. Tsong proposed that atoms could be ionised by the absorption of photons by surface electrons [181], and first-principles calculations suggest that direct electron excitation as a method to promote field evaporation is possible [177]. As the specimen tip temperature is raised, the evaporation of ions can also be thermally activated [182], and Vella et. al. note that if the photon energy is larger than the band-gap of the material, the penetration depth of the laser energy can be

less than 1μm which can lead to an isotropic thermal evaporation of surface atoms [183]. In-depth investigations into the mechanisms of field evaporation are beyond the scope of this thesis, but some aspects relating to the quantification of the oxides studied in this chapter will be discussed.

The high instances of multiple-ion evaporation events are highlighted as a possible reason for the measured composition in alumina being non-stoichiometric [175], the reason being that by biasing the evaporation towards multiple events, the probability of detector saturation is more likely [184]. In an Fe-Cr based oxide, multiple events containing Fe ions also involve oxygen ions more often than is statistically probable [185], therefore the possibility of detector saturation during the analysis of oxides requires further investigation.

## 5.2 Reference study on bulk $Y_2O_3$

### 5.2.1 Experimental conditions

The oxides were only analysed in laser pulsing mode, using the same analysis condition as for the ODS steels (30K base temperature ~0.3nJ laser power). No atomic planes were visible in order to scale the reconstruction; therefore the evaporation field of Y (23.5V/nm) was used as the basis for the reconstruction algorithm. This is likely to be an overestimate of the true evaporation field, as field evaporation of oxygen atoms typically occurs at much lower fields (1V/nm is required to remove oxygen from NiO films for example [186]). This means that the atom positions in the reconstruction are likely to be systematically incorrect and therefore no information can be extracted about the oxide crystallography.

### 5.2.2 Mass spectrum analysis

The mass spectrum is displayed in Figure 5.1. Compared with the mass spectrum taken from the ODS steel shown in §3.3.4 the peak tails are much wider. This is consistent with the poor thermal conductivity of the oxide compared to a metallic specimen. The composition of the material

calculated by counting all ions within 9/10$^{th}$ of the maximum width of the peak gives 36.7±0.8 at.% Y and 63.3±1.0at.% compared with the expected values of 40%Y and 60%O. The error limits on this measurement corresponds to the range of compositions attainable when varying the mass ranges (discussed in §3.3.4.1).These values are close to the expected composition values, but with a slight Y deficit. Reasons for this deficit will now be explored.

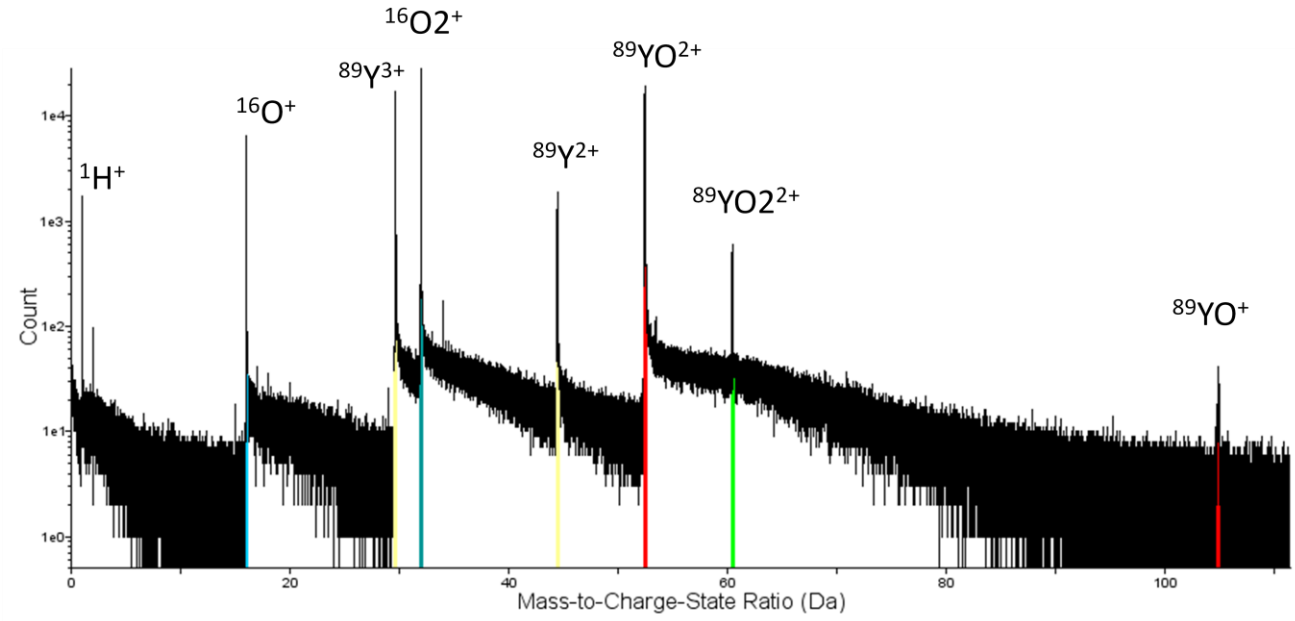


**Figure 5.1 - Mass spectrum for $Y_2O_3$ bulk oxide**

### 5.2.3 Possible causes of compositional inaccuracy

In APT all elements should be detected with equal probability. When investigating compositional accuracy across a homogenous material, the main causes of compositional inaccuracy stem from the possibility that some ions may evaporate from the surface of the specimen between pulses or that some ions are not detected due to detector saturation in a multi-hit (as explained in § 3.3.1).

#### *5.2.3.1 Evaporation between pulses*

When an ion field-evaporates at some time between the laser pulses, its time of departure is unknown, and the detector hit cannot be correlated with the time of flight. This results in a high noise floor in the mass spectrum. Figure 5.1 shows that the background counts between peak tails

are negligible. For a typical 'good quality' analysis of an ODS steel the average noise count is ~600 counts per amu for 5M ions. In this example the average noise count is ~400 counts/amu for 5M ions. This indicates that there is no significant increase in evaporation between pulses between the $Y_2O_3$ and a conducting specimen.

Aside from the noise floor, there is no other measure of this effect; therefore it will not be investigated further. However, when considering the evaporation behaviour of the material, it must always be considered as a possible source of error.

#### *5.2.3.2 Loss of ions during multiple ion evaporation events*

As stated in §4.2, information about the ion hit sequence can be obtained from the .epos file. In metallic specimens the proportion of multi-hits is typically less than 5%. For the bulk $Y_2O_3$ however, that proportion was much higher at ~30%. As explained in § 3.3.1 this may contribute to the loss of one element over another. Detailed analysis of hit behaviour will now be discussed.

Correlated evaporation of individual ion types

Saxey has shown that during the APT analysis of pure Al, there is significant correlation of specific ion types such as (AlH+ with H+) [185]. This could be due to either correlated ion evaporation, or ion dissociation during flight. Clearly, if correlations exist between some ion types more than others, this could have implications for the measured composition. Part of the script found in Appendix B.4 was used to generate Figure 5.2. It shows that within multi-hit pairs in the bulk $Y_2O_3$, the instances of pairs containing Y and YO ion-types occur much more frequently than all other combinations.

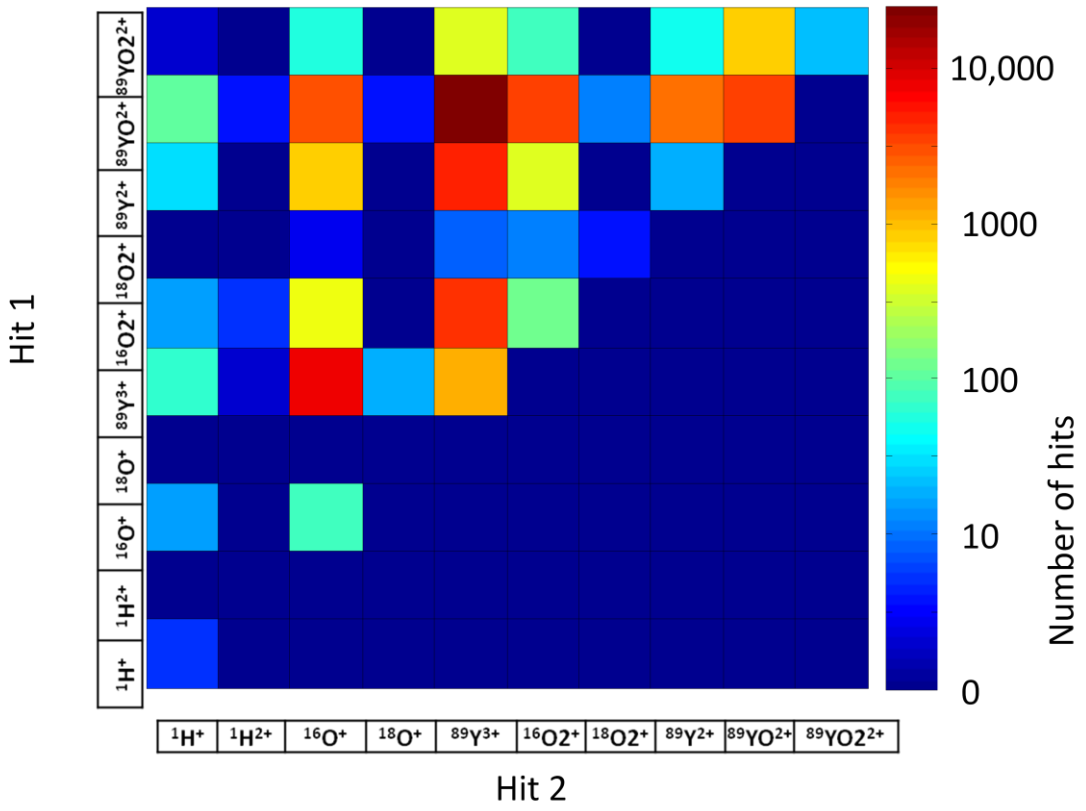


**Figure 5.2 - Number of instances of getting a specific ion pair combination in bulk $Y_2O_3$ (note the logarithmic colour-scale).**

Saxey suggested that by constructing a 'correlation table', the instances of specific ion pair combinations can be compared with the expected distribution of ion pair combinations based on the hypothesis of independent evaporation [185]. This method used a contingency table approach to create a matrix of expectation values, by using the row and column totals to calculate the probability of each specific pair combination. When this method was applied to the bulk oxides in this study, only one side of the correlation table was used as the mass to charge state ratio of the first hit is always greater than that of the second hit. When the expectation values are generated, the ion order cannot be taken into account, therefore the evaporation events (for example AB and BA) are combined because they give rise to a single observation. The expectation values are therefore also forced to be one sided by removing all $e_{ji}$ values and setting $e_{ij}=e_{ij} + e_{ji}$. It is important to note that when using Saxey's method, the self ion pairs are discounted by replacing the observed values with

the expected values (as the detector dead-time effects discussed in § 3.3.1 mean that the observed numbers of pairs are under-represented). Saxey states therefore that these correlation tables should be interpreted as the relative amount of correlation between ion-type *i* and every other ion-type except *i* itself. Figure 5.3 shows the relative correlations for the main ion types in bulk $Y_2O_3$.

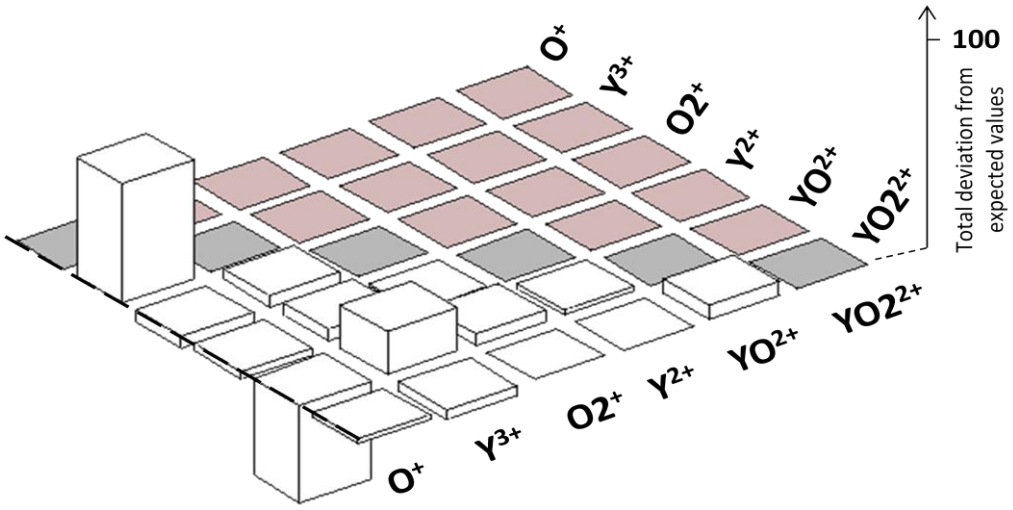


**Figure 5.3 - Total deviation of observed ion pair combinations from the expected values calculated based on the hypothesis of independent evaporation (self ion pairs discounted).**

There is a particularly strong correlation between $Y^{3+}$ and $O^{+}$ ion types. There is also a strong positive correlation between $Y^{3+}$ and $YO^{2+}$. The correlation of $Y^{3+}$ and O+ ion types could be interpreted as either as co-evaporation of each ion, or as dissociation of a combined ion 'in-flight'. Ion dissociation seems unlikely, as there is no peak corresponding to $Y_2O$ present on the mass spectrum, and in order to maintain a charge balance, a 4+ charged ion would be required. It can be concluded then that a mechanism by which the evaporation of one ion promotes the evaporation of another nearby is most plausible.

The correlation table analysis does not allow for the investigation of self-ion pairs. While it is interesting to note that some co-evaporation of certain ion types occurs, it is the correlation of self-ion pairs that are likely to have the most impact on the overall composition. The central diagonal of

Figure 5.2 shows the abundances of self-ion pairs detected. These are of particular interest, as §3.3.1 explains that detector dead-time effects mean that self-ion pairs that occur very close to each other in both space and time may not be counted. Again, there is a higher instance of Y-containing self-ion multi-hit pairs, than any other ion type. Table 5.1 shows that in fact, when the number of self-ion pairs is compared to the total number of ions detected, the number of $O_2^+$ ions detected is much lower than for any other ion type. The spatial location of these hits will now be investigated.

| $Y^{3+}$ | $O^+$ | $O_2^+$ | $YO^{2+}$ | $YO_2^{2+}$ |
|---|---|---|---|---|
| **0.3%** | 0.3% | **0.02%** | 0.3% | 0.1% |

**Table 5.1 - Percentage of self ion pairs as a proportion of the total number of detected ions. The proportion of $O_2^+$ ions is much lower than all other ion types.**

Spatial location of hits on the detector

Figure 5.4 gives an indication on the average distance between each ion in a multi-hit in two dimensions for the $Y_2O_3$ oxide. This 2-D histogram shows that there is the highest density of hits approximately 1mm from the first hit on the detector. In this instance, this equates to ~3nm on the surface of the specimen. The density of second hits is very low at (0,0). This may be partly caused by the ~3ns 'detector dead-time', but it is also related to the fact that there are fewer atoms available for field evaporation at these distances.

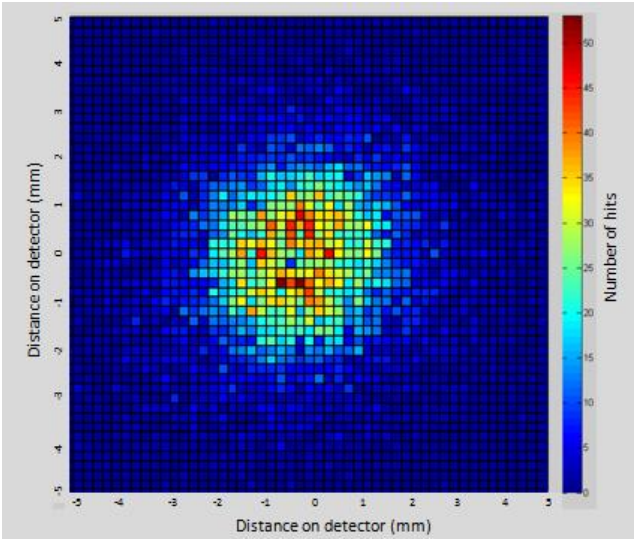


**Figure 5.4 - 2-D histogram of the distance (in mm on the detector) of the subsequent hits from the first hit for multiple ion evaporation events. All ion types are included in this plot.**

Spatially correlated ion evaporation

De Geuser et. al. report that the field evaporation of ions in atom probe tomography is highly correlated in both space and time [187]. The authors relate this to variations in the distribution of the electric field at different points on the surface. For example, there are local increases in field at particularly curved regions of the specimen, such as the edges of atomic terraces. Field ion microscopy experiments show similar results [188]. Figure 5.5(a) compares the distance between multi-hit ion pairs and ion pairs that are separated by a very short time period (within 3 picosecond laser pulses) as measured on the detector. The frequency is normalised by the square of the distance between the hits in order to account for the increased number of atoms at larger distances. When the distance between hits is less than 1mm, there is a reduction in the number of hits detected when compared to hits that occur on consecutive pulses.

Figure 5.5 shows that when ion pairs have the same mass to charge state ratio, there are very few hits within 1mm of each other on the detector, when according to Figure 5.5(a), due to the spatial correlation of evaporation, the number of hits should be highest in this region. It is believed that the hits in this region are 'lost' due to the detector saturation effect. All the $Y^{3+}$ ion pairs and $O_2^+$ ion pairs in a 5M ion 3-D reconstruction are shown, and as outlined in Table 5.1 it is clear that there are far fewer instances of $O_2^+$ ion pairs than of $Y^{3+}$ ion pairs. Again, in Figure 5.5 the frequency is normalised by $r^2$ to account for the increased number of atoms available for evaporation as the distance between the hits is increased.

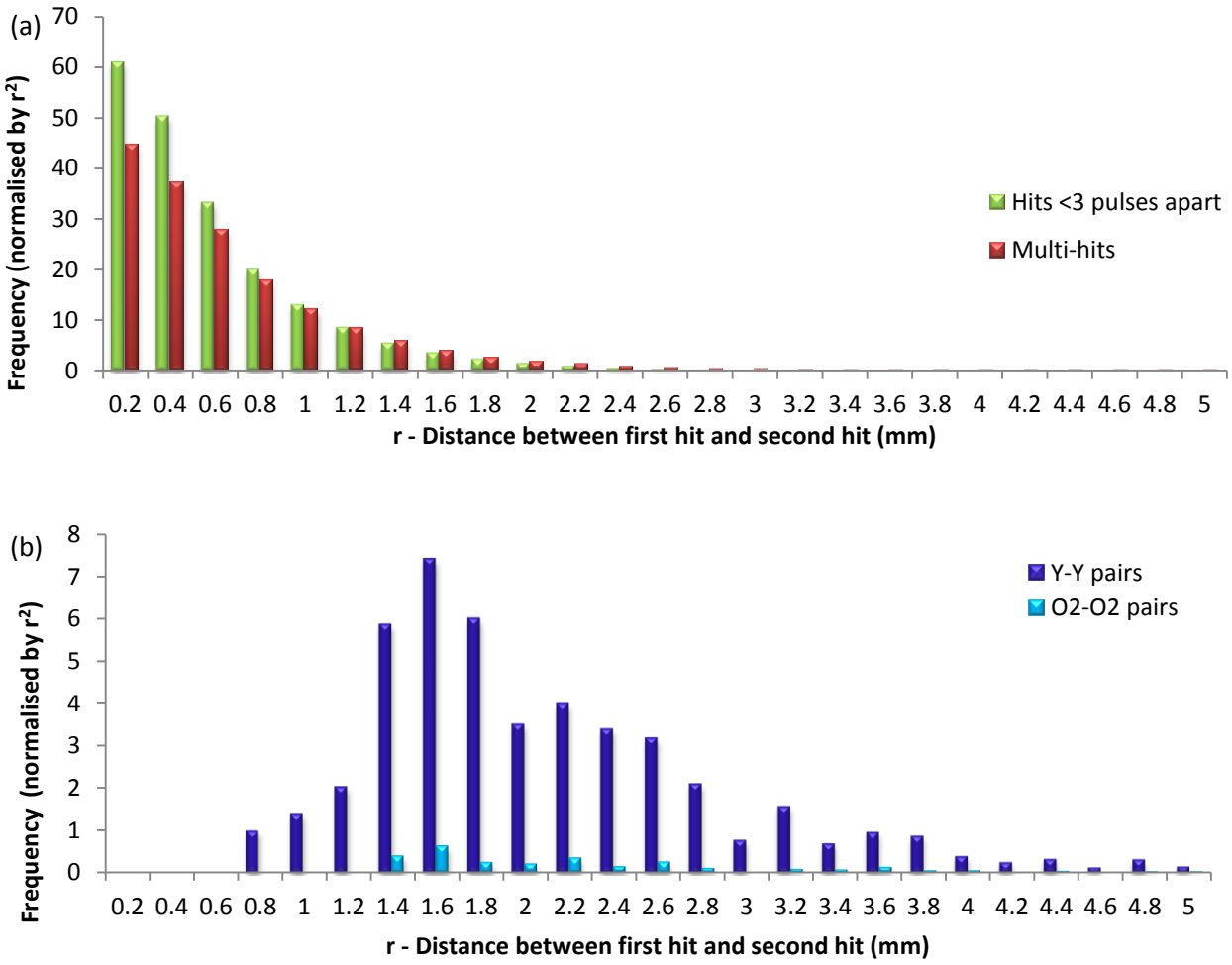


**Figure 5.5 – (a) Normalised histogram displaying the distribution of distances between one hit and the next in multi-hit ion pairs (red) and ion pairs separated by <3 pulses (green) for all ion pairs in bulk $Y_2O_3$. (b) Distance between first hit of a multi-hit pair and the second hit, measured in mm on the detector. Very few $O_2^+$ pairs are observed, and there are no multi-hit pairs recorded if the distance between hits is <0.6mm.**

### *Estimation of the number of 'lost' ions as a result of multi-hits*

In order to estimate what proportion of all ions are lost due to the detector saturation effect, it was assumed that the expected number of $Y^{3+}$-$Y^{3+}$ pairs would follow a similar distribution to the distribution of hits shown in Figure 5.5(a) for the hits separated by <3 laser pulses. The gradient of the curve of $Y^{3+}$-$Y^{3+}$ pairs when the distance between hits is >2mm was used to estimate how many hits were lost due to the detector dead-time effect.

By assuming a Gaussian distribution for the distribution of hits separated by <3 laser pulses (observed when plotted without the $r^2$ normalisation), the MATLAB curve-fitting toolbox was used to fit the data to a distribution of the form f(x) = a1*exp(-((x-b1)/c1)^2 (where a1, b1 and c1 are

numerical coefficients). A moving average for the number of Y-Y pairs was calculated at 2.3, 2.6 and 2.9 mm distance, and these values were used to generate the estimated distribution shown in Figure 5.6. From the area under this curve, it was estimated that approximately 55% of all Y-Y pairs are lost due to the effect of detector saturation. Because the number of $O_2^+$ pairs observed was so low, it was assumed that there was no significant loss of $O_2^+$ ions via this mechanism.

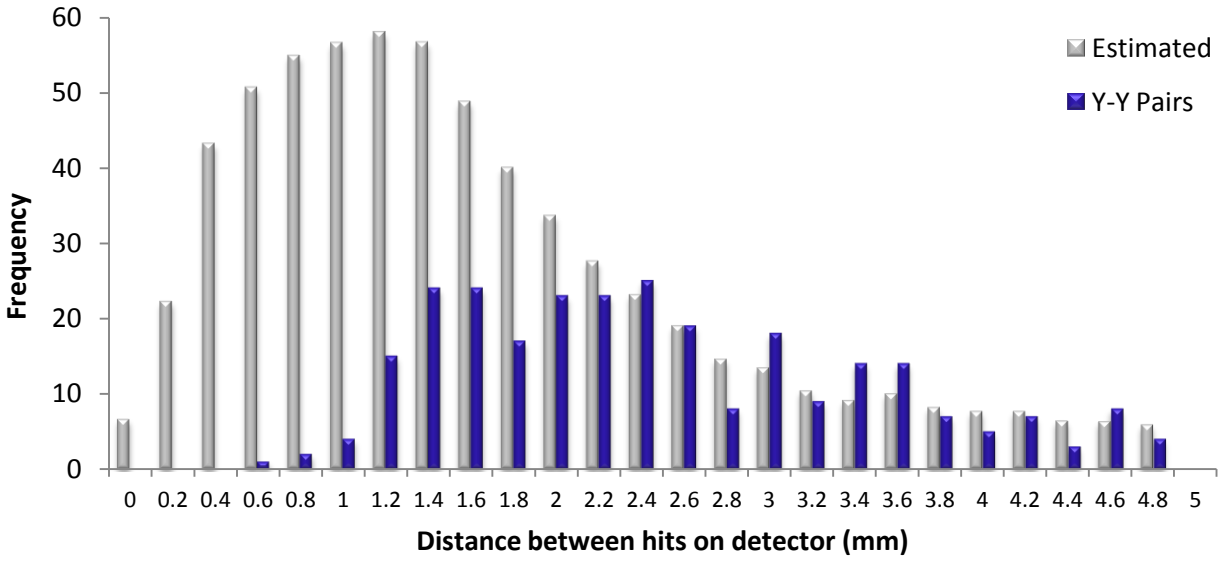


**Figure 5.6 - Histogram of the distances between Y-Y ion pairs (in the mass to charge state ratio of 29.64-29.68 only) in bulk $Y_2O_3$. The estimated number of 'lost' hits is also shown.**

This mechanism of ion loss does not necessarily have an effect on the global composition measured from the APT data, as it affects all self-ion pairs. If the proportion of self-ion pairs is equal across all self-ion pairs there will be no net change in overall composition. In this material, 37% of all detected Y containing ions were detected as part of a multi-hit, whereas that figure is much lower for O (~18%). When all permutations of Y-Y pairs are taken into account, the total loss of Y via this mechanism is estimated to be 0.5±0.1%.

By investigating possible spatial correlations that exist between ions that evaporate very close to each other in time (i.e. on the very next pulse) it is possible to gain some insight into the likely behaviour of self-ion pairs in a multi-hit. As previously discussed, De Geuser et. al. have shown that spatial correlation relates directly to the mean size of the high field regions on the surface of the

specimen [187]. Figure 5.7(a) shows the distribution distances between one $Y^{3+}$ hit and the subsequent $Y^{3+}$ hit in $Y_2O_3$ (single hits only). There is an initial peak which corresponds to the correlated evaporation in high field regions. There is also an underlying linear distribution – this case, data was not normalised by $r^2$ for clarity. This linear relationship is expected if the process of field evaporation is purely a thermally activated process; the number of hits is increased as the distance between the hits is increased because the area (and hence the number of atoms available for evaporation) is greater. A similar plot for $O_2^+$ pairs is shown in Figure 5.7(b). In this case, there is no initial peak corresponding to the correlated field evaporation. This is consistent with what would be expected if all ions at any location on the specimen surface are subjected to a field higher than is required for field evaporation.

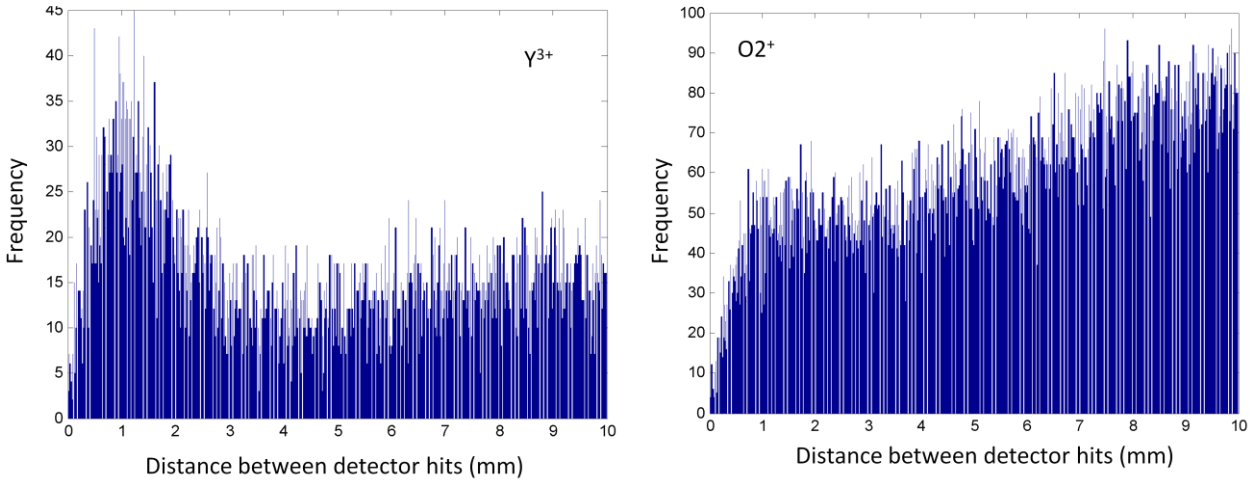


**Figure 5.7 - Distribution of the distances between (a) one $Y^{3+}$ hit and the next and (b) one $O2^+$ hit and the next. The initial peak is an indication of spatially correlated evaporation on $Y^{3+}$.**

The majority of ion pair combinations show a distribution of distances between hits on the detector similar to Figure 5.7(a). It is only the $O_2^+$ ions that show very little (or no) spatial correlation. One explanation for this could be that the evaporation field required for $O_2^+$ (once the molecule has formed on the surface) is less than for $O^+$ for example. Therefore as soon as the molecule is formed, it is likely to field evaporate regardless of whether it is in a 'high-field' region of the surface or not.

This is consistent with theoretical work that suggests that O ad-atoms on a metal surface can have strong lateral interactions that cause the formation of $O_2$ molecules [189].

This implies that the probability of $O_2^+$ ions not being detected due to detector saturation during a multi-hit is reduced because they are less likely to evaporate close together. If this theory is true, then it also explains why the proportion of Y detected as multi-hits is greater than O.

#### *5.2.3.3 Summary*

For the particular analysis conditions chosen in this study (30K base temperature and 0.3nJ laser energy) the compositional analysis of $Y_2O_3$ was found to be slightly deficient in Y. The possible causes for compositional inaccuracy were reviewed, and spatially correlated ion evaporation together with detector saturation effects was identified as one source of error. Differences in the evaporation behaviour of Y and O ions may also apply to the evaporation of oxide nanoclusters in ODS steels.

## 5.3 Y-O nanoclusters in the EPFL-PA-$Fe_2Y$ alloy

The accuracy of the measured composition of the nanoclusters is one of the fundamental questions of this chapter. The extent to which spatially correlated ion evaporation (which affects the composition of the bulk oxide) will affect the measured composition of the nanoclusters should be considered. Additionally, the difference in the field required for ion evaporation between the matrix and the bulk is another major concern. As a higher field is required to evaporate atoms from the matrix than from the oxide, this results in the oxide experiencing a field greater than is required to induce field evaporation in the bulk $Y_2O_3$ investigated above. This may change the evaporation behaviour of the cluster and/or matrix ions.

The difference in the field required to evaporate atoms from the matrix compared to atoms from the oxide also leads to the trajectory aberrations described in §3.3.7. The influence of the matrix inclusion must be investigated to see what influence this has on the measured composition.

### 5.3.1 Influence of laser power on the characterisation of the clusters

By investigating the composition of the particles under different evaporation conditions, both the influence of the applied field, and the trajectory aberrations can be examined. Proxigram analyses of the clusters under different conditions also give us some indication of the interface chemistry and possible evaporation artefacts that arise due to the interface. A systematic study on the evaporation behaviour of the Y-O containing particles was carried out by increasing the laser power after the evaporation of ~10million ions. This limits the error due to variation from specimen to specimen as much as possible. The voltage history of the experiment is given shown in Figure 5.8. There was very little change in specimen tip radius as the data was collected. A specimen with similar end radius and shank angle was also analysed in voltage pulsing mode.

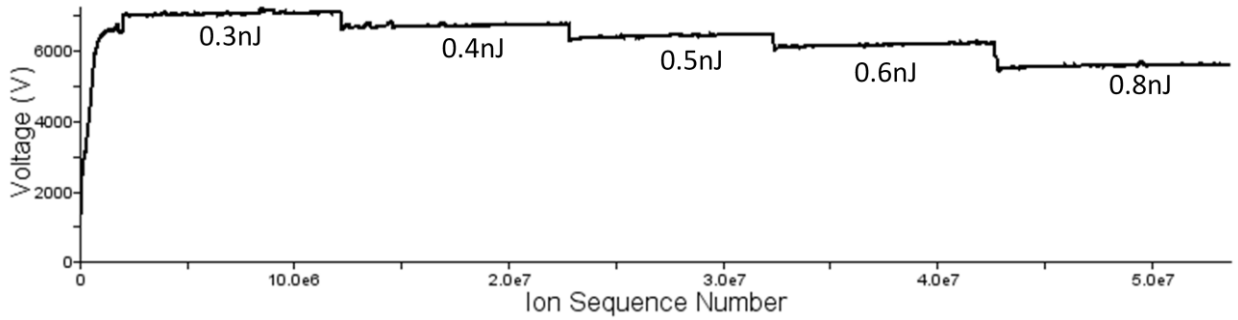


**Figure 5.8 - Voltage history of EPFL-PA-FE$_2$Y specimen analysed at varying laser power. There is very little change in specimen end radius during analysis.**

A comparison of the interface chemistry between analyses using the highest possible field condition (Voltage – 15% pulse fraction) and using lower field conditions (0.5nJ and 0.8nJ laser power) is shown in Figure 5.9. There is a striking difference in the apparent levels of Fe at the core of the clusters. This is an indication that the influence of trajectory aberrations is highly dependent on the field condition, seen by the change in the levels of Fe at the core of the particles in each case. There

is a gradual decrease in apparent Fe at the core as the laser power is increased, as shown in Table 5.2.

This can be understood qualitatively by considering the relative evaporation field of the matrix and particle. It has been shown by field-ion microscopy that the particles evaporate at a lower field to the surrounding matrix [2]. By using a lower evaporation field for the matrix, this brings the evaporation field closer to that required to evaporate the oxide. The oxide therefore does not evaporate as quickly relative to the matrix as it would in a high field condition.

Interestingly, the apparent $R_g$ of the clusters also increases with increasing laser power, and there is a slight decrease in the apparent density of the clusters. The density of atoms was calculated by dividing the total number of atoms isolated using the maximum separation method by the volume of the nanocluster (defined as the $R_g^3$).

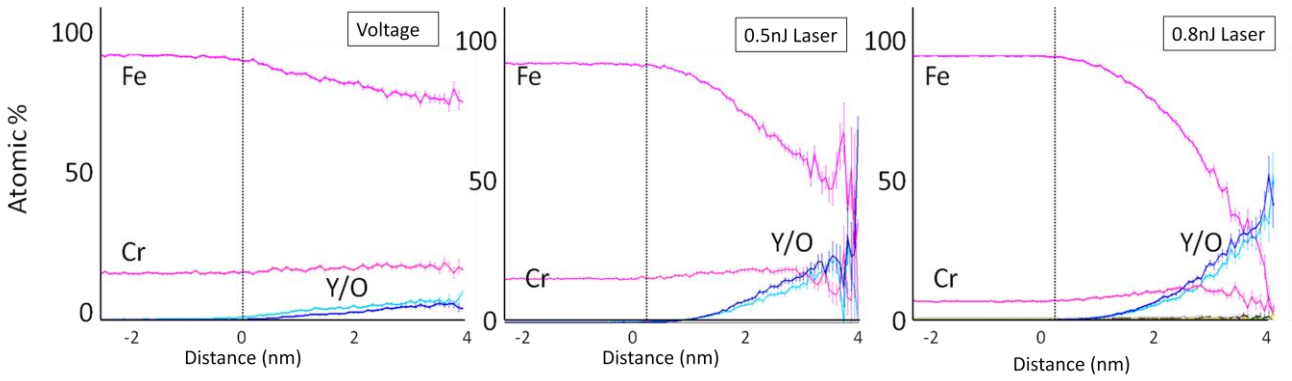


**Figure 5.9 - Proxigram taken from ~20 clusters in each example, showing the variation in concentration of elements from a 1.5at.% O-Y isosurface for EPFL-Fe2Y material analysed in (a) voltage mode 15%pf and (b) laser mode using 0.5nJ laser power (c) laser mode using 0.5nJ laser power. The level of Fe at the core is significantly reduced from left to right.**

| Laser Energy (nJ) | 0.3 | 0.4 | 0.5 | 0.6 | 0.8 |
|---|---|---|---|---|---|
| % Fe | 66.0 ±1.5 | 65.8±1.3 | 63.2±2.1 | 59.8±1.2 | 56.07±1.7 |
| Average $R_g$ (nm) | 3.47 | 3.72 | 3.9 | 4.11 | 4.17 |
| Cluster density (atoms/nm$^3$) | 72 ± 3 | 57 ± 2 | 55 ± 2 | 49 ± 2 | 48 ± 3 |

**Table 5.2 - % Fe inside the 1.5%Y-O iosoconcentration surfaces for oxide particles analysed at different laser energies (averaged over ~20 particles in each case). $R_g$ and cluster data also included.**

Using the method outlined in §4.5.2 the corrected cluster compositions were calculated, and are shown in Table 5.3. In voltage pulsing mode in particular, there is a significant decrease in the measured amount of Y (and also a ~3% increase in the measured C/N level not shown) compared to laser pulsing. There is also a notable change in the measured Cr content of the cluster depending on the laser power used. Significantly less Cr is observed at high laser power where the influence of the trajectory aberrations appears to be less. This indicates that the presence of Cr in the clusters is at least partly a consequence of the trajectory aberrations.

| Analysis Conditions | % Y | | | % O | | | % Cr | | |
|---|---|---|---|---|---|---|---|---|---|
| **Voltage (15%pf)** | 19.5 | ± | 1.2 | 34.7 | ± | 3.4 | 33.7 | ± | 3.8 |
| **0.3** | 31.1 | ± | 1.3 | 33.7 | ± | 1.9 | 29.0 | ± | 3.5 |
| **0.4** | 32.1 | ± | 1.4 | 32.5 | ± | 1.6 | 28.4 | ± | 2.5 |
| **0.5** | 33.1 | ± | 1.5 | 28.8 | ± | 2.4 | 31.2 | ± | 2.8 |
| **0.6** | 35.2 | ± | 1.0 | 31.6 | ± | 1.4 | 26.0 | ± | 2.2 |
| **0.8** | 36.8 | ± | 1.8 | 32.0 | ± | 1.4 | 22.5 | ± | 2.6 |

**Table 5.3 - Matrix corrected compositions of clusters in EPFL-PA-FE$_2$Y (error calculated as standard error from all clusters in an analysis volume of 10M ions)**

The ratio of Y:O also varies slightly depending on the analysis condition used, as seen in Figure 5.10. Figure 5.10 also shows some indication that O is detected further from the core under high field conditions. This effect has been previously observed in relation to similar oxide particles in the ODS-Eurofer alloy [84, 155]. It was proposed that the O was spread further from the core of the particles as a result of surface migration of oxygen prior to evaporation. Table 5.2 shows that the $R_g$ of the clusters increases significantly as the laser energy is increased, and this distance corresponds to the distance of 'oxygen spreading'. The apparent density of the clusters also decreases as the laser power is increased. In light of the analysis of the bulk $Y_2O_3$, it is possible that rather than surface migration of O, another explanation is a reduction in the detection of Y under high field conditions.

By further investigating the multi-hits in the clusters, this can be clarified.

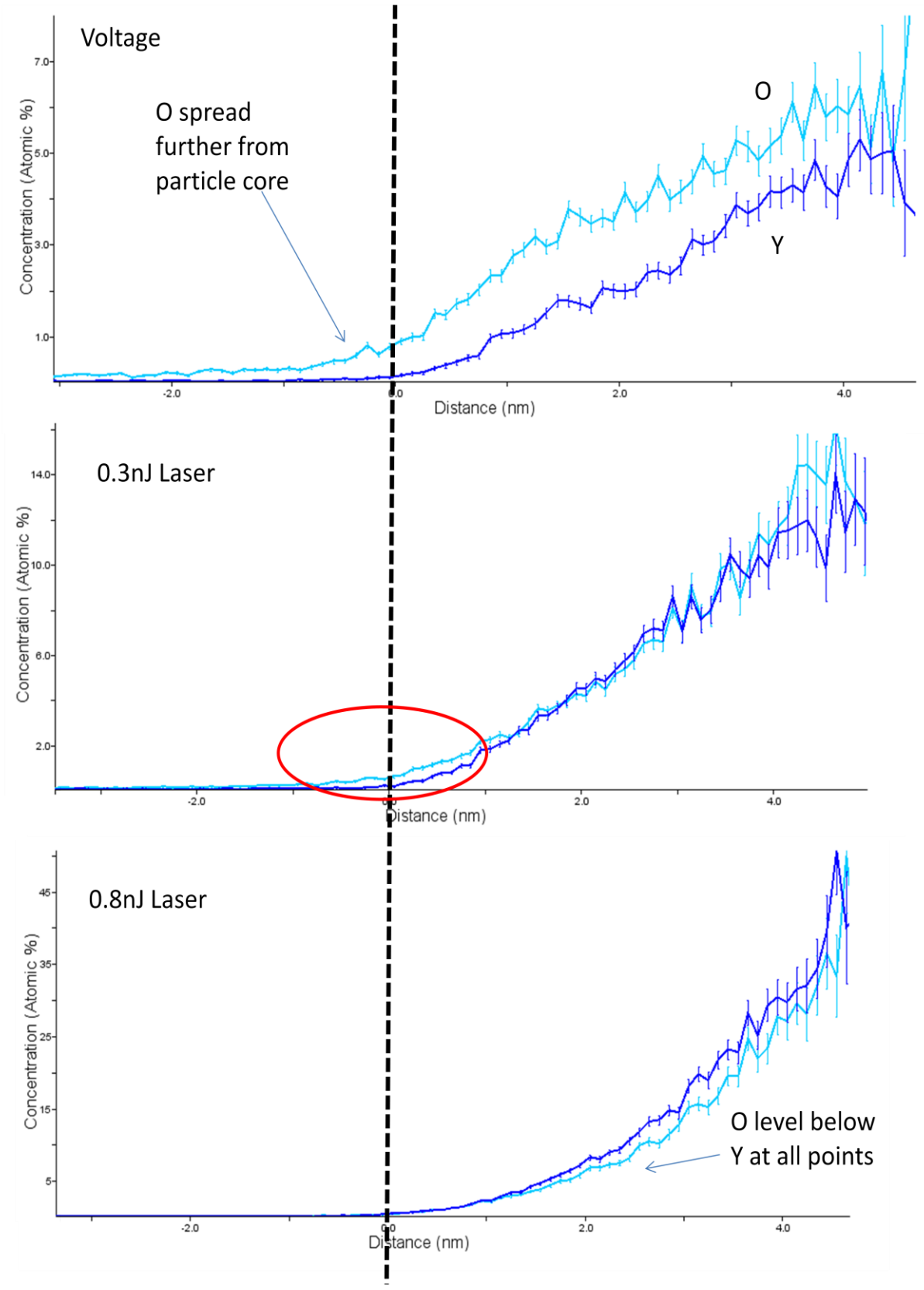


**Figure 5.10 - Variation in Y:O depending on analysis conditions. Using voltage pulsing, the O level is higher than that of Y. Oxygen is also seen further from the core of the nanocluster in high field conditions, but not in low field conditions.**

### 5.3.2 Multi-hit analysis

Figure 5.11 shows that the instances of multi-hits are significantly increased in regions containing oxide clusters. Table 5.4 shows the total number of multi-hits in the clusters decreases as the laser power is increased.

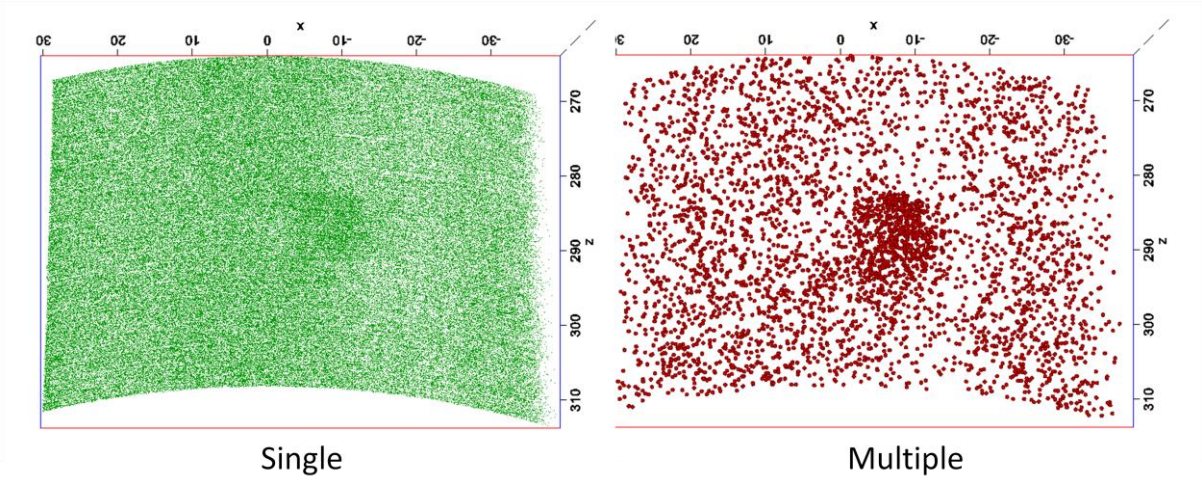


**Figure 5.11 - Distribution of (a) Single hits and (b) multiple hits in EPFL-Fe2Y. 2nm thick slice of data containing 1 oxide cluster.**

| Laser Energy (nJ) | Voltage (15% pf) | 0.3 | 0.4 | 0.5 | 0.6 | 0.8 |
|---|---|---|---|---|---|---|
| % multi-hits | 21.5 | 8.4 | 7.6 | 6.1 | 5.2 | 2.2 |

**Table 5.4 – Proportion of all cluster ions that are detected as part of a multi-hit at various laser energies.**

The spatial correlations of ions evaporated from the clusters are on average considerably closer together than the results presented above for the bulk oxide. The maximum peak of the histogram is around 0.5mm compared with 1mm for the bulk oxide, as seen in Figure 5.12. This implies that the loss of Y due to detector saturation will be increased. The proportion of multi-hits is greatest at the particle-matrix interface, therefore this may explain why there is less Y detected at the interface regions for the example shown in Figure 5.10(b). The large increase in the proportion of multi-hits in voltage mode, and corresponding decrease in detected Y is another indicator that this is a likely explanation.

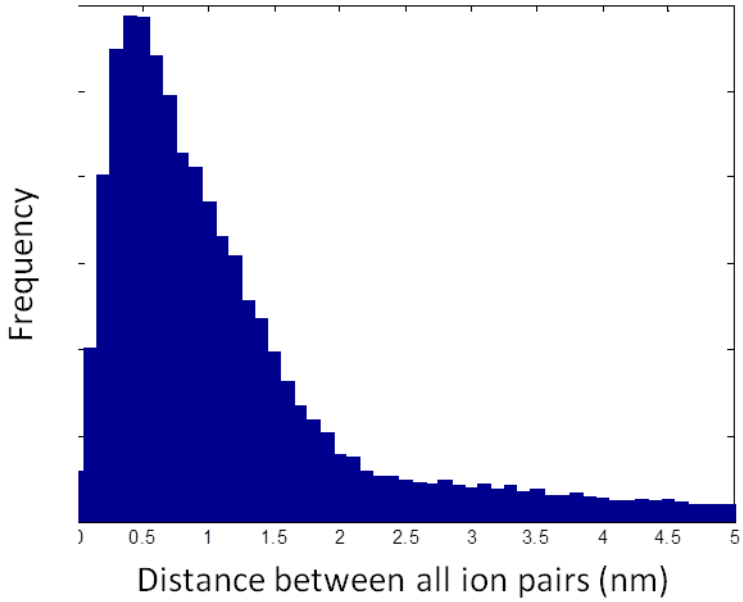


**Figure 5.12 - distance between multi-hit ion pairs from cluster ions (all ions included, data obtained using laser pulsing at 0.3nJ)**

### *5.3.2.1 Correlated ion evaporation in Y-O clusters*

The instances of multi-hits are highest in voltage pulsing mode. In the EPFL-PA-$FE_2Y$ material, ~10% of all ions are detected as part of a multi-hit. Cluster-forming elements are most likely to be part of a multi-hit, with 90% of all Y and O ions detected as part of a multi-hit under very high field conditions (15%pf voltage). Using Saxey's correlation analysis method (similar to §5.2.3.2) the frequency of all ion pair combinations was examined. The number of observed ion pairs were tallied, and the deviations from the expected number of ion pair combinations were calculated. The deviation from the expected values (referred to as 'relative correlations') of the $O^+$ ions (16 amu) and $Y^{3+}$ ions (29.6 amu) are shown in Figure 5.13. In general, there is a tendency for correlated evaporation of ion types associated with the clusters. This is consistent with the theory that multi-hits are often the result of sympathetic co-evaporation.

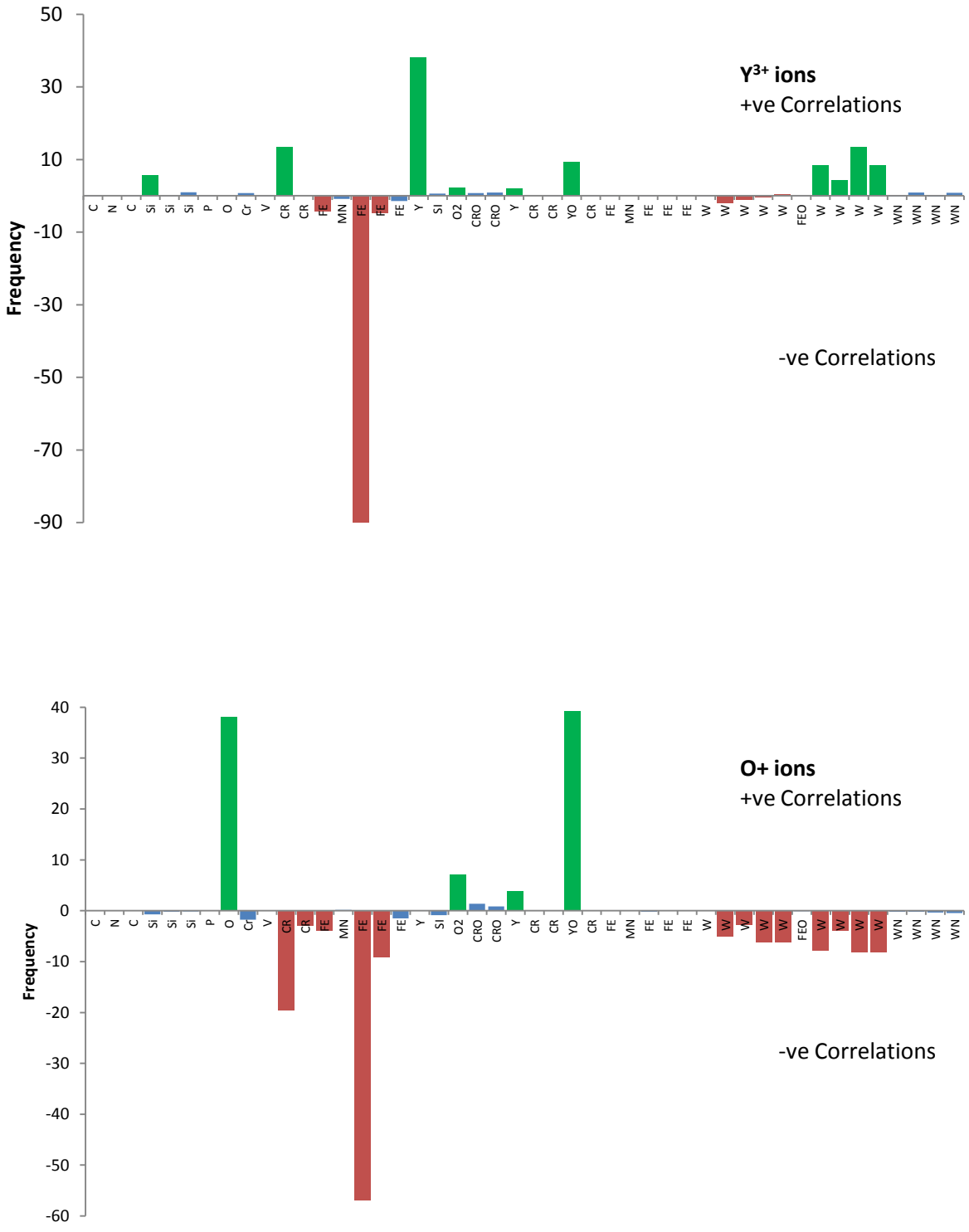


**Figure 5.13 - relative correlations of (a) $O^+$ ions and (b) $Y^{3+}$ ions with all other ions within a multi-hit event. High positive values signify that there are more instances of evaporation of these ion types than is statistically probable based on a theory of independent evaporation. These are indicated in green, and ion types that evaporate less often than is statistically probable are indicated in red. Each column represents a particular window of mass-to-charge-state ratios corresponding to a particular ion type.**

A summary of the most significant relative correlations of ions are summarised in Table 5.5. The correlations of Y/O containing elements are broadly similar to the correlations seen in the bulk oxide. The trends in relative correlations of different ion types are the same across all laser energies used. The only difference is that at higher laser energies, the relative anti-correlations with matrix elements are not as prominent. This is most probably due to the decrease in the number of matrix atoms found in the clusters.

The most significant finding of this analysis is that there is a tendency for strong negative correlations between cluster ions and matrix ions. Fe-containing multi-hits are far more likely to be Fe-Fe or Fe-Cr pairs than Fe-Y pairs. This is reflected in the compositions of the clusters presented in Table 5.3, where there difference in measured composition of Y and O is <5% despite large changes in laser power. The positive correlations of cluster ions with other cluster ions are also an indication that the assumption that there is no Fe in the clusters may be justified. If there is no Fe in the clusters, then sympathetic co-evaporation of neighbouring species involving Fe within the cluster cannot happen.

| Element | Strong positive correlations | Strong negative correlations |
|---|---|---|
| **O/O2** | Y/YO and Cr | Fe |
| **Y** | Y and YO | W |
| **Cr** | Cr and Fe | Y/YO |
| **CrO** | YO | W |
| **Fe** | W | Y |

**Table 5.5 - Significant relative correlations between ion pairs within a multi-hit for EPFL-PA-FE$_2$Y**

#### *5.3.2.2 Implications for the accuracy of the measured composition of the oxide clusters*

So far, the results presented indicate the Y-O based clusters in the EPFL-PA-FE$_2$Y alloy have a Y:O ratio of approximately 1:1, with appreciable levels of Cr. The Cr is likely to be present in the particles at the interface only, as the total amount of Cr measured in the clusters decreases as the effect of the trajectory aberrations is reduced. The observation that the Fe level in the clusters is reduced to zero at the core of the clusters analysed at 0.8nJ laser is a strong indication that clusters

do not contain Fe. The negative correlation of Fe multi-hits with cluster elements is another indication of this.

A non-stoichiometric Y-O sub-oxide is therefore likely to be the most accurate description of these clusters. This is discussed further in Chapter 8.4.2. Further confirmation of this can be shown by analysing clusters in the material after annealing at 1200°C for 100 hours (more details on this can be found in Chapter 6.3). In this case both stoichiometric, and non-stoichiometric clusters co-exist in the same volume of analysis. There is no significant difference in cluster size. In this particle, an increase of Cr at the interface is also visible, but the Cr level falls to 0 at the core.

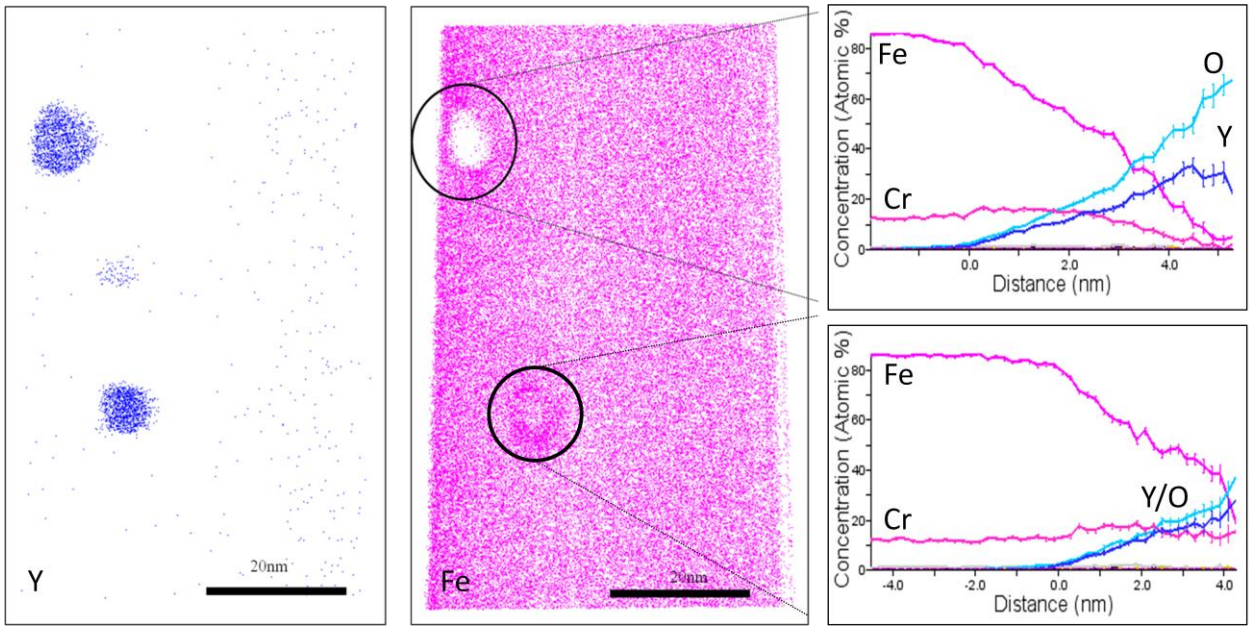


**Figure 5.14 - Clusters in EPFL-PA-FE$_2$Y material after annealing 1200C for 100hrs. Proxigram shows stoichiometric particle with $Y_2O_3$ composition and also a non-stoichiometric particle with Y:O 1:1. Analysis carried out at 0.3nJ laser energy.**

## 5.4 Titanium-containing oxides

As outlined in §2.4.2.3, the inclusion of low levels of Ti (typically >0.5%) in ODS alloys has a profound effect on the oxide particle dispersion. Oxide nanoclusters are found to be enriched in Ti, but there is currently significant ambiguity over the composition and structure of the Ti containing nanoclusters [60]. In the literature review, §2.3.3.2 points out that APT measurements of the nanocluster compositions are often contradictory, and it is therefore necessary to understand more of the field evaporation behaviour of Ti-containing oxides. As for the $Y_2O_3$, both bulk oxide phases and Y-Ti-O nanoclusters in the EPFL-PA-$Y_2O_3$ alloy were investigated.

### 5.4.1 Bulk oxide analysis

The majority of published literature (reviewed in §2.3.3.2) indicates that the nanoclusters are likely to have a $Y_2Ti_2O_7$ or $Y_2TiO_5$ structure, therefore both these oxides were chosen as reference materials to investigate the field evaporation behaviour. The oxides were analysed using the standard conditions chosen for the analysis of the ODS steels; that is, a 30K base temperature and ~0.3nJ laser energy with 200kHz pulse repetition rate.

#### *5.4.1.1 Mass Spectrum analysis*

An example of the mass spectrum from $Y_2TiO_5$ is shown in Figure 5.15. The distribution of mass peaks is exactly the same in both $Y_2TiO_5$ and $Y_2Ti_2O_7$. For both oxides there is the added complication of the overlap of the $O_2^+$ peak and the $TiO^{2+}$ peak at a mass to charge state ratio of 32. This overlap is deconvoluted as described in §3.3.4.2, and the effect of the deconvolution is summarised in Table 5.6.

The composition is significantly reduced in Y compared to the expected composition. The Y deficiency in both the Ti-containing oxides is far greater than the ~3% discrepancy observed in the $Y_2O_3$ (§5.2.2). The multi-hits in the Ti-containing oxides will next be investigated to determine whether the mechanism of Y loss due to multi-hits can account for the Y deficiency.

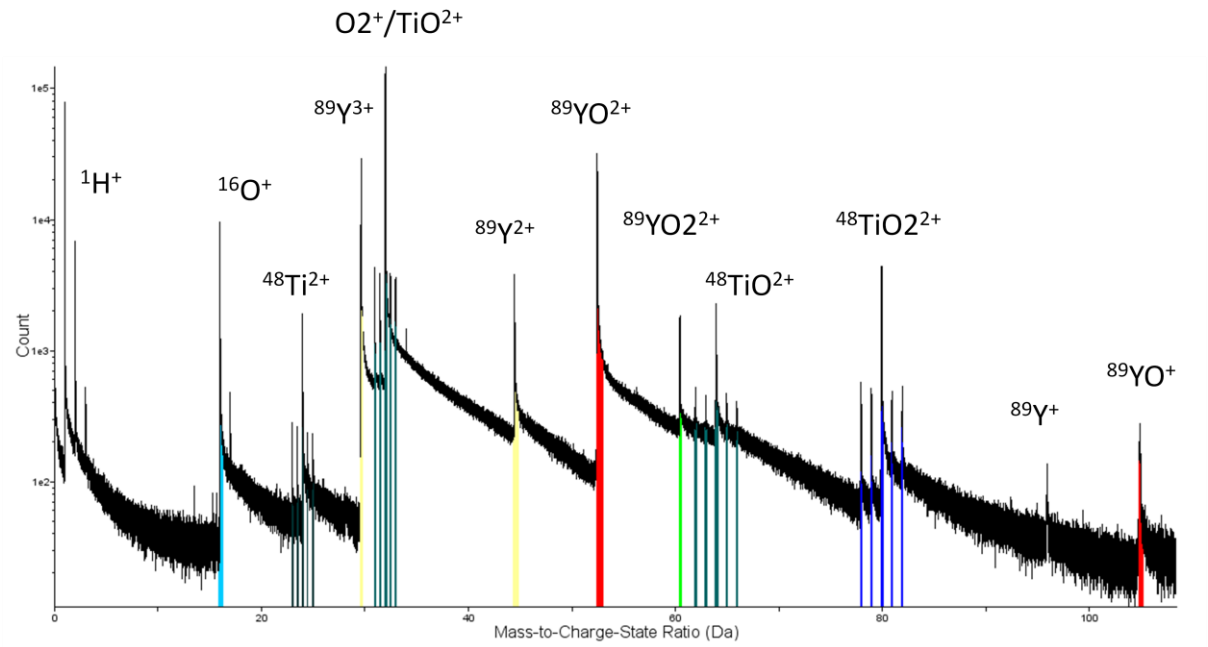


**Figure 5.15 - Mass spectrum from the $Y_2TiO_5$ bulk oxide.**

| Element | % with the peak at 32 amu identified as $O_2^+$ | % with the peak at 32 amu identified as $TiO^{2+}$ | % after deconvolution of the peak at 32 amu | Expected |
|---|---|---|---|---|
| **Y ($Y_2TiO_5$)** | 18.1 | 18.1 | 18.1 | 25 |
| **Ti** | 6.8 | 33.1 | 13.2 | 12.5 |
| **O** | 75.1 | 48.8 | 68.7 | 62.5 |
| **Y ($Y_2Ti_2O_7$)** | 11 | 10.0 | 10.0 | 18.2 |
| **Ti** | 11 | 38.7 | 20.3 | 18.2 |
| **O** | 78 | 51.3 | 69.7 | 63.6 |

**Table 5.6 - Composition of Ti containing oxides. The impact of how the mass peak at 32 amu is assigned is shown by calculating the composition with the 32 amu peak ranged first as $O_2^+$, then $TiO^+$, then deconvoluted as a mixture of $O_2^+$ and $TiO^+$.**

### *5.4.1.2 Multi-hit analysis*

Table 5.7 shows there is a twofold increase in the proportion of multi-hits between the $Y_2O_3$ and the Ti-containing oxides, and the fraction of Y multi-hits is also significantly higher than for either Ti or O. The correlation of ion pairs is shown in Figure 5.16.

| Element | % of hits that are multiple | | |
|---|---|---|---|
| | $Y_2O_3$ | $Y_2TiO_5$ | $Y_2Ti_2O_7$ |
| **Ti** | - | 38 | 29 |
| **Y** | 37 | 63 | 57 |
| **O** | 18 | 37 | 50 |

**Table 5.7 - Proportion of detector hits that are part of a multiple ion evaporation event**

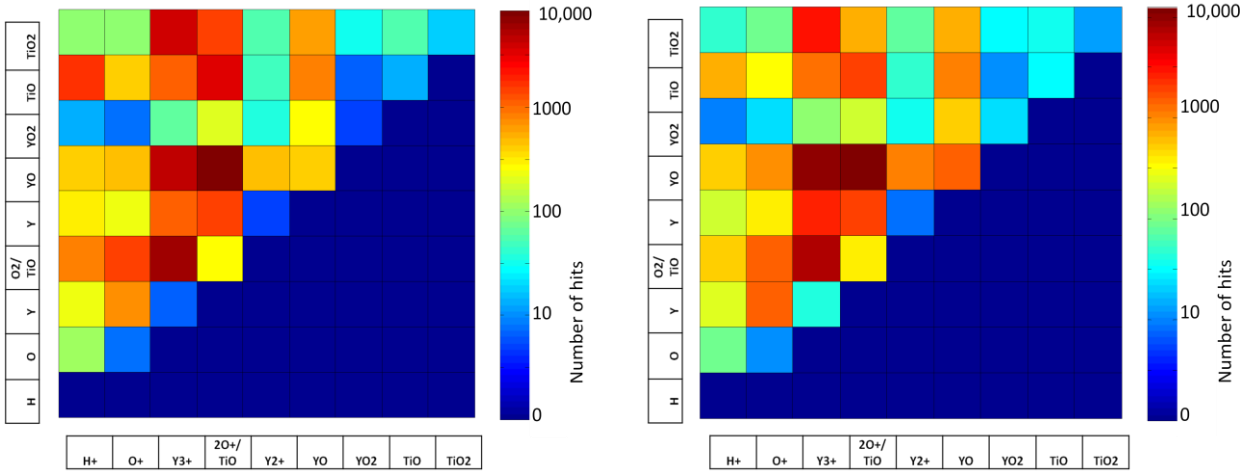


**Figure 5.16 - 2-D histogram of the abundances of multi-hit ion pairs in (a) $Y_2TiO_5$ and (b) $Y_2Ti_2O_7$**

There is a similar pattern of ion-pair correlations for both oxides, with an increase in Y-containing pairs in the $Y_2TiO_5$ as expected due to the higher Y content. When compared with the $Y_2O_3$ in Figure 5.2, the major difference is that there are a higher number of ion pairs associated with the peak at 32 amu. This is likely to be due to the $TiO^{2+}$ contribution to this peak.

### *5.4.1.3 Correlated ion evaporation*

The 'relative correlations' (as defined in §5.2.3.2 and §5.3.2.1 ) for all ion pair combinations were calculated. An example of the relative correlations of $Y^{3+}$ with all other ion types is shown in Figure 5.17. As with the $Y_2O_3$, there is a strong positive correlation of $Y^{3+}$ with the mass ranges corresponding to $TiO_2^{2+}$. There is however less correlation with $O_2^{+}/TiO^{2+}$ than expected. Table 5.8 summarises all significant positive and negative correlations.

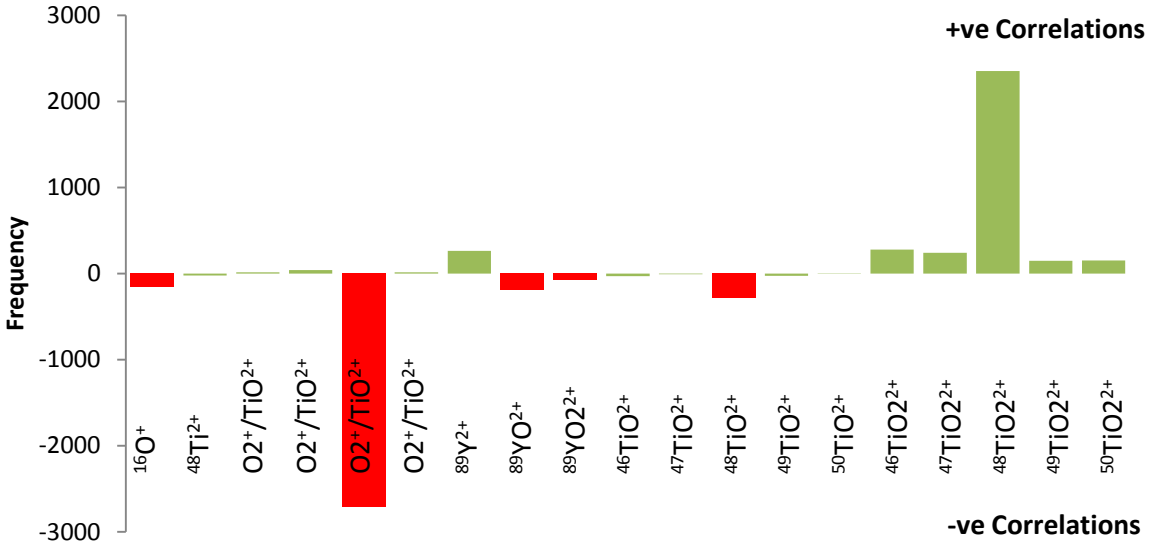


**Figure 5.17 – 'Relative correlation' between Y3+ and all other ion types in bulk $Y_2Ti_2O_7$**

| Positive correlations | Negative correlations |
|---|---|
| $^{89}Y^{3+}$ with $^{48}TiO_2^{2+}$ | $^{89}Y^{3+}$ with $O_2^+/TiO^{2+}$ |
| $O_2^+/TiO^{2+}$ with $^{48}TiO^{2+}$ | $O_2^+/TiO^{2+}$ with $^{48}TiO_2^{2+}$ |
| $O_2^+/TiO^{2+}$ with $^{89}YO^{2+}$ | $^{89}YO^{2+}$ with $^{48}TiO_2^{2+}$ |

**Table 5.8 – Summary of most significant relative correlations in $Y_2Ti_2O_7/Y_2TiO_5$ calculated using the Saxey correlation table approach (as in Figure 5.3)**

A negative deviation value does not necessarily correspond to an anti-correlation. As the correlation table shows relative correlations, a negative deviation value should be interpreted as being 'significantly less correlated' than the positive values. Where there were strong positive and negative correlations in the bulk $Y_2O_3$, differences were also observed in the spatial correlation of the hits on the detector. For these Ti-containing oxides, despite an apparent difference in relative correlation between different ion types, there is minimal difference in the spatial correlation of the ion hits. The histogram of distances between first hit and the second hit for multi hit pairs where the first hit is $Y^{3+}$ and the second hit is $^{48}TiO_2^{2+}$ (most positive correlation in Figure 5.17) is shown in Figure 5.18. There is very little difference between this, and the distribution of distances between multi-hits where the first hit is $Y^{3+}$ and the second hit corresponds to the mass peak at 32 amu (i.e. either $O2^+$ or $TiO^{2+}$ - these are the least correlated species in Figure 5.17). There is still a slight

tendency towards more spatial correlation for the positively correlated $^{48}TiO_2^{2+}$ ions, but this will not affect the composition (via the detector saturation effect) in any way.

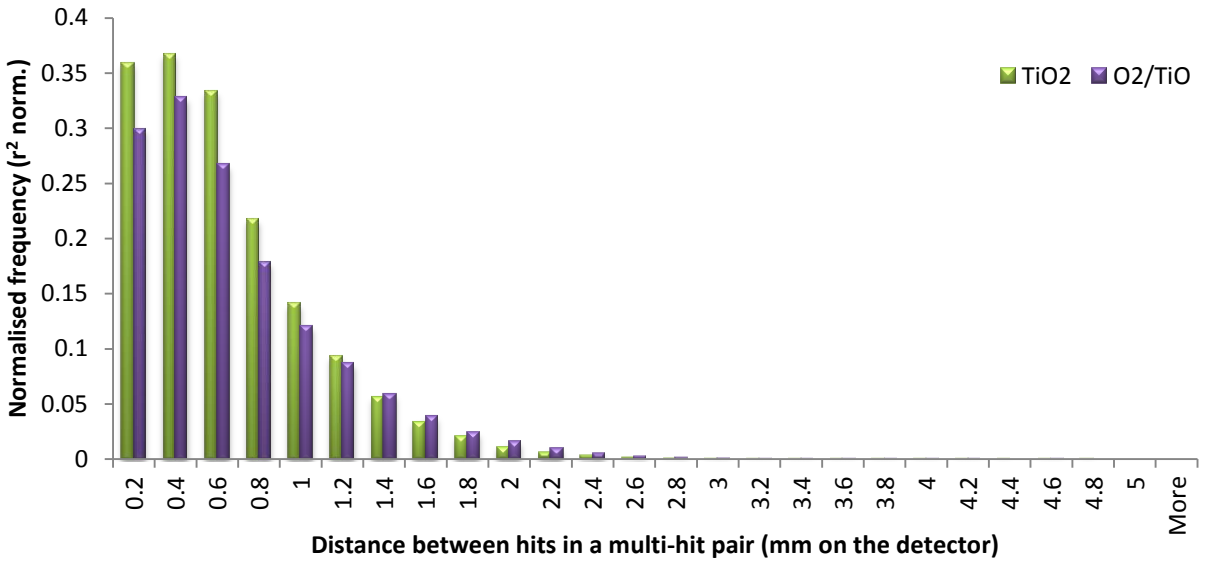


**Figure 5.18 – Normalised histogram of distances between first hit and second hit in a multi-hit pair where the first hit is $Y^{3+}$ and the second hit is $TiO_2^+$ (blue – positive correlation) and for $Y^{3+}$ and $O2^+/^{48}TiO^{2+}$ (red – negative correlation). The tendency for the positively correlated species to evaporate closer together is marginal.**

### *5.4.1.4 Self-ion pairs*

Another major difference when Ti-containing oxides are compared with the $Y_2O_3$ is the proportion of self-ion pairs. In the $Y_2O_3$, the proportion of self-ion pairs registered was ~0.3% for most ion types (with the exception of $O_2^+$ ions, which is much lower as previously discussed in §5.2.3.2). In the $Y_2Ti_2O_7$, as shown in Table 5.9, there are far fewer recorded instances of self-ion pairs. The levels are so low that any reduction in measured concentration due to the detector saturation effect cannot be calculated. There is insufficient data in order to fit a curve and estimate the number of missing ions as was done for the $Y_2O_3$, shown in Figure 5.6. The effect of detector saturation on the Ti-containing oxides is therefore assumed to be negligible. An alternative explanation for the Y-deficient composition measurement must be found.

| $Y^{3+}$ | $O^+$ | $Ti^{2+}$ | $O2^+/TiO^{2+}$ | $TiO^+$ | $YO^{2+}$ | $YO2^{2+}$ | $TiO2^+$ |
|---|---|---|---|---|---|---|---|
| **0.02%** | 0.04% | 0.00% | 0.02% | 0.00% | 0.11% | 0.02% | 0.01% |

**Table 5.9 – Proportion of all ions detected as self-ion pairs in $Y_2Ti_2O_7$**

### *5.4.1.5 Incorrect ion identification within multi-hits*

Figure 5.19 shows a scatter plot of the mass to charge state ratios of the first hit and second hit in a multi-hit pair. If the evaporation of the multi-hit pair was to occur exactly on the pulse, there would be a high density of overlapping points corresponding to the m/e of each individual ion. Instead, there is a long tail of points following each of the major coordinates. Saxey suggests that all the points in the tail correspond to multi-hit pairs that evaporate shortly after the pulse. There are thus a large number of pairs that are not being included in the overall composition because they fall outside the designated mass ranges. In some cases ion-pairs can be incorrectly identified. This delayed evaporation is thought to be one of the major contributors to the long peak tails that we see in the mass spectrum in Figure 5.1.

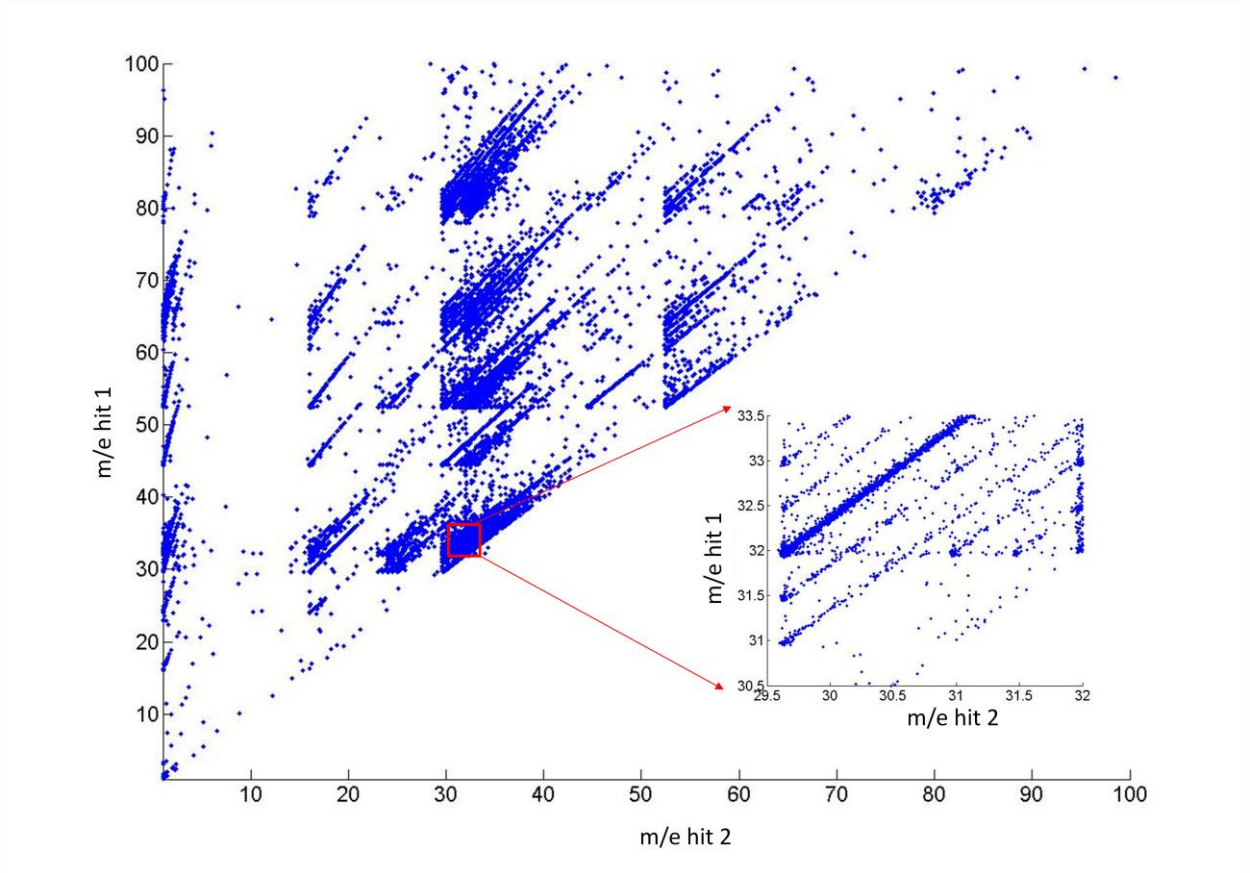


**Figure 5.19- Scatter plot of mass to charge state ratio of hit 1 against hit 2 in bulk $Y_2Ti_2O_7$**

By applying a peak-tail correction as described in §3.3.4 (using MATLAB code given in Appendix B.3), it is possible to correct for the composition differences caused by the delayed evaporation. The hits that form part of the tail are added to the maximum point of the peak, and the composition is re-calculated as shown in Figure 5.20. Only the main peak corresponding to the major isotopes are corrected, as in most cases the peak tails of the minor isotopes cannot be resolved. Due to this, the overlap of the $TiO^{2+}/O_2^{+}$ peak at 32 amu cannot be deconvoluted using the relative abundances of the minor $TiO^{2+}$ peaks. Instead, the proportion of the main peak that corresponds to $TiO^{2+}$ is calculated by assuming that proportion is the same as in the uncorrected mass spectrum. In the case on the $Y_2Ti_2O_7$, 32% of the main $TiO^{2+}/O_2^{+}$ peak is estimated to be $TiO^{2+}$; therefore the same fraction is used to deconvolute the peak in the corrected mass spectrum.

It is important to note that the multi-hits are not the only contributing factor to the peak tails, and these are also closely linked to the APT analysis conditions. Long peak tails are often also associated with excessive heating of the specimen during analysis. This correction therefore also accounts for delayed evaporation due to poor thermal conductivity of the specimen.

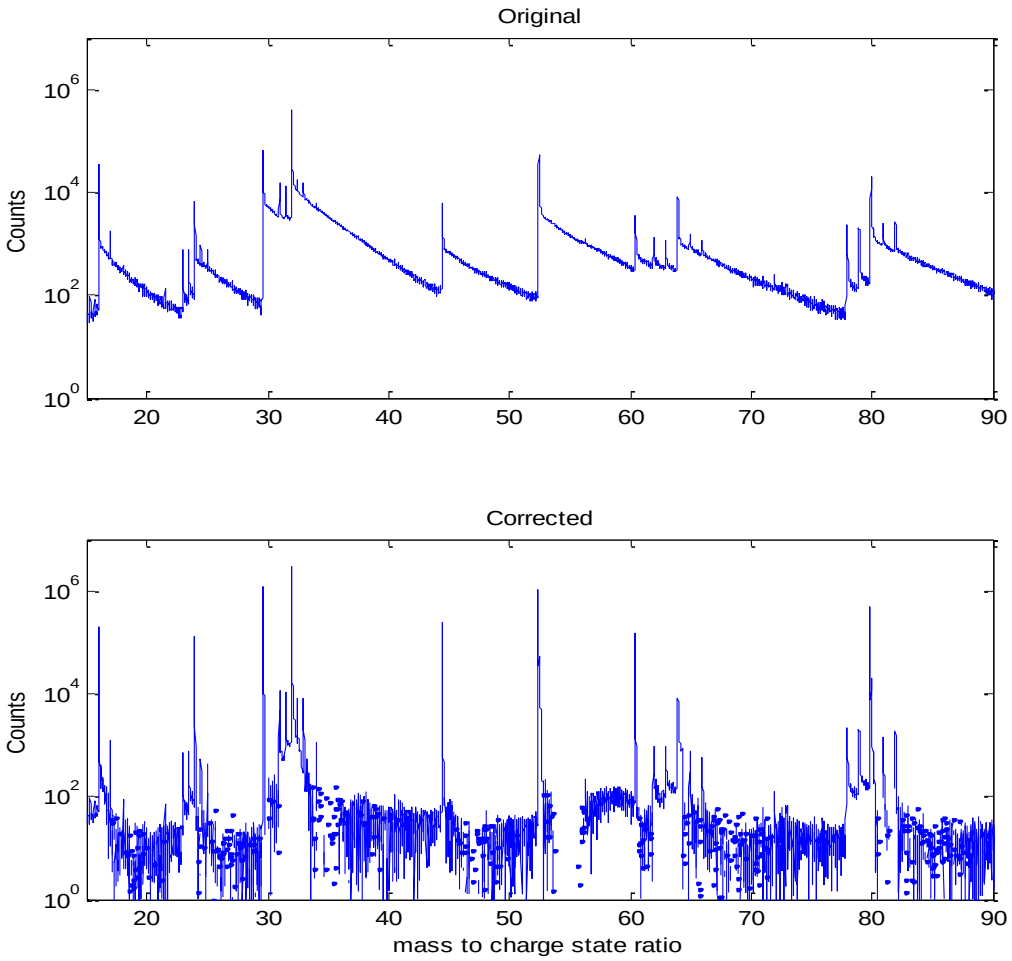


**Figure 5.20 - Mass spectrum of $Y_2Ti_2O_7$ before and after peak tail correction**

The compositions of the Ti-containing oxides after the peak tail correction and the $TiO^{2+}/O_2^+$ peak deconvolution are summarised in Table 5.10. The peak tail correction decidedly increases the measured proportion of Y in the oxide, but the exact stoichiometry is still not achieved.

| Element | Expected composition | Measured after 32 peak deconvolution | Measured after peak tail correction and 32 peak deconvolution |
|---|---|---|---|
| **Y ($Y_2TiO_5$)** | 25.0 | 18.1 | 21.4 |
| **Ti** | 12.5 | 13.2 | 13.6 |
| **O** | 62.5 | 68.7 | 65.0 |
| **Y ($Y_2Ti_2O_7$)** | 18.2 | 10.0 | 19.1 |
| **Ti** | 18.2 | 20.3 | 15.2 |
| **O** | 63.6 | 69.7 | 65.6 |

**Table 5.10 - Composition of $Y_2TiO_5$ and $Y_2Ti_2O_7$ after peak tail correction and 32 amu peak deconvolution**

#### *5.4.1.6 Discussion*

The evaporation behaviour of Ti-containing oxides appears to be different to that of the $Y_2O_3$, and this may be due to the difference in band-gap between to two materials (~6eV for the $Y_2O_3$ [190]and ~3.0 eV for $Y_2Ti_2O_7$ [191]). Table 5.7 shows that in the Ti-containing oxides, ~60% of all Y hits are multiples compared with ~30% in the $Y_2O_3$. Ti-containing ions tend to evaporate often as part of a multi-hit, as seen in Figure 5.16 and the addition of Ti allows more combinations of Y-containing ion complexes to form. As the evaporation of the Ti-containing ions is highly correlated both spatially, and with many Y and Ti-containing species within multi-hits, this conveys an increase in 'sympathetic co-evaporation' of all ion types, and an increase in the overall level of multi-hits. By applying a peak-tail correction, some of these effects on the measured composition can be minimised, but the expected stoichiometry is not recorded. This is most likely to be due to the relatively crude method attempting to correct for the long peak tails and overlaps in the mass spectrum.

The peak overlap and long tails appears to be the most significant factor in influencing the measured composition, and it has been shown that the measured Y concentration is particularly low if this is not accounted for. APT is not an ideal method for measuring oxide composition, particularly when the oxide has a complicated mass spectrum with many overlapping peaks. Decreasing the laser wavelength during analysis has been shown to reduce the width of the peak tails during analysis, therefore if possible, this work should be repeated using a shorter wavelength [156].

## 5.5 Y-Ti-O nanoclusters in the EPFL-PA-$Y_2O_3$ alloy

The evaporation behaviour of Ti-containing nanoclusters is now investigated in a similar manner to the Y-O clusters, and considered together with the findings of the bulk oxide analysis described above. It is important to note that not only is the composition of the nanoclusters different, but that they are also considerably smaller than the Y-O containing clusters.

### 5.5.1 Mass spectrum analysis

The analysis of the bulk oxides has indicated that accounting for long peak tails and deconvolution of the 32 amu peak are important when attempting to quantify the oxide composition. Due to the improved thermal conductivity afforded by the metal matrix, the long peak tails of the Y and Ti based peaks are reduced. With careful specimen preparation and selection of analysis parameters, it is possible to analyse a specimen where the main peaks associated with the nanoclusters are very well defined, as shown in Figure 5.21. The peak tail correction is therefore not required for the nanoclusters.

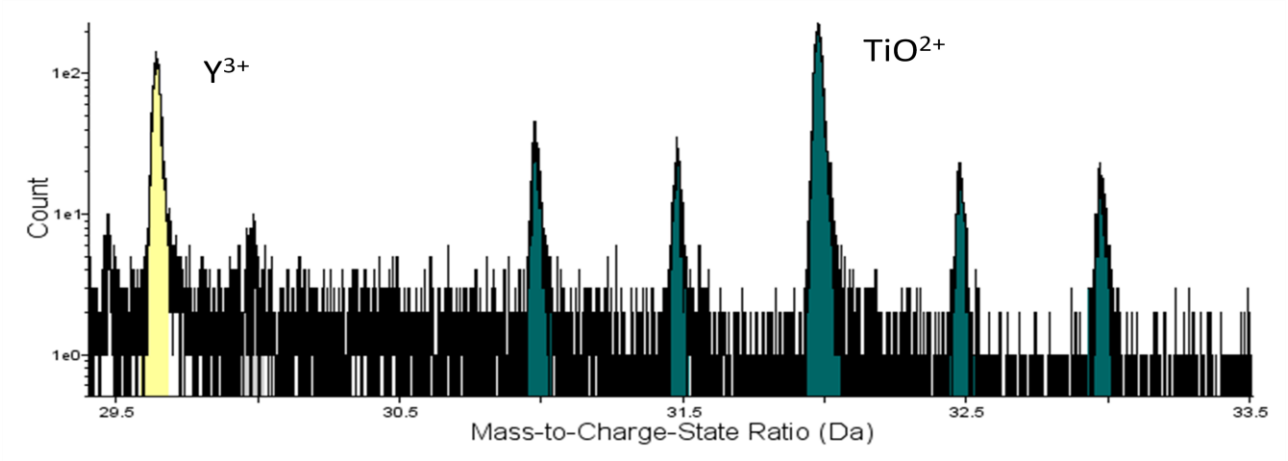


**Figure 5.21 - Mass spectrum of Y-Ti-O nanoclusters (only ions isolated using the cluster selection algorithm)**

The ratio of the $TiO^{2+}$ ion peaks in this case is roughly stoichiometric, indicating that there is no significant contribution of $O_2^+$ ions in the nanoclusters.

### 5.5.2 Evaporation behaviour of the nanoclusters under varying field conditions

Figure 5.22 shows that for the Y-O nanoclusters the Cr content varied depending on the laser energy used. The Ti-Y-O nanoclusters in the EPFL-PA-$Y_2O_3$ material was also analysed at various laser energies. There is a marginal decrease in the % Fe at the core, and Table 5.11 shows the Cr concentration in the clusters decreases by 14%. The clusters still show an increased level of Cr all the way to the core therefore it is not possible to conclude whether the Cr is only present at the

interface, but the decrease in Cr content of the clusters when analysed with a high laser energy is an indication that this is possible. Once the mass-balance effect due to the reduction in Cr concentration is taken into account, there is no significant change in the proportions of Y, Ti and O.

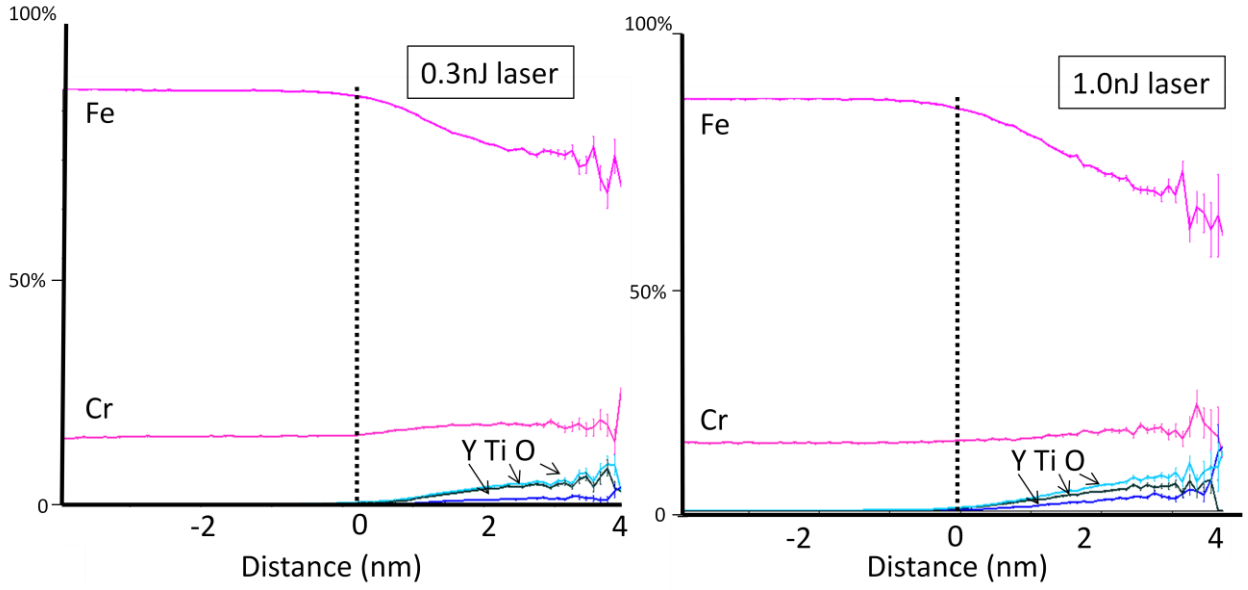


**Figure 5.22 - Proxigram showing the variation in concentration around a 1% Y/Ti/O isoconcentration surface after APT analysis at (a) 0.3nJ laser energy and (b) 1nJ laser energy. Fe level is apparently reduced at the core of the nanoclusters when a higher laser energy is used during analysis**

| Element | 0.3nJ laser | 1nJ laser |
|---|---|---|
| **Cr** | 44.3 ± 0.9 | 30.3 ± 0.5 |
| **Ti** | 21.1 ± 0.4 | 23.8 ± 0.2 |
| **Y** | 5.6 ± 0.2 | 8.9 ± 0.1 |
| **O** | 24.3 ± 0.4 | 28.8 ± 0.2 |
| **% multi-hits in clusters** | 5.6% | 2.2% |

**Table 5.11 - Corrected cluster compositions for nanoclusters in EPFL-PA-$Y_2O_3$ material (error calculated as standard error from all clusters in an analysis volume of 10M ions)**

### 5.5.3 Correlated ion evaporation

Figure 5.23 shows that as in Figure 5.13, the cluster ions (Y, Ti and O this time) tend to evaporate together preferentially together with matrix atoms such as Fe. In some respects, it is surprising that there is a negative correlation with Cr, as this is a major constituent of the nanoclusters. If Cr was strongly positively correlated with other cluster elements, it would be an indication that the Cr formed part of the core of the cluster. Due to the low numbers of ion pairs, and the fact that the correlation analysis only shows relative strengths of correlation, no definitive conclusions can be

drawn from these results. It is however worth drawing attention to the fact that no such positive correlation is observed, as this suggests that sympathetic co-evaporation of Cr with other cluster ions is not very likely.

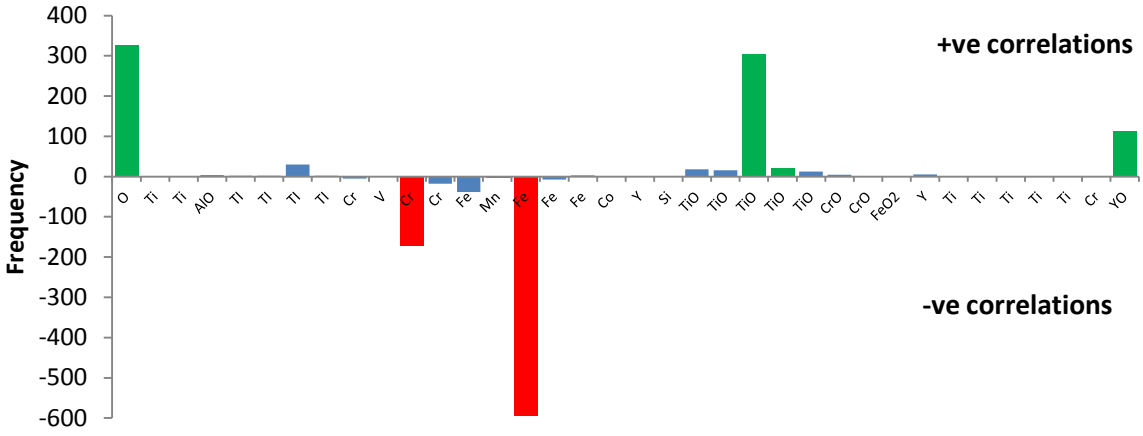


**Figure 5.23 – 'Relative correlations' of $Y^{3+}$ ions with all other ion types from multi-hit pairs in the EPFL-PA-$Y_2O_3$ material containing Y-Ti-O nanoclusters. The most positive correlations are with other cluster elements, and are shown in green. The most negative correlations are with matrix elements such as Fe, and are shown in red. Each bin corresponds to a particular mass range corresponding to the indicated ion on the mass spectrum.**

### 5.5.4 Implications for the accuracy of the measured composition of the nanoclusters

Table 5.11 shows that at high laser power, the proportion of multi-hits in the nanoclusters is very low, yet the measured composition of the nanoclusters does not change significantly (with the exception of the Cr content). Combined with the data presented on the low proportions of self ion pairs registered in the Ti-containing bulk oxides, it can be concluded that the effect of detector saturation is unlikely to influence the measured composition of the nanocluster significantly.

The effect of peak overlap and delayed evaporation was shown to have a major effect on the measured composition of the bulk oxide, and while this effect is reduced in the ODS steel due to high matrix thermal conductivity, it is important to consider that in some specimens where the thermal conductivity is poor, a lower level of Y may be recorded in the nanoclusters. During the course of this research 20+ specimens of the EPFL-PA-$Y_2O_3$ material have been analysed, and there is very little scatter in the Y:Ti ratio. This is a good indication that this effect does not affect the

overall composition significantly for ‘good quality’ data. The fact that the $TiO^{2+}$ isotopic peak ratio is approximately stoichiometric is an indication that the nanoclusters contain significantly less oxygen than the bulk oxide.

There are obvious similarities in the evaporation behaviour of the Y-O and Y-Ti-O nanoclusters which indicates that the measured Cr content of the nanoclusters is partly due to the influence of the trajectory aberrations, and that the absolute value of Cr in the nanoclusters is dependent on the APT analysis conditions. These results suggest that the Y-Ti-O nanoclusters also have a sub-stoichiometric oxygen content that does not correspond to a known oxide phase. The Y:Ti ratio is reliably ~1:2, which also does not correspond to the known stable oxide phases. This is discussed further in §8.4.3.

## 5.6 Summary

- Nanoclusters all contain appreciable levels of Cr, and are either a Y-O based cluster with Y:O ratio of ~1:1 or a complex Y-Ti-O based cluster with Y:Ti:O of approximately 1 : 1.75 : 3.5.
- From the analysis of bulk oxides, the accuracy of the APT measurement of O content has been demonstrated. The APT measurements indicate that the nanoclusters are likely to have a sub-stoichiometric O content.
- Detector saturation effects mean that there is a likely under-estimation of the Y content in the Y-O clusters. This is likely to be greater than the ~0.5% deficit calculated for the bulk $Y_2O_3$ oxide, but in the same order of magnitude.
- Peak overlaps may cause the Y:Ti ratio in the Ti-containing oxides to vary if the thermal conductivity of the specimens is poor, but this effect is thought to be negligible in 'good quality' data.
- In the case of the (~4nm radius) Y-O clusters the apparent Cr content of the clusters decreases when the evaporation field used for analysis is decreased. When a laser energy of 0.8nJ is used for analysis, the level of Cr at the core of the nanoclusters is reduced to zero. This indicates that Cr is present as a shell around the nanocluster, but it remains unclear as to whether the shell is part of the oxide, or purely Cr segregation to the interface.
- Ti-containing nanoclusters are smaller with ~2nm radius, therefore resolving the interface is more difficult. The Ti-containing nanoclusters show a similar decrease in Cr content when the evaporation field is decreased, indicating that the in this case the Cr level is also increased at the interface.

# 6 Stability of oxide nanoclusters at high temperatures

*This chapter concerns the characterisation of ODS steels developed by Baluc et. al. The following key aspects will be discussed:*

*Characterisation of* ***EPFL-PA-$Y_2O_3$*** *and* ***EPFL-PA-$FE_2Y$*** *alloys*

*The core-shell structure of the oxide nanoclusters*

*The stability of the nanoclusters at high temperature*

## 6.1 Introduction

At EPFL, a team of researchers have been working on the processing of ODS steels for ~8 years and have built up a wealth of expertise in producing high quality material. As outlined in the literature review (§2), the exact processing conditions can affect the microstructure and mechanical properties of the final material quite considerably. In order to reduce the required milling time during MA, it is common to pre-alloy the matrix composition, and then gas atomise to produce the base powder for the matrix [60]. Oksiuta et. al. report that impact properties can be improved by MA with $Fe_2Y$ starting powder rather than $Y_2O_3$ [116]. A summary of some differences between the two materials is given in Table 6.1.

| | EPFL-PA-$FE_2Y$ | EPFL-PA-$Y_2O_3$ |
|---|---|---|
| **DBTT (°C)** | -24 | 77 |
| **Upper shelf energy (J)** | 8.8 | 2.4 |
| **Nanocluster type** | Y-O | Y-Ti-O |
| **Nanocluster radius** | ~5nm | ~2nm |

**Table 6.1 – Some properties of the EPFL-PA-$FE_2Y$ and EPFL-PA-$Y_2O_3$ alloys from [116]**

The nanoclusters in the material MA with $Fe_2Y$ are larger and the population is less dense than the material which is MA with $Y_2O_3$. The higher number density of nanoclusters in EPFL-PA-$Y_2O_3$ is believed to improve the materials resistance to radiation damage, and is therefore advantageous. The

improved impact properties afforded by the material MA with $Fe_2Y$ means that the EPFL-PA-$FE_2Y$ material should also be considered as a potential structural material for a fusion reactor.

The composition of the nanoclusters as measured by APT has been investigated in detail in Chapter 5. Here, an overview of the microstructure of both the EPFL-PA-$Y_2O_3$ material and the EPFL-PA-$FE_2Y$ material is presented. The stability of the nanoclusters is then investigated by high temperature annealing. Any potential changes to the microstructure at high temperature are likely to occur at lower temperatures in service as diffusion is accelerated by irradiation. Understanding the coarsening mechanisms of the nanoclusters will allow better prediction of how the microstructure might evolve in a fusion reactor.

## 6.2 Characterisation of EPFL pre-alloyed ODS alloys

### 6.2.1 EPFL-PA-$F_{E2}Y$ material

Figure 6.1 shows the EPFL-PA-$FE_2Y$ material encompasses many of the characteristics associated with ODS steels. The average grain size is <5μm, and an even distribution of spherical oxide particles is visible within grains. Larger oxides up to ~50nm are also observed at grain boundaries, and energy dispersive x-ray analysis (EDX) revealed the grain boundary oxides to be rich in Y and Ti.

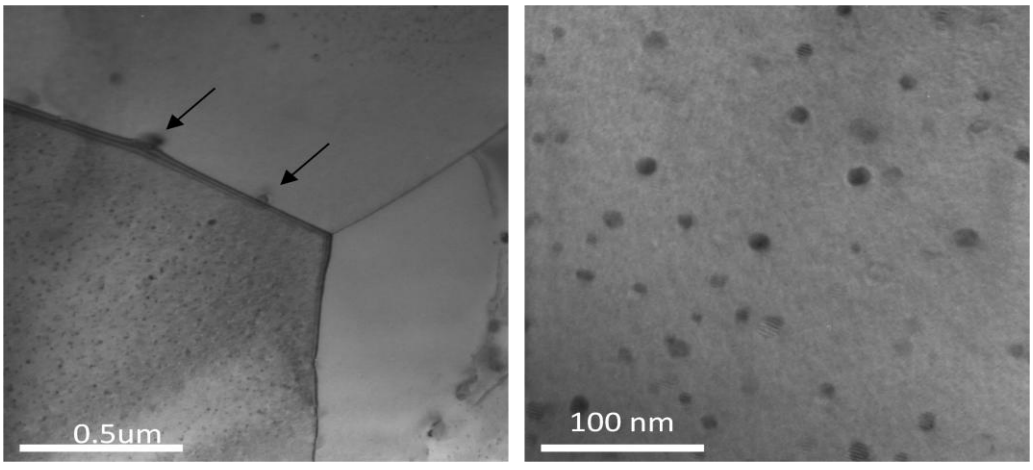


**Figure 6.1 - (i) bright field TEM image of the in EPFL-PA-$FE_2Y$ material. Larger oxide particles on a grain boundary are indicated. (ii) bright field TEM image of nanoclusters in EPFL-PA-$FE_2Y$**

Details of the composition of the clusters can be found in Figure 6.2. The average radius of gyration of the clusters is 3.8 ± 0.2 nm, with a number density of 4.3 ± 0.6 x $10^{21}$ $m^{-3}$. Their composition as measured by the matrix-corrected maximum separation method is approximately 32% Y, 27% O and 34%Cr. Figure 6.2(a) shows that there is considerable scatter in the measured composition of individual clusters. It is important to recognise that the Cr introduced by the trajectory aberrations is not included due to the matrix correction process outlined in § 4.5.2.1.

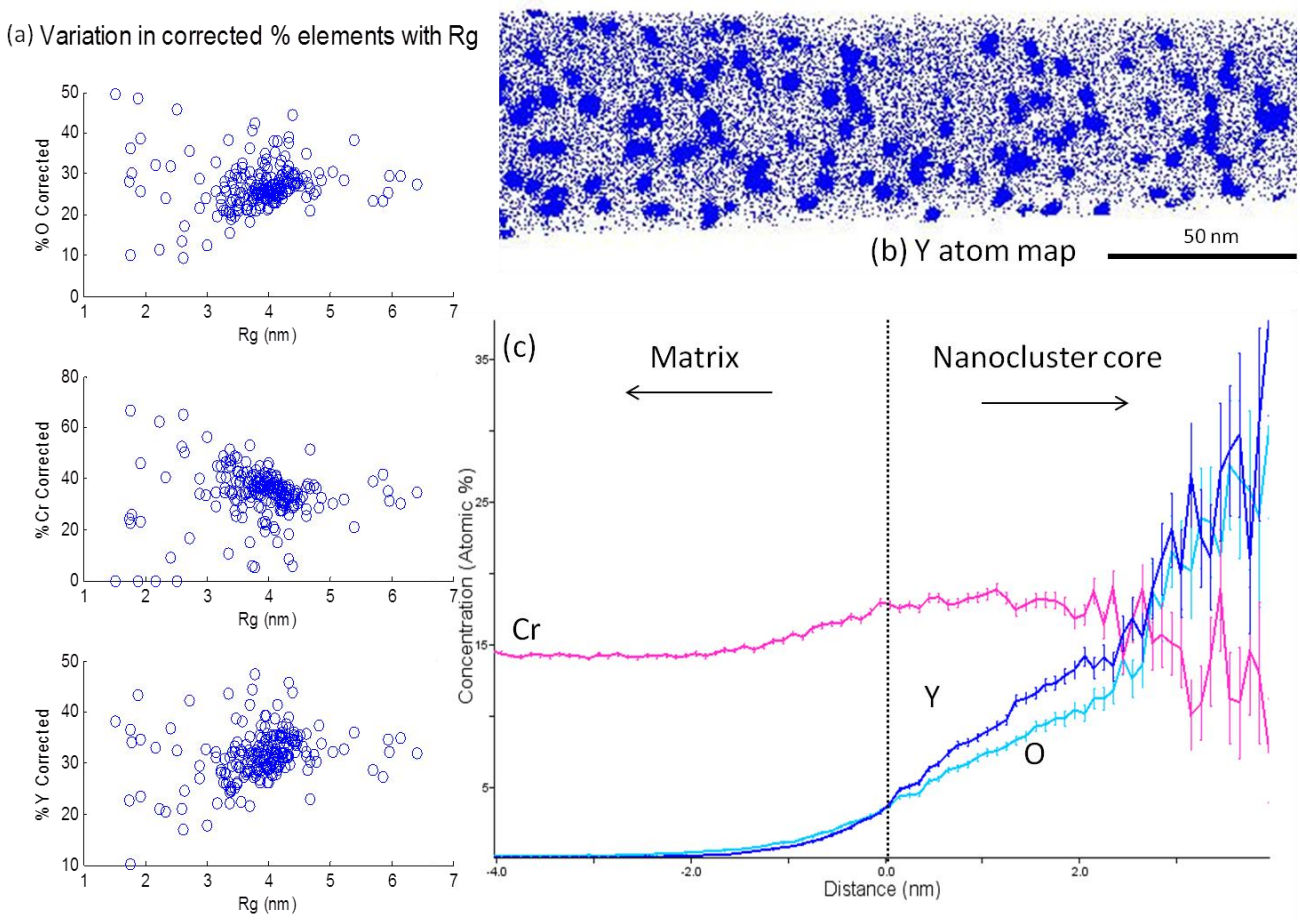


**Figure 6.2 - (a) Scatter plot of the matrix-corrected compositions of the clusters for each cluster in the analysis volume (b) Y atom map corresponding to the cluster compositions in (a) and (c) Proxigram showing the variation in composition around a 3% Y/O iso-concentration surface for all clusters in the dataset. The Cr is seen predominately in the region of the interface.**

#### *6.2.1.1 Core-shell structure*

The oxide nanoclusters in ODS steels are widely reported to have a core-shell type structure [60, 84, 92]. Figure 6.2(c) shows the Cr level appears to drop off at the core of the nanocluster indicating the Cr is likely to be a shell at the interface of the particle. The proxigram in Figure 6.2(c) suggests that the Cr shell is part of the oxide but this could be an effect of the trajectory aberrations explained in §3.3.7. The nature of the Cr shell and possible causes will be discussed in detail in §8.4.

### 6.2.2 EPFL-PA-$Y_2O_3$ material

As with the EPFL-PA-$FE_2Y$ material, the EPFL-PA-$Y_2O_3$ material has a uniform dispersion of oxide nanoclusters within grains, shown in Figure 6.3. The nanoclusters are however on average much smaller with $R_g$ ~2nm. The nanoclusters in this case are also enriched in Ti along with Y, Cr and O. The average matrix corrected compositions of the nanoclusters are 48%Cr, 25% O, 13%Ti, and 7%Y. In this case the number density of nanoclusters is ~16x higher than in the EPFL-PA-$FE_2Y$ material at $7.1 \pm 0.7 \times 10^{22}$ $m^{-3}$.

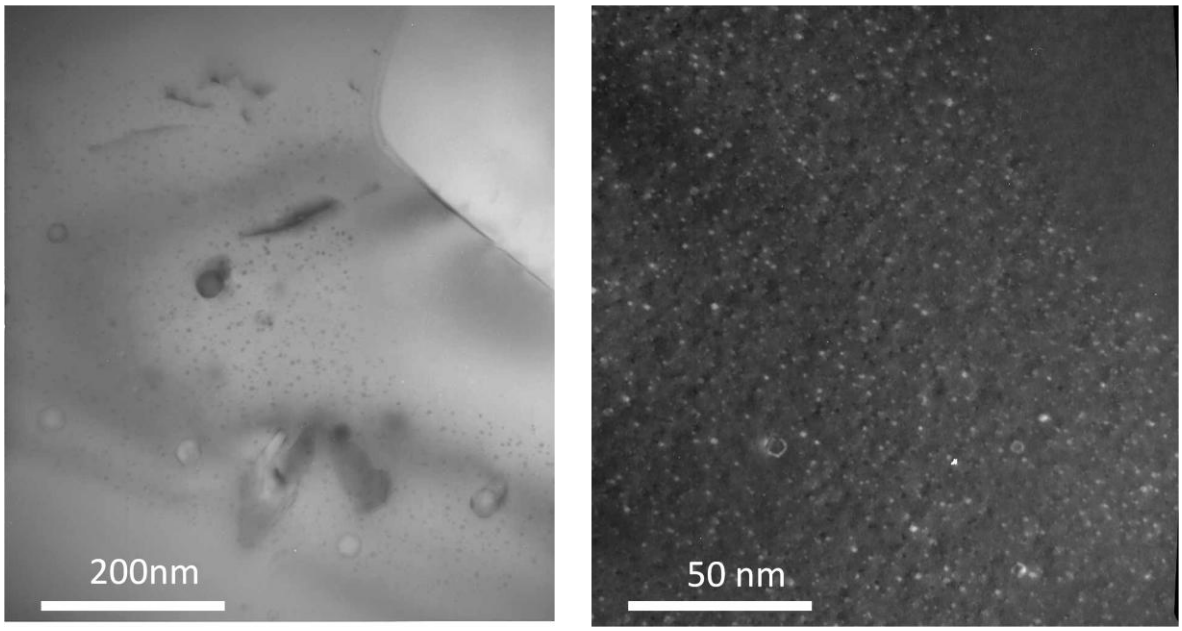


**Figure 6.3 (i) Bright field TEM image of EPFL-PA-Y2O3 material (ii) Dark field TEM image of nanoclusters**

#### *6.2.2.1 Core-shell structure of the nanoclusters*

The proxigram shown in Figure 6.4(c) highlights the distribution of elements around the nanocluster-matrix interface. The level of Cr is raised at the core of the nanoclusters along with Y, Ti and O. Unlike the Y-O clusters in the EPFL-PA-$FE_2Y$ material, there is no evidence to suggest that the Cr forms a shell. This may be due to the smaller size of the nanoclusters in the EPFL-PA-$Y_2O_3$ material, making it impossible to resolve the shell; alternatively, the Cr may be present as part of the oxide phase. If Cr is included as part of the oxide, again the M:O ratio is >>1, suggesting that this is unlikely, as charge balance needs to be maintained. Interestingly, a Cr shell was not observed around larger Y-Ti-O particles seen at grain boundaries in the EPFL-PA-$Y_2O_3$ material as shown in Figure 6.4(d). In fact, the Cr observed at the core of these larger particles probably due to the trajectory aberrations, as in some of the largest particles, the level of Cr falls to zero at the core in a similar manner to the Fe level. There is clearly considerable debate surrounding the nature of the interaction of Cr with the nanoclusters, and this is discussed in detail together with a number of other results in § 8.4.

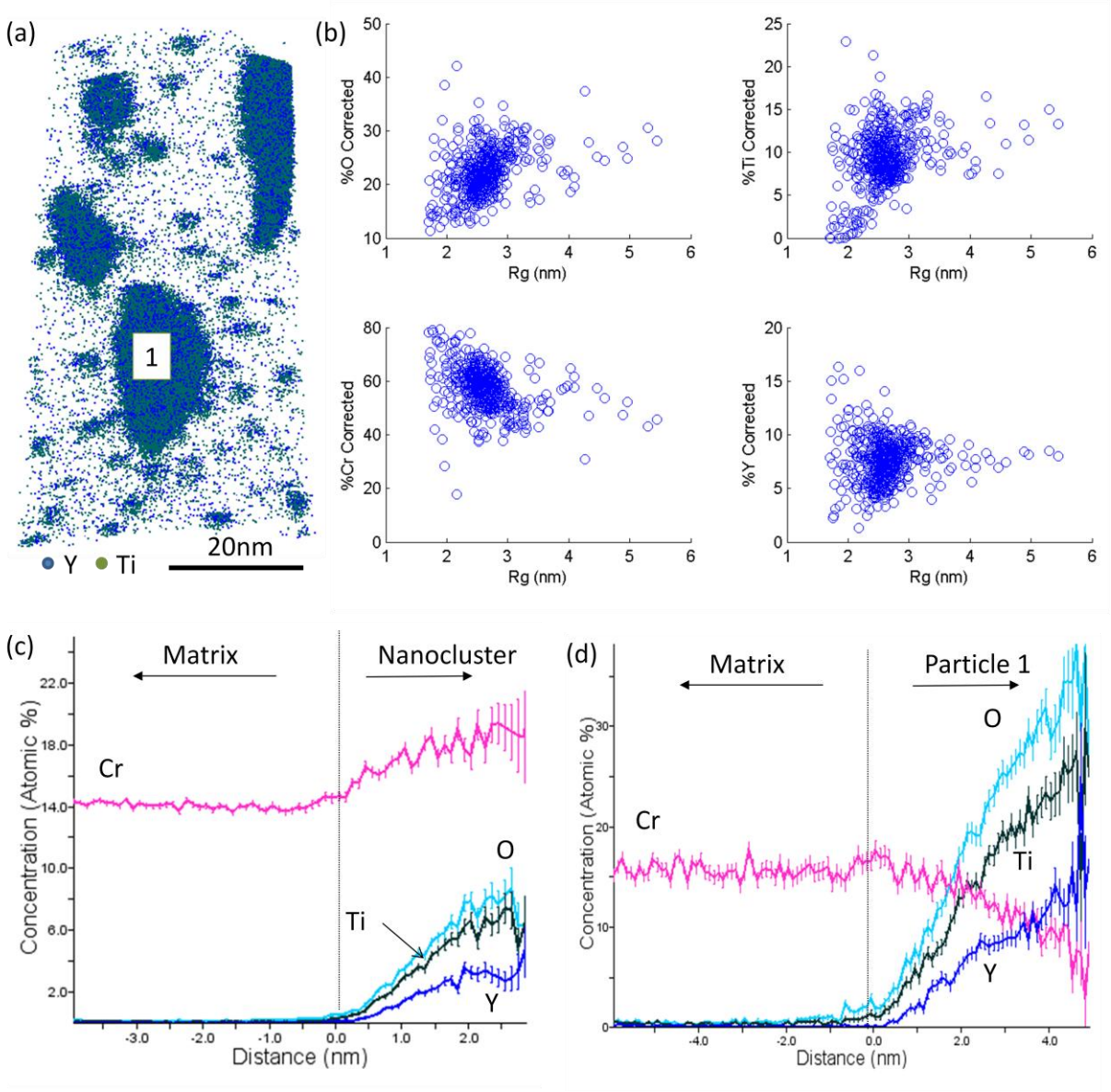


**Figure 6.4 - (a) atom map showing both nanoclusters and larger grain boundary oxides in EPFL-Y2O3 (b) scatter plot of all nanoclusters in a typical analysis volume (~5x larger than the volume shown in a). (c) proxigram of ~500 nanoclusters based on a 0.3%Y/Ti isoconcentration surface (d) proxigram of grain boundary particle labelled 1, based on a 0.3%Y/Ti isoconcentration surface.**

## 6.3 Annealing at high temperature – 1200°C

Alinger et. al. studied the high temperature stability of the Y-Ti-O nanoclusters in the MA957 material using SANS, and found that aging at the processing temperature of 1150°C had little effect, but that systematic coarsening was observed at 1200°C [192]. Therefore the pre-alloyed EPFL-PA-$FE_2Y$ alloy (reinforced with Y-O based particles) and pre-alloyed EPFL-PA-$Y_2O_3$ alloy (with Y-Ti-O particles) were encapsulated in evacuated silica tubes, and annealed at 1200°C for up to 100 hours.

### 6.3.1 EPFL-PA-$FE_2Y$ material

#### *6.3.1.1 Effect on nanocluster distribution*

Figure 6.5 shows a distinct change in particle size distribution as the material is annealed, indicating coarsening of the nanoclusters. The increase in the average nanocluster radius is shown in Figure 6.6. The time exponent of coarsening is extracted later in § 6.3.3.

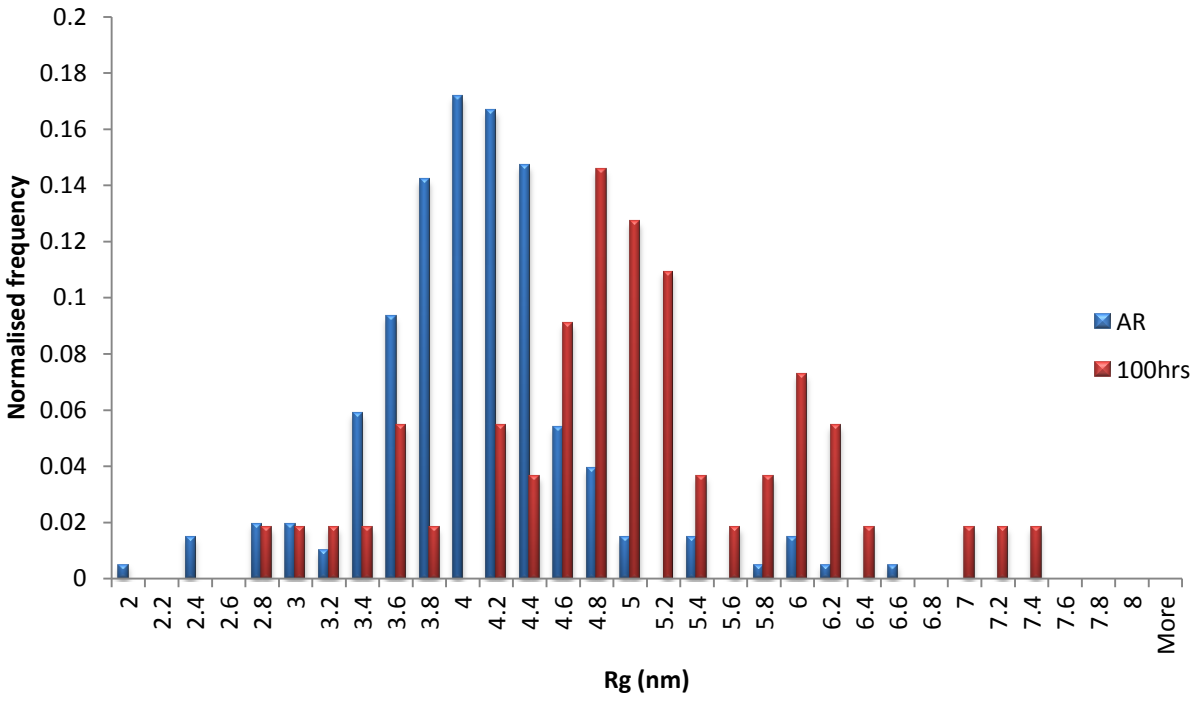


**Figure 6.5 - Particle size distribution for nanoclusters in the EPFL-PA-$FE_2Y$ material in the as-received condition (blue) and after annealing for 100 hours at 1200°C (red)**

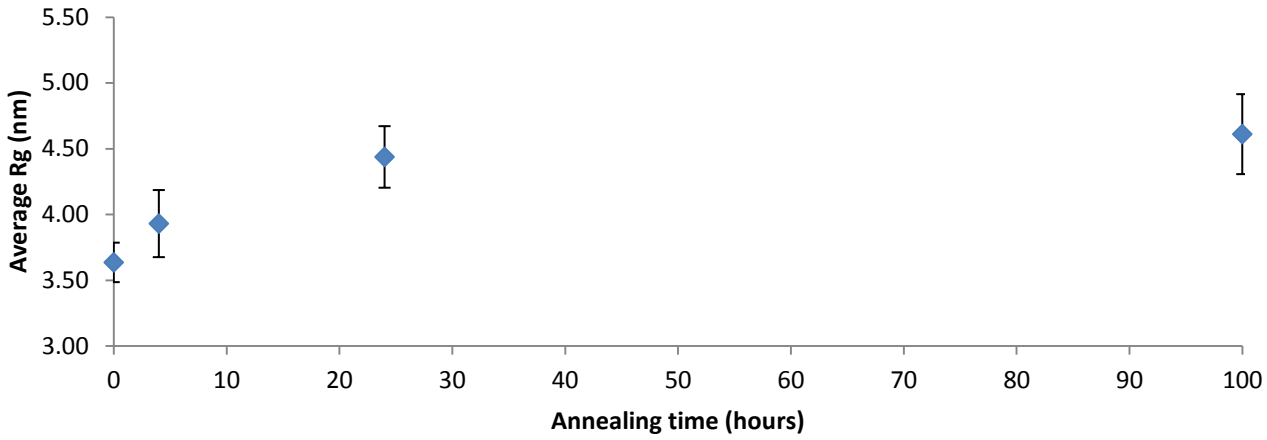


**Figure 6.6 - Change in average particle radius with annealing time. Standard error of average Rg from at least 50 nanoclusters in each condition**

### *6.3.1.2 Effect on nanocluster composition*

The composition of the nanoclusters remained unchanged after annealing up to 24 hours. As previously described in Chapter 5, in one instance, after annealing for 100 hours at 1200°C, four nanoclusters with a Y:O ratio of 2:3 were observed. A proxigram taken from one of these clusters is shown in Figure 6.7a. This represented ~10% of all clusters analysed in that specimen. All other clusters had a Y:O ratio of 1:1 (Figure 6.7b).

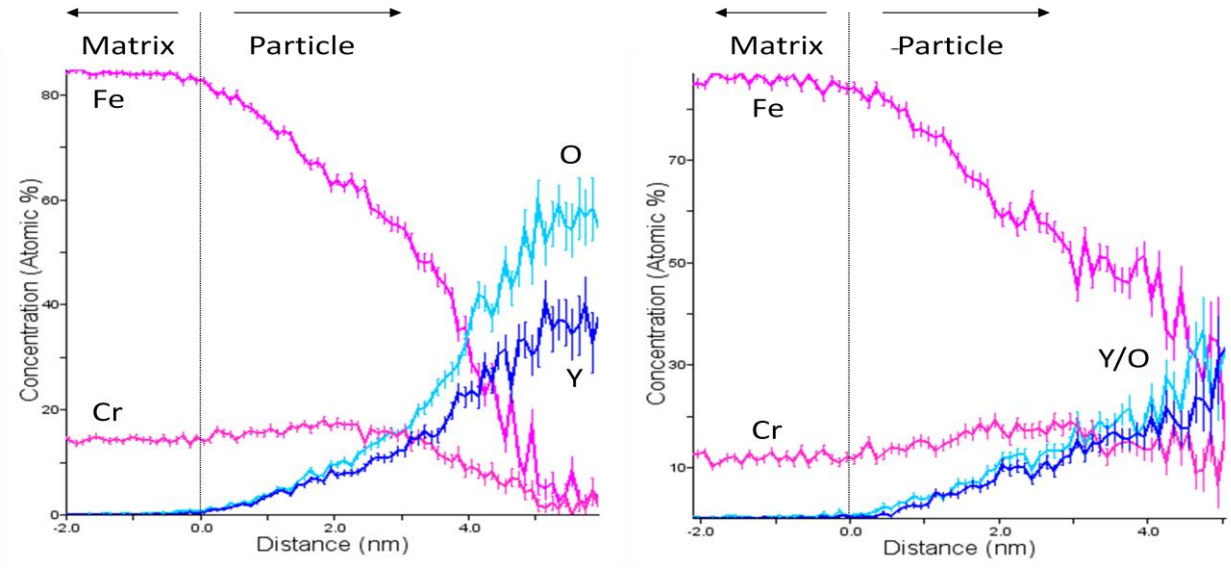


**Figure 6.7 - Proxigram of nanoclusters in EPFL-PA-FE2Y material after annealing at 1200C for 100 hours (i) Y:O of 2:3 (ii) more typical Y:O 1:1**

It is not possible to conclude that these clusters were only present after annealing for 100 hours, as so few were recorded but these clusters all have $R_g$ values of ~5nm. This is above the average $R_g$ of annealed material (4.6 ± 0.4nm after 100hrs annealing) and much larger than the average $R_g$ for the 'as-received' material (3.8 ± 0.2nm).

It appears likely that these Y-O clusters transform from one phase to another during the annealing, but it is not clear where the extra oxygen originates from. There is no change in the amount of oxygen measured in the matrix after annealing, but very little extra oxygen would be required for this transformation. The clusters with Y:O of 2:3 do not appear to lie along any obvious grain boundary, and the composition of the smaller clusters in the same volume of analysis appear to have much the same O content after annealing as those in the 'as-received' condition.

Effect of annealing on the Cr shell

The Cr shell appears to form a sharper peak at the interface of the Y-O nanoclusters after annealing for 100 hours. There are a number of possibilities as to why this may occur, and the explanation depends on how the Cr shell is interpreted prior to annealing.

If the shell is seen to be there purely as segregation of Cr to the nanocluster-matrix interface, then the change in Cr profile can be explained by the fact that the clusters analysed after annealing are on average ~1nm larger in radius. This will in turn influence the nature of the trajectory aberrations, and could account for the difference in Cr profile. It is also plausible that during annealing there is some increase in the amount of Cr segregated to the interface from the matrix. If the shell is assumed to be part of the oxide phase, another explanation may stem from the fact that Cr has a lower affinity for O than Y (see Table 8.1). During annealing Cr may be ejected from the growing oxide phase to create a more thermodynamically stable oxide. This will be discussed further in §8.4.1.

### 6.3.2 EPFL-PA-$Y_2O_3$ material

#### *6.3.2.1 Effect on nanocluster distribution*

Despite differences in the initial dispersion of nanoclusters, the behaviour of the EPFL-PA-$Y_2O_3$ material after annealing is very similar to the EPFL-PA-$FE_2Y$ material. The difference between the nanocluster distributions in the 'as-received' material is compared with that after annealing for 100 hours in Figure 6.8. The radii of the nanoclusters increase on annealing as shown in Figure 6.9.

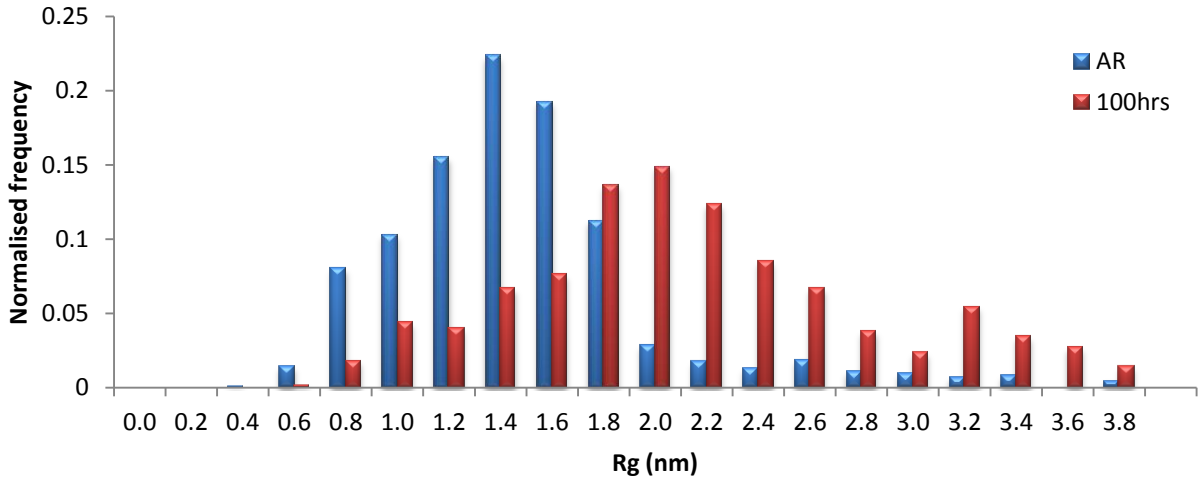


**Figure 6.8 - Cluster size distribution for 'as-received' EPFL-PA-$Y_2O_3$ (blue) and after annealing at 1200°C for 100 hours (red)**

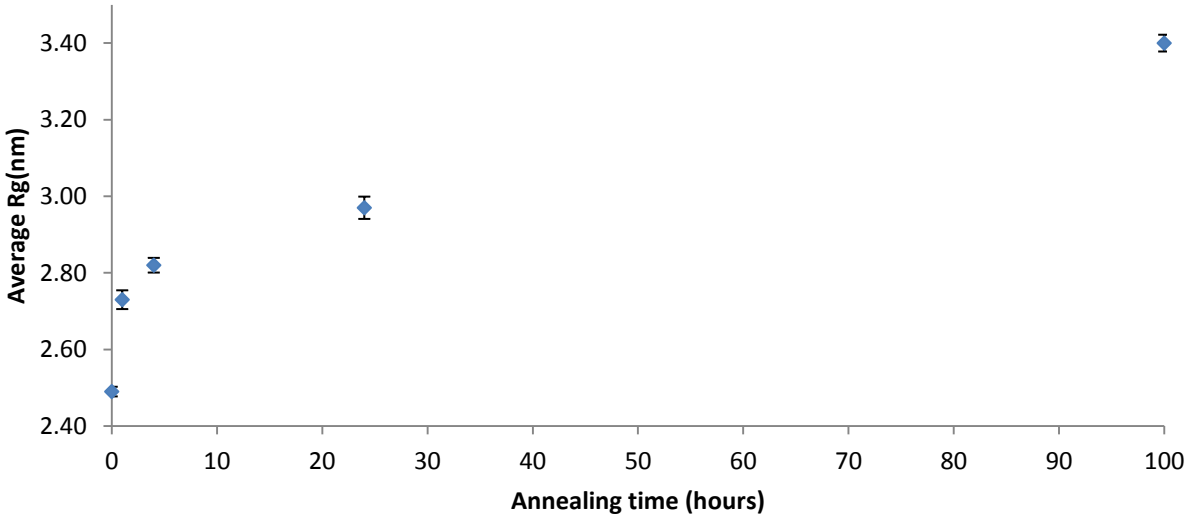


**Figure 6.9 - Change in average particle radius (Rg) with annealing time**

### *6.3.2.2 Effect on nanocluster composition*

There is no obvious difference in nanocluster composition after annealing. Figure 6.10 shows that there is considerable scatter in the measured composition between clusters in the same volume of analysis. The average composition across all particles remains unchanged, as shown in Table 6.2, but there is a significant minimum in Cr content after 24 hours annealing (with corresponding increases in other elements due to a 'mass-balance' effect). This apparently anomalous result was found reproducibly in 5 repeated experiments, with over 500 nanoclusters analysed in each experiment. The matrix concentration of Cr in these experiments is also reduced by ~0.5%. One explanation for this could be that the vacuum seal during annealing was inadequate, and Cr was lost due to oxidation. Unfortunately there was not sufficient material to repeat the experiment. Interestingly the $R_g$ of nanoclusters in this set of experiments is also less than expected (see Figure 6.11).

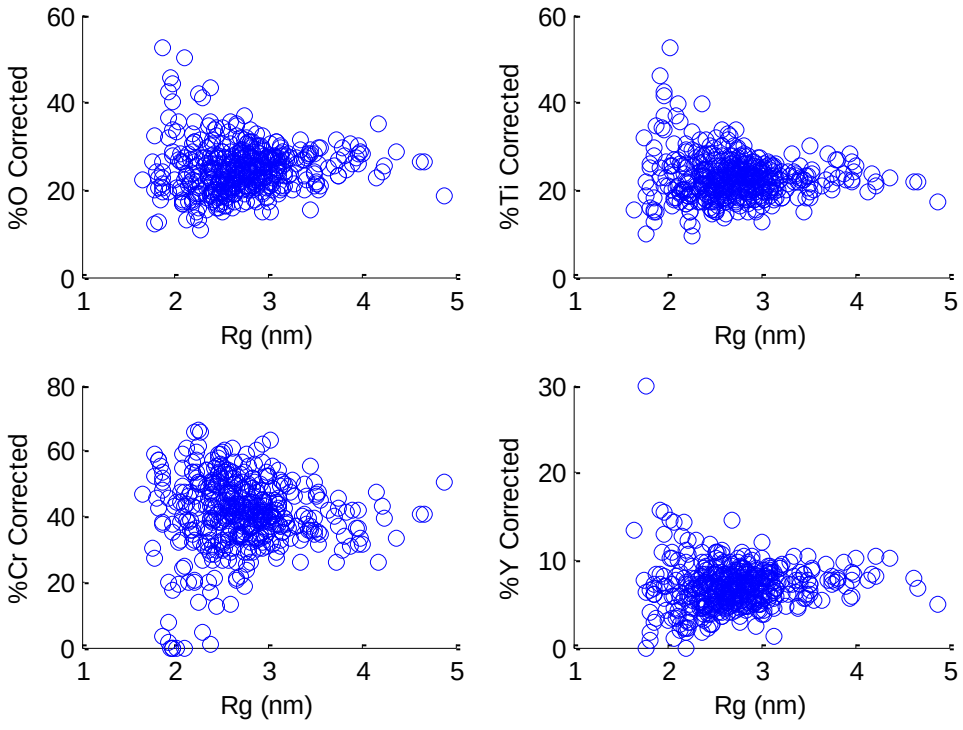


**Figure 6.10 - Scatter plot of per cluster compositions after annealing for 100hours**

| Annealing time (hours) | O | | | Ti | | | Cr | | | Y | | |
|---|---|---|---|---|---|---|---|---|---|---|---|---|
| **AR** | 25.01 | ± | 0.2 | 22.33 | ± | 0.19 | 42.75 | ± | 0.42 | 5.61 | ± | 0.09 |
| **1** | 25.28 | ± | 0.26 | 21.97 | ± | 0.23 | 40.45 | ± | 0.52 | 7.38 | ± | 0.12 |
| **4** | 25.21 | ± | 0.14 | 21.9 | ± | 0.13 | 40.9 | ± | 0.29 | 6.86 | ± | 0.06 |
| **24** | 30.63 | ± | 0.26 | 26.16 | ± | 0.24 | 29.95 | ± | 0.53 | 9.11 | ± | 0.15 |
| **100** | 24.72 | ± | 0.17 | 17.09 | ± | 0.12 | 44.38 | ± | 0.3 | 8.19 | ± | 0.09 |

**Table 6.2 - Average composition values for different annealing treatments in EPFL-PA-$Y_2O_3$**

### 6.3.3 Influence of Ti on particle stability

Particle coarsening is expected to follow an $r^3 \alpha t$ relationship according to the classical Lifshitz Slyozov and Wagner (LSW) theory of coarsening for a dilute binary system, and Ma has expanded the original LSW equation to accommodate the coarsening of compound precipitates in binary systems [193]. Figure 6.11 shows a clear linear relationship between the particle radius and $(\text{annealing time})^{1/3}$, consistent with classical coarsening behaviour. There does not appear to be any significant difference in coarsening rate between the two particle types, contrary to the findings of Ratti et. al. [72], when annealing was carried out for 1 hour at 1100°C. The annealing time of 1 hour used by Ratti et. al. is considerably shorter than the maximum of 100 hours used in this study, and the temperature was also 100°C lower, but a higher temperature and longer annealing time would be expected to heighten any differences in coarsening rates. It should be also be noted that the difference in Ti content between the two alloys studied by Ratti et. al. is much greater (0 and 0.8% Ti compared with 0.1% and 0.3% in this study), and the SANS technique may include the coarsening of larger oxides not seen in the volume of analysis of the atom probe.

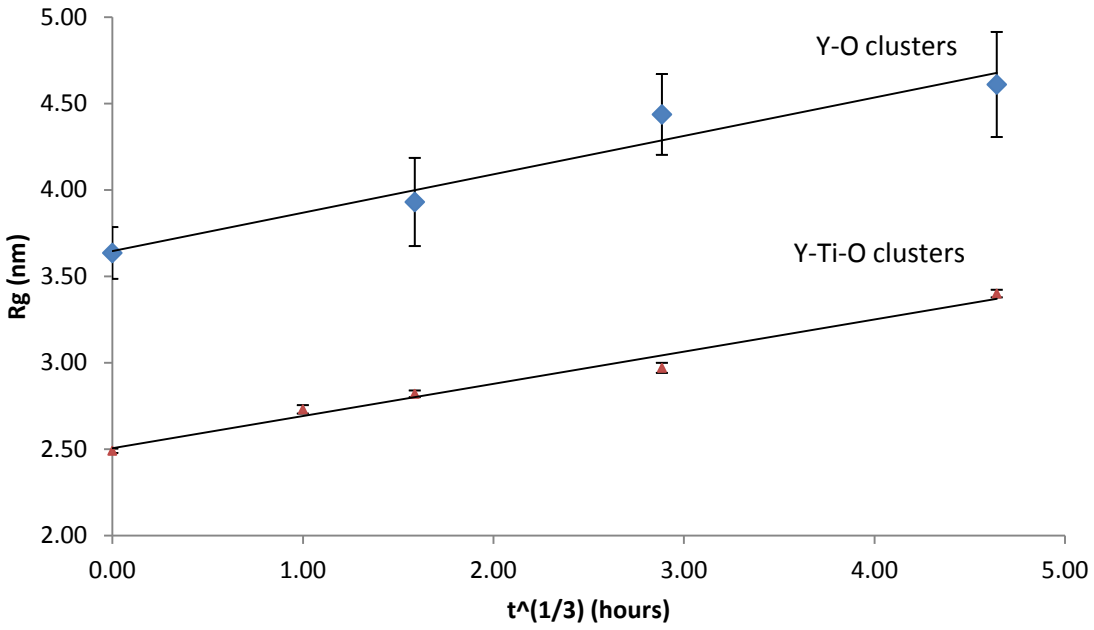


**Figure 6.11 - Nanocluster radius vs. $t^{1/3}$ for the EPFL-PA-$FE_2Y$ (blue) and EPFL-PA-$Y_2O_3$ materials (red). The time exponent of coarsening is equal (within error).**

Classical coarsening assumes a diffusion controlled mechanism. The comparable rates seen in Figure 6.11 suggests that the same solute species control the coarsening in both alloys, as all other experimental conditions were kept constant. The effective diffusion coefficient controlling the coarsening in this case will be that of the slowest diffusing species. Table 6.2 shows that the diffusion coefficient of Y in bcc-Fe at 1200°C is four orders of magnitude lower than that of the next fastest diffusing cluster element (Cr). Y is likely to be the controlling element in this case.

| Element | Diffusion Coefficient ($m^2s^{-1}$) |
|---|---|
| **O** | $8.9 \times 10^{-13}$ |
| **Ti** | $2.5 \times 10^{-15}$ |
| **Cr** | $7.5 \times 10^{-16}$ |
| **Y** | $6.3 \times 10^{-20}$ |

**Table 6.3 - Diffusion coefficients for cluster forming species in bcc-Fe at 1200°C [113](Ti) and[80]**

### *6.3.3.1 Effect of the Cr shell on nanocluster coarsening*

The similarities between the coarsening rates of the different types of nanocluster indicate that the Cr shell does not affect the coarsening of the nanoclusters. The consistency of the Cr content in the nanoclusters indicates no change in Cr distribution after annealing in the EPFL-PA-$Y_2O_3$ material,

whereas a sharper interface was observed in the EPFL-PA-$FE_2Y$ material. The independence of coarsening rate on equilibrium segregation of Cr at the particle-matrix interface also indicates that the Cr is not the rate controlling factor for the coarsening of the nanoclusters.

## 6.4 Annealing at operating temperatures - 700°C

The blanket structures in a fusion reactor are expected to operate at temperatures in excess of 500°C. The hotter the structure is able to operate at, the more efficient the reactor is, therefore there is a drive to create materials suitable for operation at >600°C. Our collaborators at EPFL chose to anneal the EPFL-PA-$Y_2O_3$ material in air, just above the required operating temperature for up to 10,000 hours. An example of the nanocluster dispersion, before and after annealing is shown in Figure 6.12.

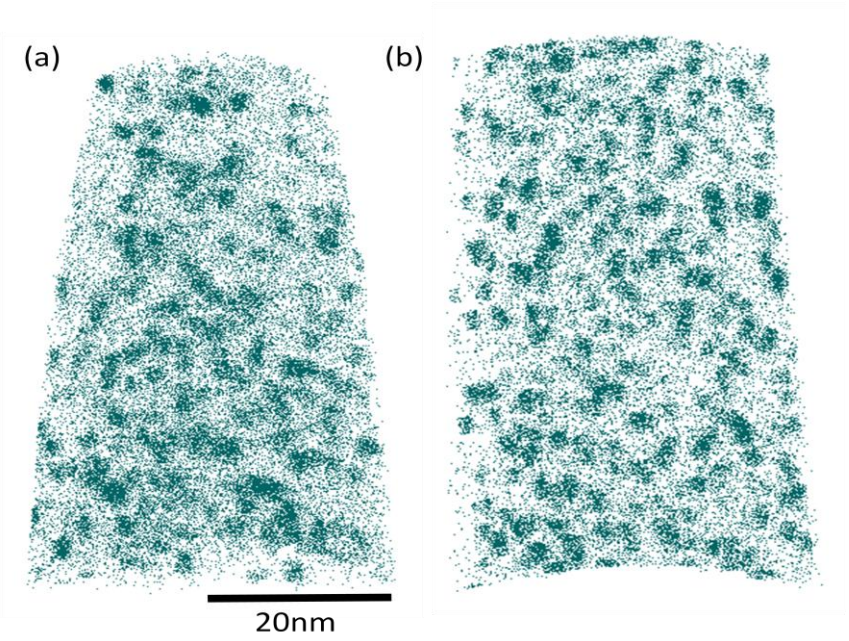


**Figure 6.12 – (a) Comparison of clusters in 'as-received' EPFL-PA-$Y_2O_3$ material, and (b) clusters after annealing at 700°C for 10,000 hours.**

There is no observable change in the nanocluster distribution after annealing, as shown in Table 6.4. This is expected, as at 700°C, the diffusion coefficient of Y is reduced to near zero. This is a good indication that the material will perform well in service.

| Annealing time (hrs) | 'As-received' | 2500 | 5000 | 10,000 |
|---|---|---|---|---|
| Average Rg (nm) | 2.49 ± 0.2 | 2.68 ± 0.2 | 2.77 ± 0.2 | 2.61 ± 0.2 |

**Table 6.4 - Average Rg values for EPFL-PA-$Y_2O_3$ after annealing at 700°C (Minimum of 1500 nanoclusters analysed in each condition)**

## 6.5 Summary

The oxide nanoclusters are observed to coarsen classically at 1200°C. The coarsening rate is not affected when the clusters contain Ti. It can be concluded therefore that Ti does not inhibit coarsening of the nanoclusters at this temperature. Ti certainly plays a role in refining the nanocluster population but, as the number densities of the clusters are much higher in the EPFL-$Y_2O_3$ material. As the coarsening rates are the same, we can therefore conclude that Ti must play a role in the nucleation process. This will now be investigated in more detail.

The core-shell structure seen in the EPFL-PA-$FE_2Y$ material was observed to become more sharply defined on annealing, whereas no such effect was seen in the EPFL-PA-$Y_2O_3$ material. This implies that the interfaces of the two types of nanocluster may be different, and that the chemistry of the interface is not the rate determining step for the coarsening.

# 7 Development of ODS microstructure during processing

*This chapter investigates the formation of the nanoclusters and grain boundary oxides during processing. This involves:*

*Characterisation of EPFL-E-$Y_2O_3$ alloy at all stages of processing*

*Investigating the influence of MA with $Fe_2Y$*

## 7.1 Introduction

Understanding the formation and development of the oxide particles in ODS steels is one of the main aims of this research. In this chapter, the mechanisms of formation of the oxide nanoclusters are investigated to try to elucidate how the Y-O and Y-Ti-O nanoclusters (introduced in the previous chapters) form. For the material mechanically alloyed with $Y_2O_3$, the oxide particle development was investigated by characterising the nanoclusters and larger oxide particles at the following stages during the processing route:

1. Powder, immediately after MA
2. Powder, after a short anneal at 800°C (10 minutes)
3. Powder, after degassing (annealing at 800°C for 2 hours)
4. After degassing and consolidation by HIP at 1150°C for 4 hours
5. After degassing, consolidation and further annealing for 100 hours at 1150°C

The material mechanically alloyed with $Fe_2Y$ was characterised in a similar manner after the following stages:

1. Powder, immediately after MA
2. After degassing and consolidation by HIP at 1150°C for 4 hours

The base alloy composition was not available as a pre-alloyed powder for this study, therefore the material was processed by our collaborators at EPFL by mixing elemental powders to the same composition (Fe-14Cr-2W-0.3Ti). Details of the processing are outlined in Chapter 3. These materials are referred to as EPFL-E-$Y_2O_3$ and EPFL-E-$FE_2Y$ for clarity.

## 7.2 Evolution of microstructure after mechanical alloying with $Y_2O_3$

### 7.2.1 Overall microstructure

Figure 7.1 shows the microstructural evolution in the powder after MA, in the powder after degassing, and in the consolidated material. The SEM image of a sectioned powder flake (Figure 7.1a) after MA shows some porosity and small pieces of powder loosely fused together. TEM of the MA powder reveals a nanocrystalline structure, with the average distance between grain or sub-boundaries <20nm.

The nano-grained structure seen in a section of powder flake immediately after MA remains present in over 90% of the powder volume after degassing. A number of recrystallised grains is also observed in areas near the edge of the powder flakes after degassing. A dispersion of small oxide nanoclusters is observed within these grains, together with a small fraction of larger oxide particles 10-50nm in diameter. The consolidated material is fully recrystallised, and also shows a bimodal distribution of oxide nanoclusters. There is no significant change in the microstructure after annealing for 100hrs at 1150°C.

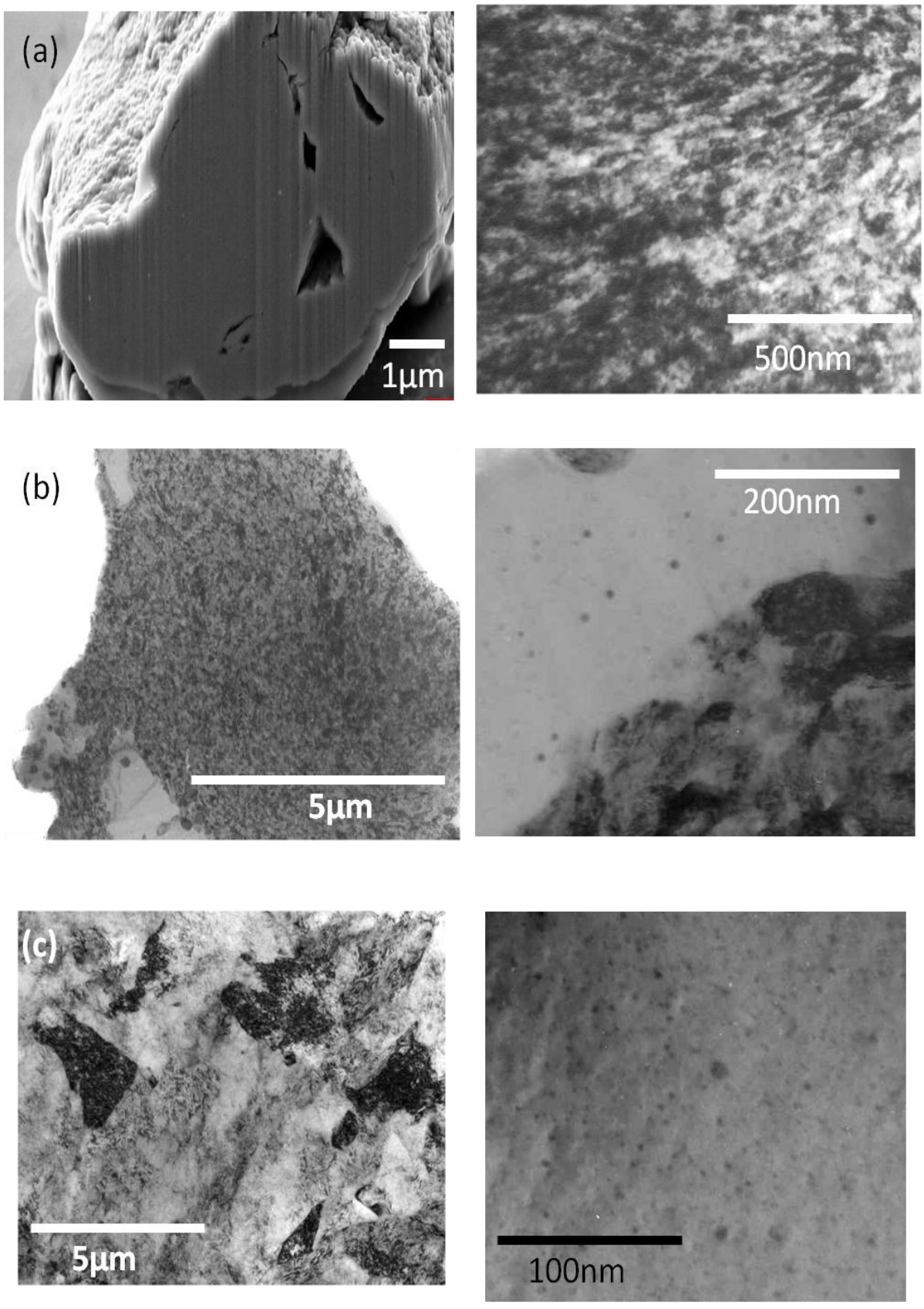


**Figure 7.1 - SEM and TEM observations of the microstructure of the EPFL-E-$Y_2O_3$ ODS steel after the three main stages of processing: (a) powder after MA (b) powder after degassing (c) consolidated material**

The overall composition as measured by APT for each condition is given in Table 7.1 in atomic percent, along with the nominal composition for the alloy. Bulk composition measurements are calculated by counting the total number of each element in a complete APT analysis (typically 20-50 million ions), and the values are averaged over multiple datasets. The matrix compositions quoted in Table 7.1 are calculated in a similar manner, but atoms defined as part of a cluster by the maximum separation algorithm are not included. The composition of the consolidated material was independently verified by electron microprobe analysis, which is also shown in Table 7.1.

As expected, the measured compositions are very similar in each case. After MA, the level of O is much higher than in subsequent stages of processing. A likely cause is a higher level of dissolved O in the matrix at this stage of the processing. As will be discussed in §8.6, this excess oxygen is believed to migrate to grain boundaries. The bulk composition measurements taken from the powder flakes are less consistent in terms of solute content than in the consolidated material - which is reflected in the larger errors on the Cr levels in particular. This is assumed to be due to slight variations in the composition of each powder flake following the MA process.

| | Nominal Comp | Powder after MA | | | | Powder after 800°C 2hr anneal | | | | Consolidated material | | | | Consolidated material |
|---|---|---|---|---|---|---|---|---|---|---|---|---|---|---|
| | Bulk | Bulk | σ | Matrix | σ | Bulk | σ | Matrix | σ | Bulk | σ | Matrix | σ | EPMA |
| **Fe** | 83.61 | **84.1** | 0.7 | **84.3** | 0.6 | **84.8** | 0.7 | **86.2** | 0.7 | **85.3** | 0.3 | **86.0** | 0.2 | 84.3 ± 0.2 |
| **Cr** | 15.07 | **13.9** | 0.6 | **13.8** | 0.6 | **13.3** | 0.5 | **12.6** | 0.6 | **13.0** | 0.2 | **12.7** | 0.2 | 14.7 ± 0.2 |
| **W** | 0.61 | **0.4** | 0.1 | **0.4** | 0.1 | **0.6** | 0.0 | **0.6** | 0.0 | **0.4** | 0.0 | **0.4** | 0.0 | 0.4 ± 0.02 |
| **Y** | 0.15 | **0.2** | 0.0 | **0.1** | 0.0 | **0.1** | 0.0 | **0.1** | 0.0 | **0.1** | 0.0 | **0.1** | 0.0 | 0.1 ± 0.01 |
| **Ti** | 0.35 | **0.4** | 0.0 | **0.3** | 0.0 | **0.3** | 0.1 | **0.1** | 0.0 | **0.2** | 0.0 | **0.1** | 0.0 | 0.4 ± 0.02 |
| **O** | 0.21 | **0.8** | 0.1 | **0.7** | 0.1 | **0.7** | 0.1 | **0.3** | 0.0 | **0.3** | 0.0 | **0.2** | 0.0 | - |
| **C** | - | **0.1** | 0.0 | **0.1** | 0.0 | **0.0** | 0.0 | **0.0** | 0.0 | **0.1** | 0.0 | **0.1** | 0.0 | - |
| **N** | - | **0.2** | 0.1 | **0.2** | 0.1 | **0.1** | 0.0 | **0.1** | 0.0 | **0.4** | 0.0 | **0.4** | 0.1 | - |

**Table 7.1 –Nominal composition, composition of bulk EPFL-E-$Y_2O_3$ material from each condition measured by APT, and composition of consolidated material measured by EPMA (all in at. %)**

A series of atom maps from a representative APT 3-D reconstruction of the powder after degassing is shown in Figure 7.2. This figure highlights the local variations in chemical composition that correspond to the grain boundaries and the oxide particle distribution. The grain structure is revealed by the segregation of W (see Section 7.2.3). Ti, Y and O ions indicate the location of the oxide particles. In this particular case, nanoclusters rich in Ti-Y-O are visible within grains, and larger Ti-rich oxide particles are located at grain boundaries.

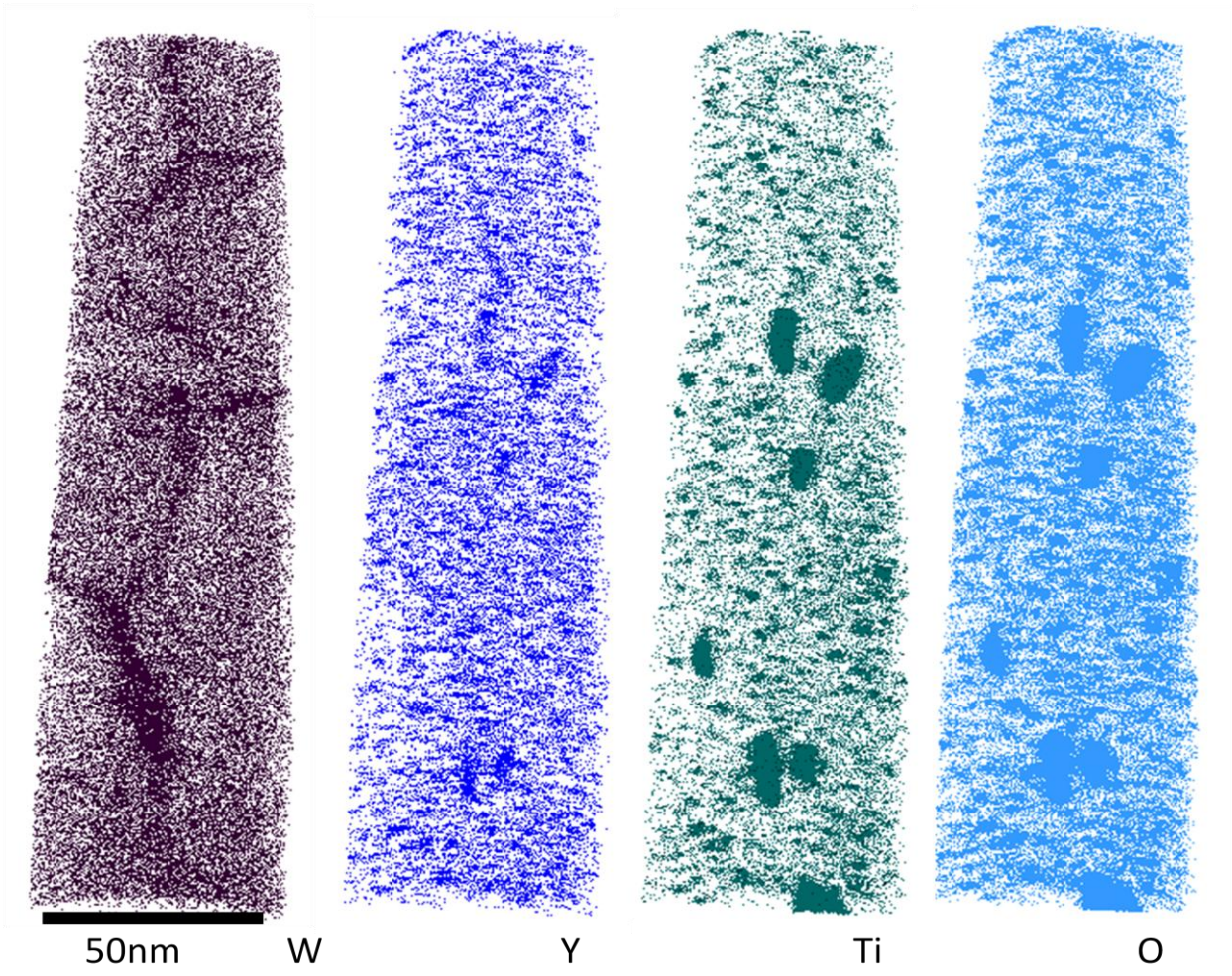


**Figure 7.2 – Atom maps from APT 3-D reconstruction highlighting (a) W ions (b) Y ions (c) Ti ions and (d) O ions. This example is taken from the powder (that forms the basis of the EPFL-E-$Y_2O_3$ material) after degassing at 800°C for 2 hours. The W highlights the grain boundaries, which are decorated with Ti rich oxides. Y-Ti-O nanoclusters are visible within grains.**

### 7.2.2 Oxide nanocluster development

Figure 7.1 shows the microstructure to be inhomogeneous. To investigate the nanocluster development only regions of uniform nanocluster distribution within grains were analysed. Due to the wide field of view attainable with the local electrode atom probe, it was possible to analyse multiple volumes containing 500+ clusters for each processing condition. The atom maps for Ti-O and Y ions shown in Figure 7.3 highlight the evolution of the nanoclusters during processing. The clusters are analysed using the adaptable cluster selection parameters (as described in Chapter 4).

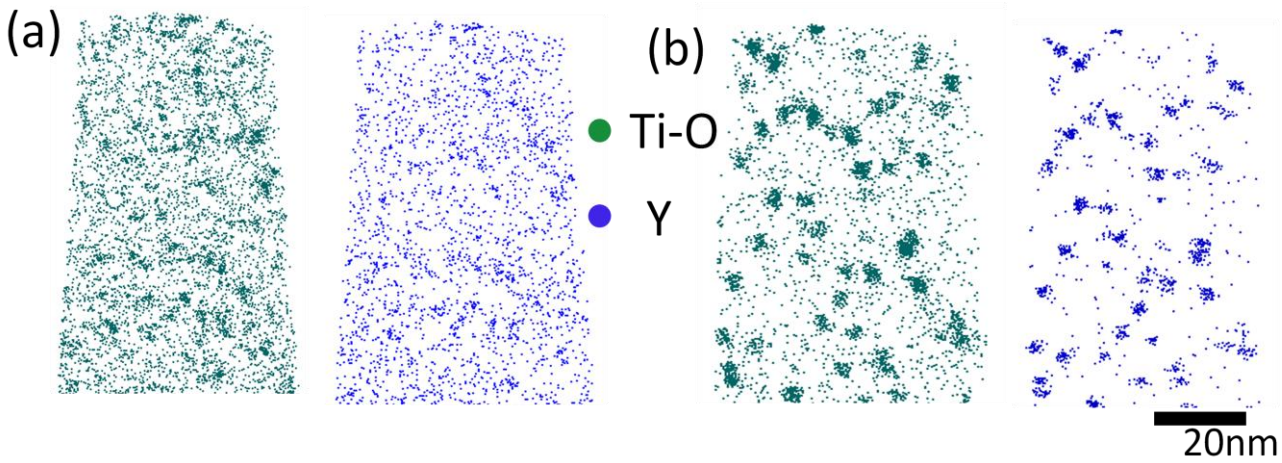


**Figure 7.3 – Atom maps showing the distribution of Ti-O ions and Y ions for (a) powder after MA (b) Consolidated material. The 3-D reconstruction is taken from a 10nm thick slice of the data for clarity.**

Figure 7.4 shows that substantial changes occur in the distribution of the nanoclusters as the alloy is processed. The number density of clusters in the MA powder is initially very high, but decreases slightly after annealing the powder for 10 minutes at 800°C. As the annealing process is continued, the number density of clusters falls, and after consolidation the number density reduces even further. The volume fraction occupied by the nanoclusters would be expected to increase during processing, as a decrease in Ti and O in the matrix is evident from Table 1. This trend is observed for the shortest annealing time, but for all subsequent stages of processing, Figure 7.4(b) shows a continuous decrease in volume fraction. This is most likely to be due to the formation of larger oxides at grain boundaries during the latter stages of processing. This is a strong indication that the grain boundary oxide formation takes precedence over the formation of the nanoclusters.

Figure 7.5 shows that the proportion of larger clusters increases during processing. However, it is not until after consolidation that the median size of the clusters increases significantly. It is clear that when the number density of nanoclusters is much higher, the average size of nanoclusters in the powder is smaller.

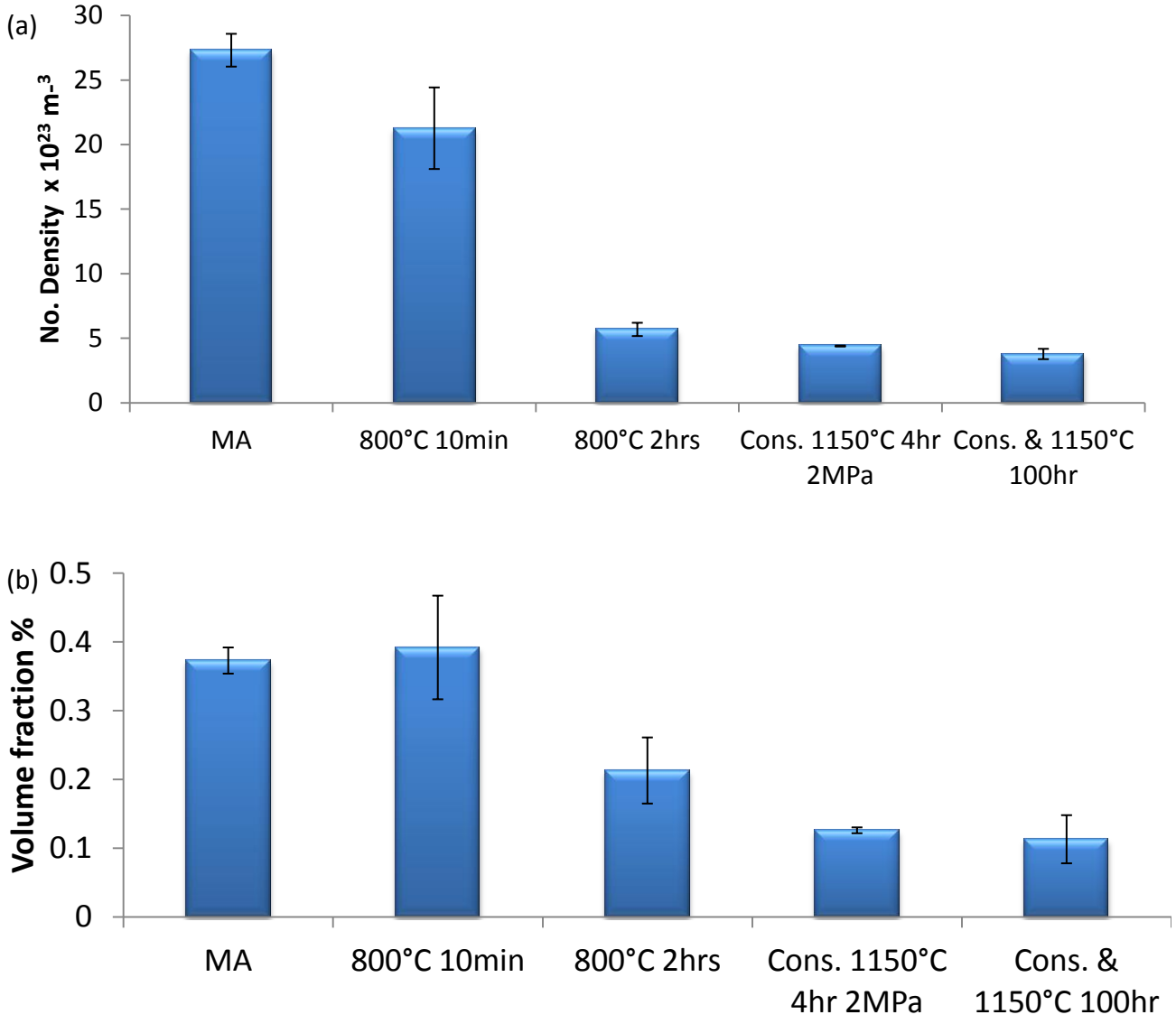


**Figure 7.4 – After each stage in the processing this figure shows (a) Average number density of nanoclusters (b) Volume fraction occupied by the nanoclusters**

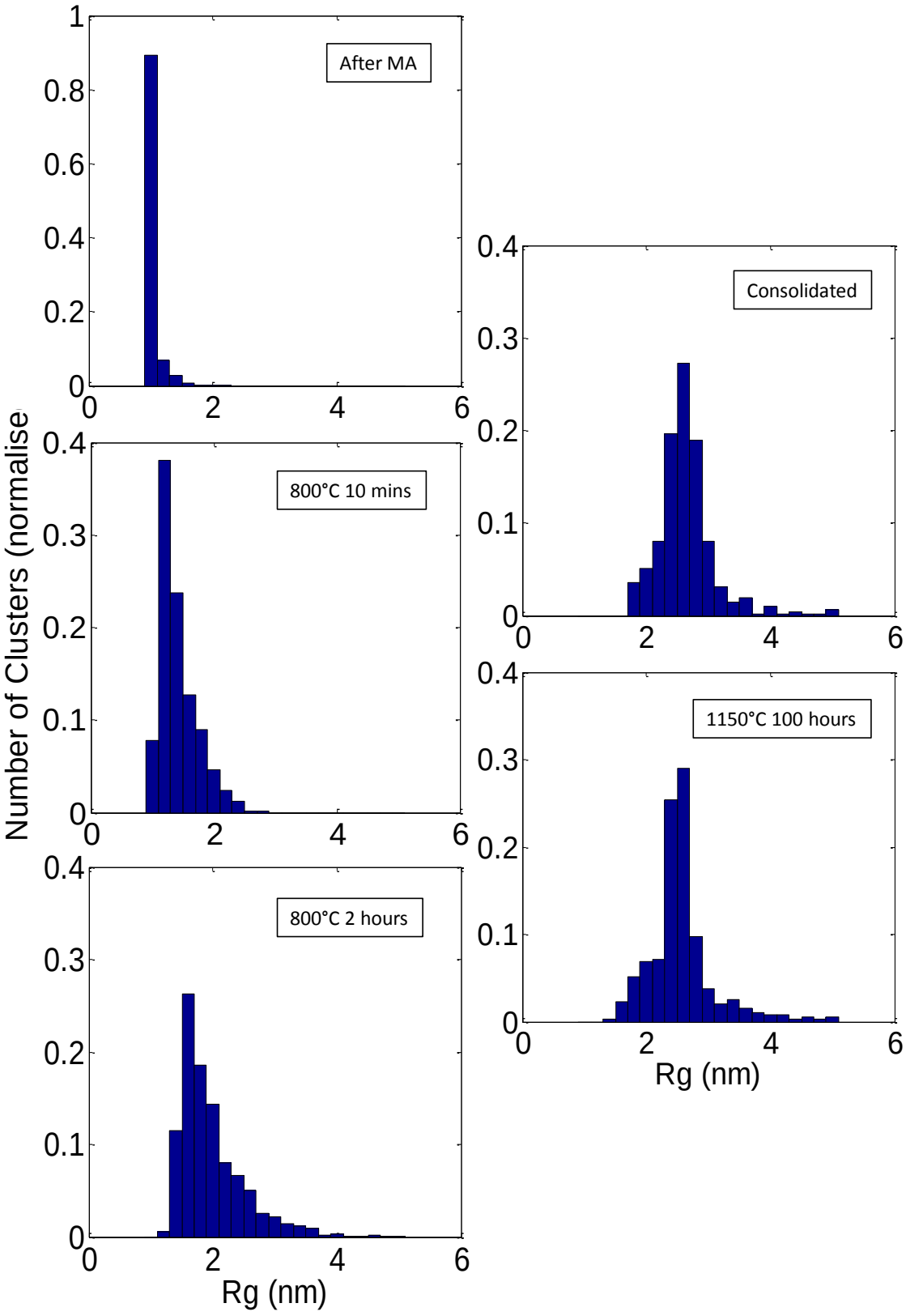


**Figure 7.5 - Size distribution of nanoclusters measured after cluster selection using the maximum separation method, normalised (includes 1500+ clusters for each condition).**

Table 7.2 shows that the clusters in each condition all contain Y, Ti, O and a large proportion of Cr even after the matrix contribution has been removed. Significantly more oxygen is observed in the clusters immediately after MA. There is however greater consistency between the nanocluster compositions in the annealed powders and the consolidated materials. The proportion of Y in the nanoclusters increases by a factor of two after consolidation. This is likely to related to the slower rate of diffusion of Y at 800°C, as will be discussed in § 8.5.1.

| Element | After MA | 800°C 10mins | Degassed 800°C 2hrs | Consolidated 1150°C 4hrs 2MPa | Annealed 1150°C 100hrs |
|---|---|---|---|---|---|
| **Fe** | - | - | - | - | - |
| **Cr** | 45.22±7.38 | 43.22±3.13 | 51.77±3.37 | 47.80±0.21 | 52.44±0.64 |
| **Ti** | 16.03±2.18 | 20.46±0.85 | 15.73±1.70 | 12.75±0.55 | 11.92±0.31 |
| **Y** | 4.46±0.69 | 4.10±0.38 | 4.82±0.22 | 7.30±0.85 | 8.04±0.2 |
| **O** | 31.82±4.41 | 28.62±2.28 | 23.37±2.08 | 25.55±0.79 | 23.96±0.35 |
| **W** | 0.94±0.19 | 1.35±0.07 | 1.75±0.26 | 0.49±0.04 | 0.23±0.11 |
| **C** | 0.56±0.03 | 0.46±0.14 | 0.41±0.01 | 0.52±0.19 | 0.59±0.03 |
| **N** | 0.81±0.08 | 1.48±0.06 | 1.80±0.11 | 5.35±0.98 | 2.09±0.11 |

**Table 7.2 – 'Corrected' cluster compositions for matrix nanoclusters at each stage of processing of the EPFL-E-$Y_2O_3$ material**

### 7.2.3 Grain boundary analysis (including grain boundary oxides)

Grain boundaries are only readily observed in APT data if they exhibit solute segregation. Despite analysing more than 10 specimens, no solute segregation indicating the presence of grain boundaries was observed in the powder directly after MA. In all the subsequent stages of processing (the annealed powders and the consolidated materials), grain boundaries were observed in >50% of specimens. The W segregation is clearly observable in Figure 7.2(b), and the grain boundary profiles shown in Figure 7.6 also show enrichment of Cr and C.

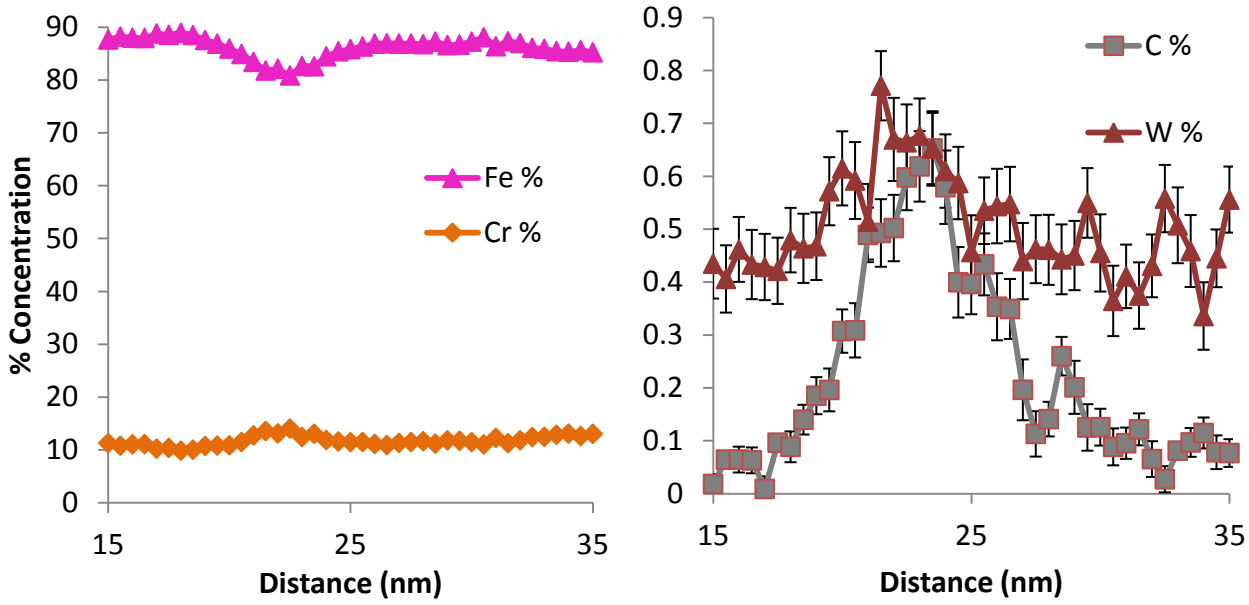


**Figure 7.6 - Grain boundary profiles showing Cr, W and C enrichment in the consolidated EPFL-E-$Y_2O_3$ material**

The larger >5nm oxide particles were observed at grain boundaries in all the annealed powders and consolidated material but in the powder directly after MA, no clusters larger than 2nm diameter were observed either by TEM or APT (except for W inclusions ~50nm in diameter, believed to be present due to incomplete mixing of elemental powders). Due to the complex nanocrystalline structure and high dislocation density seen in the MA powder in Figure 7.1, identifying the particles in the TEM is difficult. This lack of observations suggests that solute segregation to grain boundaries and the formation of larger oxides largely occurs after the MA stage.

Particles >5nm in diameter were also observed occasionally within grains in recrystallised regions. It is most likely that the >5nm particles observed within grains initially formed at grain boundaries, and that the grain boundaries moved during recrystallisation. While the compositions of the nanoclusters are comparable at each processing stage, those of the larger particles found at grain boundaries were seen to vary substantially depending on the stage of processing.

Figure 7.7 shows how the interface chemistry of particles >5nm in diameter changes during processing. After annealing at 800°C for 10 minutes, the largest observed particle size was ~15nm diameter. The measured composition at the core of these 8-15nm particles is ~35%Cr and 55%O which is consistent with a slightly oxygen deficient $Cr_2O_3$ stoichiometry. Each particle has a shell of ~2nm thickness enriched in Ti, Cr and O.

Where the powder was annealed for 2 hours at 800°C, a number of particles ~15nm in diameter were observed at grain boundaries. In these particles, the same core-shell structure is observed, but the Ti rich shell has grown to be 4-5nm wide. In the case of the consolidated material, similar Ti-Cr-O particles were observed (5-15nm diameter). For particles larger than 15nm, the core-shell structure was also observed however, the core of the particles no longer shows a $Cr_2O_3$ type stoichiometry, but instead the core is enriched with Ti and Y, to give a composition close to that of the matrix nanoclusters described in §7.2.2.

These results suggest that the initial ‘grain boundary’ oxide to form is $Cr_2O_3$, and that a Ti rich shell forms at the interface between the chromium oxide and the matrix on annealing. During consolidation, the core of the particle then transforms to a Y-Ti based oxide.

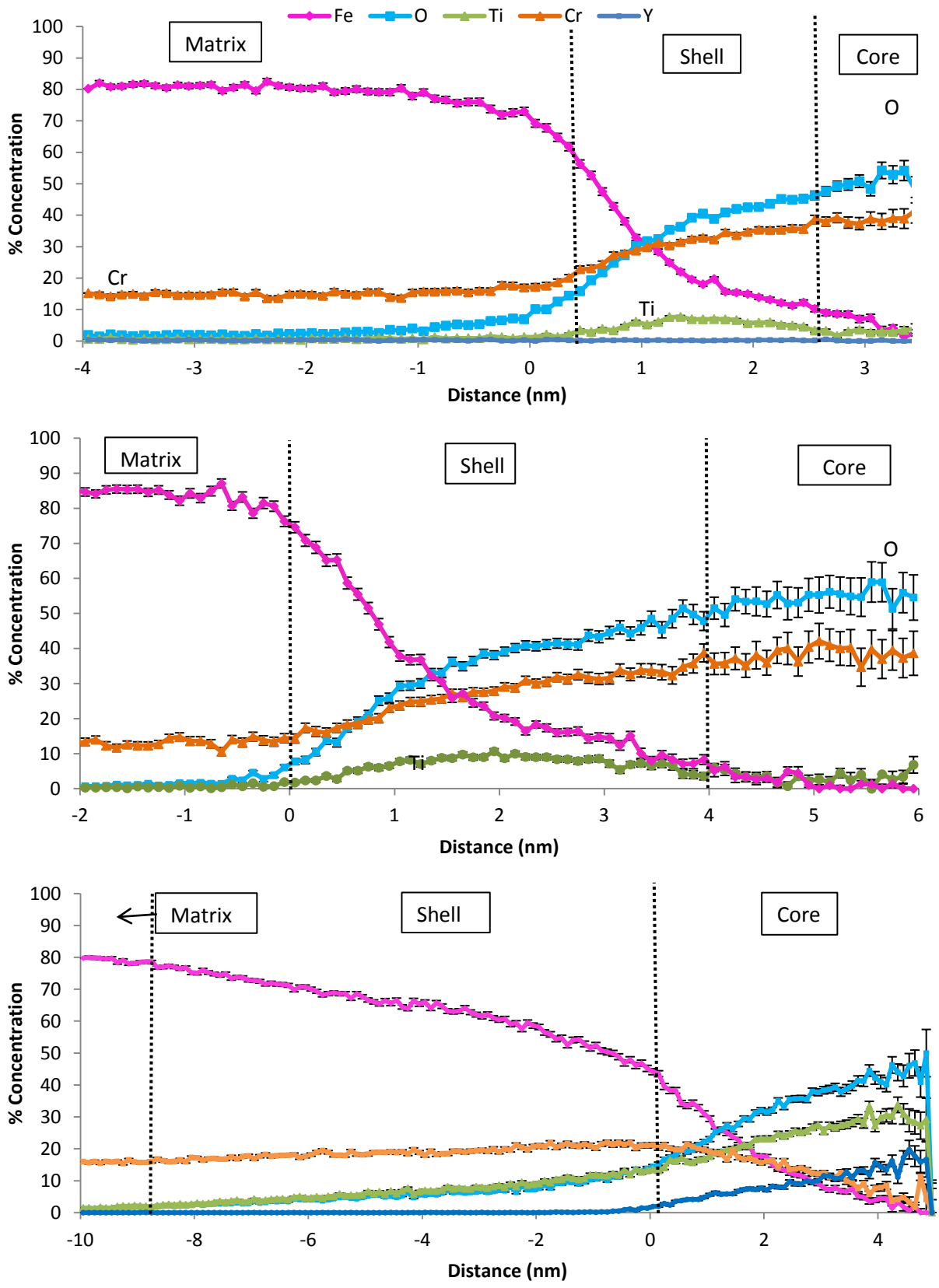


**Figure 7.7 - Proxigram based on a 1%Y-Ti isoconcentration surface of representative grain boundary oxides (a) 800°C 10 minutes (b) 800°C 2 hours (c) Consolidated material. Ti-shell thickness increases during processing.**

## 7.3 Evolution of microstructure after mechanically alloying with $Fe_2Y$

Oksiuta et. al. report that MA with $Fe_2Y$ produces a different particle dispersion compared with using $Y_2O_3$ during the MA process [116]. Chapters 5 and 6 have characterised the composition and high temperature stability of the nanoclusters in both the EPFL-PA-$Y_2O_3$ and EPFL-PA-$FE_2Y$ alloys. Somewhat surprisingly, the distribution of nanoclusters in the powder after MA with $Fe_2Y$ (initial processing stage of the EPFL-E-$FE_2Y$ alloy) showed very similar characteristics to the powder MA with $Y_2O_3$, (initial processing stage of the EPFL-PA-$Y_2O_3$ alloy).

### 7.3.1 Comparison of powder after MA with $Fe_2Y$ and $Y_2O_3$

An example of the distribution of solutes in the powder after mechanical alloying with $Fe_2Y$ is shown in Figure 7.8. There is no significant change in the average nanocluster radius, or composition and only a slight increase in number density of clusters, when compared to the powder after MA with $Y_2O_3$ as shown in Table 7.3.

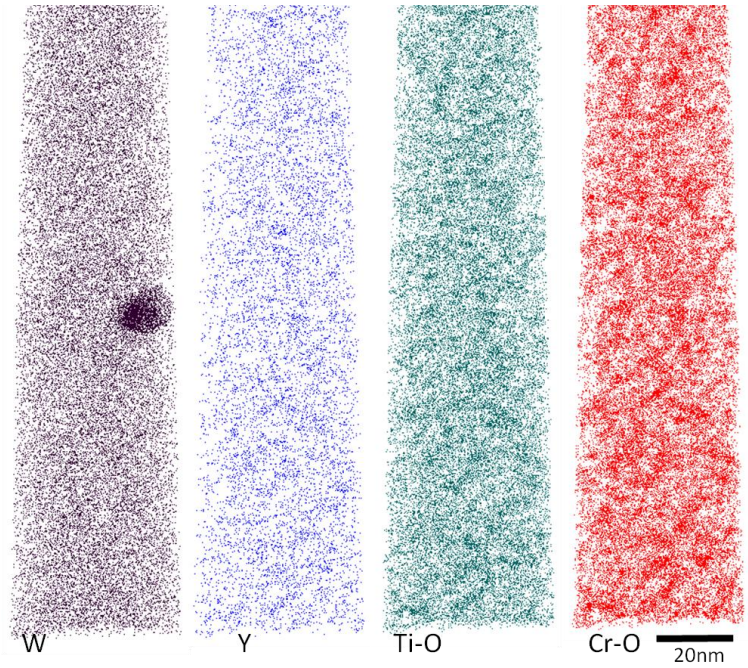


**Figure 7.8 - Distribution of solutes in powder after mechanical alloying with $Fe_2Y$. Nanoscale clustering of Y-Ti-Cr-O is visible, and also a W particle caused by incomplete milling of the elemental powders.**

| Element | Powder MA with $Y_2O_3$ (at%) | Powder MA with $Fe_2Y$ (at. %) |
|---|---|---|
| Cr | 45.2±7.4 | 39.8±1.1 |
| Ti | 16.0±2.2 | 13.5±2.0 |
| Y | 4.5±0.7 | 3.5±0.9 |
| O | 31.8±4.4 | 34.0±5.4 |
| W | 0.9±0.2 | 1.2±1.1 |
| C | 0.5±0.03 | 0.8±0.3 |
| N | 0.8±0.08 | 3.2±1.0 |
| **Number density (x $10^{24}$ m-3)** | **1.15±0.5** | **7.8±1.8** |
| **Average Rg (nm)** | **0.94±0.02** | **0.99±0.05** |

**Table 7.3 - Composition of clusters in powder after mechanical alloying (elemental powders) for both the Y2O3 and Fe2Y MA powder. Statistics of the nanocluster distribution are also shown.**

### *7.3.1.1 Grain boundary analysis*

Similarly to the EPFL-E-$Y_2O_3$ material, the observation of segregation of elements such as W,C, N and Cr was not regularly observed in the powder directly after mechanical alloying, suggesting that the majority of segregation of solutes to grain boundaries occurs after the MA stage. One observation of a grain boundary was made in the Fe2Y powder directly after MA, as shown in Figure 7.9. No segregation of W, C or N was observed but a composition profile taken across the grain boundary in Figure 7.9 shows that there is enrichment of Cr and O. This boundary is most likely to be either a high-angle boundary, or possibly a prior particle-particle boundary created during the MA process.

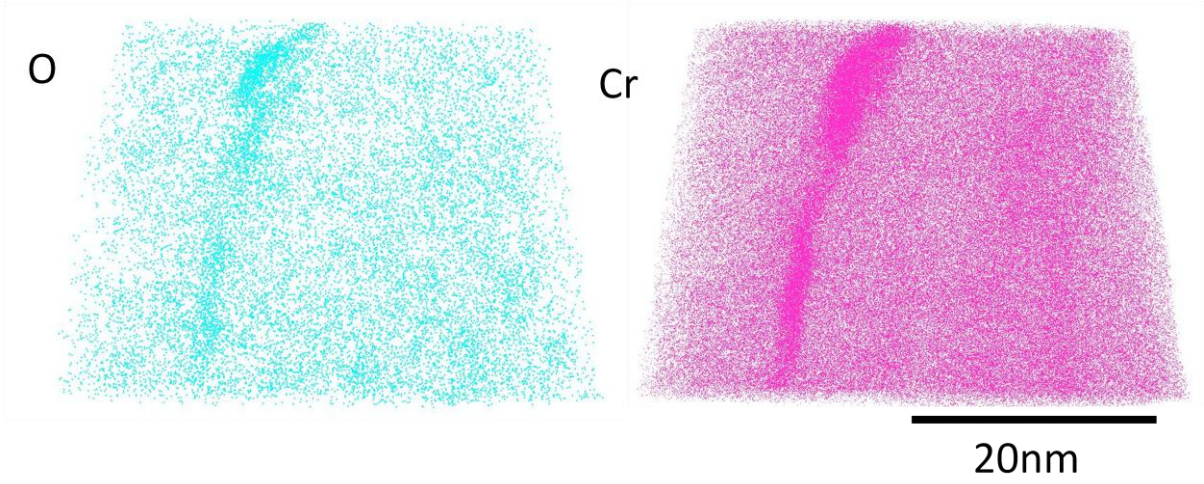


**Figure 7.9 - Cr and O segregation at a grain boundary in powder MA with $Fe_2Y$**

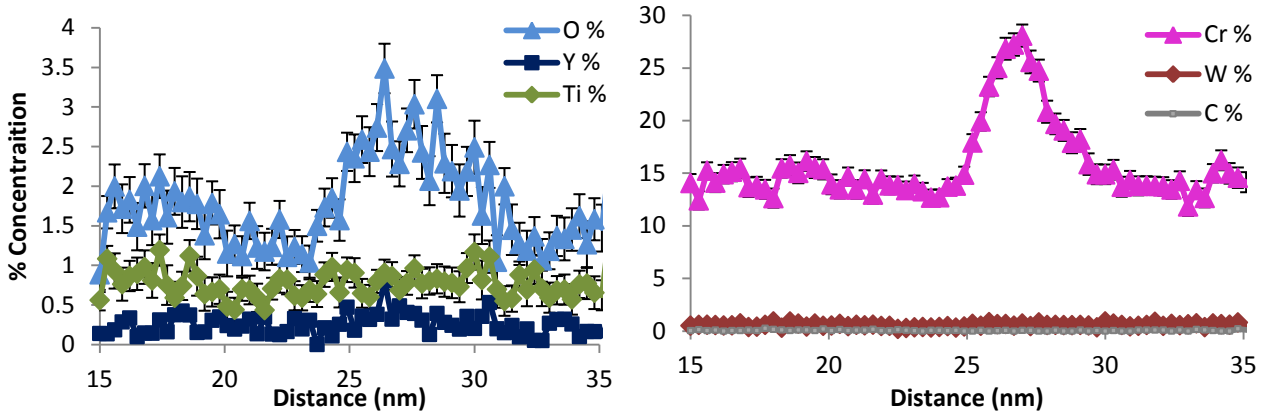


**Figure 7.10 - 1-D concentration profile across the grain boundary shown in Figure 7.9**

### 7.3.2 Consolidated material made from elemental powders MA with $Fe_2Y$

The surprising similarity between the clusters seen in both powders after MA prompted the analysis of consolidated material (EPFL-E-$FE_2Y$) made from the same batch of powder. In this case, the composition of the clusters is very different from the clusters in the material made by MA with pre-alloyed powder (EPFL-PA-$FE_2Y$ as shown in Table 7.4). In fact, the clusters now have the same composition as the material MA with $Y_2O_3$ (both the EPFL-E-$Y_2O_3$, and the EPFL-PA-$Y_2O_3$) as shown in Table 7.4, and Figure 7.11 shows that the size distribution is equivalent to that of the material MA with $Y_2O_3$. As the Y-O clusters were not observed, this is not helpful in determining the mechanisms of formation of the Y-O based clusters analysed in the previous chapter, it does provide useful information on the role of various elements in the cluster formation process. This will be discussed in greater detail in §7.3.3.

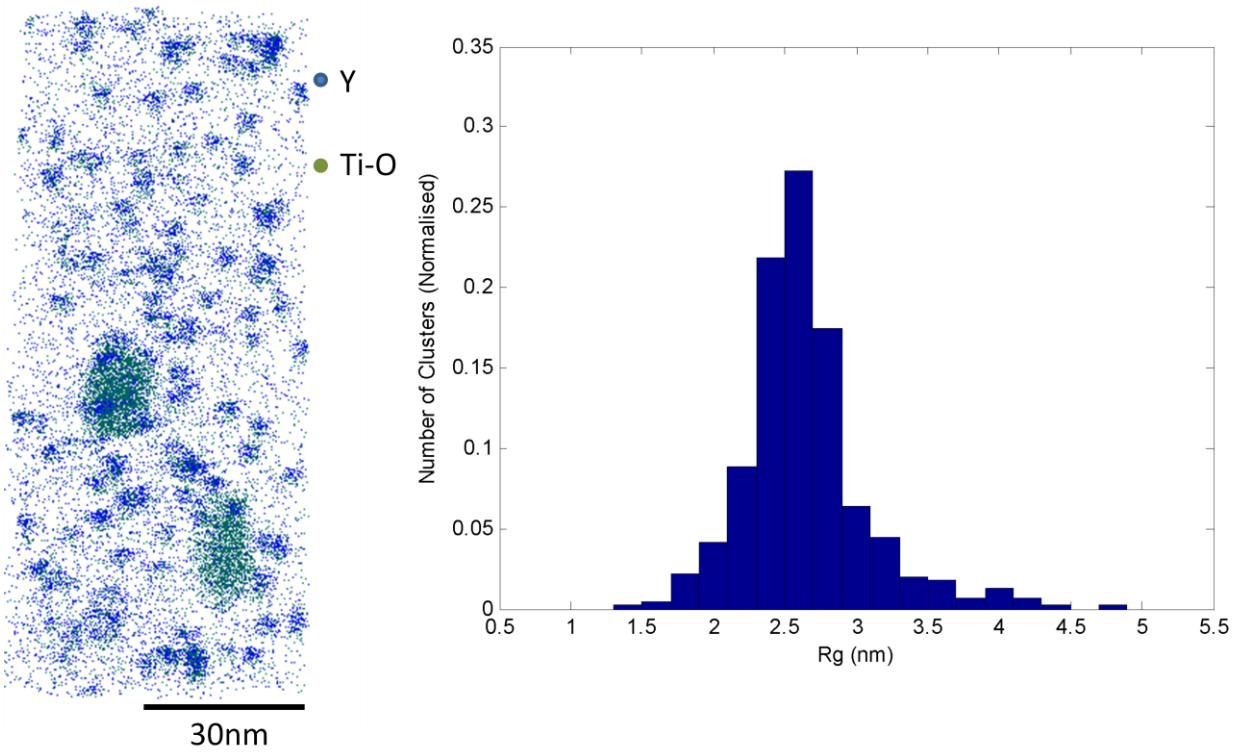


**Figure 7.11 - Nanocluster distribution in the consolidated EPFL-E-FE$_2$Y material (milled from elemental powders). The atom map shows both Y-Ti-O nanoclusters and larger Ti-based grain boundary oxides.**

| Element | EPFL-E-$Y_2O_3$ | EPFL-E-$FE_2Y$ | EPFL-PA-$FE_2Y$ |
|---|---|---|---|
| | (Materials consolidated after MA with elemental powders) | | (from pre-alloyed) |
| **Fe** | - | - | - |
| **Cr** | 47.80±0.21 | 49.5±1.5 | 31.2±1.6 |
| **Ti** | **12.75±0.55** | **12.2±0.4** | **3.12±0.4** |
| **Y** | 7.30±0.85 | 6.9±0.3 | 33.1±0.7 |
| **O** | 25.55±0.79 | 24.7±1.1 | 28.8±0.8 |
| **W** | 0.49±0.04 | 0.59±0.2 | 0.6±0.3 |
| **C** | 0.52±0.19 | 0.56±0.1 | 0.1±0.1 |
| **N** | 5.35±0.98 | 5.6±0.3 | 0.1±0.3 |

**Table 7.4 - Comparison of cluster compositions in consolidated material made from elemental powders. The composition of the clusters in the EPFL-E-$Y_2O_3$ and EPFL-E-$FE_2Y$ materials are almost identical.**

### *7.3.2.1 Comparison of EPFL-PA-$FE_2Y$ (MA with pre-alloyed powder) and EPFL- E-$FE_2Y$ (MA with elemental powder) using EPMA*

It was expected that the composition of the nanoclusters would be similar using the pre-alloyed and elemental powders, but Table 7.4 shows that the compositions are very different. A significant

difference is that the clusters in the material made from elemental powders contain appreciable levels of Ti. EPMA analysis was therefore carried out to see if the material contained similar levels of Ti over a larger volume than that seen by APT. It can be seen in Table 7.5 that there is less Ti present in the overall microstructure in the material made from pre-alloyed powder. This is in contrast to the results reported by Oksiuta et. al. who found that the Ti levels were similar in both the EPFL-PA-FE2Y AND EPFL-PA-$Y_2O_3$ materials. One possible explanation is that that as Oksiuta et. al. made the measurements before consolidation, the Ti is lost during the consolidation stage.

| Element | EPFL-E-$FE_2Y$ (MA with elemental powder) | EPFL-PA-$FE_2Y$ (MA with pre-alloyed powder) |
|---|---|---|
| **Fe** | Bal. | Bal. |
| **Cr** | 13.7±0.2 | 13.5±0.2 |
| **Ti** | **0.36±0.02** | **0.16±0.05** |
| **Y** | 0.21±0.01 | 0.24±0.06 |
| **O** | n/a | n/a |
| **W** | 0.59±0.2 | 1.8±0.02 |
| **C** | n/a | n/a |
| **N** | n/a | n/a |

**Table 7.5 - EPMA analysis of consolidated materials MA with $Fe_2Y$ (wt.%)**

### 7.3.3 Significance of MA with $Fe_2Y$

From the results presented above, it would appear that the way in which Y and O are incorporated into the powder before consolidation has no effect on the final particle dispersion provided the Ti content is the same. When MA for 50 hours using elemental powders, cluster compositions are the same regardless of whether $Y_2O_3$ or $Fe_2Y$ is used. Table 7.6 summarises the types of nanocluster observed in each separate consolidated material. Y-O nanoclusters were only observed in the EPFL-PA-$FE_2Y$ alloy. Oksiuta et. al. reported that the $Fe_2Y$-prealloyed material (EPFL-PA-$FE_2Y$) has a lower oxygen content than the EPFL-PA-$Y_2O_3$ material and that the concentrations of other elements are the same [116], but it was found by EPMA analysis that the Ti content of the EPFL-PA-$FE_2Y$ material was also reduced compared to the other alloys studied.

| | Pre-alloyed | Elemental |
|---|---|---|
| $Y_2O_3$ | Y-Ti-O | Y-Ti-O |
| $Fe_2Y$ | Y-O | Y-Ti-O |

**Table 7.6 - Summary table of the nanocluster types observed in each material condition**

It is well known that increasing milling time increases the amount of oxygen incorporated during the milling process [101]. The difference in cluster compositions can therefore be attributed to the differences in the Ti content, and/or the increased O level in the material made from elemental powders due to the increased milling time. Given that the major difference in the cluster compositions is the difference in Ti rather than a difference in O, it is more likely that the Ti level is the controlling factor, as there is no particular difference in overall measurement of O in APT analyses between the two materials.

It is therefore possible to conclude that there is no particular advantage in using $Fe_2Y$ in terms of the final microstructure produced. Milling times can be reduced by MA with $Fe_2Y$ - empirical observations show that it is incorporated into the alloy powder more readily than $Y_2O_3$ [194], but any potential benefit may be outweighed by the added cost of the $Fe_2Y$ powder.

## 7.4 Summary

APT analysis of the EPFL ODS alloys at various stages during processing has yielded several interesting observations which reveal how the ODS microstructure develops.

- The nanoclusters nucleate either as a Y-Ti-O oxide or a Y-Ti-Cr-O oxide that is stable through processing.
- Growth of the nanoclusters is complete by the end of the degassing stage (800°C, 2 hours), and any subsequent increase in nanocluster radius is due to coarsening
- The nanocluster distribution is not affected by using $Fe_2Y$ rather than $Y_2O_3$ to introduce Y during the MA process
- Larger oxides (>10nm) form at grain boundaries and are initially $Cr_2O_3$

- During annealing at 800°C Ti migrates to stabilise these larger oxides
- After consolidation the grain boundary oxides also contain Y
- Oxide particles >5nm observed at grain boundaries have a Ti-Cr-O rich shell, and contain no Y before consolidation, but have similar composition to the nanoclusters at the core after consolidation.

How these observations correspond with wider research in this thesis and beyond will be discussed in the next chapter. The formation and evolution of the nanoclusters and grain boundary oxides are complex issues, but these observations show the role of the cluster-forming elements and the processing conditions on the final microstructure.

# 8 Understanding aspects of the ODS microstructure

*This chapter draws together the major results from the previous three chapters and compares with HREM work carried out by our collaborators at EPFL, along with other published research. The formation and evolution of both nanoclusters and grain boundary oxides will be discussed in depth.*

## 8.1 Key results from APT analysis of EPFL alloys

### 8.1.1 APT analysis of oxide composition

The detailed analysis of the measured oxide composition in Chapter 5 indicates that while there is some uncertainty over the Cr content of the nanoclusters, the measured Y:(Ti):O ratios are robust. Evaporation between pulses, multi-hits, and incorrect identification of ions undergoing delayed evaporation were identified as the most likely mechanisms of loss of ions during analysis. It was shown that none of these mechanisms were likely to affect the M:O ratio appreciably, and that therefore reasons for the measured composition of (Y + Ti):O of ~1:1 must be considered when discussing the formation of the nanoclusters.

### 8.1.2 Stability of nanoclusters after high temperature annealing

The similarities between the classical coarsening behaviour of the both the Y-O and Y-Ti-O (§6.3.3) nanoclusters indicates that both cluster types coarsen at the same rate. The Y-Ti-O nanoclusters however are much smaller and have a much higher number density. Ti is therefore thought to influence the nucleation of the nanoclusters.

### 8.1.3 Evolution of nanoclusters and grain boundary particles

Y-Ti-O based nanoclusters nucleate with a similar composition to those seen at later stages of processing (§7.2.2), whereas the grain boundary oxides nucleate first as $Cr_2O_3$ then transform on subsequent processing (§7.2.3).

## 8.2 HREM observations

Collaborators at EPFL and Warsaw have undertaken high resolution electron microscopy of some of the materials analysed in this thesis. This gives insight into the crystal structure of some of the larger oxides, and when combined with the information gained from APT analysis, gives some insight into the controlling factors in the nanocluster nucleation.

### 8.2.1 EPFL-PA-$FE_2Y$ material

Similar to the results presented in chapter 6, HREM EDS revealed that the smallest nanoclusters were Y-O based, and that the larger oxides were either titanium oxide, yttrium oxide or a mixed Ti-Y-O type [116]. The selected area diffraction pattern from a larger Y based oxide shows that the crystal structure is consistent with an fcc structure, despite a bcc structure being expected [116].

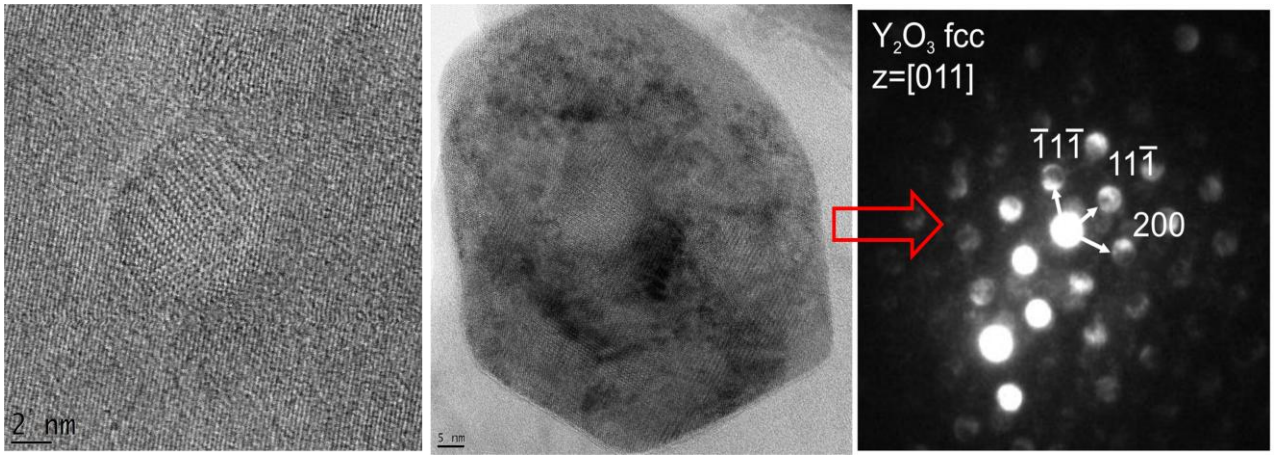


**Figure 8.1 - HREM of Y-O oxides in EPFL-PA-$FE_2Y$ alloy together with SED diffraction pattern from a larger oxide (Courtesy of P. Unifantowicz and T. Plocinski)**

### 8.2.2 EPFL-E-$Y_2O_3$ material

Dr. P. Unifantowicz used chemical extraction to isolate the nanoclusters before using electron diffraction. The smallest of these clusters was ~3nm radius, seen in Figure 8.2(a). These nanoclusters were identified as having a geometrical relations corresponding to an orthorhombic $YTiO_3$ oxide lattice. This is best described as a distorted perovskite with the $Y^{3+}$ cations surrounded by mutually tilted octahedra of $O^{2-}$ and $Ti^{3+}$ ions [195]. Unifantowicz et. al. suggest that because the

$YTiO_3$ phase is observed to form in a reducing atmosphere (Navi et. al. [196]) the fact that the **EPFL-E-$Y_2O_3$** material was mechanically alloyed in a $H_2$ atmosphere may encourage the appearance of Ti in the lower (3+) oxidation state than the more common 4+ oxidation state [195].

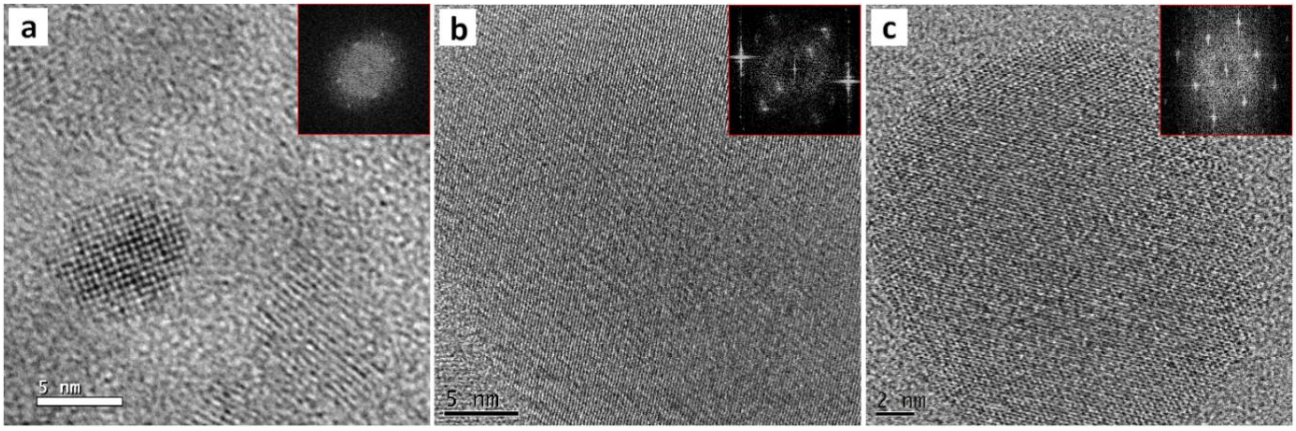


**Figure 8.2 - HREM image of a typical nanocluster in the EPFL-E-$Y_2O_3$ material with corresponding fast Fourier transformed image (a) [010] (b) [322] and (c) [135] zone axes (Courtesy of P. Unifantowicz)**

## 8.3 Thermodynamically stable oxide phases

The precipitation of the nanoclusters is driven by the supersaturation of Y/O in the matrix. The formation of complexes with Y and Ti is expected given that these elements have a high affinity for oxygen. The heat of formation of the most thermodynamically stable oxides containing Cr, Ti, and Y are given in descending order towards the most stable oxide in Table 8.1. As $Y_2O_3$ is the most stable oxide, it is expected to be the end composition of the nanoclusters, but it is clear from the results in Chapter 6 that when there is sufficient Ti in the base alloy, the nanoclusters contain appreciable levels of Ti together with Y, O and Cr.

| Stoichiometric oxide phase | M:O ratio | Enthalpy of formation - $\Delta H_f$ per mole of oxide | Enthalpy of formation -$\Delta H_f$ per mole O |
|---|---|---|---|
| (least -ve) $CrO_2$ | 1:2 | 583 | 292 |
| $Cr_2O_3$ | 2:3 | 1130 | 377 |
| $TiO_2$ | 1:2 | 944 | 472 |
| $Ti_3O_5$ | 1:1.67 | 2457 | 491 |
| $YCrO_3$ | 2:3 | 1493 [197] | 497 |
| $Ti_2O_3$ | 2:3 | 1522 | 507 |
| TiO | 1:1 | 543 | 543 |
| $Y_2Ti_2O_7$ | 1:1.75 | 3874 [198] | 553 |
| (most –ve) $Y_2O_3$ | 2:3 | 1907 | 636 |

**Table 8.1 – Enthalpy of formation of oxides (data for 298K) from [113] unless otherwise stated.**

### 8.3.1 Possible stable oxide phases for nanoclusters

For the case of the EPFL-PA-$FE_2Y$ material with Y-(Cr)-O clusters, if Cr is not part of the oxide phase, the thermodynamically stable oxide phase should be one that exists in the Y-O binary phase diagram as shown in Figure 8.3(a). If Cr is included, the $Y_2O_3$-$Cr_2O_3$ oxide phase diagram shown in Figure 8.3(b) may be more appropriate. It is clear that there is no significant intermixing between Y and Cr oxide phases, apart from the stoichiometric $YCrO_3$ perovskite phase.

Reprinted with permission from Elsevier. © 2007 Elsevier B.V.

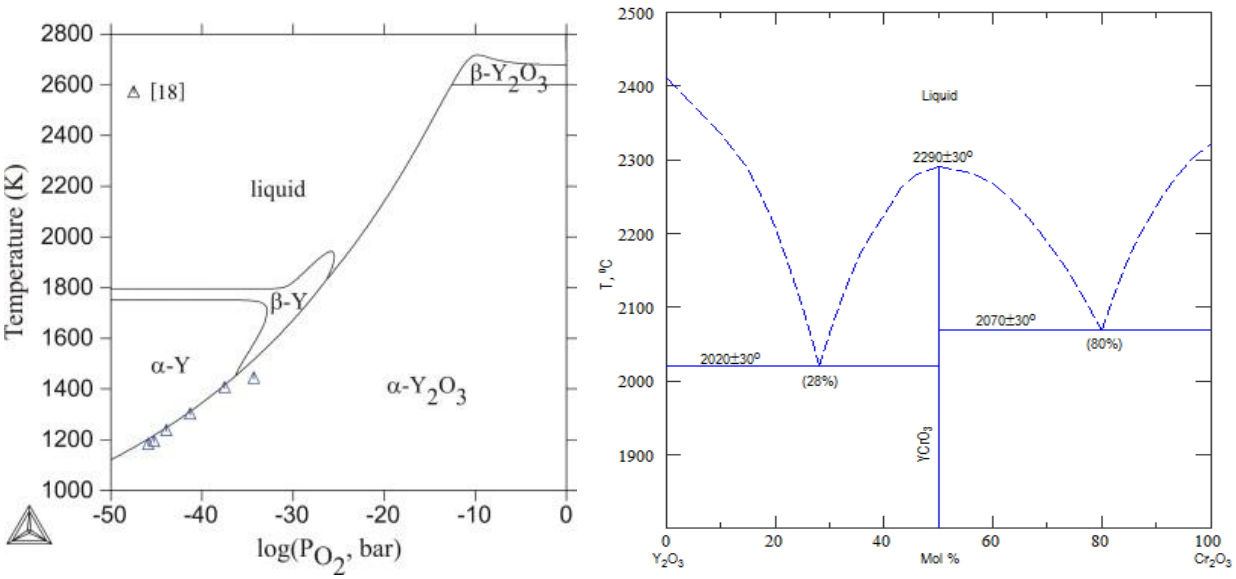


**Figure 8.3 – (a) Y-O binary phase diagram [199] (b) $Y_2O_3$-$Cr_2O_3$ phase diagram [200]**

In the case of the Y-Ti-(Cr)-O clusters seen in the EPFL-E-$Y_2O_3$, EPFL-PA-$Y_2O_3$ and EPFL-E-$FE_2Y$ materials, Cr is part of the nanocluster either within the oxide, or as segregation to the nanocluster

interface. There is however, no evidence in the available literature to suggest that nanoclusters form within grains without the presence of Y/Ti. For this reason, it is assumed that Cr is not influential in the nucleation of the nanoclusters, and therefore will not be considered as an essential part of the nucleation stage.

The clusters are most likely to be based on an oxide present on the ternary phase diagram for the Y-Ti-O system, one representation of which is shown in Figure 8.4 [201]. Unfortunately there are several inconsistencies between this and other published literature which report other stable yttrium titanate phases including $Y_2TiO_5$, $Y_2Ti_2O_7$. These phases are seen as stable at 1100°C in Figure 8.5 [202]. The $YTiO_3$ structure is also stable under certain conditions [203].

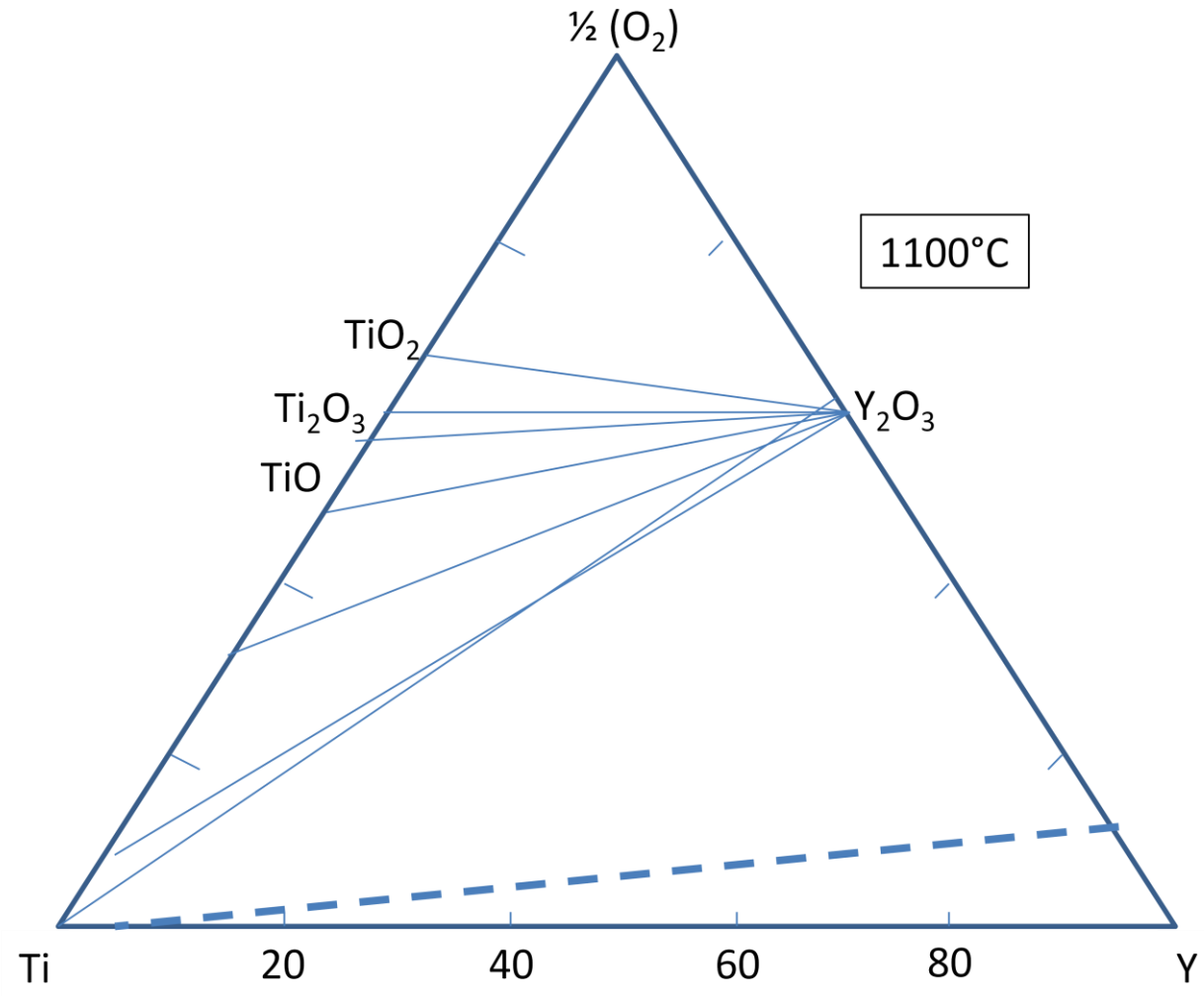


**Figure 8.4 - Y-Ti-O ternary system (based on [201])**

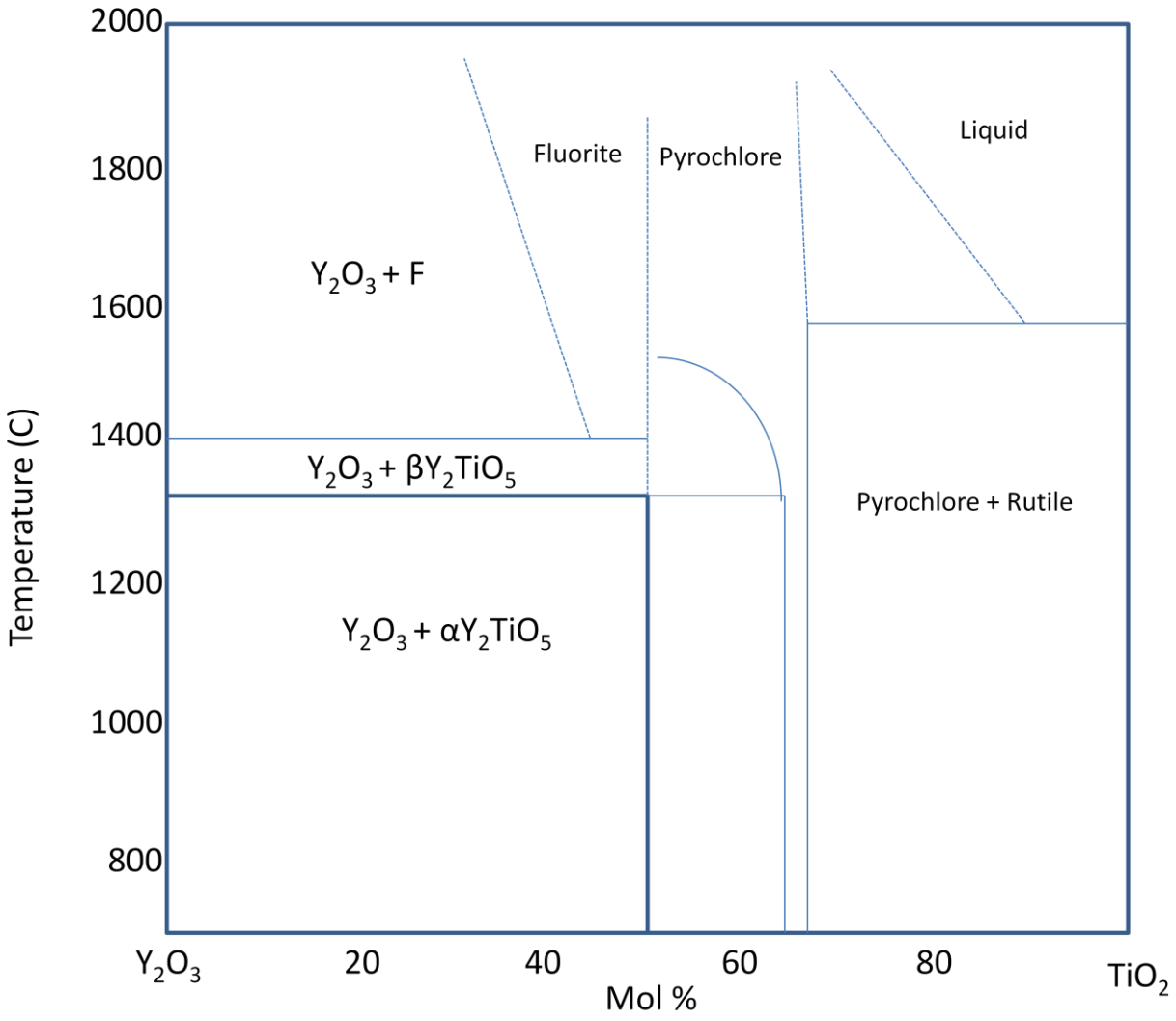


**Figure 8.5 - $Y_2O_3$-$TiO_2$ phase diagram ( based on [202])**

### 8.3.2 Crystal structures of stable oxide phases

The crystal structures and associated lattice constants for the most likely stable oxide phases are shown in Table 8.2. The lattice constant for a bcc-Fe matrix is also shown for reference. The misfit between the Fe-matrix and the most thermodynamically stable oxide phase ($Y_2O_3$) can be up to 50% (considering only the {100} type planes) therefore it is unlikely to be able to maintain coherency with the matrix for anything other than very small clusters [204]. The lattice constants for $Y_2Ti_2O_7$ and $Y_2TiO_5$ are also considerably larger than the Fe matrix and therefore from the point of view of coherency with the matrix, these phases are unfavourable, if only the primitive unit cells are

considered. The structure of the interface between oxides with large and complex unit cells is non-trivial, and has been investigated in relation to the nanoclusters in ODS steels as discussed below.

| Oxide | Crystal structure | Lattice constant (nm) |
|---|---|---|
| **TiO [205]** | Rock-salt | a = b = c = 0.423 |
| **$TiO_2$ [205]** | Anatase (tetragonal) | a = b = 0.378 and c = 0.952 |
| | Rutile (tetragonal) | a = b = 0.459 and c= 0.296 |
| | Brookite (orthorhombic) | a = b = 0.916 and c= 0.513 |
| **$Ti_2O_3$ [205]** | Corundum | a = b = c = 0.515 |
| **$Y_2O_3$ [204]** | Cubic | a = b = c = 1.06 |
| **$Y_2Ti_2O_7$ [206]** | Pyrochlore | a = b = c = 1.009 |
| **$Y_2TiO_5$ [206]** | Orthorhombic | a = 1.035 b = 0.37 c = 1.125 |
| **$YTiO_3$ [203]** | Perovskite | a = 0.567 b= 0.532 c = 0.761 |
| **$Cr_2O_3$ [207]** | Corundum | a = b = 0.495 c = 1.358 |
| **$YCrO_3$ [208]** | Orthorhombic | a = 0.552 b = 0.753 c = 0.524 |
| **Fe Matrix** | **bcc** | **a = b = c = 0.287** |

**Table 8.2 - Crystallographic data for known oxide phases**

### 8.3.3 Interface coherency and the influence of 'lattice matching'

Interface coherency and the influence of 'lattice matching' are likely to affect how easily a nanocluster is formed in the steel matrix. In the EPFL-E-$Y_2O_3$ alloy, Unifantowicz et. al. note that half of the b oxide parameter for $YTiO_3$ with a distorted perovskite structure (0.284nm) is very close to the lattice constant of the a bcc-Fe matrix at 0.287nm. This suggests a degree of coherency at the nanocluster-matrix interface. Clearly, the orientation of the nanocluster with respect to the matrix is an important consideration. The Y-O particle in the EPFL-PA-$FE_2Y$ alloy shown in Figure 8.1 shows faceting at the interface.

Ribis and de Carlan have investigated the orientation relationships of $Y_2Ti_2O_7$ and $Y_2O_3$ nanoclusters with the matrix, as previously discussed in §2.3.3. The material under investigation was very similar in composition to the EPFL-E-$Y_2O_3$ alloy (14Cr-1W-0.3Ti-0.3 $Y_2O_3$). After annealing for one hour at 1300°C, a 'cube-on-cube' orientation relationship for the $Y_2Ti_2O_7$ nanoclusters was inferred from TEM observations. The authors present orientations whereby the {110} Fe planes and {440} $Y_2Ti_2O_7$ planes can be perfectly matched (the nanoclusters are cubic in this case). $Y_2O_3$ nanoclusters were observed in the same material. The majority of these clusters had an fcc structure similar to those observed in EPFL-PA-$FE_2Y$ alloy, but $Y_2O_3$ nanoclusters with a bcc structure were also observed. For the fcc $Y_2O_3$ nanoclusters, the authors propose a 'cube-on-edge' orientation, which results in a coherent domain in the ⟨200⟩ direction and an incoherent domain in the ⟨100⟩ direction. This corresponds with Ribis and de Carlan's observations that the nanoclusters have a bevelled-cube shape. However, larger $Y_2O_3$ oxide particles in the ODS-Eurofer alloy are found not to have the same type of orientation relationship [81].Given the size of the nanoclusters in this present work, a low energy interface orientation relationship similar to that proposed by Ribis and de Carlan is likely. What remains to be discussed is whether the nanoclusters in the EPFL alloys share similar characteristics to those analysed by Ribis and de Carlan.

## 8.4 Composition of the oxide nanoclusters

The nature and composition of the nanoclusters will now be considered based on the information presented above, and on the APT results presented in chapters 5-7.

### 8.4.1 Cr content of the nanoclusters

Contrary to the APT results, Cr was not detected by EELS in the extracted particles similar to those shown in Figure 8.2 [195]. It is possible that the analysed particles may not be the same type as those analysed by APT. Also if Cr is only at the nanocluster-matrix interface, the Cr may be preferentially etched away along with the matrix in the TEM specimen preparation. There are added

complications in there is overlap of peaks in the EELS spectrum. The Cr $M_{4,5}$ and Fe $M_{4,5}$ edges are said to overlap in low loss, and the O K and Cr $L_{2,3}$ in core loss also overlap, therefore Cr at the core of the nanoclusters cannot be excluded through these results [195].

Throughout Chapters 5-7 is apparently conflicting evidence regarding the Cr distribution in the nanoclusters. The evidence for and against Cr in the nanoclusters will now be reviewed.

#### *8.4.1.1 Evidence in favour of a Cr shell around the nanoclusters*

- For larger 5nm Y-O nanoclusters, Cr is resolved as a shell around the Y-O core. It appears to be part of the oxide, but this could be due to trajectory aberrations (§6.2.1). This may also be the case for the smaller Y-Ti-O nanoclusters (§6.2.2), but because the nanoclusters are now much smaller (~2nm radius, which is similar to the width of the shell in the Y-O particles of ~5nm radius) the core and shell are not resolved.
- The proportion of Cr in the nanoclusters as measured using the corrected cluster selection process shows that the overall amount of Cr in the nanoclusters is reduced if high laser energy is used during analysis (in both the Y-O (§5.3.1) and Y-Ti-O nanoclusters (§5.5.2)). This suggests that the Cr is at least partly due to trajectory aberrations, but could also be explained by surface migration of Cr due to the high laser energy used in the APT analysis.
- Negative correlation of Cr with other cluster ions in multihits is also an indication that the majority of Cr evaporation does not occur in the vicinity of other cluster elements, and therefore is likely to be due to trajectory aberrations (see §5.2.3.1 and §5.5.2 though, this is not a particularly strong argument, as there is no way of knowing whether a positive correlation is likely. The identification of CrO ions on the mass spectrum however indicates that it is possible).

- ~50% Cr proportion in the nanoclusters as measured by the matrix-corrected cluster selection method leads to a M:O ratio of ~7:3. This is far beyond the maximum charge balance that any ionic compound allows (§8.3).
- Larger (>10nm) Y-Ti-O oxides in the EPFL-PA-$Y_2O_3$ alloy show no Cr at the core. See §6.2.2.

#### *8.4.1.2 Evidence in favour of Cr at the nanocluster core*

- The Ti-Y-O clusters show no evidence of a decrease in Cr content at the core (§6.2.2).
- Larger (>10nm) Y-Ti-O oxides in the EPFL-PA-$Y_2O_3$ alloy show no increase in Cr at the interface - See Figure 6.4.
- The mass spectra for the nanoclusters show distinct peaks corresponding to CrO ions (Figure 3.9), concentrated in regions associated with the nanoclusters in both the Y-O and Y-Ti-O nanoclusters. Some Cr therefore evaporates from the same location as O (though the possibility of surface migration of one or other of the Cr/O species cannot be excluded).
- There is no change in the overall composition of the nanoclusters throughout the various stages of processing characterised in §7.2.2, despite the clusters being below 1nm radius at the outset. During processing the surface to volume ratio of the nanoclusters decreases significantly, therefore if the Cr was only at the interface, the Cr would be expected to decrease accordingly.

#### *8.4.1.3 Discussion*

The evidence supporting the theory that Cr forms a shell around the Y-O clusters is compelling, and given the similarities between the Y-O clusters and the Y-Ti-O clusters in terms of Y:O /(Y+Ti):O ratios and coarsening behaviour, it is not unreasonable to assume that Cr interacts with the two different types of nanocluster in a similar manner. The presence of a Cr shell around the oxide particles has been observed in several other ODS alloys [84, 92, 97]. DFT calculations have been used to investigate the interactions between various cluster-forming elements (Ti, Y and O) and the

matrix (assumed bcc Fe) [75, 209]. Murali et. al consider the interactions of the cluster-forming elements with Cr; their calculations show that Cr has a negligible interaction energy with either O or an O-vacancy pair, and repulsive interactions with Y and Ti, thereby concluding that the existence of Cr at the core of the nanoclusters is unlikely [210]. Furthermore, Matteucci et. al. investigated Cr-doped $Y_2Ti_2O_7$ pyrochlore, and conclude that the solubility of Cr in this phase is very low at only 0.06 atoms/formula unit [211]. This is consistent with the results of Marquis, who suggests that the presence of Cr is likely to be driven by interfacial effects [92].

Nonetheless, the evidence in favour of Cr at the core of the Y-Ti-O nanoclusters cannot be overlooked. There is third relatively convincing argument which encompasses all the above observations but it involves disregarding the observations of Murali et. al. and Marquis and making the assumption that the shell is in fact initially part of the freshly nucleated oxide phase. If this is the case, redistribution of the Cr within the oxide could explain the fact that the level of Cr remains unchanged throughout processing. It is conceivable that the Cr could extend a few nm into the oxide given that Cr has a high affinity for O compared to Fe. This may act to change bond lengths in the oxide at the interface to better accommodate any lattice mismatch for example. As the formation of the nanoclusters progresses, the metal in the nanoclusters may redistribute (as observed in the larger grain boundary oxides) to form a more stable oxide, and the Cr would then be pushed out to the interface, keeping the overall composition of the nanoclusters the same. As the Y-Ti-O clusters are so small, this redistribution is likely to be irresolvable in the APT data, but for the Y-O clusters, the sharpening of the Cr peak at the interface on annealing shown in §6.3.1.2 would be consistent with this. The proportion of CrO ions detected overall is also consistent with this theory. In the powder directly after MA 0.16±0.04% of all ions detected are CrO, whereas in the consolidated material there are only 0.05±0.02% CrO ions.

In cases where the nanoclusters are <2nm radius, the nanocluster could effectively be considered as entirely made up of the composition of the Cr rich oxide shell, which would then explain why Cr is observed at the core of the Y-Ti-O nanoclusters. The major concern regarding this argument is that overall charge neutrality of the nanoclusters is not maintained.

### 8.4.2 Composition of the Y-O clusters (in the EPFL-PA-FE$_2$Y alloy)

Before the formation of the nanoclusters can be considered in detail, the nature of the nanoclusters must be established. Even if the Cr content of the nanoclusters is discounted, the ~1:1 M:O ratio of the nanoclusters as measured by APT in Chapters 5-7 is far below the stoichiometric composition of $Y_2O_3$ shown in the phase diagram in Figure 8.3(a). In Chapter 5, great care has been taken to ensure the integrity of the APT measurements, and aside from the potential uncertainty over the Cr content, there is little cause to believe that the measured Y:O ratio is wildly inaccurate.

The Y:O ratio of 1:1 is particularly surprising as yttrium is only commonly found in the 3+ valence state. The existence of a YO phase however is not entirely unreasonable. $Y^{2+}$ cations have been observed experimentally by Johnson et. al. [212]. Kang and Bernsein also see abundant evidence of $Y^{2+}$ in the formation of yttrium oxide clusters using pulsed laser vaporisation. This is only in the case when the oxygen content of the seed gas used in the vaporisation process is close to zero [213]. There are reports that rare earth cations can exist in certain host lattices such as $CaF_2$ type crystals [214], and YO is reported to form trapped in an argon matrix by condensation of oxide vapour at 4K [215].

More recently, there has been interest in growing thin films of $Y_2O_3$ for electronic applications. If the films are deposited in a low oxygen atmosphere, sub-stoichiometric oxide phases are believed to form [216]. Dinh et. al. report an amorphous thin film with Y:O ratio of 1:1 grown on graphite surfaces with an oxygen partial pressure of ~5 x $10^{-2}$ Torr [217]. In thin films grown on Ni-W substrates, Cantoni et. al. report that in regions with low oxygen content, a lattice superstructure is

observed, which has better adherence to the substrate. The authors suggest that the change in nearest neighbour distances and bond lengths may improve lattice matching with the substrate [218]. The importance of lattice matching between the nanocluster and matrix was discussed in §8.3.3. While the exact crystal structure of these YO nanoclusters is unknown, and may remain unknown (in a model Fe-Cr alloy MA with 0.3wt%. $Y_2O_3$ de Castro et. al. report that while ~10% of nanoclusters were indexed as $YCrO_3$, the majority of the nanoclusters did not correspond to any known Y-Cr-O based oxide phase [219]), it is possible that a superstructure with better lattice matching with the matrix drives the formation of these YO nanoclusters.

The superlattice structure reported by Cantoni et. al. [218] can be considered as an ordering of vacancies compared with the stoichiometric cubic $Y_2O_3$ structure. The formation of such a superstructure as a basis for the YO nanoclusters would not be unexpected if the modelling by Fu et. al. [75] is taken into account. Fu et. al. show strong binding between oxygen atoms and vacancies, and suggest that once an oxygen-vacancy pair is formed, they remain bound. There will therefore be an abundance of vacancies in the vicinity of the nanoclusters, and one way of accommodating these could be by the formation of these YO nanoclusters, rather than the more thermodynamically stable $Y_2O_3$.

The HREM carried out on this material is unfortunately not sufficient to provide detailed data on the crystallography of the nanoclusters. Ideally this would be compared these clusters directly with the results of Ribis and de Carlan [87]. The nanoclusters appear spherical in the low resolution TEM in Figure 6.1, but it is possible that these nanoclusters could also have a bevelled-cube shape. The most significant observation for the purposes of identifying the nanocluster composition/phase is the observation of both stoichiometric and non-stoichiometric nanoclusters in the same volume of analysis after annealing (see Figure 6.7). It is important to recall that the nanoclusters analysed by Ribis and de Carlan have been annealed at 1300°C. A transformation from a YO type cluster to

$Y_2O_3$ type (similar to what has been proposed in §6.3.1.2 after annealing at 1200°C for 100hrs) at this temperature is not inconceivable.

This literature described above suggests that the formation of YO nanoclusters in the ODS steel is plausible, especially as the ODS steel can be considered as an oxygen deficient environment due to the low overall concentration of O in the system.

### 8.4.3 Composition of the Y-Ti-O clusters (EPFL-PA-$Y_2O_3$ and EPFL-E-$Y_2O_3$ alloys)

The ratio of Y:Ti:O (again discounting the Cr) as measured by APT is ~ 1:2:3. This does not correspond to the $YTiO_3$ stoichiometry indicated by the HREM on the EPFL-E-$Y_2O_3$ alloy in §8.2.2, or the $Y_2Ti_2O_7$ [87] [93] and $Y_2TiO_5$ [85] structures observed by HREM in other similar alloys. Furthermore, the $Y_2O_3$-$TiO_2$ phase diagram in Figure 8.5 indicates that all stable oxides in the system have Y/Ti >1. The Y:Ti of 1:2 ratio measured by APT is therefore unexpected. However, again, the results in Chapter 5 indicate that the Y:Ti:O ratios measured by APT are both reliable and reproducible.

The most obvious explanation for the discrepancy between APT and HREM is that different particle types are analysed by each method. The arduous nature of finding at least 3 independent zone axes for each particle means that only very few particles are indexed in HREM, and it is possible that different structures lend themselves more easily to this process. Furthermore, the particles shown in Figure 8.2 are chemically extracted. This has the potential to change the chemistry, and there is the potential for nanoclusters of certain compositions to be dissolved or washed away by the extraction process. One challenge which remains is to explain why the nanoclusters have the Y:Ti:O ratio of ~1:2:3 measured by APT. Odette et. al. note a disagreement between APT and SANS on this issue, as SANS suggests a Y:Ti ratio of ~1:1 in a similar alloy [220]. Atomistic modelling of the nanoclusters would very beneficial in helping to resolve this issue.

The overall M:O ratio of the Y-Ti-O nanoclusters is very similar to that of the YO nanoclusters. Additionally, the formation of a surface oxide in Ti in low oxygen environments proceeds with the formation of TiO in preference to the more common $TiO_2$ [221]. In fact, the mechanism of formation of a surface oxide in Ti is well characterised. The phase transformation from metal to oxide has been studied by inducing oxidation using electron beam irradiation. Prior to the formation of TiO (seen after 24 seconds irradiation), ordered superstructures corresponding to $Ti_3O$ (after 5 seconds irradiation) and $Ti_2O$ (12 seconds) were observed [221]. The $Ti_3O$ superstructure is reported to have an ordered arrangement with layers of vacancies [222]. If it is assumed once again that the overall system is oxygen deficient, without Y one might expect the nanoclusters to form TiO. There is also evidence of TiO seeding the nucleation of other complex titanates [223]. It seems strangely coincidental that the M:O ratio of both the Y-O and Y-Ti-O nanoclusters are the same. This suggests that there could be a low energy configuration of oxygen in the oxide which matches the lattice of the matrix and therefore favours this M:O ratio.

The explanation for the non-stoichiometric Y:Ti ratio may lie in how predisposed these ions are to be found in the 2+ valence state. For charge balance to be maintained in the nanoclusters, both Y and Ti would need to be found predominantly in the 2+ valance state. As $Ti^{2+}$ ions are more readily formed than $Y^{2+}$ ions, a dominance of these ions in the nanoclusters is unsurprising. It is safe to assume that because MA produces a microstructure so very far from equilibrium, unusual or unexpected observations will be made.

## 8.5 Formation and evolution of the oxide nanoclusters

### 8.5.1 Nanocluster nucleation

Having discussed the composition/nature of the oxide phase of the nanoclusters, factors influencing the mechanism of their formation will now be addressed. This question is made somewhat more

straightforward by the observations in §7.2.2 , which suggest that the nanoclusters observed in the powder after MA have the same composition as the nanoclusters in the consolidated material.

On a simple level, the precipitation of the nanoclusters is driven by the low saturation limit of O in the matrix. The formation of complexes with Y and Ti is expected given that these elements have a high affinity for oxygen (Table 8.1). First and foremost it is an oxidation reaction that causes a nanocluster embryo to form, driven by the change in free energy associated with that reaction.

The kinetics of the nucleation will depend on the abundances and diffusivities of the oxide forming species, and the energy barrier of nucleation. The nucleation barrier can be considered as a combination of a 'volume energy' corresponding to the change in volume associated with oxide phase, and also the extra energy associated with the formation of a metal-oxide interface. In highly deformed alloys, second phase particles are assumed to nucleate heterogeneously on dislocations [224], and there will be an abundance of such nucleation sites introduced by the MA.

#### *1.1.1.1 The influence of Y, Ti and O on the formation of the nanoclusters*

The abundances of Y, Ti and O appear to be crucial in the formation of the nanoclusters. The quantities of Y and Ti are fixed by the quantity included in the starting powder, and the O content is largely controlled by the milling time. Once MA is complete, no more solute can be added to the system. However, it is shown in Chapter 7 that solutes associate preferentially with larger grain boundary oxides and therefore the level of solute available to the nanoclusters decreases as processing progresses. Observations in Chapter 7 suggest the nanoclusters nucleate before the grain boundary oxides, and that the grain boundary oxides form as a result of segregation of excess oxygen to the grain boundaries. It can be concluded from this that the sub-stoichiometric quantity of O in the nanoclusters is not a result of there being insufficient O available from the matrix at the nucleation stage. If this were the case, the excess O would migrate to the nanoclusters rather than

grain boundaries. We must assume therefore that the amount of O in the nanoclusters is constrained by either volumetric expansion and/or interfacial energy.

The higher number density and narrow particle size distribution of nanoclusters in the EPFL-PA-$Y_2O_3$ material shown in §6 suggests that the formation of the Y-Ti-O nanoclusters happens more readily than the Y-O nanoclusters in the EPFL-PA-$FE_2Y$ material. The number of nucleation sites is unlikely to be significantly reduced in the EPFL-PA-$FE_2Y$ material as it was milled in a similar manner. Ti clearly therefore plays a role in the nucleation process.

There is also an increase in volume fraction of nanoclusters in the EPFL-PA-$Y_2O_3$ material containing Y-Ti-O clusters compared to the EPFL-PA-$FE_2Y$ material containing Y-O based clusters (§6.2). This corresponds to an overall increase in cluster-forming solute elements. The M:O ratio in both the Y-O clusters and Y-Ti-O clusters is ~1:1, and both alloys contain similar levels of Y measured by EPMA (see chapter 6, Table 7.5). APT measurements consistently indicate that in the Y-Ti-O clusters the ratio of Y:Ti is ~1:2, and chapter 5 enhances the integrity of this result. If we assume the M:O ratio is constant, then by increasing the quantity of Ti in the alloy so that the Y-Ti-O clusters form, we effectively have a threefold increase in the quantity of cluster-forming solutes (as there is likely to be a surplus of O that will only migrate to grain boundaries if it not involved in the formation of the nanoclusters). The increase in nanocluster nucleation may also be partly related to this increase in available solute. Another possibility is that the diffusivities of the cluster forming elements affect the nucleation, or that Ti affects the interface energy (discussed below in §8.5.1.1).

If the diffusivities of the cluster forming species are considered, Y appears to be the rate controlling element. Comparing the diffusion coefficients for Y, Ti and O quoted in [87], it is clear that as the temperature decreases, the diffusion of Y in bcc Fe becomes much slower than that of Ti or O. Table 6.3 shows 6 orders of magnitude difference in the diffusivity of Y compared to O at 1200°C. According to [87], at 800°C that difference is increased to 9 orders of magnitude. The exact

temperature of the powder during MA when the majority of the nucleation is taking place is unknown, but the temperature of the ball-milling drum was measured to be ~80°C at the outer surface. The difference in the diffusivities is therefore likely to be even larger. The faster diffusion of Ti compared to Y may therefore be an added factor in the increase in nucleation with Ti.

#### *8.5.1.1 The influence of volumetric expansion and interfacial energy on the formation of the nanoclusters*

As the energy barrier to nucleation is controlled by both the volumetric expansion associated with the formation of a nanocluster and the interfacial energy corresponding the nanocluster-matrix interface, both these factors are likely to influence the formation of the nanoclusters. If the combined energy cost relating to the volumetric expansion associated with the nanocluster and the creation of a nanocluster-matrix interface is too high then the nanoclusters will not form. One explanation for the higher instances of nucleation in the presence of Ti is that Ti reduces one or other of these effects compared to Y alone. Firstly if the volumetric expansion of the ions when they form the nanocluster is considered a lower O content oxide is favourable, as these will tend to expand least on formation. By contrast, because of the increase in O, $TiO_2$ has the lowest density of all the stoichiometric oxides at 4.2g/cm$^3$.

In §8.3.3 it was mentioned that there is a need to reconcile some differences between the results in this thesis and those presented by Ribis and de Carlan on nanoclusters in a very similar alloy. The main concern is the difference in the oxide stoichiometry. If this transpires to be unrelated to differences in the analysis technique (APT rather than HREM), then this notion of volumetric expansion is a plausible reason for the difference. Oxides with a higher proportion of oxygen are often associated with a greater volumetric expansion on formation. As the material analysed by Ribis and de Carlan was annealed at 1300°C, this extra thermal energy may be enough to overcome the ‘volume energy’ barrier, and therefore promote the formation of stoichiometric oxides.

Interfacial strain is therefore likely to be the dominant factor. The work of Ribis and de Carlan has shown that for stoichiometric $Y_2O_3$ and $Y_2Ti_2O_7$ nanoclusters, the interfacial energy of the Ti containing nanoclusters is less than for the $Y_2O_3$ nanoclusters [87]. A lower interfacial energy would lead to an increase the nucleation rate of the nanoclusters, and could explain the difference in the number density and size distribution of the Y-Ti-O and Y-O nanoclusters. Since the nanoclusters in this present study are non-stoichiometric, it must be assumed that the interfaces are also different, but it is not unreasonable to assume that if Ti lowers the interfacial energy for stoichiometric nanoclusters, that it may have the same effect for non-stoichiometric nanoclusters.

#### *8.5.1.2 Summary of the effect of Ti on the nanocluster formation*

The nucleation of the nanoclusters has been discussed in relation to the abundances of the cluster forming elements, their diffusivities, and the energy barrier to nucleation (thought to be a combination of the volumetric expansion and the nanocluster-matrix interfacial energy). Much of the discussion surrounds the influence of Ti in the nucleation of the nanoclusters. The following points summarise the main factors that could cause Ti to increase the prospect of nanocluster nucleation:

- Adding ~0.3% Ti give a threefold increase in the metal ions associated with the nanoclusters (excluding Cr), thereby increasing the likelihood of nanocluster nucleation.
- The diffusion of Ti in bcc Fe is faster than that of Y and may therefore increase the nucleation rate
- In a similar manner to work presented by Ribis et. al., Ti could lower the interfacial energy, and therefore reduce the energy barrier for nucleation

The mechanism of nucleation will not be considered any further, but it is clear from the results in §7.2.2 that nucleation is not complete after the ball milling step is finished. The increase in number density of nanoclusters after 10 minutes at 800°C shown in Figure 7.4 signifies that nucleation

continues during the initial stages of degassing. Some growth of the nanoclusters also occurs at this stage, because after annealing at 800°C for 2 hours there is a higher proportion of larger nanoclusters and an increase in median particle size of 0.1nm.

### 8.5.2 Nanocluster growth

For the purposes of this discussion, growth is differentiated from coarsening by defining growth as the increase in nanocluster size due to a net addition of solute atoms from the matrix. Considering the Y-Ti-O nanoclusters in §7.2.2, the 'growth' stage can be identified. The level of solute measured in the matrix shown in Table 7.1 indicates that the growth phase is complete by the end of the degassing stage (i.e. After 2hours at 800°C). The matrix solute level does not decrease beyond this level; therefore it is assumed that changes in the nanocluster distribution during consolidation occur via a coarsening mechanism.

The volume fraction of precipitates is expected to increase during the growth stages but Figure 7.4 shows this not to be the case. This is because precipitation and recrystallisation occur concurrently, and as discussed in greater detail below in §8.6, larger grain boundary oxides begin to form once external thermal energy is applied (i.e. degassing at 800°C). As mentioned in § 7.2.2 the implication of this observation is that the formation of grain boundary oxides takes precedence over the nanoclusters. This reinforces the proposition that the nanoclusters are a non-stoichiometric oxide phase, as it implies that the larger grain boundary oxides are thermodynamically more stable.

### 8.5.3 Nanocluster coarsening

The coarsening of the nanoclusters during processing should be discussed before considering the coarsening of the nanoclusters in the consolidated material. Figure 7.5 shows that after the consolidation step there is a distinct shift in median particle size. There is only a marginal increase in nanocluster size on further annealing for 100 hours at the HIP temperature, but the particle size distribution is somewhat broader. It was shown in the §6.3.3 that the nanoclusters coarsen according

to classical LSW coarsening theory, and the change in nanocluster size distributions throughout the various stages of processing is consistent with this.

The key result in Chapter 6 is that Ti does not appear to have any influence on the coarsening rate (at 1200°C). In §6.3.3 it was proposed that the coarsening rate is controlled by the diffusion of Y. This is contrary to the findings of Ratti et. al. [72], and is also one crucial difference between this present work and the results presented by Ribis and de Carlan [87]. As previously explained in § 6.3.3, the most likely explanation for this difference in the findings presented in this thesis, and the results of Ratti et. al. is that Ratti et. al. also include the larger oxides in their analysis.

Ribis and de Carlan observe much faster coarsening for the $Y_2O_3$ nanoclusters than in the $Y_2Ti_2O_7$ nanoclusters (although the material was annealed at 1300°C in this case) [87]. The authors attribute the coarsening resistance of the $Y_2Ti_2O_7$ to a lower interface energy for the Ti containing nanoclusters, and propose that it is more difficult for a solute atoms to add to a complex interface that contains three solute types. There are a number of explanations to account for the fact that the coarsening rates in the Y-O and Y-Ti-O nanoclusters in the EPFL alloys are the same. Firstly, Ribis and de Carlan make no mention of Cr at the nanocluster interface. This could change how the solute atoms add to the nanocluster. Another likely possibility is that the lower temperature used for annealing the EPFL alloys might mean that the 'breakaway coarsening' suggested in the model may not have been reached despite the increase in annealing time. The final possibility is that there is no reduction in interface energy for the Y-Ti-O nanoclusters compared to the Y-O nanoclusters. This however would contradict the hypothesis that the increase in nucleation rate with Ti is related to the interfacial energy.

Due to the lower temperature used for the annealing of the EPFL alloys it is impossible to conclude as to whether the model of Ribis and de Carlan applies to the sub-oxide structures observed in this

study. Atomistic modelling of the nanoclusters and interfaces of the sub-oxide nanoclusters would be required to further clarify these complex issues.

## 8.6 Grain boundary oxide particle formation

The formation of the larger oxides at grain boundaries appears to follow a different mechanism. Figure 7.7 shows that the chemistry of the oxides at grain boundaries changes during processing, in that a Ti rich shell forms around a Cr oxide initially, but that on consolidation the oxide also becomes enriched in Y. The grain boundary profile shown in Figure 7.9 may represent the stage prior to the formation of the particles seen after 10 minutes annealing at 800°C.

The chemistry of the grain boundaries during the ODS alloy processing needs to be understood if the mechanism of formation of the larger oxides is to be established. It was reported in Section 7.2.3 that no segregation of solutes corresponding to grain boundaries was observed (despite the TEM observations of the microstructure indicating 'grains' ~20nm in diameter) in the powder after MA, except for the example shown in Figure 7.9. As no external temperature has been applied to the powder directly after MA, it is assumed that the recrystallisation has not occurred at this stage, and that the 'grains' observed are more likely to be the result of polygonization. They are therefore probably sub-grains separated by low-angle grain boundaries comprising of a series of dislocation arrays.

As soon as the degassing temperature of 800°C was applied, segregation to grain boundaries was observed as shown in Figure 7.2. This is likely to be because a greater proportion of the boundaries are more accommodating to misfitting solute elements. If excess O from the matrix migrates to high angled boundaries, as seen in Figure 7.9, this explains the much higher levels of O in the bulk directly after MA indicated in Table 7.1. Initially the high-angle boundaries are not yet formed, therefore a higher proportion of O is still present in the matrix than after annealing.

The high levels of Cr and O at the grain boundary analysed in the MA material together with the trend indicated by Figure 7.7 suggests that $Cr_2O_3$ oxides form initially at grain boundaries despite the fact that Table 8.1 shows that $Cr_2O_3$ is not the most stable oxide. The dominant factors in the precipitation of this oxide must therefore be kinetic. Table 8.3 shows the diffusion coefficients of each of the solute elements in bcc Fe near the degassing temperature. Based on diffusion coefficients alone, a Ti based oxide would be expected, but the matrix level of 14%Cr means that fast diffusion of Cr is not such an important consideration.

Due to the high concentration of Cr in the matrix and at grain boundaries, these $Cr_2O_3$ particles are likely to be initial oxide precipitates formed due to the supersaturation of O. Table 7.1 shows that there is a high level of O in the matrix in the powder after MA, however this level is reduced after annealing. Despite the enthalpy of formation of Y and/or Ti oxides being more energetically favourable, as the O level is so far from the saturation limit of a few ppm [225], the driving force to precipitate out the excess O may result in the initial formation of $Cr_2O_3$ that subsequently transforms to the more stable Ti-Cr-O phase on annealing, then to Y-Ti-O on consolidation. At the first stage of characterisation (i.e. after 800°C for 10 minutes) if a uniform concentration gradient is assumed, the diffusion distance of Y is ~6nm whereas O can diffuse >200μm in the same time. The diffusion of Y is orders of magnitude slower than of the other clustering elements, therefore it is logical that the higher temperature and pressure during consolidation is required to allow Y to diffuse to these particles.

Hin and Wirth investigated precipitation in Fe–Y–O and Fe–Ti–O alloys using kinetic Monte Carlo methods, and found that prior to the more stable Y or Ti oxides forming, small $Fe_2O_3$ precipitates formed [80]. The authors defined the matrix to be bcc-Fe in this case. However, as Cr has a greater affinity for O than Fe, the formation of $Cr_2O_3$ by a similar mechanism is plausible. It would appear that avoiding the formation of the metastable $Cr_2O_3$ would only be possible by minimising the O

uptake in the powder, and this is difficult to control. The particles may not stabilise without the Ti rich shell, therefore reducing the Ti content of the material may help to avoid these, but a Ti level of >0.16% is required to ensure the formation of the Y-Ti-O nanoclusters over the Y-O nanoclusters seen in the EPFL-PA-$FE_2Y$ material.

| Element | Diffusion Coefficient ($m^2s^{-1}$) |
|---|---|
| **O** | $8.9 \times 10^{-13}$ |
| **Ti [226]** | $2.5 \times 10^{-15}$ |
| **Cr** | $7.5 \times 10^{-16}$ |
| **Y** | $6.3 \times 10^{-20}$ |

**Table 8.3 - Diffusion coefficients at 827°C. Calculated from [204] unless otherwise stated.**

The structure of these particles are the reverse of the structure reported for larger 100-200nm oxides in the MA957 material [227]. In this case $TiO_2$ particles with a Y shell were observed, and therefore the mechanism of formation must be entirely different.

## 8.7 Summary

The APT analysis of EPFL alloys at various stages during processing reported in Chapters 5-7 has given many clues as to how the microstructure in ODS steels forms and develops. The influences various alloying elements including Y, Ti and Cr have been discussed and the following conclusions are proposed:

**On the nanoclusters:**

- The nanoclusters are enhanced in Cr, but the Cr is unlikely to be part of the oxide phase. Cr may form an interfacial layer between the nanocluster and the matrix. If the interfacial layer is 1-2nm, the APT observations of Cr at the core of the Y-Ti-O clusters are rationalised.
- Discounting the Cr level, M:O ratio of the nanoclusters is ~1:1 in both the Y-O and Y-Ti-O clusters. This is reasoned by assuming a cation deficient sub-oxide structure whereby the missing cations are preferentially Y.

- The oxide nanoclusters nucleate very readily during mechanical alloying. This is enhanced by the presence of Ti in the matrix, and it is believed that the exact composition of the nanoclusters is defined by how readily the crystal structure of the oxide matches the matrix of the lattice.
- Ti appears to reduce the energy barrier for nucleation. This is believed to be due to the possibility that Ti reduces the energy of the interface. Ti may also affect nucleation due to its increased diffusion coefficient compared to Y, and also that it by including Ti, the overall quantity of 'clustering solutes' is increased.
- Because the total level of solute available to the nanoclusters decreases during processing, the level of solute is believed to be the defining feature controlling the final number density of the nanoclusters.
- The size and composition of the nanoclusters cannot be controlled by thermal treatments before or after consolidation at industrially applicable conditions.

**On the grain boundary oxides:**

- Excess oxygen (beyond what is required to form the nanoclusters) is the most likely cause for the formation of the grain boundary oxides
- The composition of the grain boundary oxides is controlled by the kinetics of the diffusion of the oxide forming elements (Cr, Ti and Y)
- More research is required to investigate as to whether the formation of larger grain boundary oxides can be controlled by varying the degassing conditions, and controlling the rate at which grains form and develop.

# 9 Effects of irradiation of ODS microstructure

*This chapter investigates the stability of the ODS microstructure under irradiation. The following main points are addressed:*

*The viability of using ion-implantation as a simulation of fusion reactor conditions*

*The effect of ion-implantation on the nanocluster distribution*

*Radiation-enhanced solute segregation to dislocations*

## 9.1 Introduction

ODS-Eurofer is an alloy very similar in microstructure to the EPFL-PA-$FE_2Y$ material. The material is an official European candidate material for testing in the ITER and DEMO power plants, therefore its stability under irradiation is of particular importance. Heavy-ion implantation was used to simulate displacement cascades, similar to those created by fast-neutron damage.

Neutron irradiation introduces two main types of defects into the microstructure. An incoming high energy neutron (as expected in a fusion reactor) knocks an atom out of its lattice site creating a vacancy and corresponding self-interstitial atom. As the energy of incoming neutrons is relatively high, the displaced atom can in turn displace other atoms, creating a displacement cascade. There is a minimum threshold energy required to create a vacancy that is dependent on the material, irradiation temperature, and the orientation of the lattice with respect to the ion beam.

Molecular dynamics simulations show that where the self-interstitials and vacancies are in close proximity, they recombine, but that because interstitials migrate more quickly than vacancies, that typically leaves a vacancy-rich cascade core surrounded by a shell of self-interstitials [228]. Solute atoms can bind with point defects forming solute-defect clusters. Many of the defects migrate to

sinks away from the cascade region, thus causing evolution of the microstructure at distances much further from the initial entry point of the neutron. There is also likelihood that the incoming neutron will be absorbed by one of the atoms in the matrix causing transmutation into potentially radioactive isotopes, and the production of H or He.

At present there is no 14MeV neutron source that is able to replicate the type of radiation likely to be experienced in a fusion reactor, therefore similar damage must be replicated using other methods. As outlined in §2.6, ion-implantation is an attractive option, as it is fast, relatively inexpensive, and the microstructure can be freely analysed without any residual radioactivity. Table 9.1 below shows that compared to other irradiation types, the typical recoil feature is most similar to neutron damage.

| Particle Type | Typical recoil or primary knock-on (PKA) | Typical recoil/PKA energy (eV) | Dominant defect type created |
|---|---|---|---|
| **Electron** | 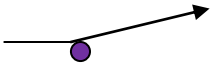 | 25 | Frenkel pairs |
| **Proton** | 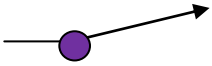 | 500 | Frenkel pairs |
| **Fe ion** | 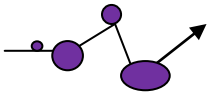 | 24,000 | Cascades and sub-cascades |
| **Neutron`** | 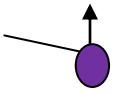 | 45,000 | Cascades and sub-cascades |

**Table 9.1 - differences in damage created by irradiation experiments (based on Was[229])**

There are a number of factors that need to be considered when using ion implantation as an analogue for fusion reactor conditions.

Firstly, the penetration depth of the displacement cascade is much shorter when using ions, therefore, only the top few microns of the specimen can be irradiated (depending on the ion type and energy). By comparison, several cm or more are irradiated using neutrons.

The dose rate also varies by several orders of magnitude (approximately $3x10^{-7}$ dpa/s is expected for the first fusion reactor, whereas a typical ion-implantation experiment is of the order of $10^{-3}$ dpa/s). This creates a very different flux of defects, and therefore the damage induced may not be comparable. There is also a strong link between observable damage, irradiation temperature and dose rate. As the temperature is increased, the effect of the point defects is reduced, and therefore a higher dose-rate can be used to create similar levels of damage [229-230]. Recent work has shown that the effect of dose rate and temperature on segregation phenomena such as radiation-induced segregation at grain boundaries is different to that of void formation, therefore caution should be used when comparing ion-implanted material with neutron irradiated material [231].

Another issue with ion-implantation is that at the peak damage region, there can be a significant number of ions being inserted into the matrix. This does not happen with neutron irradiation, and can increase the defect density in a relatively narrow region of the specimen, distorting the matrix quite significantly in some cases. Neutron sources also tend to produce a broad spectrum of neutron energies, which spreads out the damaged region, which is also not the case for the ions.

The conclusions which can be made about the behaviour of the ODS microstructure under fusion reactor conditions are clearly limited because there are differences between the damage caused by neutron irradiation, and that of self-ion implantation, but it is possible that some understanding of the processes involved can be gained from these experiments.

## 9.2 Ion implantation of ODS-Eurofer 97

The experimental conditions for the ion irradiation are outlined in §3.4. The irradiation was carried out at 400°C to two total dose levels. The 'low-dose' irradiation equates nominally to ~2 dpa and the 'high dose' irradiation equates to ~6 dpa.

### 9.2.1 Nanocluster analysis after irradiation

The ODS-Eurofer has been extensively characterised by APT in a previous study [84, 155]. The clusters are primarily Y and O based with a V and Cr rich shell. Figure 9.1 shows that there is no significant change to the distribution of nanoclusters after irradiation. Table 9.2 shows no change in the compositions or average $R_g$ of the nanoclusters after high-dose irradiation, and those subjected to the same thermal cycles but shielded from the ion beam. This indicates that the irradiation has no measurable effect on the clusters at these doses at this temperature.

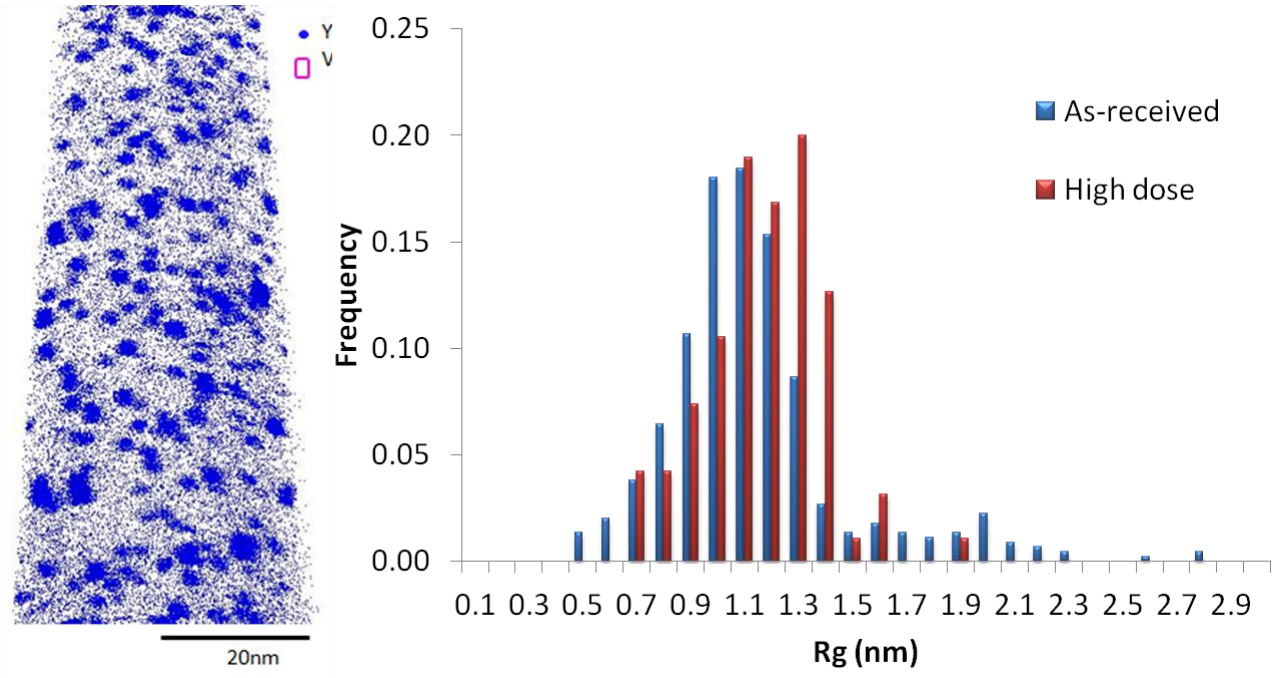


**Figure 9.1 – (a) Nanocluster dispersion in ODS-Eurofer (b) nanocluster size distribution before and after high-dose irradiation**

| Element | As-received | Low-dose ( ~2 dpa) (at.%) | High-dose (~6 dpa) |
|---|---|---|---|
| **Y** | 13.1±0.2 | 13.3±0.4 | 14.9±0.3 |
| **V** | 19.9±0.2 | 10.6±0.4 | 15.5±0.3 |
| **Cr** | 36.4±0.4 | 36.0±0.9 | 35.8±0.7 |
| **O** | 22.6±0.2 | 23.2±0.5 | 21.7±0.5 |
| **N** | 5.2±0.1 | 4.2±0.2 | 6.7±0.2 |
| | | | |
| **Rg (nm)** | 3.23±0.1 | 3.76±0.2 | 3.24±0.1 |
| **Nanocluster density** | 2.7 | 1.3 | 2.4 |

**Table 9.2 - Average Rg values for ODS-Eurofer before and after irradiation**

If anything, there is an increase in the average nanocluster radius after low-dose irradiation. This increase may be due to an increase in the coarsening rate of the clusters due to the irradiation, but it is also possible that it is related to the inhomogeneity of the microstructure. A number of the specimens analysed particularly in the low-dose irradiation showed alignment of fractionally larger nanoclusters that may correspond to prior grain boundaries as shown in Figure 9.2. Analysis of grain boundaries showing solute segregation show solute segregation profiles that correspond to moving grain boundaries, as shown in Figure 9.3. The distribution of Mn and Cr is particularly one-sided, and the Cr profile is similar to those simulated by Takahashi et. al. [232]. Figure 9.3 is evidence that the grain boundaries move during irradiation, this means that identifying where the grain boundaries were originally in the material is difficult. There is therefore more error introduced when attempting to analyse regions of nanoclusters away from grain boundaries.

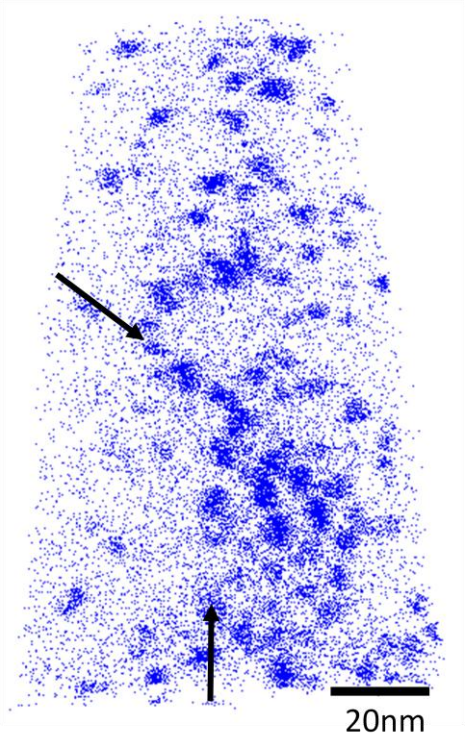


**Figure 9.2 –Y atoms in ODS-Eurofer after low-dose irradiation. Arrows indicate possible prior grain boundaries**

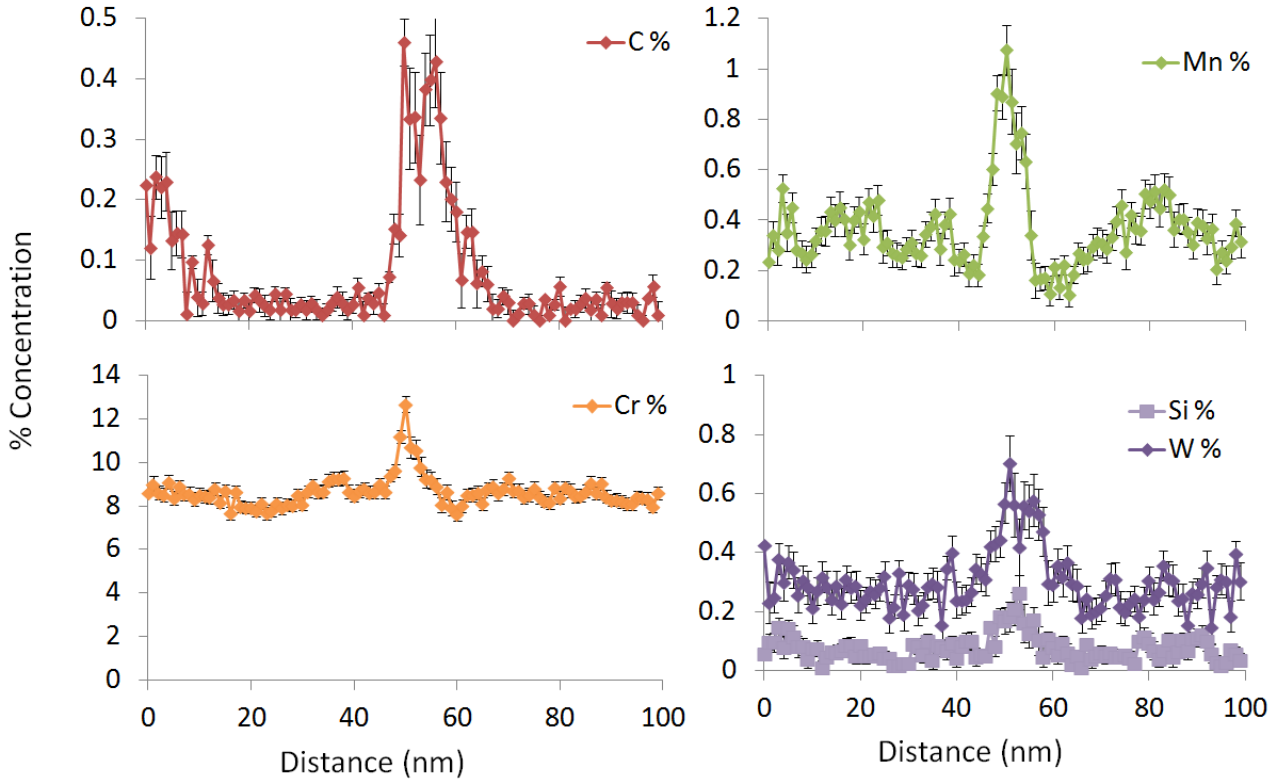


**Figure 9.3 - grain boundary profile of solute segregation after irradiation.**

### 9.2.2 Dislocation analysis

#### *9.2.2.1 As-received material*

In regions of low particle density in the 'as-received' material, enrichment of Cr, V, and N is occasionally seen along linear features (Figure 9.4), which strongly suggests that these elements segregate to dislocations. The radial composition profile in Figure 9.5 shows that segregation of solute atoms extends ~2nm from the dislocation core.

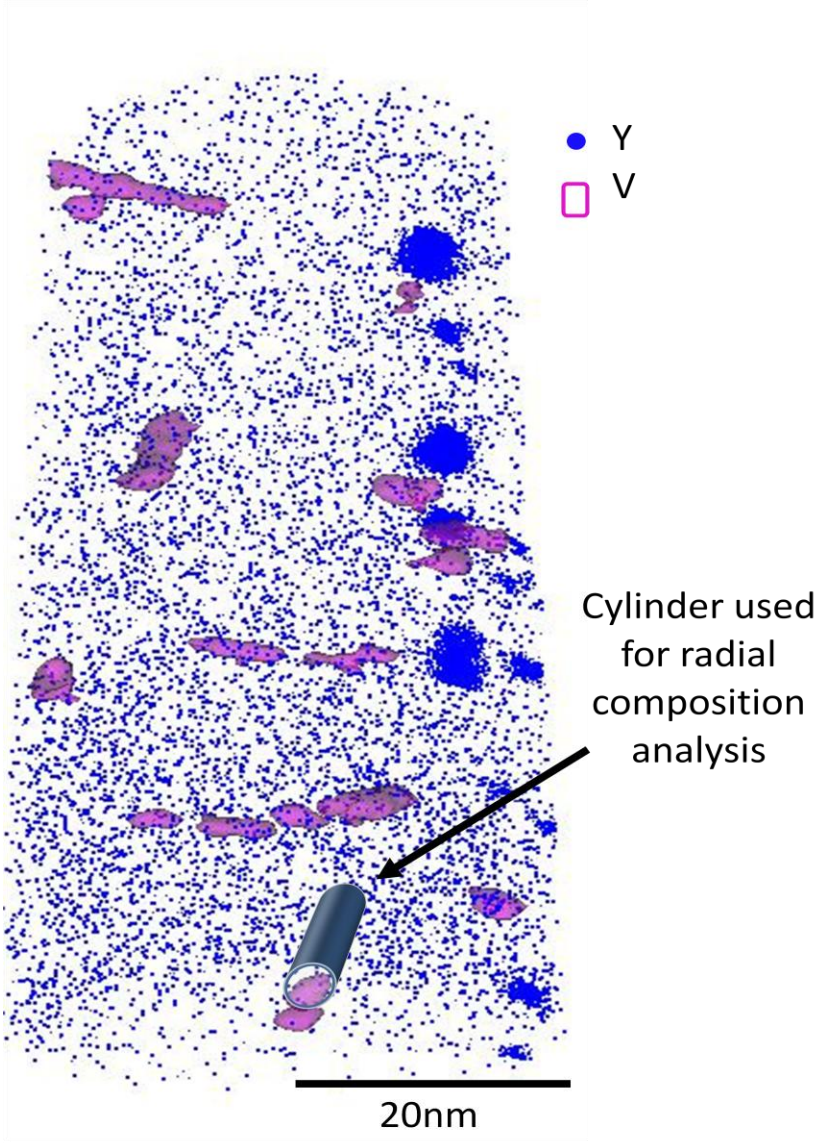


**Figure 9.4 - 3D reconstruction in a region of low particle density. The 0.2% V isodensity surfaces (in purple) indicate 1-D linear features or dislocations decorated by V atoms**

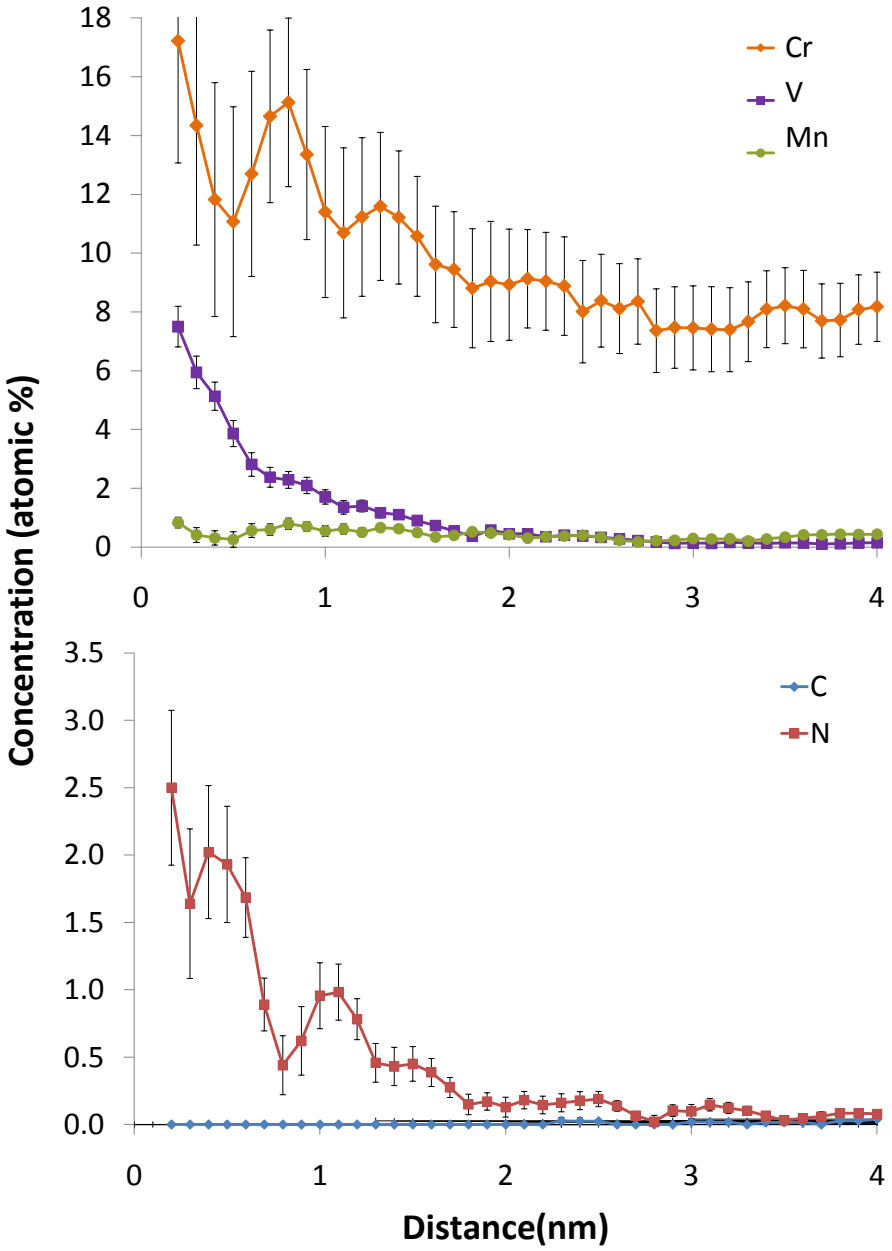


**Figure 9.5 - Radial composition profile of dislocation showing concentration of (a) Cr, V and Mn and (b) C and N as a function of distance from the dislocation core.**

The amount of segregation at dislocations was quantified by comparing solute concentrations in a cylinder containing a dislocation (diameter=5nm, length 15nm) with the concentrations taken from a cylinder of the same dimensions in the matrix. From this simple method, estimates of the relative increase of solutes near the dislocation core ($C_{dislocation}$/ $C_{matrix}$) were calculated, along with the percentage of excess solute within the cylinder. These results are presented in Table 9.3. With the

exception of C, the proportions of all solutes are increased in the vicinity of the dislocation. In terms of the absolute amount of excess solute, Cr is the most segregated element. However, in terms of the nature of the solute concentration at the dislocations compared to that in the matrix, the segregation of V and N is most significant. It is likely that the segregation of V is linked to the significant quantities of N detected at the dislocation core (Figure 9.5c) as V is known to have a strong affinity for N [18].

| | Concentration at dislocation core (1nm cylinder) | | | Concentration in 5nm cylinder centered on dislocation | | | Matrix | | | % excess solute | | | Fractional increase of solute | | |
|---|---|---|---|---|---|---|---|---|---|---|---|---|---|---|---|
| | $C_{max}$ (atomic %) | | | $C_{dis}$ (atomic %) | | | $C_m$ (atomic %) | | | $C_{dis}$-$C_m$ (atomic %) | | | $C_{dis}/C_m$ | | |
| **Fe** | 83.9 | ± | 3 | 84.19 | ± | 0.39 | 91.58 | ± | 1.2 | -7.4 | ± | 0.78 | 0.92 | ± | 0.03 |
| **Cr** | 17.2 | ± | 1.5 | 12.35 | ± | 0.23 | 7.52 | ± | 0.27 | 4.83 | ± | 0.47 | 1.64 | ± | 0.22 |
| **W** | 0.4 | ± | 0.1 | 0.41 | ± | 0.01 | 0.17 | ± | 0.05 | 0.25 | ± | 0.01 | 2.48 | ± | 0.28 |
| **P** | 0 | ± | 0.1 | 0.03 | ± | 0.00 | 0.02 | ± | 0.00 | 0.01 | ± | 0.01 | 1.23 | ± | 0.84 |
| **C** | 0 | ± | 0.1 | 0.01 | ± | 0.00 | 0.02 | ± | 0.03 | -.01 | ± | 0.01 | 0.48 | ± | 0.83 |
| **Si** | 0 | ± | 0.1 | 0.12 | ± | 0.02 | 0.02 | ± | 0.02 | 0.09 | ± | 0.03 | 4.96 | ± | 1.92 |
| **O** | 0.2 | ± | 0.1 | 0.1 | ± | 0.01 | 0.07 | ± | 0.02 | 0.03 | ± | 0.02 | 1.42 | ± | 0.95 |
| **V** | 7.5 | ± | 0.8 | 1.61 | ± | 0.08 | 0.05 | ± | 0.04 | 1.56 | ± | 0.16 | 33.79 | ± | 11.5 |
| **Mn** | 0.8 | ± | 0.2 | 0.54 | ± | 0.02 | 0.36 | ± | 0.07 | 0.18 | ± | 0.04 | 1.50 | ± | 0.35 |
| **Y** | 0.1 | ± | 0.1 | 0.03 | ± | 0.00 | 0.05 | ± | 0.01 | -.01 | ± | 0.01 | 0.71 | ± | 0.04 |
| **N** | 2.5 | ± | 0.2 | 0.7 | ± | 0.03 | 0.07 | ± | 0.02 | 0.63 | ± | 0.06 | 9.77 | ± | 3.17 |

**Table 9.3 - Quantification of solute segregation at dislocations in 'as-received' material. Data averaged from 8 dislocations.**

### *9.2.2.2 Irradiated Material*

Segregation of manganese to dislocations was observed in the irradiated specimens. Figure 9.6 shows an example of a complex network of dislocations present in the 'low-dose' irradiated material, revealed by the distribution of Mn atoms. Significant variations in dislocation density were also observed between regions of low and high particle density. Note that Figure 9.6 is

representative of the complex dislocation structure in a region free from oxide particles. In such regions, the dislocation density observed is ~ 4 times greater than the 'as-received' example in Figure 9.4 and at least 20 times greater than in regions of high particle density in the irradiated material. However it should be noted that dislocations that do not exhibit solute segregation are not usually visible in the APT data and so could not be included in these statistics.

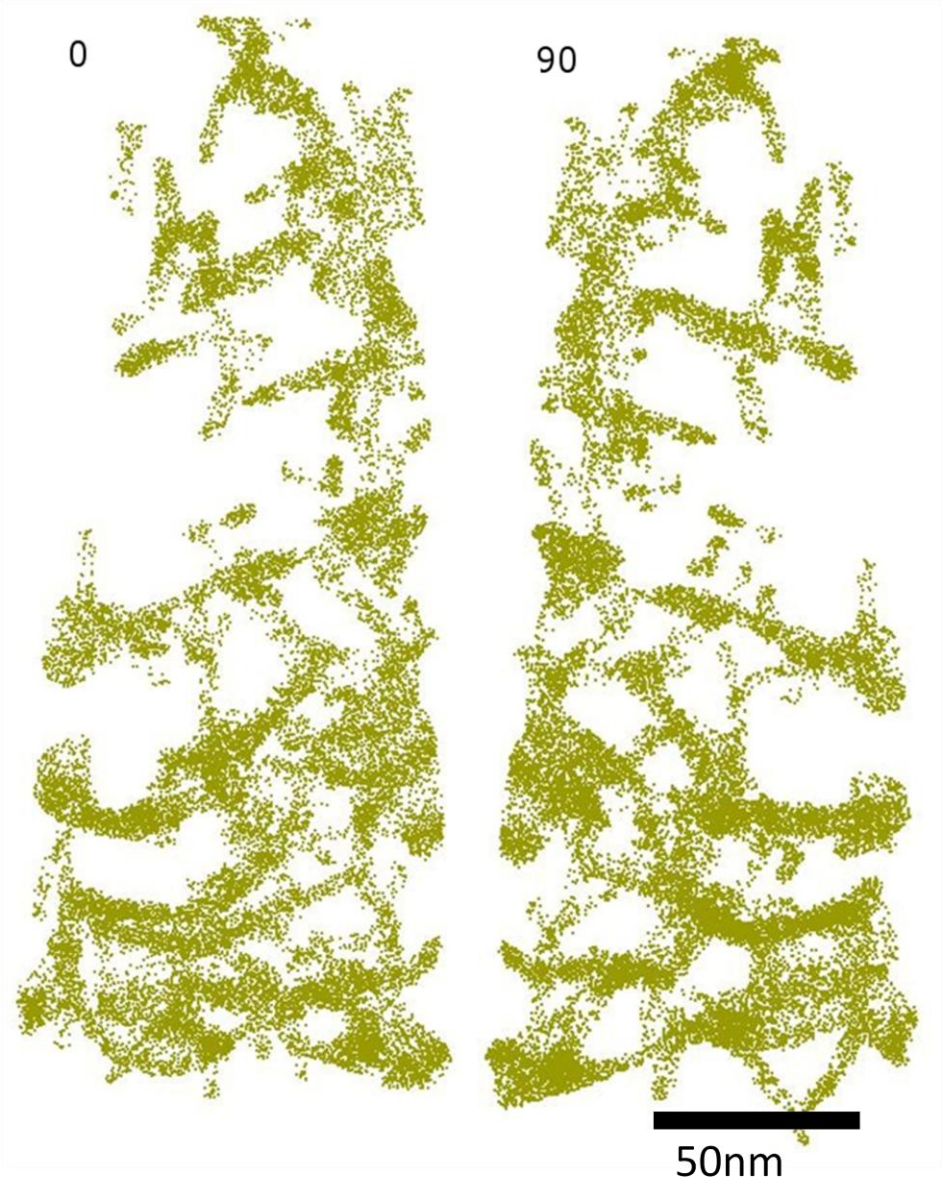


**Figure 9.6 - ODS Eurofer97 irradiated to 2 dpa at 400°C. Orthogonal views of a 3-D reconstruction showing Mn atoms at dislocations (No oxide particles are present in this reconstruction, and all other atoms removed for clarity).**

Besides Mn segregation, the presence of N, Cr, and C is also apparent at many dislocations. Table 9.4 compares the solute segregation at dislocations with the matrix level in the irradiated material. Mn was found to be at ~4.5 times higher at dislocations than the matrix after irradiation, whereas in the as-received condition the effect is much smaller (as seen in Table 9.4). In terms of absolute concentrations, up to 3% Mn was observed within 1nm of the dislocation cores after irradiation, but V was not detected. The level of Cr at the dislocations after irradiation was significantly less than in the as-received condition. In a 1nm cylinder at the core, the level of Cr was measured to be 13.5%. While this is significantly higher than the matrix level, it is much lower than the 17.5% that was measured in the as-received case. As no information on the dislocation type is available from the APT data, it is not possible to deduce whether the dislocation types are different between each condition.

| | **Concentration at dislocation core (1nm cylinder)** | | | **Concentration in 5nm cylinder centered on dislocation** | | | **Matrix** | | | **% excess solute** | | | **Fractional increase of solute** | | |
|---|---|---|---|---|---|---|---|---|---|---|---|---|---|---|---|
| | Cmax (atomic %) | | | Cdis (atomic %) | | | Cm (atomic %) | | | Cdis-Cm (atomic %) | | | Cdis/Cm | | |
| **Fe** | 83.9 | ± | 3 | 88.35 | ± | 0.85 | 90.34 | ± | 0.29 | -2.0 | ± | 0.28 | 1.0 | ± | 0.1 |
| **Cr** | 13.5 | ± | 1.5 | 9.56 | ± | 0.62 | 8.97 | ± | 0.36 | 0.60 | ± | 0.24 | 1.1 | ± | 0.04 |
| **W** | 0.4 | ± | 0.1 | 0.16 | ± | 0.04 | 0.18 | ± | 0.02 | -.03 | ± | 0.01 | 0.8 | ± | 0.02 |
| **P** | 0.0 | ± | 0.1 | 0.01 | ± | 0.00 | 0.00 | ± | 0.01 | 0.01 | ± | 0.01 | 1.8 | ± | 0.5 |
| **C** | 0.0 | ± | 0.1 | 0.08 | ± | 0.05 | 0.01 | ± | 0.01 | 0.07 | ± | 0.02 | 12.5 | ± | 0.1 |
| **Si** | 0.0 | ± | 0.1 | 0.05 | ± | 0.01 | 0.01 | ± | 0.01 | 0.04 | ± | 0.01 | 3.8 | ± | 0.32 |
| **O** | 0.4 | ± | 0.1 | 0.06 | ± | 0.02 | 0.04 | ± | 0.01 | 0.02 | ± | 0.01 | 1.5 | ± | 0.64 |
| **V** | 0.0 | ± | 0.1 | 0.15 | ± | 0.04 | 0.07 | ± | 0.03 | 0.08 | ± | 0.02 | 2.1 | ± | 0.5 |
| **Mn** | 2.7 | ± | 0.1 | 1.49 | ± | 0.15 | 0.33 | ± | 0.10 | 1.16 | ± | 0.06 | 4.5 | ± | 0.1 |
| **Y** | 0.0 | ± | 0.1 | 0.03 | ± | 0.02 | 0.01 | ± | 0.02 | 0.02 | ± | 0.01 | 2.1 | ± | 0.08 |
| **N** | 0.0 | ± | 0.1 | 0.05 | ± | 0.04 | 0.01 | ± | 0.00 | 0.04 | ± | 0.08 | 5.0 | ± | 0.47 |

**Table 9.4 - Quantification of solute segregation at dislocations in material irradiated to ~2dpa at 400°C. Data averaged from 8 dislocations.**

Figure 9.7 shows the distribution of all solute atoms in relation to the dislocation core in the irradiated material. It is clear from this radial composition profile that the segregation extends much further from the dislocation core than in the 'as-received' case. In this instance the Mn segregation does not return to the matrix level until ~4nm from the dislocation core.

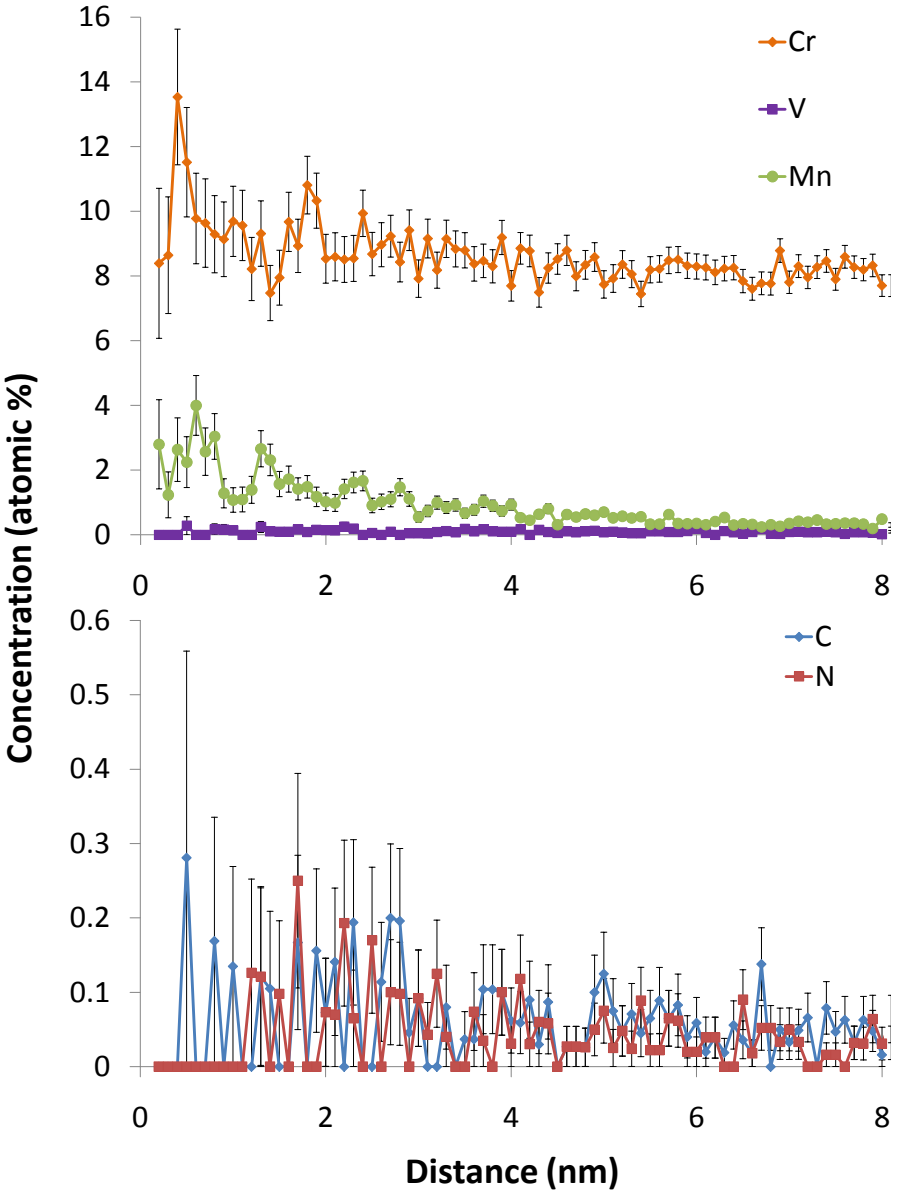


**Figure 9.7 - Radial composition profile of dislocation of ODS-Eurofer irradiated to ~2dpa at 400°C (from 3-D reconstruction shown in Figure 3)**

Dislocations in regions of low oxide particle density (<0.01x$10^{23}$ $m^{-3}$) exhibit higher quantities of Mn within a 5nm diameter cylinder than dislocations observed in regions of high oxide particle density (1.4±0.2 x$10^{23}$ $m^{-3}$). The percentage of excess Mn is reduced from 1.4±0.3% to 0.7±0.2% when the dislocations are found within a high density region of oxide particles. The levels of other elements are not changed significantly, and the width of the segregation also remains unchanged.

#### *9.2.2.3 Annealed Material*

To confirm that the observed segregation behaviour is a consequence of irradiation and not simply a thermal annealing effect, specimens were also exposed to the same thermal cycles (i.e. 400°C for ~5 hours), while shielded from the ion beam, and subsequently analysed using APT. In the annealed material (Figure 9.8), the solute distribution was found to be similar to the 'as-received' condition, with a slight reduction in the segregation of Cr, V and N. V segregation remained present at the dislocation cores, and small amounts of Mn were also observed, as indicated in Table 9.5. In this case, segregation of all elements had returned to the matrix level within 2nm of the dislocation core, as seen in the composition profile in Figure 9.8.

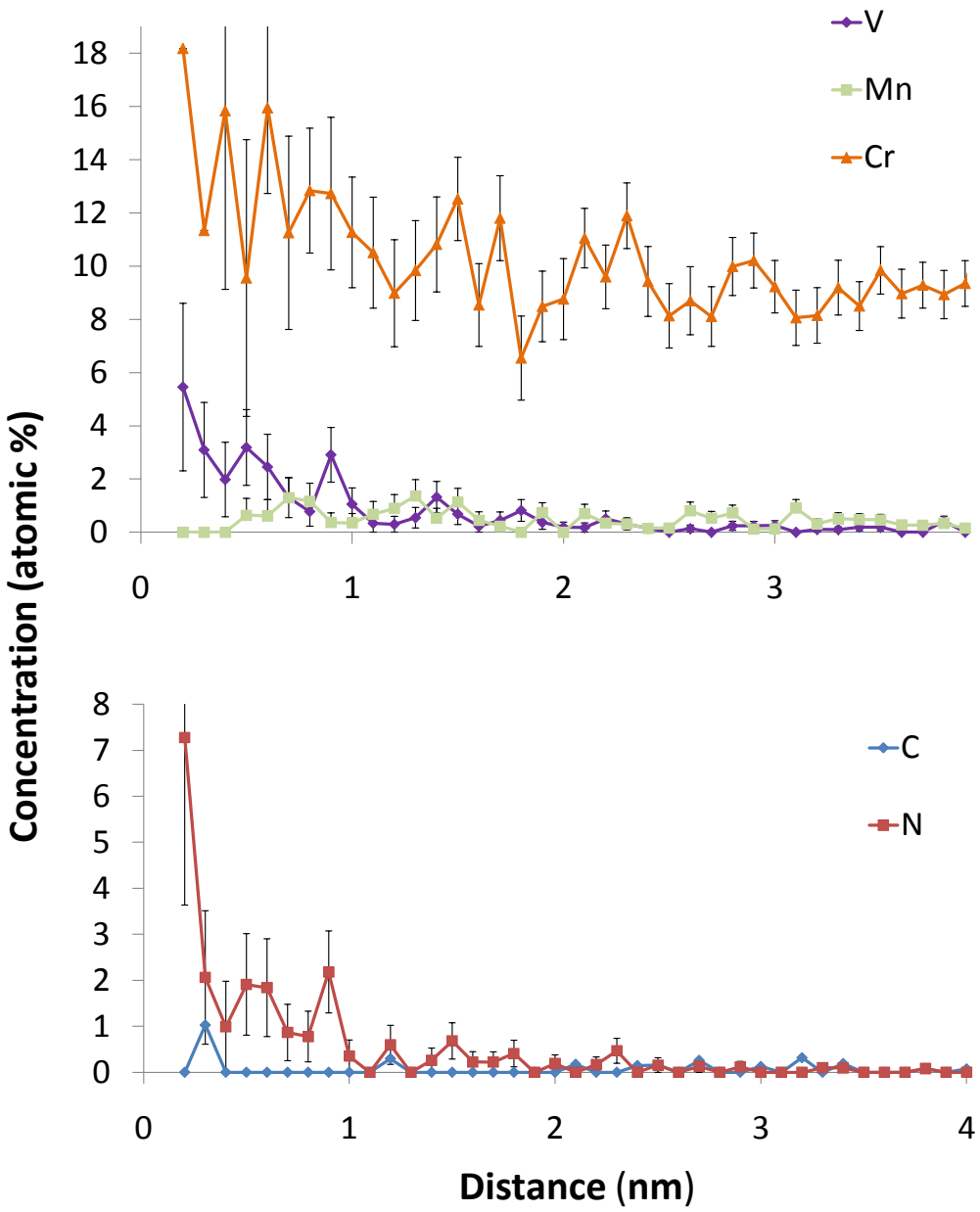


**Figure 9.8 - Radial composition profile of dislocation of ODS-Eurofer after annealing at 400°C for ~5 hours**

| | Concentration at dislocation core (1nm cylinder) | | | Concentration in 5nm cylinder centered on dislocation | | | Matrix | | | % excess solute | | | Fractional increase of solute | | |
|---|---|---|---|---|---|---|---|---|---|---|---|---|---|---|---|
| | Cmax (atomic %) | | | Cdis (atomic %) | | | Cm (atomic %) | | | Cdis-Cm (atomic %) | | | Cdis/Cm | | |
| **Fe** | 85.5 | ± | 3 | 86.77 | ± | 0.53 | 90.58 | ± | 1.01 | -3.8 | ± | 1.06 | 0.96 | ± | 0.12 |
| **Cr** | 12.6 | ± | 1.5 | 10.7 | ± | 0.46 | 8.45 | ± | 0.31 | 2.25 | ± | 0.92 | 1.27 | ± | 0.07 |
| **W** | 0.5 | ± | 0.1 | 0.34 | ± | 0.04 | 0.24 | ± | 0.05 | 0.1 | ± | 0.07 | 1.43 | ± | 0.08 |
| **P** | 0.05 | ± | 0.1 | 0.02 | ± | 0.02 | 0 | ± | 0 | 0.02 | ± | 0.03 | 0 | ± | 0.03 |
| **C** | 0.08 | ± | 0.1 | 0.01 | ± | 0.01 | 0.02 | ± | 0.02 | -.01 | ± | 0.02 | 0.46 | ± | 0.37 |
| **Si** | 0.25 | ± | 0.1 | 0.1 | ± | 0.03 | 0.03 | ± | 0.02 | 0.07 | ± | 0.06 | 3.06 | ± | 0.03 |
| **O** | 0.2 | ± | 0.1 | 0.1 | ± | 0.06 | 0.02 | ± | 0.02 | 0.08 | ± | 0.12 | 4.62 | ± | 0.08 |
| **V** | 1.5 | ± | 0.1 | 0.98 | ± | 0.14 | 0.14 | ± | 0.04 | 0.84 | ± | 0.29 | 7.19 | ± | 0.05 |
| **Mn** | 0.6 | ± | 0.1 | 0.5 | ± | 0.06 | 0.44 | ± | 0.07 | 0.06 | ± | 0.11 | 1.14 | ± | 0.06 |
| **Y** | 0.1 | ± | 0.1 | 0.04 | ± | 0.02 | 0.02 | ± | 0.02 | 0.02 | ± | 0.05 | 1.73 | ± | 0.04 |
| **N** | 0.5 | ± | 0.1 | 0.38 | ± | 0.02 | 0.02 | ± | 0.02 | 0.36 | ± | 0.05 | 16.76 | ± | 3.44 |

**Table 9.5 - Quantification of solute segregation at dislocations in material annealed at 400°C. Data averaged from 3 dislocations.**

## 9.3 Discussion

### 9.3.1 Validity of the experimental set-up

Before discussing the results in detail, it is important to consider the validity of the set-up as a simulation of fusion reactor conditions and to assess what comparisons can be made with other irradiation studies.

There are a number of differences between neutron irradiation and self-ion implantation. The temperature, ion energy, dose and dose rate are all seen as important parameters to control. The complex geometry of the APT specimens unfortunately means that in this particular study, many of these parameters are poorly defined. The temperature calibration does not account for the large surface to volume ratio of the specimen, and therefore even if it is assumed that there is perfect heat transfer throughout the base-plate, the initial temperature of the specimen is likely to be lower than the nominal temperature, as heat is radiated from the surface. As radiation decays by $T^4$ and the

temperatures involved in this study are well below red heat, this effect is believed to be relatively small. As soon as the irradiation begins, the bombardment of the specimen with high energy ions is inevitably going to introduce some heat into the specimen; but the magnitude of that increase is unknown.

The estimation of dpa by using a SRIM calculation based on an infinite flat surface has been used in previous studies on APT specimens [133-134], but the presence of a large area of free surface brought about by the geometry of the APT specimen is likely to influence the effective damage, as many point defects and point defect clusters will annihilate at those surfaces. One could assume therefore that the effective damage is therefore less than the value estimated using SRIM. In fact, the effect of the surface is likely to be more complicated. Stoller showed by molecular dynamics simulations that cascades that form near a free surface create an uneven concentration of vacancies compared to interstitials [233]. Stoller indicated that because interstitials are more mobile they are more likely to annihilate at the surface, leaving an excess concentration of vacancies. This could mean that the effective damage is greater, as there is a net increase in vacancies compared to when there is no free surface. Without complex models to account for the geometry of the specimen it is impossible to deduce which effect dominates.

Two ion energies were used to create a relatively uniform damaged region 200-800nm below the surface with respect to total average dpa. This introduces two other sources of error when attempting to assess the extent of damage induced in the specimen. Firstly the dose rate of the 0.5MeV ion implantation was ~25% slower than for the 2MeV ions. Secondly the end location of the 0.5MeV ions ideally would be taken into account. The majority of specimens are believed to have been analysed 100-400nm below the surface as the first 60-80nm of the specimens were oxidised.

Despite these issues, the changes in microstructural features reported above are still of importance, as the differences in doses and temperatures are still significant, despite systematic uncertainties

regarding the initial values. It was outlined in §9.1 that there is disparity between the damage created during neutron irradiation and ion irradiation particularly in dose rate. What these results indicate is possible trends in behaviour. In a fusion reactor effects such as Mn segregation to dislocations may not occur at 400°C at 2 dpa, but there will be a temperature and dose at which it does occur, and it is vital that this is taken into consideration when utilising Mn containing steels under irradiation.

It is clear that by irradiating flat polished samples and using one ion dose at a controlled rate will minimise many of these issues. It will also allow better comparison with other irradiation experiments provided all the parameters are defined the same way in each study. However, this will not necessarily allow better comparison with potential fusion reactor conditions until a complete model of the interdependencies of irradiation particle energy, dose, dose rate and temperature is developed, and there is an enormous amount of research required before that will happen.

### 9.3.2 Stability of nanoclusters under irradiation

The stability of the particles under the irradiation conditions outlined in Table 3.3 is consistent with some studies on the stability of ODS particles under irradiation [134, 137, 234]. Pareige et. al. for example used 150keV ions up to 0.7dpa at 300°C and reported no change to a distribution of Y-Ti-O nanoclusters [134]. Dissolution of the nanoclusters however is a more common observation. Allen et. al. [133], Certain et. al. [235] and Monnet et. al. [136] all reported some dissolution of the nanoclusters depending on the irradiation conditions used. The nanoclusters in all the above studies were of Y-Ti-O type.

A reduction in nanocluster size was observed in a previous study on the ODS-Eurofer material after irradiation to 5dpa at 300°C [155]. The results presented in this thesis are comparable to that experiment, as the material and conditions used are exactly the same. Mechanisms of how

nanocluster dissolution might occur are reviewed in §2.6. In relation to the results presented above, the main questions raised are

Why does dissolution of the nanoclusters occur at 300°C but not at 400°C?

Why do other studies observe nanocluster dissolution at temperatures above 400°C?

The results presented in [155] show a decrease in average nanocluster $R_g$ of 0.15±0.04nm. Due to differences in the data analysis, the raw data from this study was re-analysed using the same analysis methods as for the results presented (which are more sensitive to changes in $R_g$ due to the larger Dmax value used in the cluster selection stage). The decrease in average $R_g$ was therefore revised to 0.5±0.05nm. This represents a volume reduction on average per nanocluster of almost 40%. This is a sizable difference compared with the observations shown in this thesis of no change after irradiation at 400°C.

Allen et. al. suggested that the nanoclusters are likely to be fully disrupted by the displacement cascades generated using heavy-ion implantation [133]. Given that the displacement cascades typically extend over a range of 5-50nm, it is possible that the nanoclusters are completely destroyed and reform under each displacement cascade. Allen et. al. stated that in general, solute that is ejected from an oxide can either diffuse back to rejoin the original nanocluster, diffuse to another nanocluster, help nucleate a new nanocluster, or remain in the matrix.

The theory of oxide particle stability under high displacement-cascade irradiation developed by Russell suggests that the stability of the particles is governed by the balance between the ejection of solute into the matrix by the displacement cascade, and the diffusion of the solute so as to enable re-precipitation [140]. One explanation for the dissolution of the nanoclusters seen at 300°C is that once the nanocluster is destroyed by the displacement cascade, the outer solute atoms are displaced so far from the nanocluster that it is energetically favourable to nucleate a new nanocluster in some cases (hence the increase in nanocluster number density). When the temperature is increased to

400°C the ability to back-diffuse is increased, therefore the creation of new nanoclusters is less likely.

The results of this study are in full agreement the model proposed by Russell, in that as the temperature is increased, no dissolution of the nanoclusters is observed. The results of this study however are contrary to the findings of Certain et. al [235] and Allen et. al. [133] who found that dissolution of nanoclusters occur at temperatures up to 700°C, and that dissolution occurs faster at higher temperatures. The differences in these two sets of results may well relate to the fact that the composition of the nanoclusters is different. The results of Chapter 6 indicate that Ti does not affect the stability of the nanoclusters, but that it promotes nanocluster nucleation. As the ODS-Eurofer alloy does not contain Ti, the formation of new nanoclusters is less likely, hence at higher temperatures the nanoclusters are most likely to reform by back-diffusion.

In the Ti-containing ODS alloys, because the barrier for the nucleation of new clusters is reduced, the formation of new nanoclusters and hence overall number density of nanoclusters increases, and there is a subsequent decrease in average nanocluster size to compensate for this.

As previously mentioned, the exact temperature during these experiments is questionable, therefore it is difficult to ascertain which mechanisms of defect migration are likely to dominate. As the dose rates and temperatures of many of the experiments mentioned above are different, the only conclusion that can be made is that there are differences in the response of the microstructure to ion implantation. A significant amount of further work is required to establish what these are and what the implications are for the material as a structural material in a fusion reactor.

### 9.3.3 Effect of irradiation on dislocations

As a misfitting solute atom, Mn is expected to segregate to defects to relieve strain energy. However, as the size difference between the solute and the matrix is only +4.9% for Mn in bcc Fe [236], the elastic contribution is expected to be small and therefore such a significant enhancement

of Mn at dislocations after irradiation was unexpected. The quantities of Mn must therefore be due to either chemical effects and/or diffusion controlled effects. Segregation of Mn after irradiation has been well documented in austenitic RPV steels [237-238], and some studies have reported segregation of Mn at dislocations [237]. Substantial work on the co-segregation of Mn and P to grain boundaries has also been reported in RPV steels [239-241], but in the ODS-Eurofer alloy, the levels of P are so low, that there is no evidence of P at the dislocations. While traces of C were observed at some dislocations, the concentration is very low and unlikely to contribute to the segregation of Mn.

Baird and Jamison suggested that Mn and N co-segregate, particularly at 400°C [242]. The levels of N at dislocations in the irradiated material are significantly less than in either the as-received or annealed conditions. This suggests that while co-segregation with N may contribute to the Mn enhancement around dislocations in thermally annealed specimens, the segregation of Mn observed here is more likely to be radiation-induced. The broader compositional profile observed in the irradiated case cannot be explained by co-segregation alone. The behaviour of Mn therefore is likely to have resulted from either accelerated diffusion of solutes caused by the increase in point defects during irradiation or from or radiation induced non-equilibrium segregation [243]. In the latter case, a steady flux of defect-impurity complexes is set up producing a steady-state saturation of solute atoms near sinks for point defects, similar to the Kirkendall effect. The concentration gradient of this steady state is dependent on the radiation dose, rate and temperature, and could help to explain the change in the width of the segregation profiles.

The relative increase of Mn is ~25% less in regions with a high density of oxide particles than in regions free of particles. As shown in [60], the oxide particles act as trapping sites for point defects, therefore in regions containing a high density of oxide particles, the number of available point defects needed for Mn diffusion is likely to be lower than in regions free of particles. The collapse

of point defects into loops will also likely be reduced for the same reason. Reduced Mn mobility or reduced dislocation density in regions of high particle density, or combinations of the two phenomena are plausible reasons for the reduced Mn segregation. These are indirect effects of the local high density of defect sinks brought about by the presence of particle/matrix interfaces.

Previous studies have shown that irradiation produces significant hardening in ODS-Eurofer [244]. It is widely accepted that hardening is primarily caused by an increase in dislocation density [24], but, there is also evidence that Mn strongly pins dislocation loops [245]. The segregation behaviour observed in this study could therefore act as an additional hardening mechanism in Mn–containing steels, and this effect should be considered when designing steels for fusion applications. The significance of the present observations will need to be confirmed in neutron-irradiated ODS steels for which the irradiation rate is significantly lower.

## 9.4 Conclusions

Despite the limitations in the experimental set-up used, these initial ion implantation experiments yielded valuable clues as to the potential behaviour of ODS steels under irradiation. The changes (or lack thereof) observed regarding the stability of the nanoclusters are significant. The results above show that the nanoclusters are stable at 400°C, and when compared with the results of [155] indicate a temperature dependence regarding the stability of the nanoclusters under irradiation that is consistent with the typical mixing/demixing competition occurring in irradiated structures.

There is a possibility that the stability of the nanoclusters in the ODS-Eurofer under irradiation at 400°C is related to the nanocluster composition, and the fact that the nanoclusters do not contain Ti. The inclusion of Ti in the nanoclusters may promote nucleation of new nanoclusters under irradiation but further research is required to clarify this.

The segregation effects observed in this study, particularly after irradiation at 400°C, suggest that Mn segregation could contribute to the hardening that occurs during irradiation. Consequently, the

inclusion of Mn in steels designed for fusion applications needs careful consideration, especially at the lower limit of the operating temperature for blanket structures. The presence of the ODS particles however, tends to suppress the segregation of Mn to dislocations, reducing the fractional increase in Mn by ~25%. This study is another example of the strong influence of nanoscale particles on the behaviour of point defects under irradiation, and highlights the need for a uniform dispersion of particles throughout the alloy.

# 10 Summary and Conclusions

One of the main issues determining the progression of commercial fusion power is the design of sound structural materials capable of operating at high temperature under an intense neutron flux. Fission reactors face similar difficulties, and to maximise reactor efficiency, it is highly desirable that critical structural components (in both fusion and fourth generation fission reactors) should be able to operate at >600˚C, with total damage of up to 200 displacements per atom. Despite ODS steels being widely regarded as the most viable solution, many aspects of the microstructure and stability of the alloys were not well understood. The aim of this thesis was to gain a clearer understanding of how the ODS microstructure forms and develops, and to assess its suitability for use in a fusion reactor.

The present work has contributed to the global research on this topic though the findings outlined below:

### 10.1.1 APT analysis of oxide nanoclusters

The oxide nanoclusters require ultra-high resolution techniques to fully characterise their structure and composition, and no technique is currently able to give a full understanding by itself. APT is considered to be one of the best techniques for this purpose but artefacts such as trajectory aberrations were shown to influence the measured composition of the nanoclusters quite considerably.

- A procedure for reproducibly selecting appropriate parameters for cluster selection was established in order to minimise the influence of the cluster selection process on the measured size and composition of the clusters, and to account for the matrix contribution to the measured composition caused by the trajectory aberrations (§4.5.3).

- Multiple-ion evaporation events were considered as a possible mechanism for ion loss during APT analysis. It was shown in §5.2.3.2 that multi-hits can directly cause a slight reduction in measured Y content, but is unlikely to affect the O content of the nanoclusters.
- The evaporation of O ions was found to be less spatially correlated than expected (§0).
- Delayed evaporation (partly associated with multi-hits) was identified as a cause of compositional inaccuracy for oxides, and a 'peak-tail' correction method was developed to compensate for this (§5.4.1.5).
- Nanoclusters were found to be enriched in Cr, but this was agreed to be most likely Cr segregation to the nanocluster-matrix interface (§8.4.1).
- APT analysis indicates that the metal to oxygen ratio in the nanoclusters is ~1:1, and consistent with a Y deficient sub-oxide structure, likely to be promoted by coherence of the oxide phase with the matrix (§5.3, §5.5 and §8.4).

### 10.1.2 Oxide particle formation

The development of Y-Ti-O nanoclusters and larger grain boundary oxides in the EPFL-E-$Y_2O_3$ alloy was characterised at various stages during the ODS processing.

- The oxide nanoclusters were observed to nucleate during the mechanical alloying stage, and followed near classical nucleation and growth characteristics, keeping the same Y-Ti-O phase (§7.2.2).
- The volume fraction of the nanoclusters is defined by the available quantities of Y and Ti in the system (§7.2.2).
- The nucleation of the oxide nanoclusters is believed to be enhanced by the addition of Ti (§6.3.3). This may be related to how readily the crystal structure of the oxide matches that of the matrix of the lattice, and the energy of the nanocluster-matrix interface.
- Larger oxides >10nm that are initially $Cr_2O_3$ form at grain boundaries (§7.2.3).

- During annealing at 800°C Ti migrates (and later Y during consolidation at 1150°C) preferentially to stabilise these larger oxides.
- Larger oxides are believed to be the result of excess O in the system.

### 10.1.3 Oxide nanocluster stability

#### *10.1.3.1 After annealing*

The stability of the nanoclusters is crucial to the success of the material in a fusion reactor. After annealing for 100 hours at high temperature (1200°C) a limited amount of coarsening was observed in the nanoclusters. The coarsening was not dependent on the composition of the nanoclusters, in that the same coarsening rate was observed regardless of whether the clusters were Y-O based or Y-Ti-O based (§6.3.3). At the upper limit of the operating temperature (700°C) no observable change to the nanocluster distribution was noted even after 10,000 hours annealing (§6.4).

#### *10.1.3.2 After irradiation*

Irradiation conditions were simulated by using $Fe^{2+}$ ion implantation up to 6dpa at 400°C in §9.2. No change to the nanocluster distribution in ODS-Eurofer was noted at this temperature, but significant amounts of Mn segregation to dislocations were observed. This could be linked to radiation induced hardening, and requires further investigation.

## 10.2 Implications of these findings

The in-depth APT analysis in this thesis provides a framework for future research into ODS steels using APT. The data analysis protocols developed allow for very small changes in the nanocluster distribution to be observed, thereby giving useful insights into the stability of the microstructure.

By characterising the nanocluster distribution during processing, it has become clear the amount of cluster-forming solutes (Y, Ti and O) need to be tightly controlled in order to tailor the appropriate

distribution of nanoclusters. in particular, excess oxygen must be avoided to promote the formation of the nanoclusters over the grain boundary oxides.

The study on the effects of irradiation yielded promising results, that the microstructure will be stable during service, but it is now clear that the design of the experimental set-up in order to accurately replicate fusion reactor conditions requires considerably more work. It has also been shown that the inclusion of Mn into ODS steels requires careful consideration.

## 10.3 Future research

The most obvious avenue for future research in this area lies in the investigation into the behaviour of the microstructure under irradiation. There is a clear link between particle stability and irradiation temperature, and this requires further investigation, not least because the blanket structure of a fusion reactor (one area for which these steels have been designed) experience a range of temperatures.

It is important to recognise that one of the primary functions of the oxide nanoclusters is to trap helium. This aspect of research is beyond the scope of this thesis, but it should be noted that this requires significant further research. The nature of the nanocluster-matrix interface is key to this area, and some questions remain regarding what role Cr plays at the nanocluster-matrix. One relatively simple extension to this work would be to analyse the nanocluster distribution generated in a pure Fe matrix.

There is also scope for atomistic modelling of the nanocluster structure and interface to confirm some of the findings in this thesis.

# 11 References

[1] A. Ramar, Z. Oksiuta, N. Baluc, R. Schaublin,**Effect of mechanical alloying on the mechanical and microstructural properties of ODS EUROFER 97,** *Fusion Engineering and Design***,** 82 (2007) 2543-2549.

[2] M.K. Miller, E.A. Kenik, K.F. Russell, L. Heatherly, D.T. Hoelzer, P.J. Maziasz,**Atom probe tomography of nanoscale particles in ODS ferritic alloys,** *Materials Science and Engineering a-Structural Materials Properties Microstructure and Processing***,** 353 (2003) 140-145.

[3] G. McCracken, P. Stott, **Fusion: the energy of the universe**, *Elsevier Academic Press*, 2005.

[4] M.A. Pick, J. Team,**The technological achievements and experience at JET,** *Fusion Engineering and Design***,** 46 (1999) 291-298.

[5] R. Aymar, P. Barabaschi, Y. Shimomura, I. Team,**The ITER design,** *Plasma Physics and Controlled Fusion***,** 44 (2002) 519-565.

[6] ITER, www.iter.org 2011.

[7] S. Pestchanyi,**Diverter armour issues: lifetime, safety and influence on ITER performance,** *Problems of Atomic Science and Technology***,** (2009) 52-57.

[8] K. Ehrlich,**The development of structural materials for fusion reactors,** *Philosophical Transactions of the Royal Society of London Series a-Mathematical Physical and Engineering Sciences***,** 357 (1999) 595-617.

[9] P. Norajitra, L. Buhler, U. Fischer, S. Gordeev, S. Malang, G. Reimann,**Conceptual design of the dual-coolant blanket in the frame of the EU power plant conceptual study,** *Fusion Engineering and Design***,** 69 (2003) 669-673.

[10] K. Ehrlich,**The development of structural materials for fusion reactors,** *Materialwissenschaft Und Werkstofftechnik***,** 34 (2003) 39-48.

[11] N. Baluc, K. Abe, J.L. Boutard, V.M. Chernov, E. Diegele, S. Jitsukawa, A. Kimura, R.L. Klueh, A. Kohyama, R.J. Kurtz, R. Lasser, H. Matsui, A. Moslang, T. Muroga, G.R. Odette, M.Q. Tran, B. Van der Schaaf, Y. Wu, I. Yu, S.J. Zinkle,**Status of R&D activities on materials for fusion power reactors,** *Nuclear Fusion***,** 47 (2007) S696-S717.

[12] C.P.C. Wong, R.E. Nygren, C.B. Baxi, P. Fogarty, N. Ghoniem, H. Khater, K. McCarthy, B. Merrill, B. Nelson, E.E. Reis, S. Sharafat, R. Schleicher, D.K. Sze, M. Ulrickson, S. Willms, M. Youssef, S. Zinkle, A. Team,**Helium-cooled refractory alloys first wall and blanket evaluation,** *Fusion Engineering and Design***,** 49 (2000) 709-717.

[13] R.H. Jones, H.L. Heinisch, K.A. McCarthy,**Low activation materials,** *J Nucl Mater***,** 271 (1999) 518-525.

[14] Klueh, Gelles, Okada, **Reduced Activation Materials for Fusion Reactors**, *American Society for Testing and Materials*, 1990.

[15] R.L. Klueh, P.J. Maziasz,**Reduced activation austenitic stainless-steels - the Fe-Mn-Cr-C system,** *Reduced Activation Materials for Fusion Reactors***,** 1047 (1990) 7-18.

[16] Y. Hosoi,**A proposal to alloy design for low activation high manganese austenitic stainless-steel - role of carbon and nitrogen,** *J Nucl Mater***,** 179 (1991) 143-147.

[17] M. Merola, M. Zucchetti,**The design of low-activation steels for a fusion-reactor 1st wall - a proposal for a new austenitic alloy,** *Fusion Technology***,** 21 (1992) 129-141.

[18] M. Onozuka, T. Saida, S. Hirai, M. Kusuhashi, I. Sato, T. Hatakeyama,**Low-activation Mn-Cr austenitic stainless steel with further reduced content of long-lived radioactive elements,** *J Nucl Mater***,** 255 (1998) 128-138.

[19] Y. Suzuki, T. Saida, F. Kudough,**Low activation austenitic Mn-steel for in-vessel fusion materials,** *J Nucl Mater***,** 258 (1998) 1687-1693.

[20] J. Straalsu, H.R. Brager,**Effects of cold work and heat-treatment on swelling in types-304 and 316 stainless-steels,** *Transactions of the American Nuclear Society***,** 15 (1972) 251.

[21] H.R. Brager, E.R. Gilbert, Straalsu.Jl,**Microstructure of stainless-steel stressed during neutron-irradiation,** *Scripta Metallurgica***,** 7 (1973) 847-850.

[22] G.R. Odette,**On mechanisms controlling swelling in ferritic and martensitic alloys,** *J Nucl Mater***,** 155 (1988) 921-927.

[23] R.L. Klueh, K. Ehrlich, F. Abe,**Ferritic Martensitic Steels - Promises and Problems,** *J Nucl Mater***,** 191 (1992) 116-124.

[24] R.L. Klueh,**Elevated temperature ferritic and martensitic steels and their application to future nuclear reactors,** *International Materials Reviews***,** 50 (2005) 287-310.

[25] R.L. Klueh, D.J. Alexander, P.J. Maziasz,**Bainitic chromium-tungsten steels with 3 pct chromium,** *Metallurgical and Materials Transactions a-Physical Metallurgy and Materials Science***,** 28 (1997) 335-345.

[26] R.L. Klueh,**Reduced-activation bainitic and martensitic steels for nuclear fusion applications,** *Current Opinion in Solid State & Materials Science***,** 8 (2004) 239-250.

[27] R.L. Klueh, J.P. Shingledecker, R.W. Swindeman, D.T. Hoelzer,**Oxide dispersion-strengthened steels: A comparison of some commercial and experimental alloys,** *J Nucl Mater***,** 341 (2005) 103-114.

[28] Y. de Carlan, J.L. Bechade, P. Dubuisson, J.L. Seran, P. Billot, A. Bougault, T. Cozzika, S. Doriot, D. Hamon, J. Henry, M. Ratti, N. Lochet, D. Nunes, P. Olier, T. Leblond, M.H. Mathon,**CEA developments of new ferritic ODS alloys for nuclear applications,** *J Nucl Mater***,** 386 (2009) 430-432.

[29] D.S. Gelles,**Void swelling in binary Fe-Cr alloys at 200 dpa,** *17th International Symposium on the Effects of Radiation on Materials***,** 225 (1994) 163-174.

[30] E.A. Little, D.A. Stow,**Void-swelling in irons and ferritic steels .2. experimental survey of materials irradiated in a fast-reactor,** *J Nucl Mater***,** 87 (1979) 25-39.

[31] N. Baluc, D.S. Gelles, S. Jitsukawa, A. Kimura, R.L. Klueh, G.R. Odette, B. van der Schaaf, J.N. Yu,**Status of reduced activation ferritic/martensitic steel development,** *J Nucl Mater***,** 367 (2007) 33-41.

[32] R.L. Klueh, E.E. Bloom,**The development of ferritic steels for fast induced-radioactivity decay for fusion-reactor applications,** *Nuclear Engineering and Design-Fusion***,** 2 (1985) 383-389.

[33] S. Jitsukawa, A. Kimura, A. Kohyama, R.L. Klueh, A.A. Tavassoli, B. van der Schaaf, G.R. Odette, J.W. Rensman, M. Victoria, C. Petersen,**Recent results of the reduced activation ferritic/martensitic steel development,** *J Nucl Mater***,** 329-33 (2004) 39-46.

[34] P.J. Maziasz, R.L. Klueh,**Precipitation sensitivity to alloy composition in fe-cr-mn austenitic steels developed for reduced activation for fusion application,** *Reduced Activation Materials for Fusion Reactors***,** 1047 (1990) 56-79.

[35] Q.Y. Huang, J.G. Li, Y.X. Chen,**Study of irradiation effects in China low activation martensitic steel CLAM,** *J Nucl Mater***,** 329-33 (2004) 268-272.

[36] Y.F. Li, Q.Y. Huang, Y.C. Wu, Y.N. Zheng, Y. Zuo, S.Y. Zhu,**Effects of addition of yttrium on properties and microstructure for China Low Activation Martensitic (CLAM) steel,** *Fusion Engineering and Design***,** 82 (2007) 2683-2688.

[37] M.G. Horsten, E.V. van Osch, D.S. Gelles, M.L. Hamilton,**Irradiation behavior of ferritic-martensitic 9-12%Cr steels,** *Effects of Radiation on Materials: 19th International Symposium***,** 1366 (2000) 579-593.

[38] E. Lucon, P. Benoit, P. Jacquet, E. Diegele, R. Lasser, A. Alamo, R. Coppola, F. Gillemot, P. Jung, A. Lind, S. Messoloras, P. Novosad, R. Lindau, D. Preininger, M. Klimiankou, C. Petersen, M. Rieth, E. Materna-Morris, H.C. Schneider, J.W. Rensman, B. van der Schaaf, B.K. Singh, P. Spaetig,**The European effort towards the development of a demo structural material: Irradiation behaviour of the European reference RAFM steel EUROFER,** *Fusion Engineering and Design***,** 81 (2006) 917-923.

[39] S.J. Zinkle, M. Victoria, K. Abe,**Scientific and engineering advances from fusion materials R&D,** *J Nucl Mater***,** 307 (2002) 31-42.

[40] E. van Osch, M. Horsten, G.E. Lucas, G.R. Odette,**Mechanical properties of four 7-9%Cr reduced activation martensitic steels after 2.5 dpa, 300 degrees C irradiation,** *Effects of Radiation on Materials: 19th International Symposium***,** 1366 (2000) 612-625.

[41] F. Tavassoli, H. Burlet, A. Lind, B.N. Singh, S. Tahtinen, E. van Osch,**Effect of irradiation on structural materials in fusion reactors,** *Effects of Radiation on Materials: 19th International Symposium***,** 1366 (2000) 1093-1108.

[42] B. van der Schaaf, C. Petersen, Y. De Carlan, J.W. Rensman, E. Gaganidze, X. Averty,**High dose, up to 80 dpa, mechanical properties of Eurofer 97,** *13th International Conference on Fusion Reactor Materials (ICFRM-13)***,** 386 (2007) 236-240.

[43] E. Gaganidze, C. Petersen, E. Materna-Morris, C. Dethloff, O. Weiß, J. Aktaa, A. Povstyanko, A. Fedoseev, O. Makarov, V. Prokhorov,**Mechanical properties and TEM examination of RAFM steels irradiated up to 70 dpa in BOR-60,** *J Nucl Mater***,** 417 (2009) 93-98.

[44] A. Alamo, J.L. Bertin, V.K. Shamardin, P. Wident,**Mechanical properties of 9Cr martensitic steels and ODS-FeCr alloys after neutron irradiation at 325 degrees C up to 42 dpa,** *J Nucl Mater***,** 367 (2007) 54-59.

[45] G. Yu, N. Nita, N. Baluc,**Thermal creep behaviour of the EUROFER 97 RAFM steel and two European ODS EUROFER 97 steels,** *Fusion Engineering and Design***,** 75-9 (2005) 1037-1041.

[46] R.L. Klueh,**Reduced-activation steels: Future development for improved creep strength,** *J Nucl Mater***,** 378 (2008) 159-166.

[47] R.L. Klueh, N. Hashimoto, P.J. Maziasz,**New nano-particle-strengthened ferritic/martensitic steels by conventional thermo-mechanical treatment,** *J Nucl Mater***,** 367 (2007) 48-53.

[48] R. Kiessling, N. Lange, **Non-metallic inclusions in steel**, 1 ed., *Iron and Steel Institute*, London, 1966.

[49] U. Martin, D.V. Kudashov, M. Heilmaier, H. Oettel,**Microstructure and deformation behaviour of ultra-fine-grained ODS copper prepared by mechanical alloying,** *High Performance Structures and Materials Ii***,** (2004) 341-350.

[50] H. Bhadeshia,**Recrystallisation of practical mechanically alloyed iron-base and nickel-base superalloys,** *Materials Science and Engineering a-Structural Materials Properties Microstructure and Processing***,** 223 (1997) 64-77.

[51] N. Hansen,**Dispersion strengthening of aluminium-aluminium-oxide products,** *Acta Metallurgica***,** 18 (1970) 137-145.

[52] R. Kasada, N. Toda, K. Yutani, H.S. Cho, H. Kishimoto, A. Kimura,**Pre- and post-deformation microstructures of oxide dispersion strengthened ferritic steels,** *J Nucl Mater***,** 367 (2007) 222-228.

[53] J.S. Benjamin,**Mechanical Alloying,** *Scientific American***,** 234 (1976) 40-49.

[54] H. Okada, S. Ukai, M. Inoue,**Effects of grain morphology and texture on high temperature deformation in oxide dispersion strengthened ferritic steels,** *Journal of Nuclear Science and Technology***,** 33 (1996) 936-943.

[55] S. Ukai, M. Harada, H. Okada, M. Inoue, S. Nomura, S. Shikakura, T. Nishida, M. Fujiwara, K. Asabe,**Tube manufacturing and mechanical-properties of oxide dispersion-strengthened ferritic steel,** *J Nucl Mater***,** 204 (1993) 74-80.

[56] S. Ukai, T. Narita, A. Alamo, P. Parmentier,**Tube manufacturing trials by different routes in 9CrW-ODS martensitic steels,** *J Nucl Mater***,** 329 (2004) 356-361.

[57] R. Lindau, M. Schirra,**First results on the characterisation of the reduced-activation-ferritic-martensitic steel EUROFER,** *Fusion Engineering and Design***,** 58-9 (2001) 781-785.

[58] V. de Castro, T. Leguey, A. Munoz, M.A. Monge, R. Pareja, E.A. Marquis, S. Lozano-Perez, M.L. Jenkins,**Microstructural characterization of Y2O3 ODS-Fe-Cr model alloys,** *J Nucl Mater***,** 386 (2009) 449-452.

[59] Z. Oksiuta, N. Baluc,**Optimization of the chemical composition and manufacturing route for ODS RAF steels for fusion reactor application,** *Nuclear Fusion***,** 49 (2009).

[60] G.R. Odette, M.J. Alinger, B.D. Wirth,**Recent developments in irradiation-resistant steels,** *Annual Review of Materials Research***,** 38 (2008) 471-503.

[61] A. Verma, T.R. Anantharaman,**Internal oxidation of rapidly solidified silver tin indium alloy powders,** *J Mater Sci***,** 27 (1992) 5623-5628.

[62] A. Undisz, U. Zeigmeister, M. Rettenmayr, M. Oechsle,**On the mechanism of internal oxidation in platinum-zirconium alloys - A TEM study,** *Journal of Alloys and Compounds***,** 438 (2007) 178-183.

[63] J.H. Schneibel, S. Shim,**Nano-scale oxide dispersoids by internal oxidation of Fe-Ti-Y intermetallics,** *Materials Science and Engineering a-Structural Materials Properties Microstructure and Processing***,** 488 (2008) 134-138.

[64] J.H. Schneibel, C.T. Liu, D.T. Hoelzer, M.J. Mills, P. Sarosi, T. Hayashi, U. Wendt, H. Heyse,**Development of porosity in an oxide dispersion-strengthened ferritic alloy containing nanoscale oxide particles,** *Scripta Materialia***,** 57 (2007) 1040-1043.

[65] K. Verhiest, A. Almazouzi, N. De Wispelaere, R. Petrov, S. Claessens,**Development of oxides dispersion strengthened steels for high temperature nuclear reactor applications,** *J Nucl Mater***,** 385 (2009) 308-311.

[66] T. Igarashi, M. Ihara, T. Kusunoki, K. Ohno, T. Isobe, M. Senna,**Relationship between optical properties and crystallinity of nanometer Y2O3 : Eu phosphor,** *Applied Physics Letters***,** 76 (2000) 1549-1551.

[67] R. Schaublin, A. Ramar, N. Baluc, V. de Castro, M.A. Monge, T. Leguey, N. Schmid, C. Bonjour,**Microstructural development under irradiation in European ODS ferritic/martensitic steels,** *J Nucl Mater***,** 351 (2006) 247-260.

[68] D.A. McClintock, D.T. Hoelzer, M.A. Sokolov, R.K. Nanstad,**Mechanical properties of neutron irradiated nanostructured ferritic alloy 14YWT,** *13th International Conference on Fusion Reactor Materials (ICFRM-13)***,** 386 (2007) 307-311.

[69] T. Okuda, M. Fujiwara,**Dispersion behaviour of oxide particles in mechanically alloyed ODS steel,** *Journal of Materials Science Letters***,** 14 (1995) 1600-1603.

[70] P. Olier, A. Bougault, A. Alamo, Y. de Carlan,**Effects of the forming processes and Y2O3 content on ODS-Eurofer mechanical properties,** *J Nucl Mater***,** 386 (2009) 561-563.

[71] M. Brocq, B. Radiguet, S. Poissonnet, F. Cuvilly, P. Pareige, F. Legendre,**Nanoscale characterization and formation mechanism of nanoclusters in an ODS steel elaborated by reactive-inspired ball-milling and annealing,** *J Nucl Mater***,** 409 (2011) 80-85.

[72] M. Ratti, D. Leuvrey, M.H. Mathon, Y. de Carlan,**Influence of titanium on nano-cluster (Y, Ti, O) stability in ODS ferritic materials,** *J Nucl Mater***,** 386 (2009) 540-543.

[73] S. Sakuma, S. Yamashita, K. Oka, S. Ohnuki, L.E. Rehn, E. Wakai,**Y2O3 nano-particle formation in ODS ferritic steels by Y and O dual ion-implantation,** *J Nucl Mater***,** 329 (2004) 392-396.

[74] H. Sakasegawa, M. Tamura, S. Ohtsuka, S. Ukai, H. Tanigawa, A. Kohyama, M. Fujiwara,**Precipitation behavior of oxide particles in mechanically alloyed powder of oxide-dispersion-strengthened steel,** *Journal of Alloys and Compounds***,** 452 (2008) 2-6.

[75] C.L. Fu, M. Krcmar, G.S. Painter, X.Q. Chen,**Vacancy mechanism of high oxygen solubility and nucleation of stable oxygen-enriched clusters in Fe,** *Physical Review Letters***,** 99 (2007) 225502.

[76] Y.D. Ou, W.S. Lai,**Vacancy formation and clustering behavior in Y(2)O(3) by first principles,** *Nuclear Instruments & Methods in Physics Research Section B-Beam Interactions with Materials and Atoms***,** 269 (2011) 1720-1723.

[77] J. Xu, C.T. Liu, M.K. Miller, H.M. Chen,**Nanocluster-associated vacancies in nanocluster-strengthened ferritic steel as seen via positron-lifetime spectroscopy,** *Physical Review B***,** 79 (2009) 020204.

[78] M.J. Alinger, B.D. Wirth, H.J. Lee, G.R. Odette,**Lattice Monte Carlo simulations of nanocluster formation in nanostructured ferritic alloys,** *J Nucl Mater***,** 367 (2007) 153-159.

[79] M.K. Miller,**Atom probe tomography characterization of solute segregation to dislocations,** *Microsc Res Techniq***,** 69 (2006) 359-365.

[80] C. Hin, B.D. Wirth,**Formation of oxide nanoclusters in nanostructured ferritic alloys during anisothermal heat treatment: A kinetic Monte Carlo study,** *Materials Science and Engineering a-Structural Materials Properties Microstructure and Processing***,** 528 (2011) 2056-2061.

[81] M. Klimiankou, R. Lindau, A. Moslang,**HRTEM Study of yttrium oxide particles in ODS steels for fusion reactor application,** *Journal of Crystal Growth***,** 249 (2003) 381-387.

[82] A. Alamo, H. Regle, G. Pons, J.L. Bechade,**Microstructure and textures of ODS ferritic alloys obtained by mechanical alloying,** *Mechanical Alloying***,** 88 (1992) 183-190.

[83] M. Klimenkov, R. Lindau, A. Moslang,**New insights into the structure of ODS particles in the ODS-Eurofer alloy,** *J Nucl Mater***,** 386 (2009) 553-556.

[84] C.A. Williams, E.A. Marquis, A. Cerezo, G.D.W. Smith,**Nanoscale characterisation of ODS-Eurofer 97 steel: An atom-probe tomography study,** *J Nucl Mater***,** 400 (2010) 37-45.

[85] H. Kishimoto, R. Kasada, O. Hashitomi, A. Kimura,**Stability of Y-Ti complex oxides in Fe-16Cr-0.1Ti ODS ferritic steel before and after heavy-ion irradiation,** *J Nucl Mater***,** 386 (2009) 533-536.

[86] M. Klimiankou, R. Lindau, A. Moslang,**Energy-filtered TEM imaging and EELS study of ODS particles and argon-filled cavities in ferritic-martensitic steels,** *Micron***,** 36 (2005) 1-8.

[87] J. Ribis, Y. De Carlan,**Interfacial strained structure and orientation relationships of the nanosized oxide particles deduced from elasticity driven morphology in oxide dispersion strengthened materials,** *Acta Materialia***,** 60 (2012) 238-252.

[88] M.K. Miller, K.F. Russell, D.T. Hoelzer,**Characterization of precipitates in MA/ODS ferritic alloys,** *J Nucl Mater***,** 351 (2006) 261-268.

[89] D.J. Larson, P.J. Maziasz, I.S. Kim, K. Miyahara,**Three-dimensional atom probe observation of nanoscale titanium-oxygen clustering in an oxide-dispersion-strengthened Fe-12Cr-3W-0.4Ti+Y2O3 ferritic alloy,** *Scripta Materialia***,** 44 (2001) 359-364.

[90] M.K. Miller, D.T. Hoelzer, E.A. Kenik, K.F. Russell,**Stability of ferritic MA/ODS alloys at high temperatures,** *Intermetallics***,** 13 (2005) 387-392.

[91] M.K. Miller, D.T. Hoelzer, E.A. Kenik, K.F. Russell,**Nanometer scale precipitation in ferritic MA/ODS alloy MA957,** *J Nucl Mater***,** 329-33 (2004) 338-341.

[92] E.A. Marquis,**Core/shell structures of oxygen-rich nanofeatures in oxide-dispersion strengthened Fe-Cr alloys,** *Applied Physics Letters***,** 93 (2008) 181904.

[93] K. Oka, S. Ohnuki, S. Yamashita, N. Akasaka, S. Ohtsuka, H. Tanigawa,**Structure of nano-size oxides in ODS steels and its stability under electron irradiation,** *Materials Transactions***,** 48 (2007) 2563-2566.

[94] M.J. Alinger, G.R. Odette, D.T. Hoelzer,**On the role of alloy composition and processing parameters in nanocluster formation and dispersion strengthening in nanostuctured ferritic alloys,** *Acta Materialia***,** 57 (2009) 392-406.

[95] M.J. Alinger, G.R. Odette, D.T. Hoelzer,**The development and stability of Y-Ti-O nanoclusters in mechanically alloyed Fe-Cr based ferritic alloys,** *11th International Conference on Fusion Reactor Materials (ICFRM)***,** 329 (2003) 382-386.

[96] A. Ramar, N. Baluc, R. Schaublin,**On the lattice coherency of oxide particles dispersed in EUROFER97,** *J Nucl Mater***,** 386 (2009) 515-519.

[97] M. Klimiankou, R. Lindau, A. Moslang,**TEM characterization of structure and composition of nanosized ODS particles in reduced activation ferritic-martensitic steels,** *J Nucl Mater***,** 329-33 (2004) 347-351.

[98] R. Lindau, A. Moslang, M. Schirra,**Thermal and mechanical behaviour of the reduced-activation-ferritic-martensitic steel EUROFER,** *Fusion Engineering and Design***,** 61-2 (2002) 659-664.

[99] R. Lindau, A. Moslang, M. Rieth, M. Klimiankou, E. Materna-Morris, A. Alamo, A.A.F. Tavassoli, C. Cayron, A.M. Lancha, P. Fernandez, N. Baluc, R. Schaublin, E. Diegele, G. Filacchioni, J.W. Rensman, B. van der Schaaf, E. Lucon, W. Dietz,**Present development status of EUROFER and ODS-EUROFER for application in blanket concepts,** *Fusion Engineering and Design***,** 75-9 (2005) 989-996.

[100] R. Lindau, A. Moslang, M. Schirra, P. Schlossmacher, M. Klimenkov,**Mechanical and microstructural properties of a hipped RAFM ODS-steel,** *J Nucl Mater***,** 307 (2002) 769-772.

[101] V. de Castro, T. Leguey, M.A. Monge, A. Munoz, R. Pareja, D.R. Amador, J.M. Torralba, M. Victoria,**Mechanical dispersion of Y2O3 nanoparticles in steel EUROFER 97: process and optimisation,** *J Nucl Mater***,** 322 (2003) 228-234.

[102] J.H. Ahn, H.J. Kim, I.H. Oh, Y.J. Kim,**Preparation of nano-sized ODS alloys by ball-milling using metallic salts,** *Journal of Alloys and Compounds***,** 483 (2009) 247-251.

[103] S. Ukai, S. Mizuta, T. Yoshitake, T. Okuda, M. Fujiwara, S. Hagi, T. Kobayashi,**Tube manufacturing and characterization of oxide dispersion strengthened ferritic steels,** *J Nucl Mater***,** 283 (2000) 702-706.

[104] M.J. Alinger, G.R. Odette, G.E. Lucas,**Tensile and fracture toughness properties of MA957: implications to the development of nanocomposited ferritic alloys,** *J Nucl Mater***,** 307 (2002) 484-489.

[105] W.J. Yang, G.R. Odette, T. Yamamoto, P. Miao, M.J. Alinger, M. Hribernik, J.H. Lee,**A critical stress-critical area statistical model of the K-Jc(T) curve for MA957 in the cleavage transition,** *J Nucl Mater***,** 367 (2007) 616-620.

[106] S. Ohtsuka, S. Ukai, H. Sakasegawa, M. Fujiwara, T. Kaito, T. Narita,**Nano-mesoscopic structural characterization of 9Cr-ODS martensitic steel for improving creep strength,** *J Nucl Mater***,** 367 (2007) 160-165.

[107] S. Ukai, S. Mizuta, M. Fujiwara, T. Okuda, T. Kobayashi,**Development of 9Cr-ODS martensitic steel claddings for fuel pins by means of ferrite to austenite phase transformation,** *Journal of Nuclear Science and Technology***,** 39 (2002) 778-788.

[108] Z. Oksiuta, N. Baluc,**Effect of mechanical alloying atmosphere on the microstructure and Charpy impact properties of an ODS ferritic steel,** *J Nucl Mater***,** 386 (2009) 426-429.

[109] S. Ukai, T. Nishida, H. Okada, T. Okuda, M. Fujiwara, K. Asabe,**Development of oxide dispersion strengthened ferritic steels for FBR core application .1. Improvement of mechanical properties by recrystallization processing,** *Journal of Nuclear Science and Technology***,** 34 (1997) 256-263.

[110] H. Bhadeshia,**Mechanically alloyed metals,** *Materials Science and Technology***,** 16 (2000) 1404-1411.

[111] T. Narita, S. Ukai, T. Kaito, S. Ohtsuka, T. Kobayashi,**Development of two-step softening heat treatment for manufacturing 12Cr-ODS ferritic steel tubes,** *Journal of Nuclear Science and Technology***,** 41 (2004) 1008-1012.

[112] H. Kishimoto, K. Yutani, R. Kasada, O. Hashitomi, A. Kimura,**Heavy-ion irradiation effects on the morphology of complex oxide particles in oxide dispersion strengthened ferritic steels,** *J Nucl Mater***,** 367 (2007) 179-184.

[113] W. Gale, T. Totemeier, **Smithells Metals Reference Book**, Eighth ed., *Elsevier*, 2004.

[114] R. Schaeublin, T. Leguey, P. Spatig, N. Baluc, M. Victoria,**Microstructure and mechanical properties of two ODS ferritic/martensitic steels,** *J Nucl Mater***,** 307 (2002) 778-782.

[115] C. Cayron, E. Rath, I. Chu, S. Launois,**Microstructural evolution of Y2O3 and MgAl2O4ODS EUROFER steels during their elaboration by mechanical milling and hot isostatic pressing,** *J Nucl Mater***,** 335 (2004) 83-102.

[116] Z. Oksiuta, M. Lewandowska, P. Unifantowicz, N. Baluc, K. Kurzydlowski,**Influence of Y2O3 and Fe2Y additions on the formation of nano-scale oxide particles and the mechanical properties of an ODS RAF steel,** *Fusion Engineering and Design***,** Volume 86, Issues 9-11, October 2011, Pages 2417-2420 (2011) 2417-2420.

[117] D.K. Smith, D.L. Finnegan, S.M. Bowen,**An inventory of long-lived radionuclides residual from underground nuclear testing at the Nevada test site, 1951-1992,** *Journal of Environmental Radioactivity***,** 67 (2003) 35-51.

[118] I.S. Kim, B.Y. Choi, C.Y. Kang, T. Okuda, P.J. Maziasz, K. Miyahara,**Effect of Ti and W on the mechanical properties and microstructure of 12% Cr base mechanical-alloyed nano-sized ODS ferritic alloys,** *Isij International***,** 43 (2003) 1640-1646.

[119] S. Ohtsuka, S. Ukai, M. Fujiwara, T. Kaito, T. Narita,**Improvement of creep strength of 9CrODS martensitic steel by controlling excess oxygen and titanium concentrations,** *Materials Transactions***,** 46 (2005) 487-492.

[120] D.T. Hoelzer, J. Bentley, M.A. Sokolov, M.K. Miller, G.R. Odette, M.J. Alinger,**Influence of particle dispersions on the high-temperature strength of ferritic alloys,** *J Nucl Mater***,** 367 (2007) 166-172.

[121] S. Ukai, M. Fujiwara,**Perspective of ODS alloys application in nuclear environments,** *J Nucl Mater***,** 307 (2002) 749-757.

[122] S. Ohtsuka, S. Ukai, A. Fujiwara, T. Kaito, T. Narita,**Nano-structure control in ODS martensitic steels by means of selecting titanium and oxygen contents,** *Journal of Physics and Chemistry of Solids***,** 66 (2005) 571-575.

[123] C. Capdevila, M.K. Miller, K.F. Russell, J. Chao, J.L. Gonzalez-Carrasco,**Phase separation in PM 2000 (TM) Fe-base ODS alloy: Experimental study at the atomic level,** *Materials Science and Engineering a-Structural Materials Properties Microstructure and Processing***,** 490 (2008) 277-288.

[124] M. Klimenkov, R. Lindau, A. Moslang,**TEM study of internal oxidation in an ODS-Eurofer alloy,** *J Nucl Mater***,** 386 (2009) 557-560.

[125] P. Miao, G.R. Odette, T. Yamamoto, M. Alinger, D. Klingensmith,**Thermal stability of nano-structured ferritic alloy,** *J Nucl Mater***,** 377 (2008) 59-64.

[126] J.S. Lee, C.H. Jang, I.S. Kim, A. Kimura,**Embrittlement and hardening during thermal aging of high Cr oxide dispersion strengthened alloys,** *J Nucl Mater***,** 367 (2007) 229-233.

[127] V.K. Shamardin, V.N. Golovanov, T.M. Bulanova, A. Povstyanko, A.E. Fedoseev, Z.E. Ostrovsky, Y.D. Goncharenko,**Evolution of the mechanical properties and microstructure of ferritic-martensitic steels irradiated in the BOR-60 reactor,** *J Nucl Mater***,** 307 (2002) 229-235.

[128] H. Kinoshita, N. Akasaka, H. Takahashi, I. Shibahara, S. Onose,**Microstructural change on electron-irradiated oxide dispersion strengthened ferritic steels,** *J Nucl Mater***,** 191 (1992) 874-878.

[129] J. Saito, T. Suda, S. Yamashita, S. Ohnuki, H. Takahashi, N. Akasaka, M. Nishida, S. Ukai,**Void formation and microstructural development in oxide dispersion strengthened ferritic steels during electron-irradiation,** *J Nucl Mater***,** 263 (1998) 1264-1268.

[130] J. Chen, P. Jung, W. Hoffelner, H. Ullmaier,**Dislocation loops and bubbles in oxide dispersion strengthened ferritic steel after helium implantation under stress,** *Acta Materialia***,** 56 (2008) 250-258.

[131] J. Chen, P. Jung, M.A. Pouchon, T. Rebac, W. Hoffelner,**Irradiation creep and precipitation in a ferritic ODS steel under helium implantation,** *J Nucl Mater***,** 373 (2008) 22-27.

[132] M.A. Pouchon, J. Chen, M. Dobeli, W. Hoffelner,**Oxide dispersion strengthened steel irradiation with helium ions,** *J Nucl Mater***,** 352 (2006) 57-61.

[133] T.R. Allen, J. Gan, J.I. Cole, M.K. Miller, J.T. Busby, S. Shutthanandan, S. Thevuthasan,**Radiation response of a 9 chromium oxide dispersion strengthened steel to heavy ion irradiation,** *J Nucl Mater***,** 375 (2008) 26-37.

[134] P. Pareige, M.K. Miller, R.E. Stoller, D.T. Hoelzer, E. Cadel, B. Radiguet,**Stability of nanometer-sized oxide clusters in mechanically-alloyed steel under ion-induced displacement cascade damage conditions,** *J Nucl Mater***,** 360 (2007) 136-142.

[135] D.S. Gelles,**Microstructural examination of commercial ferritic alloys at 200 dpa,** *J Nucl Mater***,** 233 (1996) 293-298.

[136] I. Monnet, P. Dubuisson, Y. Serruys, M.O. Ruault, O. Kaitasov, B. Jouffrey,**Microstructural investigation of the stability under irradiation of oxide dispersion strengthened ferritic steels,** *J Nucl Mater***,** 335 (2004) 311-321.

[137] N. Akasaka, S. Yamashita, T. Yoshitake, S. Ukai, A. Kimura,**Microstructural changes of neutron irradiated ODS ferritic and martensitic steels,** *J Nucl Mater***,** 329-33 (2004) 1053-1056.

[138] S. Yamashita, K. Oka, S. Ohnuki, N. Akasaka, S. Ukai,**Phase stability of oxide dispersion-strengthened ferritic steels in neutron irradiation,** *J Nucl Mater***,** 307 (2002) 283-288.

[139] S. Yamashita, N. Akasaka, S. Ukai, S. Ohmiki,**Microstructural development of a heavily neutron-irradiated ODS ferritic steel (MA957) at elevated temperature,** *J Nucl Mater***,** 367 (2007) 202-207.

[140] K.C. Russell,**Phase Instability under Cascade Damage Irradiation,** *J Nucl Mater***,** 206 (1993) 129-138.

[141] H.J. Frost, K.C. Russell,**Particle stability with recoil resolution,** *Acta Metallurgica***,** 30 (1982) 953-960.

[142] W. Voegeli, K. Albe, H. Hahn,**Simulation of grain growth in nanocrystalline nickel induced by ion irradiation,** *6th International Conference on Computer Simulation of Radiation Effects in Solids***,** 202 (2002) 230-235.

[143] B. Radiguet, A. Etienne, P. Pareige, X. Sauvage, R. Valiev,**Irradiation behavior of nanostructured 316 austenitic stainless steel,** *J Mater Sci***,** 43 (2008) 7338-7343.

[144] T.D. Shen,**Radiation tolerance in a nanostructure: Is smaller better?,** *Nuclear Instruments & Methods in Physics Research Section B***,** 266 (2008) 921-925.

[145] S. Wurster, R. Pippan,**Nanostructured metals under irradiation,** *Scripta Materialia***,** 60 (2009) 1083-1087.

[146] U. Fischer, S.P. Simakov, P.P.H. Wilson,**Transmutation behaviour of Eurofer under irradiation in the IFMIF test facility and fusion power reactors,** *J Nucl Mater***,** 329-33 (2004) 228-232.

[147] H. Kishimoto, K. Yutani, R. Kasada, A. Kimura,**Helium cavity formation research on oxide dispersed strengthening (ODS) ferritic steels utilizing dual-ion irradiation facility,** *Fusion Engineering and Design***,** 81 (2006) 1045-1049.

[148] K. Yutani, H. Kishimoto, R. Kasada, A. Kimura,**Evaluation of Helium effects on swelling behavior of oxide dispersion strengthened ferritic steels under ion irradiation,** *J Nucl Mater***,** 367 (2007) 423-427.

[149] T. Yamamoto, G.R. Odette, P. Miao, D.J. Edwards, R.J. Kurtz,**Helium effects on microstructural evolution in tempered martensitic steels: In situ helium implanter studies in HFIR,** *J Nucl Mater***,** 386 (2009) 338-341.

[150] T. Yamamoto, G.R. Odette, P. Miao, D.T. Hoelzer, J. Bentley, N. Hashimoto, H. Tanigawa, R.J. Kurtz,**The transport and fate of helium in nanostructured ferritic alloys at fusion relevant He/dpa ratios and dpa rates,** *J Nucl Mater***,** 367 (2007) 399-410.

[151] R.J. Kurtz, G.R. Odette, T. Yamamoto, D.S. Gelles, P. Miao, B.M. Oliver,**The transport and fate of helium in martensitic steels at fusion relevant He/dpa ratios and dpa rates,** *J Nucl Mater***,** 367 (2007) 417-422.

[152] M.K. Miller, **Atom Probe Tomography**, *Kluwer Academic/Plenum*, New York, 2000.

[153] G.L. Kellogg, T.T. Tsong,**Pulsed Laser-Induced Atom-Probe Mass-Spectroscopy,** *Ultramicroscopy***,** 5 (1980) 259-260.

[154] in, 2011.

[155] C.A. Williams, in, University of Oxford, 2008.

[156] J.H. Bunton, J.D. Olson, D.R. Lenz, T.E. Kelly,**Advances in pulsed-laser atom probe: Instrument and specimen design for optimum performance,** *Microscopy and Microanalysis***,** 13 (2007) 418-427.

[157] D.R. Kingham,**The Post-Ionization Of Field Evaporated Ions - A Theoretical Explanation Of Multiple Charge States,** *Surf Sci***,** 116 (1982) 273-301.

[158] D. Hudson, G.D.W. Smith, B. Gault,**Optimisation of mass ranging for atom probe microanalysis and application to the corrosion processes in Zr alloys,** *Ultramicroscopy***,** 111 (2011) 480-486.

[159] P. Bas, A. Bostel, B. Deconihout, D. Blavette,**A general protocol for the reconstruction of 3d atom-probe data,** *Applied Surface Science***,** 87-8 (1995) 298-304.

[160] B. Gault, M.P. Moody, F. de Geuser, G. Tsafnat, A. La Fontaine, L.T. Stephenson, D. Haley, S.P. Ringer,**Advances in the calibration of atom probe tomographic reconstruction,** *J Appl Phys***,** 105 (2009) 034913.

[161] Cameca, **Cameca IVAS User Guide**, 2011.

[162] T.T. Tsong,**Field-Ion Image-Formation,** *Surf Sci***,** 70 (1978) 211-233.

[163] B.P. Geiser, T.F. Kelly, D.J. Larson, J. Schneir, J.P. Roberts,**Spatial distribution maps for atom probe tomography,** *Microscopy and Microanalysis***,** 13 (2007) 437-447.

[164] J.F. Ziegler, J.P. Biersack, U. Littmark, **Stopping and Range of Ions in Matter**, *Pergamon*, New York, 1984.

[165] J.C. Sublet, G.J. Butterworth,**The neutronic basis for elemental substitution in martensitic steels,** *J Nucl Mater***,** 212-215 (1994) 695-700.

[166] O.C. Hellman, J.A. Vandenbroucke, J. Rusing, D. Isheim, D.N. Seidman,**Analysis of three-dimensional atom-probe data by the proximity histogram,** *Microscopy and Microanalysis***,** 6 (2000) 437-444.

[167] J.M. Hyde, C.A. English,**An analysis of the structure of irradiation induced Cu-enriched clusters in low and high nickel welds,** *MRS 2000 Fall Meeting***,** 650 (2000) R6.6.1.

[168] D. Vaumousse, A. Cerezo, P.J. Warren,**A procedure for quantification of precipitate microstructures from three-dimensional atom probe data,** *Ultramicroscopy***,** 95 (2003) 215-221.

[169] A. Morley, G. Sha, S. Hirosawa, A. Cerezo, G.D.W. Smith,**Determining the composition of small features in atom probe: bcc Cu-rich precipitates in an Fe-rich matrix,** *Ultramicroscopy***,** 109 (2009) 535-540.

[170] S. Esmaeili, D. Vaumousse, M.W. Zandbergen, W.J. Poole, A. Cerezo, D.J. Lloyd,**A study on the early-stage decomposition in the Al-Mg-Si-Cu alloy AA6111 by electrical resistivity and three-dimensional atom probe,** *Philos Mag***,** 87 (2007) 3797-3816.

[171] L.T. Stephenson, M.P. Moody, P.V. Liddicoat, S.P. Ringer,**New techniques for the analysis of fine-scaled clustering phenomena within atom probe tomography (APT) data,** *Microscopy and Microanalysis***,** 13 (2007) 448-463.

[172] R.K.W. Marceau, L.T. Stephenson, C.R. Hutchinson, S.P. Ringer,**Quantitative atom probe analysis of nanostructure containing clusters and precipitates with multiple length scales,** *Ultramicroscopy***,** 111 (2011) 738-742.

[173] R.P. Kolli, D.N. Seidman,**Comparison of compositional and morphological atom-probe tomography analyses for a multicomponent Fe-Cu steel,** *Microscopy and Microanalysis***,** 13 (2007) 272-284.

[174] L.S. J.M. Hyde and C.A. English In: G.E. Lucas, M.A. Kirk Jr. and R.G. Elliman, Editors,, in, Materials Research Society, Pittsburgh, PA (2001), Boston, MA, 2000, pp. R6.6.1.

[175] E.A. Marquis, N.A. Yahya, D.J. Larson, M.K. Miller, R.I. Todd,**Probing the improbable: imaging C atoms in alumina,** *Materials Today***,** 13 (2010) 34-36.

[176] Y.M. Chen, T. Ohkubo, M. Kodzuka, K. Morita, K. Hono,**Laser-assisted atom probe analysis of zirconia/spinel nanocomposite ceramics,** *Scripta Materialia***,** 61 (2009) 693-696.

[177] M. Tsukada, H. Tamura, K.P. McKenna, A.L. Shluger, Y.M. Chen, T. Ohkubo, K. Hono,**Mechanism of laser assisted field evaporation from insulating oxides,** *Ultramicroscopy***,** 111 (2011) 567-570.

[178] F. Li, T. Ohkubo, Y.M. Chen, M. Kodzuka, F. Ye, D.R. Ou, T. Mori, K. Hono,**Laser-assisted three-dimensional atom probe analysis of dopant distribution in Gd-doped CeO(2),** *Scripta Materialia***,** 63 (2010) 332-335.

[179] M. Bachhav, R. Danoix, F. Danoix, B. Hannoyer, S. Ogale, F. Vurpillot,**Investigation of wustite (Fe(1-x)O) by femtosecond laser assisted atom probe tomography,** *Ultramicroscopy***,** 111 (2011) 584-588.

[180] K. Oh-Ishi, C.L. Mendis, T. Ohkubo, K. Hono,**Effect of laser power and specimen temperature on atom probe analyses of magnesium alloys,** *Ultramicroscopy***,** 111 (2011) 715-718.

[181] T.T. Tsong,**Pulsed-Laser-Stimulated Field-Ion Emission from Metal and Semiconductor Surfaces - a Time-of-Flight Study of the Formation of Atomic, Molecular, and Cluster Ions,** *Physical Review B***,** 30 (1984) 4946-4961.

[182] A. Cerezo, G.D.W. Smith, P.H. Clifton,**Measurement of temperature rises in the femtosecond laser pulsed three-dimensional atom probe,** *Applied Physics Letters***,** 88 (2006) 154103.

[183] A. Vella, B. Mazumder, G. Da Costa, B. Deconihout,**Field evaporation mechanism of bulk oxides under ultra fast laser illumination,** *J Appl Phys***,** 110 (2011) 044321.

[184] T.T. Tsong, Y.S. Ng, S.V. Krishnaswamy,**Quantification of atom-probe FIM data and an application to investigation of surface segregation of alloys,** *Applied Physics Letters***,** 32 (1978) 778-780.

[185] D.W. Saxey,**Correlated ion analysis and the interpretation of atom probe mass spectra,** *Ultramicroscopy***,** 111 (2011) 473-479.

[186] W. Steurer, S. Surnev, G. Barcaro, A. Fortunelli, F. Netzer,**Reduction of a polar oxide surface in a strong DC-field,** *American Physical Society Meeting***,** (2011) Z10.012.

[187] F. De Geuser, B. Gault, A. Bostel, F. Vurpillot,**Correlated field evaporation as seen by atom probe tomography,** *Surf Sci***,** 601 (2007) 536-543.

[188] M. Miller, A. Cerezo, M. Heatherington, G.D.W. Smith, **Atom Probe Field Ion Microscopy**, *Clarendon Press*, Oxford, 1996.

[189] N.V. Petrova, I.N. Yakovkin,**Monte Carlo simulation of CO and O coadsorption and reaction on Pt(111),** *Surf Sci***,** 578 (2005) 162-173.

[190] W.C. Wang, M. Badylevich, V.V. Afanas'ev, A. Stesmans, C. Adelmann, S. Van Elshocht, J.A. Kittl, M. Lukosius, C. Walczyk, C. Wenger,**Injection and trapping of electrons in Y(2)O(3) layers on Si,** *Fundamentals and Technology of Multifunctional Oxide Thin Films (Symposium G, Emrs 2009 Spring Meeting)***,** 8 (2010) 012028.

[191] H.Y. Xiao, F. Gao, W.J. Weber,**Ab initio investigation of phase stability of Y(2)Ti(2)O(7) and Y(2)Zr(2)O(7) under high pressure,** *Physical Review B***,** 80 (2009) 212102.

[192] M.J. Alinger, G.R. Odette, D.T. Hoelzer,**The development and stability of Y-Ti-O nanoclusters in mechanically alloyed Fe-Cr based ferritic alloys,** *J Nucl Mater***,** 329-33 (2004) 382-386.

[193] Q. Ma,**Coarsening of intermetallic or compound precipitates in binary systems,** *Metallurgical and Materials Transactions A (Physical Metallurgy and Materials Science)***,** 31A (2000).

[194] Z. Oksiuta, *Private Communication*, (2009)

[195] P. Unifantowicz, T. Plocinski, C.A. Williams, R. Schaublin, N. Baluc,**Structure of complex oxide nanoparticles in a Fe-14Cr-2W-0.3Ti-0.3Y2O3 ODS RAF steel,** *J Nucl Mater***,** Submitted article (2011).

[196] N.U. Navi, G. Kimmel, J. Zabicky, S.V. Ushakov, R.Z. Shneck, M.H. Mintz, A. Navrotsky,**Yttrium Substitution in MTiO(3) (M=Ca, Sr, Ba and Ca plus Sr plus Ba)**

**Perovskites and Implication for Incorporation of Fission Products into Ceramic Waste Forms,** *Journal of the American Ceramic Society***,** 94 (2011) 3112-3116.

[197] K. Kawamura, T. Maruyama, K. Nagata,**The equilibrium oxygen pressure over the Cr-Y2O3-YCrO3 coexistence measured with the galvanic cell using stabilized ZrO2 solid electrolyte,** *Metallurgical and Materials Transactions B-Process Metallurgy and Materials Processing Science***,** 26 (1995) 289-294.

[198] K.B. Helean, S.V. Ushakov, C.E. Brown, A. Navrotsky, J. Lian, R.C. Ewing, J.M. Farmer, L.A. Boatner,**Formation enthalpies of rare earth titanate pyrochlores,** *Journal of Solid State Chemistry***,** 177 (2004) 1858-1866.

[199] D. Djurovic, M. Zinkevich, F. Aldinger,**Thermodynamic modeling of the yttrium-oxygen system,** *Calphad-Computer Coupling of Phase Diagrams and Thermochemistry***,** 31 (2007) 560-566.

[200] E.M. Levin, H.F. McMurdie,**Cr2O3-Y2O3 Phase Diagram,** *NIST Standard Reference Database***,** 31 (1975) 04402.

[201] M.X. Zhang, Y.A. Chang,**Phase diagrams of Ti-AL-C, Ti-Y-O, Nb-Y-O, and Nb-Al-O at 1100C,** *Journal of Phase Equilibria***,** 15 (1994) 470-472.

[202] N. Mizutani, Y. Tajima, M. Kato,**Phase Relations in System Y2O3-TiO2,** *Journal of the American Ceramic Society***,** 59 (1976) 168-168.

[203] H. Fujitani, S. Asano,**Full-Potential Band Calculations on YTiO3 with a Distorted Perovskite Structure,** *Physical Review B***,** 51 (1995) 2098-2102.

[204] C. Hin, B.D. Wirth, J.B. Neaton,**Formation of Y2O3 nanoclusters in nanostructured ferritic alloys during isothermal and anisothermal heat treatment: A kinetic Monte Carlo study,** *Physical Review B***,** 80 (2009) 134118.

[205] Q. Guo, W.S. Oh, D.W. Goodman,**Titanium oxide films grown on Mo(110),** *Surf Sci***,** 437 (1999) 49-60.

[206] Y. Jiang, J.R. Smith, G.R. Odette,**Prediction of structural, electronic and elastic properties of Y(2)Ti(2)O(7) and Y(2)TiO(5),** *Acta Materialia***,** 58 (2010) 1536-1543.

[207] C.F. Chen, H.B. Yu, S.Q. Zheng,**First-principles study of hydrogen diffusion mechanism in Cr(2)O(3),** *Science China-Technological Sciences***,** 54 (2011) 88-94.

[208] M. Tamura, H. Sakasegawa, K. Shiba, H. Tanigawa, K. Shinozuka, H. Esaka,**Decomposition of Y(2)Ti(2)O(7) Particles in 8 Pct Cr Oxide-Dispersion-Strengthened Martensitic Steel during Tempering,** *Metallurgical and Materials Transactions a-Physical Metallurgy and Materials Science***,** 42A (2011) 2176-2188.

[209] Y. Jiang, J.R. Smith, G.R. Odette,**Formation of Y-Ti-O nanoclusters in nanostructured ferritic alloys: A first-principles study,** *Physical Review B***,** 79 (2009) 064103

[210] D. Murali, B.K. Panigrahi, M.C. Valsakumar, S. Chandra, C.S. Sundar, B. Raj,**The role of minor alloying elements on the stability and dispersion of yttria nanoclusters in nanostructured ferritic alloys: An ab initio study,** *J Nucl Mater***,** 403 (2010) 113-116.

[211] F. Matteucci, G. Cruciani, M. Dondi, G. Baldi, A. Barzanti,**Crystal structural and optical properties of Cr-doped Y2Ti2O7 and Y2Sn2O7 pyrochlores,** *Acta Materialia***,** 55 (2007) 2229-2238.

[212] D.J. Johnson, D.T. Amm, T. Laursen, S.K. Gupta,**Langmuir-Blodgett Deposition of Yttrium Arachidate,** *Thin Solid Films***,** 232 (1993) 245-251.

[213] W.Y. Kang, E.R. Bernstein,**Formation of yttrium oxide clusters using pulsed laser vaporization,** *Bulletin of the Korean Chemical Society***,** 26 (2005) 345-348.

[214] D.S. McClure, Z. Kiss,**Survey of the Spectra of the Divalent Rare Earth Ions in Cubic Crystals,** *Journal of Chemical Physics***,** 39 (1963) 3251-3258.

[215] H.J. Emeleus, **Advances in inorganic chemistry and radiochemistry**, *Academic press inc.*, London, 1986.

[216] D. Kumar, J. Sankar, K.G. Cho, V. Craciun, R.K. Singh,**Enhancement of cathodoluminescent and photoluminescent properties of Eu : Y2O3 luminescent films by vacuum cooling,** *Applied Physics Letters***,** 77 (2000) 2518-2520.

[217] L.N. Dinh, K.D. Frischknecht, M.A. Schildbach, T. Anklam, W. McLean,**Properties of Y2O3 nanocluster films deposited by Cu-vapor laser at room temperature,** *Journal of Vacuum Science & Technology a-Vacuum Surfaces and Films***,** 17 (1999) 3397-3400.

[218] C. Cantoni, E.D. Specht, A. Goyal, X. Li, M. Rupich,**Influence of oxygen deficiency on the out-of-plane tilt of epitaxial Y(2)O(3) films on Ni-5%W tapes,** *Journal of Materials Research***,** 24 (2009) 520-525.

[219] V. de Castro, E.A. Marquis, S. Lozano-Perez, R. Pareja, M.L. Jenkins,**Stability of nanoscale secondary phases in an oxide dispersion strengthened Fe-12Cr alloy,** *Acta Materialia***,** 59 (2011) 3927-3936.

[220] G.R. Odette, D.T. Hoelzer,**Irradiation-tolerant Nanostructured Ferritic Alloys: Transforming Helium from a Liability to an Asset,** *Jom-Us***,** 62 (2010) 84-92.

[221] A.M. Chaplanov, A.N. Shibko, T. Djakov, G. Mladenov,**Structural and phase-transformations in electron-beam-treated titanium films** *Thin Solid Films***,** 143 (1986) 187-192.

[222] A. Jotsons, A.S. Malin,**The ordered structure of Ti3O,** *Acta Crystallographica***,** B24 (1967) 211-213.

[223] F. Vasiliu, G.J. Norga, L. Fe, D. Wounters, D. Van der Biest,**The role of TiO in the perovskite nucleation and (111) orientation selection in sol-gel PZT layers,** *Journal of Optoelectronics and Advanced Materials***,** 5 (2003) 777-785.

[224] B. Dutta, E.J. Palmiere, C.M. Sellars,**Modelling the kinetics of strain induced precipitation in Nb microalloyed steels,** *Acta Materialia***,** 49 (2001) 785-794.

[225] M. Hansen, R. Elliott, F.A. Shunk, **Constitution of binary alloys**, Second ed., *McGraw-Hill*, New York, 1958.

[226] P. Klugkist, C. Herzig,**Tracer Diffusion of Titanium in Alpha-Iron,** *Physica Status Solidi a-Applied Research***,** 148 (1995) 413-421.

[227] H. Sakasegawa, F. Legendre, L. Boulanger, M. Brocq, L. Chaffron, T. Cozzik, J. Malaplate, J. Henry, Y.d. Carlan,**Stability of non-stoichiometric clusters in the MA957 ODS ferrtic alloy,** *J Nucl Mater***,** in press (2010).

[228] R.E. Stoller, G.R. Odette, B.D. Wirth,**Primary damage formation in bcc iron,** *J Nucl Mater***,** 251 (1997) 49-60.

[229] G.S. Was, T. Allen,**Intercomparison of microchemical evolution under various types of particle irradiation,** *J Nucl Mater***,** 205 (1993) 332-338.

[230] L.K. Mansur,**Theory of transitions in dose dependence of radiation effects in structural alloys,** *J Nucl Mater***,** 206 (1993) 306-323.

[231] G.S. Was,**Use and limitation of ion beams in understanding radiation effects in reactor materials,** *Transactions of the American Nuclear Society***,** 98 (2008) 342-357.

[232] H. Takahashi, N. Hashimoto, S. Watanabe,**Defect-Flow-Induced Grain-Boundary Migration with Segregation under Electron-Irradiation,** *Ultramicroscopy***,** 56 (1994) 193-199.

[233] R.E. Stoller,**The effect of free surfaces on cascade damage production in iron,** *J Nucl Mater***,** 307 (2002) 935-940.

[234] K. Asano, Y. Kohno, A. Kohyama, T. Suzuki, H. Kusanagi,**Microstructural Evolution of an Oxide Dispersion Strengthened Steel under Charged-Particle Irradiation,** *J Nucl Mater***,** 155 (1988) 928-934.

[235] A.G. Certain, K.G. Field, T.R. Allen, M.K. Miller, J. Bentley, J.T. Busby,**Response of nanoclusters in a 9Cr ODS steel to 1 dpa, 525 degrees C proton irradiation,** *J Nucl Mater***,** 407 (2010) 2-9.

[236] H.W. King,**Quantitative size-factors for metallic solid solutions,** *J Mater Sci***,** 1 (1966) 79-90.

[237] M.K. Miller, K.F. Russell, J. Kocik, E. Keilova,**Embrittlement of low copper VVER 440 surveillance samples neutron-irradiated to high fluences,** *J Nucl Mater***,** 282 (2000) 83-88.

[238] P. Pareige, R.E. Stoller, K.F. Russell, M.K. Miller,**Atom probe characterization of the microstructure of nuclear pressure vessel surveillance materials after neutron irradiation and after annealing treatments,** *J Nucl Mater***,** 249 (1997) 165-174.

[239] M. Nastar,**A mean field theory for diffusion in a dilute multi-component alloy: a new model for the effect of solutes on self-diffusion,** *Philos Mag***,** 85 (2005) 3767-3794.

[240] R.G. Faulkner,**Radiation-induced grain boundary segregation in nuclear reactor steels,** *J Nucl Mater***,** 251 (1997) 269-275.

[241] M.J. Hackett, J.T. Busby, M.K. Miller, G.S. Was,**Effects of oversized solutes on radiation-induced segregation in austenitic stainless steels,** *J Nucl Mater***,** 389 (2009) 265-278.

[242] J.D. Baird, A. Jamison,*Journal of Iron and Steel Institute***,** 204 (1966) 793-.

[243] R.G. Faulkner, S.H. Song, P.E.J. Flewitt, M. Victoria, P. Marmy,**Grain boundary segregation under neutron irradiation in dilute alloys,** *J Nucl Mater***,** 255 (1998) 189-209.

[244] P. Spatig, R. Stoenescu, P. Mueller, G.R. Odette, D. Gragg,**Assessment of irradiation embrittlement of the Eurofer97 steel after 590 MeV proton irradiation,** *J Nucl Mater***,** 386 (2009) 245-248.

[245] G.A. Cottrell, S.L. Dudarev, R.A. Forrest,**Immobilization of interstitial loops by substitutional alloy and transmutation atoms in irradiated metals,** *J Nucl Mater***,** 325 (2004) 195-201.

# Appendix A

M/e for various ion combinations, used to identify molecular ion peaks in the mass spectrum.

| | | Ti | Ti | Ti | Ti | Ti | V | Cr2 | Cr | Mn | Fe2 | Fe | Fe | Fe | Co | Y | Y2 | W | W | W | W |
|---|---|---|---|---|---|---|---|---|---|---|---|---|---|---|---|---|---|---|---|---|---|
| **1+** | | | 46 | 47 | 48 | 49 | 50 | 51 | 104 | 52 | 53 | 55 | 112 | 54 | 56 | 57 | 58 | 59 | 89 | 178 | 182 | 183 | 184 | 186 |
| **2+** | | | 23 | 23.5 | 24 | 24.5 | 25 | 25.5 | 52 | 26 | 26.5 | 27.5 | 56 | 27 | 28 | 28.5 | 29 | 29.5 | 44.5 | 89 | 91 | 91.5 | 92 | 93 |
| **3+** | | | 15.33 | 15.67 | 16.00 | 16.33 | 16.67 | 17.00 | 34.67 | 17.33 | 17.67 | 18.33 | 37.33 | 18.00 | 18.67 | 19.00 | 19.33 | 19.67 | 29.67 | 59.33 | 60.67 | 61.00 | 61.33 | 62.00 |
| **C** | | 12 | 58 | 59 | 60 | 61 | 62 | 63 | 116 | 64 | 65 | 67 | 124 | 66 | 68 | 69 | 70 | 71 | 101 | 190 | 194 | 195 | 196 | 198 |
| | | 12 | 29 | 29.5 | 30 | 30.5 | 31 | 31.5 | 58 | 32 | 32.5 | 33.5 | 62 | 33 | 34 | 34.5 | 35 | 35.5 | 50.5 | 95 | 97 | 97.5 | 98 | 99 |
| | | 12 | 19.33 | 19.67 | 20.00 | 20.33 | 20.67 | 21.00 | 38.67 | 21.33 | 21.67 | 22.33 | 41.33 | 22.00 | 22.67 | 23.00 | 23.33 | 23.67 | 33.67 | 63.33 | 64.67 | 65.00 | 65.33 | 66.00 |
| **C2** | | 24 | 70 | 71 | 72 | 73 | 74 | 75 | 128 | 76 | 77 | 79 | 136 | 78 | 80 | 81 | 82 | 83 | 113 | 202 | 206 | 207 | 208 | 210 |
| | | 24 | 35 | 35.5 | 36 | 36.5 | 37 | 37.5 | 64 | 38 | 38.5 | 39.5 | 68 | 39 | 40 | 40.5 | 41 | 41.5 | 56.5 | 101 | 103 | 104 | 104 | 105 |
| | | 24 | 23.33 | 23.67 | 24.00 | 24.33 | 24.67 | 25.00 | 42.67 | 25.33 | 25.67 | 26.33 | 45.33 | 26.00 | 26.67 | 27.00 | 27.33 | 27.67 | 37.67 | 67.33 | 68.67 | 69.00 | 69.33 | 70.00 |
| **N** | | 14 | 60 | 61 | 62 | 63 | 64 | 65 | 118 | 66 | 67 | 69 | 126 | 68 | 70 | 71 | 72 | 73 | 103 | 192 | 196 | 197 | 198 | 200 |
| | | 14 | 30 | 30.5 | 31 | 31.5 | 32 | 32.5 | 59 | 33 | 33.5 | 34.5 | 63 | 34 | 35 | 35.5 | 36 | 36.5 | 51.5 | 96 | 98 | 98.5 | 99 | 100 |
| | | 14 | 20.00 | 20.33 | 20.67 | 21.00 | 21.33 | 21.67 | 39.33 | 22.00 | 22.33 | 23.00 | 42.00 | 22.67 | 23.33 | 23.67 | 24.00 | 24.33 | 34.33 | 64.00 | 65.33 | 65.67 | 66.00 | 66.67 |
| **N2** | | 28 | 74 | 75 | 76 | 77 | 78 | 79 | 132 | 80 | 81 | 83 | 140 | 82 | 84 | 85 | 86 | 87 | 117 | 206 | 210 | 211 | 212 | 214 |
| | | 28 | 37 | 37.5 | 38 | 38.5 | 39 | 39.5 | 66 | 40 | 40.5 | 41.5 | 70 | 41 | 42 | 42.5 | 43 | 43.5 | 58.5 | 103 | 105 | 106 | 106 | 107 |
| | | 28 | 24.67 | 25.00 | 25.33 | 25.67 | 26.00 | 26.33 | 44.00 | 26.67 | 27.00 | 27.67 | 46.67 | 27.33 | 28.00 | 28.33 | 28.67 | 29.00 | 39.00 | 68.67 | 70.00 | 70.33 | 70.67 | 71.33 |
| **O** | | 16 | 62 | 63 | 64 | 65 | 66 | 67 | 120 | 68 | 69 | 71 | 128 | 70 | 72 | 73 | 74 | 75 | 105 | 194 | 198 | 199 | 200 | 202 |
| | | 16 | 31 | 31.5 | 32 | 32.5 | 33 | 33.5 | 60 | 34 | 34.5 | 35.5 | 64 | 35 | 36 | 36.5 | 37 | 37.5 | 52.5 | 97 | 99 | 99.5 | 100 | 101 |
| | | 16 | 20.67 | 21.00 | 21.33 | 21.67 | 22.00 | 22.33 | 40.00 | 22.67 | 23.00 | 23.67 | 42.67 | 23.33 | 24.00 | 24.33 | 24.67 | 25.00 | 35.00 | 64.67 | 66.00 | 66.33 | 66.67 | 67.33 |
| | | 18 | 76 | 77 | 78 | 79 | 80 | 81 | 134 | 82 | 83 | 85 | 142 | 84 | 86 | 87 | 88 | 89 | 119 | 208 | 212 | 213 | 214 | 216 |
| | | | 47 | 47.5 | 39 | 39.5 | 40 | 40.5 | 67 | 41 | 41.5 | 42.5 | 71 | 42 | 43 | 43.5 | 44 | 44.5 | 59.5 | 104 | 106 | 107 | 107 | 108 |
| | | | 37.33 | 37.67 | 26.00 | 26.33 | 26.67 | 27.00 | 44.67 | 27.33 | 27.67 | 28.33 | 47.33 | 28.00 | 28.67 | 29.00 | 29.33 | 29.67 | 39.67 | 69.33 | 70.67 | 71.00 | 71.33 | 72.00 |
| **O2** | | 32 | 78 | 79 | 80 | 81 | 82 | 83 | 136 | 84 | 85 | 87 | 144 | 86 | 88 | 89 | 90 | 91 | 121 | 210 | 214 | 215 | 216 | 218 |
| | | 32 | 39 | 39.5 | 40 | 40.5 | 41 | 41.5 | 68 | 42 | 42.5 | 43.5 | 72 | 43 | 44 | 44.5 | 45 | 45.5 | 60.5 | 105 | 107 | 108 | 108 | 109 |
| | | 32.00 | 26.00 | 26.33 | 26.67 | 27.00 | 27.33 | 27.67 | 45.33 | 28.00 | 28.33 | 29.00 | 48.00 | 28.67 | 29.33 | 29.67 | 30.00 | 30.33 | 40.33 | 70.00 | 71.33 | 71.67 | 72.00 | 72.67 |
| | | 36 | 94 | 95 | 96 | 97 | 98 | 99 | 152 | 100 | 101 | 103 | 160 | 102 | 104 | 105 | 106 | 107 | 137 | 226 | 230 | 231 | 232 | 234 |
| | | 36 | 47 | 47.5 | 48 | 48.5 | 49 | 49.5 | 76 | 50 | 50.5 | 51.5 | 80 | 51 | 52 | 52.5 | 53 | 53.5 | 68.5 | 113 | 115 | 116 | 116 | 117 |
| | | 36 | 31.33 | 31.67 | 32.00 | 32.33 | 32.67 | 33.00 | 50.67 | 33.33 | 33.67 | 34.33 | 53.33 | 34.00 | 34.67 | 35.00 | 35.33 | 35.67 | 45.67 | 75.33 | 76.67 | 77.00 | 77.33 | 78.00 |

# Appendix B

## DMax and NMin selection

The following function was used to generate figures similar to Figure 4.7 and Figure 4.10 for all necessary APT datasets. It invokes the posgen program written by Dr. Daniel Haley using an input .xml file, and records the number of clusters for a wide range of possible combinations of DMax and Nmin. This can be applied to APT data and to the APT data with the m values randomised (the randomisation is carried out using a function built into posgen) so that the extent of clustering can be compared.

```
function NminSelection(Posfile, Rrngfile, XMLfile, Rand)

%input the .pos file and .rrng file

ReplaceOneWord(XMLfile, 'POSFILE', Posfile, 'ClusterControlNMIN_POS.xml');
ReplaceOneWord('ClusterControlNMIN_POS.xml',        'RRNGFILE',        Rrngfile,
'ClusterControlNMIN_RRNG.xml');

%write output matrix outside the loop
ParamNmin = 2:10;
ParamDmax = 0.1:0.1:2;

OutputNoC = zeros(length(ParamDmax),length(ParamNmin));
OutputAtTot = zeros(length(ParamDmax),length(ParamNmin));

%define words to be replaced
words{1} =  'DMAX';
words{2} = 'NMIN';

nClustMat = zeros(length(ParamDmax)+1,length(ParamNmin)+1);
totAtomMat = nClustMat;

curRow=1;
curCol=1;
%loop through, and replace dmax with a number then run posgen
for curCol = 1:length(ParamNmin)
    curNMin = ParamNmin(curCol);
    for curRow = 1:length(ParamDmax)
        curDMax =ParamDmax(curRow);
        ReplaceText('ClusterControlNMIN_RRNG.xml',    [curDMax;    curNMin],words,
'clusterOp.xml')
        returncode = unix('posgen clusterOp.xml')
        if returncode ~=0
            error('posgen died')
        end
```

```
        % Import the cluster stats file
        newData1 = importdata('clusterstats.txt');

        %see how many clusters there are, and write to the output
        if isstruct(newData1)
            NoOfClusters = length(newData1.data(:,1));

            %sum up the total no of atoms and write to the output
            TotalAtoms = sum(sum(newData1.data(:,1:end-1)));

        else
            NoOfClusters = 0;
            TotalAtoms=0;

        end
        disp('Nmin iteration number')
        disp(curCol)
        nClustMat(curRow+1,1) = curDMax;
        nClustMat(1,curCol+1) = curNMin;
        nClustMat(1+curRow,1+curCol) = NoOfClusters;
        totAtomMat(1+curRow,1+curCol)=TotalAtoms;

    end

end


% Save the data matrices generated above to a file
%if file has randomised pos data add rand to the name
Randomised = Rand;
if Randomised == 1
OutputTitleNoC = strcat(Posfile, 'RandNoCOutput.txt');
OutputTitleAtomTot = strcat(Posfile, 'RandAtTotOutput.txt');
dlmwrite(OutputTitleNoC, nClustMat, ' ');
dlmwrite(OutputTitleAtomTot, totAtomMat, ' ');

else
    OutputTitleNoC = strcat(Posfile, 'NoCOutput.txt');
OutputTitleAtomTot = strcat(Posfile, 'AtTotOutput.txt');
dlmwrite(OutputTitleNoC, nClustMat, ' ');
dlmwrite(OutputTitleAtomTot, totAtomMat, ' ');
end

end
```

## L Selection

The following function was used to establish the appropriate value of surrounds distance L, (similar to the example shown in Figure 4.9). for all necessary APT datasets. It invokes the posgen program written by Dr. Daniel Haley using an input .xml file, and records the average composition of all the clusters in any given dataset for each set of cluster selection parameters. The DMax and Nmin parameters are fixed, and only L is varied in this case.

```
function LSelection(Posfile)

%input the .pos file and .rrng file

ReplaceOneWord('ClusterControlLVALUE.xml',          'POSFILE',          Posfile,
'ClusterControlLVALUE_POS.xml');
ReplaceOneWord('ClusterControlMatrix.xml', 'POSFILE', Posfile, 'clusterOp.xml');
returncode = unix('posgen clusterOp.xml')
if returncode ~=0
    error('posgen died')
end


%open file for the matrix composition
MatrixData = importdata('unclusterstatsMATRIX.txt');

%decompose the molecular ions
MAll = MatrixData.data;
MatrixDecomp = zeros(1,11);
MatrixDecomp(1,1) = MAll(1,1)+MAll(1,18);
MatrixDecomp(1,2) = MAll(1,2)+MAll(1,21);
MatrixDecomp(1,3) = MAll(1,3);
MatrixDecomp(1,4) = MAll(1,4);
MatrixDecomp(1,5) = MAll(1,5)+MAll(1,17)+MAll(1,21);
MatrixDecomp(1,6) = MAll(1,6);
MatrixDecomp(1,7)                                                                =
MAll(1,7)+MAll(1,12)+MAll(1,13)+MAll(1,14)+MAll(1,14)+MAll(1,15)+MAll(1,18)+MAll
(1,19)+MAll(1,19);
MatrixDecomp(1,8) = MAll(1,8)+MAll(1,12)+MAll(1,19);
MatrixDecomp(1,9) = MAll(1,9)+MAll(1,13)+MAll(1,14)+MAll(1,17);
MatrixDecomp(1,10) = MAll(1,10);
MatrixDecomp(1,11) = MAll(1,11)+MAll(1,15);

%getmatrix%
MatrixDePer = (MatrixDecomp/sum(MatrixDecomp))*100;

%wirte output matrix outside the loop
ParamNmin = 5;
ParamDmax = 1;
ParamL = 0.1:0.1:2;

% %define words to be replaced
words{1} =  'DMAX';
```

```
words{2} = 'NMIN';
words{3} = 'LVALUE';

curRow=1;
curCol=1;
%loop through, and replace dmax with a number then run posgen
curNMin = ParamNmin;
curDMax = ParamDmax;
for curRow = 1:length(ParamL)
        curL =ParamL(curRow);
        ReplaceText('ClusterControlLVALUE_POS.xml',      [curDMax;      curNMin;
curL],words, 'clusterOp.xml')
        returncode = unix('posgen clusterOp.xml')
        if returncode ~=0
            error('posgen died')
        end

        % Import the cluster stats file
        ClusterData = importdata('clusterstats.txt');
        if isstruct(ClusterData)
        %add up all the atoms for the compositions
        CAll = ClusterData.data(:,1:21);
        %decompose the molecular ions

        CDecomp = zeros(length(ClusterData.data(:,1)),11);

        CDecomp(:,1) = CAll(:,1)+CAll(:,18);
        CDecomp(:,2) = CAll(:,2)+CAll(:,21);
        CDecomp(:,3) = CAll(:,3);
        CDecomp(:,4) = CAll(:,4);
        CDecomp(:,5) = CAll(:,5)+CAll(:,17)+CAll(:,21);
        CDecomp(:,6) = CAll(:,6);
        CDecomp(:,7)                                                                =
CAll(:,7)+CAll(:,12)+CAll(:,13)+CAll(:,14)+CAll(:,14)+CAll(:,15)+CAll(:,18)+CAll
(:,19)+CAll(:,19);
        CDecomp(:,8) = CAll(:,8)+CAll(:,12)+CAll(:,19);
        CDecomp(:,9) = CAll(:,9)+CAll(:,13)+CAll(:,14)+CAll(:,17);
        CDecomp(:,10) = CAll(:,10);
        CDecomp(:,11) = CAll(:,11)+CAll(:,15);

        %bulk cluster compositions per cluster
        ClusterTotals = sum(CDecomp,2);
        for i = 1:length(CDecomp(:,1))
        ClusterBulkPer(i,:) = (CDecomp(i,:)/ClusterTotals(i,1))*100;
        end
        %do the mcorr step per cluster
%         MCorr = zeros(size(CDecomp));
%         MCorrPer = zeros(size(CDecomp));

        OnePerFe = CDecomp(:,1)/MatrixDePer(1,1);
        MCont = OnePerFe*MatrixDePer;
        MCorr = CDecomp - MCont;
        MCorr(MCorr<0)= 0;
        MCorrSum = sum(MCorr,2);
        %MCorrPer = (MCorr/sum(MCorr,2))*100;
        MCorrPer = zeros(size(ClusterBulkPer));
        for i = 1:length(MCorr(:,1))
        MCorrPer(i,:) = (MCorr(i,:)/MCorrSum(i,1))*100;
        end
```

```
        %average cluster comps bulk and MCorr with errors
        AvgClusterCompsBulk = sum(CDecomp)/sum(sum(CDecomp))*100;
        AvgClusterCompsErrorsBulk = std(ClusterBulkPer)/sqrt(length(MCorrPer));

        AvgClusterCompsMCorr = sum(MCorr)/sum(sum(MCorr))*100;
        AvgClusterCompsErrorsMCorr = std(MCorrPer)/sqrt(length(MCorrPer));

        %For total atoms in clusters
        NAtomBulk = sum(sum(CDecomp));
        NAtomCorr = sum(sum(MCorr));

        %for averaqe Rg
        AvgRg = (sum(ClusterData.data(:,23)))/length(ClusterData.data(:,23));

        %output results (all part of the loop)
        OutputAll(curRow,1) = curDMax;
        OutputAll(curRow,2) = NAtomBulk;
        OutputAll(curRow,3) = NAtomCorr;
        OutputAll(curRow,4) = AvgRg;
        OutputAll(curRow,5) = length(ClusterData.data(:,23));%totclusters
        OutputAll(curRow,6:16) = AvgClusterCompsMCorr;
        OutputAll(curRow,17:27) = AvgClusterCompsErrorsMCorr;
        OutputAll(curRow,28:38) = AvgClusterCompsBulk ;
        OutputAll(curRow,39:49) = AvgClusterCompsErrorsBulk;

        %output the values
        else
        OutputAll(curRow,1) = curDMax;
        OutputAll(curRow,2) = 0;
        OutputAll(curRow,3) = 0;
        OutputAll(curRow,4) = 0;
        OutputAll(curRow,5) = 0;

        %save pos files and move to folder
        dmax = num2str(curL,'% 10.2f');
        PosFileName = strcat('13036-', dmax);
        movefile('cluster.pos', PosFileName)
        movefile(PosFileName,
'C:\Users\Ceri\Documents\MATLAB\Clusterselection\posfiles')

        end

        disp('dmax value')
        disp(curDMax)

end
%savefile names
FileName = strcat(Posfile, 'LSelection.txt');
fid = fopen(FileName, 'w'); % Open for writing

%FinalOutput          =          horzcat(OutputAll,          AvgClusterCompsBulk,
AvgClusterCompsErrorsBulk, AvgClusterCompsMCorr, AvgClusterCompsErrorsMCorr);
%headers
for i=1:size(OutputAll,1)
   fprintf(fid, '%d ', OutputAll(i,:));
   fprintf(fid, '\n');
end
fclose(fid);
```

## ‘Peak –tail’ Correction

The following script fits an exponential curve to the tail of each peak in the mass spectrum, and assigns hits registered in the tail region of the mass spectrum to the maximum point of the peak on the mass spectrum (as shown in Figure 5.20.). The section of the peak used in the fitting process is defined by ranging the appropriate section on the mass spectrum using IVAS, and the range file is then modified so that it can be read using the ‘import data’ function in MATLAB.

```
%open epos file
[x,y,z,m,tof,Vdc,Vp,xdet,ydet,nulls,npulse]=readepos('13291Y2TiO5',            1,
10000000);

%load ranges
RNG = importdata('Mod13199tails.txt');
%Range = 7;

%define which are the after-ranges
RNGInx = find(RNG.data(:,11)==1);

%bin range
q= 0:0.01:400;

%preassign tailcorr and Additions
TailCorr = zeros(size(q));
Additions = zeros(size(q));
Backg = 5*(ones(size(q)));

%mass spec hist
E1(1,:)=histc(m,q);

for k=1:(length(RNGInx))
    Range=RNGInx(k);

    %for each range row get the appropriate after-range then fit
    min =  RNG.data(Range,1);
    max =  RNG.data(Range,2);
    REdge = RNG.data(Range-1,2);
    REdgeRound= round((REdge*10))/10;
    MassCharge = q(q>min&q<max);

    %Tails = hist(m(m>min&m<max), 0.01);
    Tails(1,:)=histc(m(m>min&m<max),MassCharge);

    %get values for a and b in the exp eqn
    MC = MassCharge(:);
    Tails2 = Tails(:);
    Fit = fit(MC,Tails2,'exp1');
    CV = coeffvalues(Fit);

    %find point where tail is down at the bg level
    BgIntercept = (log(10/CV(1)))/CV(2); %+ (CV(3))*exp(CV(4)*1);
```

```
    %BgIround= floor((BgIntercept*10))/10;
    BgIround= ceil((BgIntercept*1))/1;

    %generate histogram with same bin width as mass spec over this range
    I1 = find(q==REdgeRound);
    I2 = find(q==BgIround);
    Index = I1:I2;


    AllBins = q(I1:I2);
    %TailCorr(1,:) = analysisresults1.yfit;
    for i = 1:length(AllBins)
        TailCorr(:,i+(I1-1)) = (CV(1))*exp((CV(2))*(AllBins(i)));
    end
    % %sum all the removed stuff and add to max point
    StartRange =  RNG.data(Range-1,1);
    MaxPointValue = round((StartRange*100))/100 +0.01;
    MaxPoint = find(q==MaxPointValue);
    Additions (MaxPoint) = sum(TailCorr(I1:I2));

    clear Tails
    clear M2C
end

E2(1,:)=histc(m,q);
%find and remove the tail
CorrectedSpec = E2-TailCorr+Additions;

figure(1)
subplot(2,1,1); semilogy(q,E2);
xlim([15 90]);
ylim([1 10^7])
title('Original')
ylabel('Counts')
subplot(2,1,2); semilogy(q,CorrectedSpec);
xlim([15 90])
ylim([1 10^7])
title('Corrected')
xlabel('mass to charge state ratio')
ylabel('Counts')

figure(2)
semilogy(q,TailCorr)
```

## Saxey correlation table analysis

The following function generates the 'correlation table' type analysis of multi-hit pairs following Saxey's method described in §xx. This includes the method used to separate the clustered atoms in the .epos file corresponding to the APT reconstruction. This function invokes the 'splicepos' program written by Dr. Daniel Haley. 'Splicepos' maps the co-ordinates of the atom positions in .pos file to another .pos file, and displays the results in a file entitles 'output-mapping.txt'. This output file can then be used to find the atom co-ordinates in a .epos file corresponding to the same APT reconstruction so that the hit order information about the atoms can be obtained.

```
function ContTable(file,rng)

%input files
 FileName = file;
 ClusterFile = strcat(file,'.cluster');
UnixInput = ['splice-pos.exe', ' ', ClusterFile, '.pos', ' ', FileName, '.pos'];
[x,y,z,m,tof,Vdc,Vp,xdet,ydet,nulls,npulse]=readepos(FileName, 1, 100000000);

% %run splicepos
    returncode = unix(UnixInput)
              if returncode ~=0
                  error('splicepos died')
              end
%open output
IDX = (importdata('output-mapping.txt')+1)';
ns = 1;
n = 5000000;

 %load ranges
RNG = importdata(rng);
NoRNG = length(RNG.data);

%reorder so that it is ascending in the same way as the epos file
VpCluster = Vp(IDX);
[ReorderedVp,ReorderIndex] = sort(VpCluster);

xCluster = x(IDX);
ROxCluster = xCluster(ReorderIndex);
npulseCluster = npulse(IDX(ReorderIndex));
%find 1st hits and 2hit

G = find(npulse(IDX)>1);
for i=1:(length(G)-1)
FirstHit(i)=IDX(G(i));
SecondHit(i) = FirstHit(i)+1;

if ismember(SecondHit(i),IDX)
    FirstHit(i)=FirstHit(i);
    SecondHit(i)=SecondHit(i);
```

```
else
    FirstHit(i)=1;
    SecondHit(i)=1;
end
end

FirstHit(FirstHit==1)=[];
SecondHit(SecondHit==1)=[];

A = m(FirstHit); %FirstHit(m>min&m<max)
B  = m(SecondHit);

%load ranges
RNG = importdata(rng);
NoRNG = length(RNG.data);
FirstHit=find(npulse==2);
SecondHit = FirstHit+1;

A = m(FirstHit);
B = m(SecondHit);
%index the ranges as numbers
for i = 1:NoRNG
    min = RNG.data(i,1);
    max = RNG.data(i,2);
    A(A>min&A<max)=i;
    B(B>min&B<max)=i;
end
%remove pairs that don't fall within the assigned ranges
C= iswhole(A);
A=A(C==1);
B=B(C==1);

D = iswhole(B);
A=A(D==1);
B=B(D==1);

%create hist of all pairs
xedges = linspace(0,NoRNG+1,NoRNG+1);
yedges = linspace(0,NoRNG+1,NoRNG+1);
X = hist2(A,B, xedges, yedges);

%take log of the numbers to get a better scale
lnX=log10(X);
%plot all pairs as a 2d hist
figure(1); pcolor(lnX); colorbar ; axis off;

%double up the pairs so that sums =0
Original = X +X'-diag(diag(X));
X2 = X +X'-diag(diag(X));

%loop to iterate removing the self ion pairs
for i=1:100

%create contingency table
Totals1 = sum(X2,1);
Totals2 = sum(X2,2);
TT = sum(Totals1);

for a=1:length(Totals1)
```

```
   for b=1:length(Totals1)

    Prob(a,b) = (Totals1(a)*Totals2(b))/TT;

   end
end
%Prob=sum(X2)/sum(sum(X2));
DiagP = diag(diag(Prob));

%replace self ion pairs with the expected value (to give table of
%correlations that look for correlations with everything but itself)
Diag = diag(diag(X2));
X2 = X2-Diag+DiagP;
end
Dev = X2-Prob;
end
```